



Palacký University
Olomouc

Modelling of Carbon Nanomaterials and Their Interactions

Mgr. Michal Langer

A thesis submitted in fulfillment of the requirements for the degree of
Doctor of Philosophy

Supervisor: prof. RNDr. Michal Otyepka, Ph.D.

Department of Physical Chemistry, 2022

Declaration of the author

I declare that this thesis and the work presented in it are my own and has been generated by me as a result of my own original research. I have duly acknowledged all the sources of information which have been used in this thesis. Neither the thesis nor any of its parts was previously used for obtaining any academic degree.

Olomouc, June 2022

Michal Langer

Acknowledgement

Firstly, I would like to convey my sincere gratitude and appreciation to my supervisor Michal Otyepka for his guidance, excellent ideas, and patience. I am thankful that he provided me the opportunity to join his research group.

I am also grateful to my family and close friends who has always supported me when pursuing my personal dreams. Děkuji.

Bibliographical identification:**Author:** Mgr. Michal Langer**Title:** Modelling of Carbon Nanomaterials and Their interactions**Type of thesis:** Dissertation**Workplace:** Department of Physical Chemistry, Palacký University in Olomouc, Faculty of Science**Supervisor:** Prof. RNDr. Michal Otyepka, Ph.D.**The year of presentation:** 2022**Keywords:** Carbon dots, molecular modelling, molecular dynamics, time dependent density functional theory, self-assembly, optical properties, photoluminescence**Number of pages:** 104**Language:** English**Abstract:**

Modelling the physicochemical properties of systems using supercomputers is one of the established approaches in chemistry today. It can complement experiments and/or shed light on phenomena that are not accessible by any experimental technique. In my research, I have focused mainly on carbon dots (CDs), but also on other nanosystems such as graphene derivatives and perovskites. CDs can be prepared from different precursors under different external conditions, resulting in different types of CDs that exhibit fluorescence. The application potential of CDs for biological imaging, sensing, etc. is promising, however, the unresolved photoluminescence of CDs needs to be addressed first. In this work, I show that we have been able to address various questions in the CD field using different theoretical approaches, e.g., molecular dynamics (MD) simulations, calculations based on time-dependent density functional theory (TDDFT), and the second-order coupled cluster model CC2. We have provided atomistic details of the dynamics and structural arrangement of quasi-spherical CDs. Our MD simulations also demonstrated the tendency of the molecular fluorophore IPCA to non-covalently bind to or incorporate into CDs. Conformational space sampling then helped us to generate configurations of IPCA and CD molecules whose optical properties were revealed by TDDFT calculations in gas and water and quantum mechanics/molecular mechanics (QM/MM) calculations in the CD environment. A combination of density functional theory (DFT) calculations and/or MD simulations and experiments then supported the explanation of the quenching of CD fluorescence after the phase transition.

List of abbreviations

AA	All-Atom
AFM	Atomic Force Microscopy
AFCP	Absorption-Fluorescence Crossing Points
AMBER	Assisted Model Building with Energy Refinement
ATPCA	1-(2-aminoethyl)-5-oxo-1,2,3,5-tetrahydroimidazo[1,2-a]pyridine-7-carboxylic acid
BSSE	Basis Set Superposition Error
CC	Coupled Clusters
CD	Carbon Dot
CHELPG	CHarges from ELeCtrostatic Potentials using a Grid-based method
COM	Center-of-Mass
CND	Carbon NanoDot
CNTs	Carbon NanoTubes
CPCM	Conductor-like Polarizable Continuum Model
CPDs	Carbonized Polymer Dot
CQD	Carbon Quantum Dot
CZA	Citrazinic Acid
cLR	corrected Linear Response
CT	Charge Transfer
DFT	Density Functional Theory
DLPNO	Domain-based Local Pair Natural Orbital
EA	Electron Affinity
EE	Electronic Embedding
EPR	Electron Paramagnetic Resonance
FF	Force Field
FWHM	Full-Width-in-Half-Maximum
FTIR	Fourier Transform InfraRed
GCN	Cyanographene
GS	Ground State
GUI	Graphical User Interface
H-bond	Hydrogen bond
HF	Hartree-Fock
HPPT	4-hydroxy-1H-pyrrolo[3,4-c]pyridine-1,3,6(2H,5H)-trione
GAFF	Generalized Amber Force Field
GGA	Generalized Gradient approximation
GQD	Graphene Quantum Dot
GROMACS	GRoningen MACHine for Chemical Simulations
IE	Ionization Energy
IEF	Integral Equation Formalism
ISC	InterSystem Crossing
IPCA	5-oxo-1,2,3,5-tetrahydroimidazo-[1,2- α]-pyridine-7-carboxylic acid
LDA	Local Density Approximation
LEPR	Light-induced Electron Paramagnetic Resonance
LJ	Lennard-Jones
LR	Linear Response

LUMO	Lowest Unoccupied Molecular Orbital
MCRTS	Monte Carlo Ray-Tracing Simulation
ME	Mechanical Embedding
MF	Molecular Fluorophore
MM	Molecular Mechanics
MD	Molecular Dynamics
NPA	Natural population analysis
NTO	Natural Transition Orbital
ONIOM	Our own N-layered Integrated molecular Orbital
OPLS-AA	Optimized Potentials for Liquid Simulations
PAHs	PolyAromatic Hydrocarbons
PCM	Polarizable Continuum Model
PE	Polarizable Embedding
PL	PhotoLuminescence
PME	Particle Mesh Ewald
PMF	Potential of Mean Forces
QCE	Quantum Confinement Effect
QM	Quantum Mechanics
QY	Quantum Yield
RISC	Reverse InterSystem Crossing
RESP	Restrained Electrostatic Potential
Rg	Radius of Gyration
RMSD	Root-Mean-Square Deviation
SAPT	Symmetry-Adapted Perturbation Theory
SCRF	Self-Consistent Reaction Field
SERS	Surface-Enhanced Raman Spectroscopy
SMD	Solvation Model based on solute electron Density
SS	State-Specific
TADF	Thermally Activated Delayed Fluorescence
TD-DFT	Time Dependent Density Functional Theory
TDM	Transition Dipole Moment
TEM	Transmission Electron Microscope
TPCA	5-oxo-3,5-dihydro-2H-thiazolo[3,2-a]pyridine-7-carboxylic acid
TPDCA	5-oxo-3,5-dihydro-2H-thiazolo[3,2-a]-pyridine-3,7-dicarboxylic acid
vdW	van der Waals
VEE	Vertical Excitation Energy
XPS	X-ray Photoelectron Spectroscopy
ZPVE	Zero Point Vibration Energy

Table of Contents

1	PREFACE OF THE THESIS	1
2	CHEMISTRY OF CARBON DOTS	3
2.1	NANOMATERIALS IN GENERAL.....	3
2.2	INTRODUCTION TO CARBON DOTS.....	4
2.3	STRUCTURE OF CARBON DOTS.....	6
2.4	INTERACTION OF CD WITH LIGHT.....	7
2.4.1	<i>Absorption of CDs</i>	<i>11</i>
2.4.2	<i>Emission of CDs.....</i>	<i>13</i>
2.4.3	<i>Molecular fluorophores in CDs</i>	<i>15</i>
3	METHODS	17
3.1	DENSITY FUNCTIONAL THEORY	17
3.1.1	<i>Calculation of excited states.....</i>	<i>20</i>
3.2	MOLECULAR MECHANICS	21
3.2.1	<i>Amber force field example.....</i>	<i>23</i>
3.3	MOLECULAR DYNAMICS.....	26
3.4	CALCULATIONS IN SOLVENTS.....	28
3.5	QM/MM.....	30
3.5.1	<i>Additive and subtractive schemes</i>	<i>31</i>
3.5.2	<i>QM/MM boundaries.....</i>	<i>31</i>
3.5.3	<i>QM/MM coupling.....</i>	<i>32</i>
3.5.4	<i>ONIOM.....</i>	<i>32</i>
4	STRUCTURAL DYNAMICS OF CARBON DOTS IN WATER AND N, N-DIMETHYLFORMAMIDE PROBED BY ALL-ATOM MOLECULAR DYNAMICS SIMULATIONS.....	34
5	CONFORMATIONAL BEHAVIOR AND OPTICAL PROPERTIES OF A FLUOROPHORE DIMER AS A MODEL OF LUMINESCENT CENTERS IN CARBON DOTS	37
6	MOLECULAR FLUOROPHORES SELF-ORGANIZE INTO C-DOT SEEDS AND INCORPORATE INTO C-DOT STRUCTURES	51
7	CONTRIBUTION OF THE MOLECULAR FLUOROPHORE IPCA TO EXCITATION-INDEPENDENT PHOTOLUMINESCENCE OF CARBON DOTS.....	61
8	CARBON DOTS DETECT WATER-TO-ICE PHASE TRANSITION AND ACT AS ALCOHOL SENSORS VIA FLUORESCENCE TURN-OFF/ON MECHANISM.....	75

9	CONCLUSION.....	81
10	REFERENCES.....	84
	LIST OF PUBLICATIONS.....	105
	APPENDIX A: PROGRESS AND CHALLENGES IN UNDERSTANDING OF PHOTOLUMINESCENCE PROPERTIES OF CARBON DOTS BASED ON THEORETICAL COMPUTATIONS.....	106

1 Preface of the thesis

Carbon dots (CDs), belong to extensively studied nanomaterials with a very broad application potential resulting from their bright photoluminescence (PL), high (photo)stability, easy surface modification, low toxicity, biocompatibility. These properties predetermine them to be used in many applications including bioimaging, optoelectronics, photocatalysis, (bio)sensing, and drug delivery and other areas. Nonetheless, the design of CDs with tailored properties is still hampered by a fairly limited understanding of the CD PL. There is still a continuing debate about the nature of fluorescence mechanism in CDs, the agreement on the origin of excitation-dependent emission in CDs is also missing. Moreover, CDs represent a broad group of matter as they can be prepared from diverse precursors under various external conditions, producing different products, which are fluorescent. Thus, they have quite a large structural complexity. This all makes them comprehensive and challenging material to study. The complexity of CDs and their interaction is concisely covered in the **chapter 2** of this thesis and in the **Appendix A**.

Here, theoretical methods and computational chemistry come to play and allow us to decompose the overall complex puzzle into pieces. Modelling of physicochemical properties can complement experiments and/or shed light on phenomena not reachable by any experimental technique. This have been the goal of my PhD research and this thesis, to understand the structural organization of CDs and other possible fluorophores present in final products of experimental synthetic procedures of CDs, and to provide the insight on their optical properties, namely absorption and light emission, using computations, while employing as real models of CDs as possible.

Theoretical works on CDs have mainly used the density functional theory (DFT) and molecular mechanics (MM) to describe their stability and properties. These techniques are briefly introduced in **chapter 3**.

I started the CDs research in 2017 and back then, only few modellings of less common amorphous CDs and some small *ad-hoc* models of small polyaromatic hydrocarbons (PAHs) were present in the field of theoretical modelling of CDs. To open the way toward complex studies of CDs, bigger models of real CDs are needed. I participated in the development of an automatic procedure for generation of a full model of real spherical CDs with graphitic core and with the

functional groups on the surface not only to perform molecular dynamics (MD) simulations of CDs. This study is shortly summarized **in chapter 4** even though it was published before my doctoral studies. Nevertheless, the automatization for creation of CDs models really helped us in other studies.

It is clear now that molecular fluorophores (MFs) are also present as side products in the final sample of some synthetic procedures of CDs, e.g., in condensation reactions of citric acid and ethylenediamine. It also appears that assemblies of MFs have absorption and emission bands in the similar regions as CDs. It is important to have full understanding of the optical properties of these MFs. Therefore, we investigated a prototypical molecular fluorophore, 5-oxo-1,2,3,5-tetrahydroimidazo-[1,2- α]-pyridine-7-carboxylic acid, IPCA. This story is presented in **chapter 5** of this work.

Knowledge of optical properties of IPCA molecules is one thing, but the knowledge of the effect of the surrounding, i.e., CDs, on their absorption and emission properties is crucial as well. First, we used MD simulations to study the structural organization of CD and IPCAs, which is described **in chapter 6**. The outcomes of MD simulations then served for the exploration of changes of optical properties when the IPCAs are confined in different positions within CD matrix, which is presented in **chapter 7**.

Finally, **chapter 8** demonstrate that theoretical methods can nicely complement experimental findings and combination of DFT and/or MD simulations and experiments were supportive in an explanation of quenching of CDs fluorescence after phase-transition.

2 Chemistry of Carbon dots

2.1 Nanomaterials in general

There are many definitions of nanomaterials in general. They can be defined as materials possessing, at minimum, one spatial dimension measuring 1–100 nm. Also, as structures with one or more dimensions in the same scale as de Broglie wavelength of electrons. The European Commission states that the particle size of at least half of the particles in the number size distribution must measure 100 nm or below to be called nanoparticle. Another definition states that if 50 % or more of the constituent particles of a material have one or more external dimensions in the size range 1 to 100 nm, then it can be called a nanomaterial.

Nanosystems can be classified according to their dimensionality (Figure 1) as zero-dimensional (0D) if all their dimensions are measured within the nanoscale; or one-dimensional (1D) if one dimension is larger than 100 nm, or two-dimensional 2D if two dimensions are outside the nanoscale. Three-dimensional nanosystems (3D) are not confined to nanoscale in any dimension. Fullerenes, carbon nanotubes (CNTs), graphene and bulk powders represent the most known carbon representants of these groups, respectively. Two principal factors causing the properties of nanomaterials to differ significantly from the bulk counterparts are quantum effects and increased relative surface area. Due to this, we could witness unusual electronic, optical, thermal, mechanical, and chemical properties. Their versatility in terms of the ability to be tailored for specific requirements highlights their enormous application potential.¹

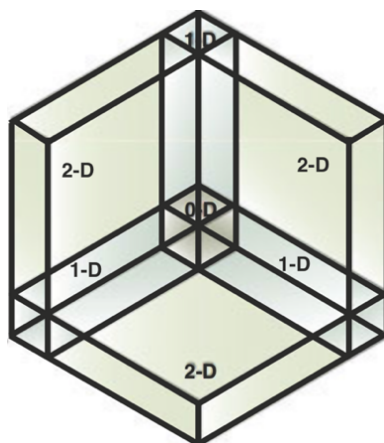


Figure 1. Classification of nanoscale dimensions.

Carbon-based materials play significant roles in the progress in the material science. From the traditional industrial carbon (e.g., activated carbon, carbon black) to new industrial carbon (e.g., carbon fibers, graphite) and new carbon nanomaterials such as graphene, CNTs and CDs, fundamental basic research and applications of carbon-based materials are popular in the fields of chemistry, materials, and other inter-disciplines due to their environmental friendliness.²

2.2 Introduction to carbon dots

Extensive review that provides an overview of theoretical studies addressing structural models and the electronic structure of various types of CDs in the context of their overall optical properties belongs to one of my several publications that I have been part of in my PhD studies.³ We (i) briefly summarized the experimental evidence on the structure and PL properties of individual classes of CDs, (ii) described state-of-the-art theoretical methods for description of absorption and fluorescence of CDs, (iii) provided an overview of theoretical studies addressing the structural models and electronic structure of CDs in the context of PL. Therefore, in this chapter, I am giving very concise introduction to the field of structure and optical properties of CDs, and for further reading, I refer the readers to the **Appendix A**, where this review paper is in its full form. If not stated otherwise, chapters 2.2–3 reference this paper. There are other excellent review papers on general information,^{4,5} synthesis,^{6,7} structure,^{8–10} applications,² toxicity,^{11,12} optical properties,¹³ of CDs.^{14–21}

CDs are still relatively new carbon nanomaterials as they were discovered in 2004. Actually, they were first observed as an fluorescent carbon by-product during the purification of single-walled carbon nanotubes, with no special interest in them.²² It was no sooner than two years later when nanoscale carbon nanoparticles, prepared by laser ablation, were referred as CDs.²³ Generally, there are several processes to create various sizes of nanomaterials, classified as top-down and bottom-up.²⁰ In top-down approaches the sample is basically a blank canvas and some external stimulus is used to write patterns, thus forming nanomaterials, i.e., producing very small structures from larger pieces of material. They usually require harsh conditions (strong oxidants, high temperatures) or severe physical techniques (laser ablation, arc discharge) to cut, decompose and/or exfoliate bulk carbonaceous materials into carbon nanoparticles.^{3,23–31} In bottom-up approaches, the final nanosystem is self-assembled into the desired arrangement from the precursors.³² Today, there are much more synthetic protocols for production of CDs (Table 1).⁷

Table 1. Overview of some top-down and bottom-up synthetic processes of CDs.⁷

Source	Method of preparation	Color of Emission	Size (nm)	Reference
Top-down				
Carbon nanotube	Electrochemical synthesis	Blue	2.8 ± 0.5	33
Carbon soot	Chemical oxidation	Green	2.0–6.0	34
Graphite electrode	Electrochemical synthesis	Bright yellow	4.0 ± 0.2	35
Graphite powders	Laser ablation	Red, black, and blue	1.5, 1.6, 1.8	36
Oligomer polyamide resin	Ultrasonic treatment	Bright white	2.0–4.0	37
Bottom-up				
L-Ascorbic acid	Hydrothermal treatment	Violet	2.0	38
Citric acid, urea	Microwave-assisted synthesis	Green	2.0–6.0	39
L-Cysteine	Thermal decomposition	Blue, yellow, red, green	1.0–3.5	40
Sodium alginate	Pyrolysis	Blue	< 10.0	41
SiCl ₄ , hydroquinone	Solvothermal treatment	Blue	7.0 ± 2.0	42
Glucose, HCl/NaOH	Ultrasonic treatment	Blue	< 5.0	43
Citric acid	Carbonization	Blue	4.8–9.0	44

CDs represent the nanomaterial of utmost importance, as they tick plenty of boxes on the list of suitable properties for calling a material having great application potential. They are low-cost, easy to synthesize, biocompatible, low toxic, chemically stable, water soluble, dispersible, biodegradable, they possess high electron mobility, high resistance to photobleaching, etc.⁴⁵ Most importantly, they have unique optical properties as not only quantum effect emerges due to zero dimensionality of CDs. This all predisposes CDs for plethora of environment-friendly applications in biomedical imaging and sensing,^{45–49} cancer therapy,⁵⁰ light-emitting devices,^{51,52} optoelectronic devices,^{20,53,54} photocatalysis,⁵⁵ functional materials,^{56,57} anti-counterfeiting.⁵⁸

2.3 Structure of carbon dots

It is commonly accepted to further classify CDs into a few subgroups — graphene quantum dots (GQDs), carbon nanodots (CNDs), carbonized polymer dots (CPDs), and carbon nitride C_3N_4 dots⁵⁹⁻⁶¹ — based on their inner structure, surface functionalities, properties, and different mechanism of formation.^{2,8,62,63}

Graphene quantum dots (GQDs)

GQDs are anisotropic CDs with lateral dimensions larger than their height (Figure 2). They are composed of one or multilayer graphitic layers with some functional chemical groups on a surface or edges.^{2,64} The thickness is usually less than 2 nm corresponding to a few (ca. 3–5) graphene layers.^{63,65} Their structure is derived from their typical top-down approach of synthesis.⁶⁶ GQDs can contain in-lattice doping and/or interlayer defects.^{67,68} This affects the electronic structure and thus PL of GQDs.

Carbon nanodots (CNDs)

CNDs can be further labelled either as carbon quantum dots (CQDs) or amorphous CNDs based on their inner structure (Figure 2).⁸ While the core of CQDs is mostly consisted of sp^2 hybridized carbon atoms, the core of amorphous CNDs possesses sp^3 hybridized carbons.⁶⁹⁻⁷⁵ CNDs are often produced from bottom-up chemical methods from small carbon containing precursors like citric acid, polymers, biomass, and others.⁷⁶ Chemically synthesized CNDs are quasi-spherical with the diameter up to 10 nm, and consist of a carbonic core (multilayer graphitic layers) and a shell made of surface functional groups.⁷⁷⁻⁸⁰ The core of the CDs is typically considered as a fragment of a π -conjugated system (sp^2 carbon domains), while the CD surface consists of bonded functional groups and may also include some MFs. Surface functional groups are typically either electron donating groups $-NH_2$, $-OH$, $-OR'$, $-OCOR'$, or electron withdrawing groups $-X$, $-CHO$, $=O$, $-COOR'$, $-COOH$, $-CN$, $-NH_3^+$, $-NO_2$.⁸¹⁻⁸³ The chemical nature of these chemical groups on the surface is dependent on the specific synthetic procedure.⁸⁴ For example, amino-functionalized fluorescent CDs have been prepared by hydrothermal treatment of glucosamine with excess pyrophosphate.⁸⁵

Carbonized polymer dots (CPDs)

CPDs are spherical core-shell hybrid nanostructures. They are composed of carbon cores with highly dehydrated crosslinking polymers or shells of abundant functional groups/polymer chains/functional groups and slight graphitization (see Figure 2). Thus, such polymeric structures present numerous functional groups attached to short polymer chains and highly cross-linked network structure generated by the process of dehydration and carbonization.^{86–88} Consequently, the CPDs not only retain the features of CNDs but also inherit important polymeric properties.^{87,89}

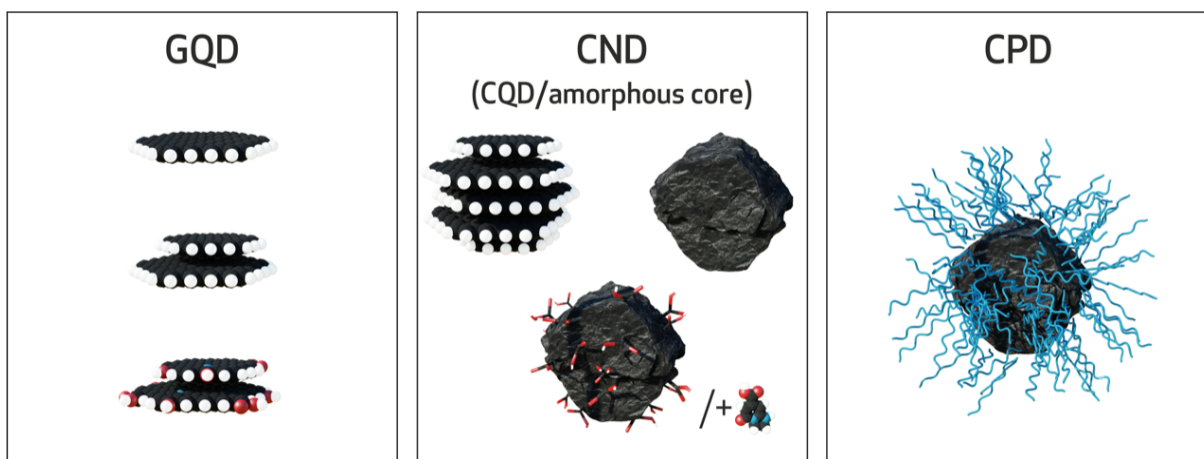


Figure 2. Three most common structural types of CDs, graphene quantum dots (GQD), carbon nanodots (CND) and carbonized polymer dots. During the synthesis of CNDs, molecular fluorophores can be found in the final fluorescent product (displayed as IPCA in bottom right of the middle panel).³

2.4 Interaction of CD with light

We mentioned above that extraordinary optical properties of CDs are the main driving force for their research. Therefore, it is relevant to shortly overview some of the effects that light can induce on the matter. Visible light (here just a light) is an electromagnetic radiation within the range of the electromagnetic spectrum that is perceived by the human eye, usually defined as having wavelengths in the range of 400–700 nm (Figure 3).

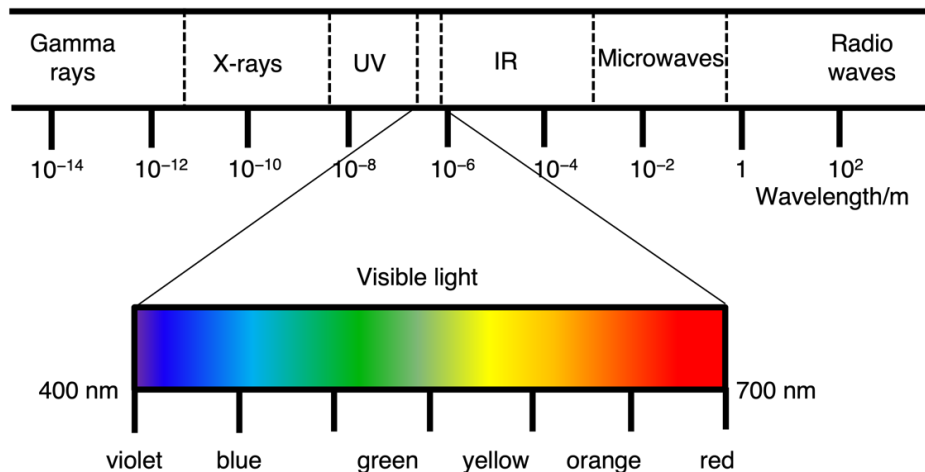


Figure 3. Electromagnetic spectrum diagram.

Classically, light–matter interactions are a result of an oscillating electromagnetic field (electric component **E** is perpendicular to magnetic component **B**). While electric and magnetic fields of the light always co-exist by virtue of Faraday’s Law, most materials only respond to **E**. Electromagnetic waves carry energy, momentum, and angular momentum away from their source particle; thus, they can resonantly interact with charged particles in the matter, most often bound electrons. Light clearly display wave–particle duality, as it behaves both as a particle and wave. Electromagnetic radiation behaves more like a classical wave at lower frequencies, but as a classical particle at higher frequencies, but never completely loses all qualities of one or the other. Also, wave characteristics is more pronounced when electromagnetic radiation is measured over relatively large timescales and distances while particle characteristics is more apparent on small timescales and distances. In quantum mechanics, the electromagnetic light is pictured as it consists of photons, uncharged elementary particles with zero rest mass which are the quanta of the electromagnetic field, responsible for all electromagnetic interactions. The interaction of electromagnetic radiation with matter on atomic level is comprehensively described with quantum electrodynamics.

Optical properties describe the interaction of light with matter. The changes in the optical properties modify some parameter of a light wave passing through a material or reflecting from it.⁹⁰ They can be observed either through changes to the light induced by the matter (absorption or emission of new light fields), or by light-induced changes to the matter (photochemistry, ionization, ...). The properties of samples can be deduced by studying such processes as a function of the control variables for the light field, such as amplitude, frequency, polarization, phase, etc.

The primary light-matter interactions are reflection, R, absorption, A and transmission, T; the secondary interactions are scattering, refraction, luminescence, diffraction (Figure 4). The conservation of energy ignoring the secondary effects can be expressed as $I_{\text{Incident-light}} = I_{\text{Reflection}} + I_{\text{Absorption}} + I_{\text{Transmission}}$, where I represents the intensity of the light. For propagation and scattering, the light acts more like electromagnetic wave, for absorption and emission, the light acts more like a bunch of particles (photons).

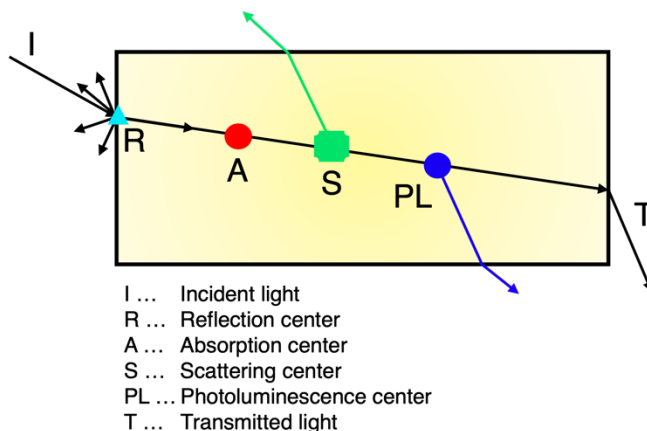


Figure 4. The schematic view on interaction of light with objects.

Incident beam of photons can be reflected at the interface, and the phenomenon called reflection is expressed by reflectivity. For example, metals appear shiny because the reflectivity is close to 100 %. Absorption of photon in chemical molecules happens only if the energy of the incident light corresponds to the energy difference between two stationary states of the molecule. The photon can also only be absorbed if the light can interact with the transition dipole moment μ_{if} (TDM, see Equation 1) between the states, characterized by the wavefunctions Ψ_i , Ψ_f .

$$\mu_{if} = \int \Psi_i^* \hat{\mu} \Psi_f d\tau \quad (1),$$

where $\hat{\mu}$ refers to the dipole moment operator.

The TDM is a vector, i.e., has an orientation in space. Also, only electronic transitions between different parity are allowed (symmetry selection rule), only transitions between states of the same spin multiplicity (spin selection rule) are allowed, and there must be nonzero differential overlap between states. The processes that may happen after the absorption of light are often expressed using the Jablonski diagram (Figure 5). The electron, populating the ground state (GS) electronic level S_0 , photoexcited by a light is vertically transitioned, according to the Franck-Condon

principle, to a vibrational state of a higher electronic level S_n . Franck-Condon principle states that when a molecule is undergoing an electronic transition, the nuclear configuration of the molecule does not experience any significant change because nuclei are much heavier than electrons, thus the electronic transition occurs on a time scale short compared to nuclear motion. As a result, the transition probability can be calculated at a fixed nuclear position.

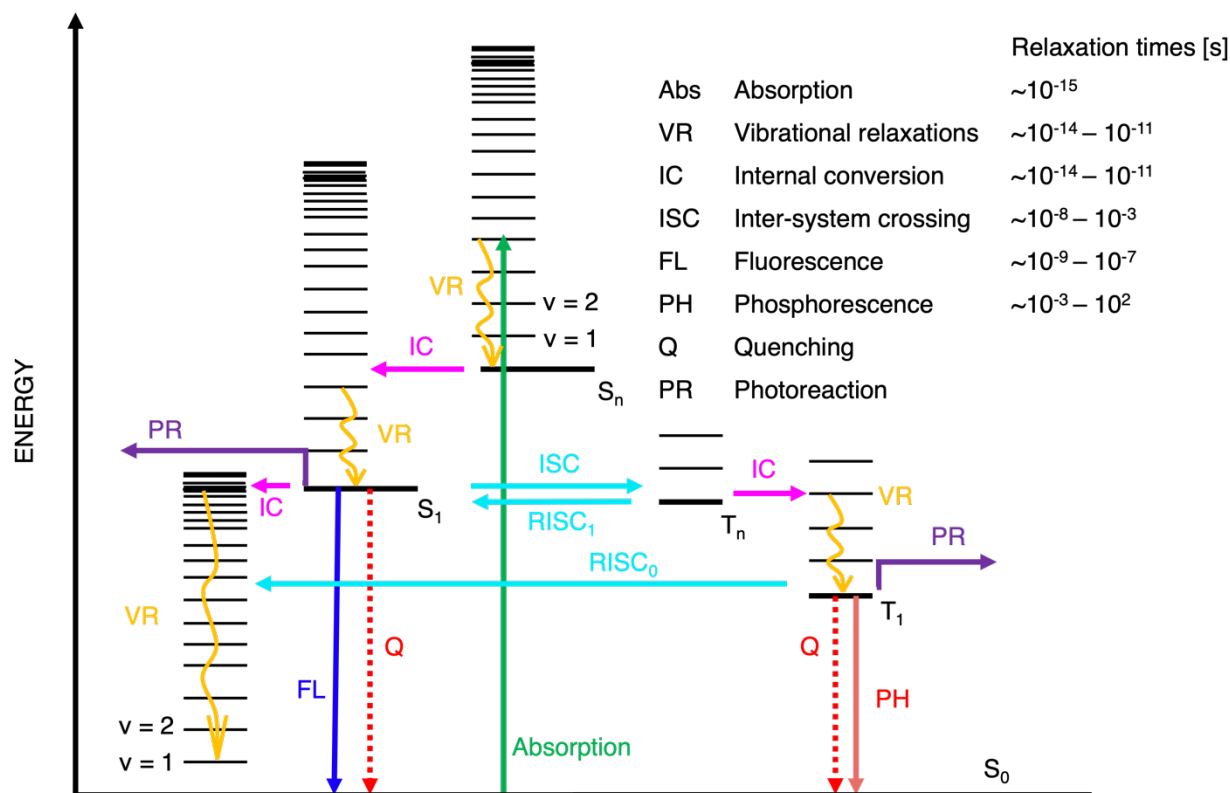


Figure 5. Jablonski diagram illustrating the electronic states of a molecule and the transitions between them.

After successful excitation, the photoexcited electron almost immediately undergoes vibrational relaxations and internal conversions to the lowest excited state (ES) S_1 , where internal conversion is the transition from S_n to S_{n-1} state. Ideally, the light is emitted. Such $S_1 \rightarrow S_0$ emission is known as Kasha emission. Kasha rule is valid for the vast majority of conjugated compounds in solution.⁹¹ Luminescence is an emission of radiation (except thermal emission) by a material due to absorption and conversion of energy. Emission is most often lower in energy than excitation. When the electron is populating the S_1 energy level, it may also undergo the so-called inter-system crossing to triplet state T_n . This can lead to the thermally activated delayed fluorescence (TADF) if the electron returns to S_1 energy level, or to phosphorescence, if the light is emitted during

$T_1 \rightarrow S_0$ transition (Figure 5). Nevertheless, other processes hindering the radiative pathway may occur. These are photoreactions and quenching of the PL.⁹²

The fraction of beam that is not reflected or absorbed is transmitted through the material. Thus, the fraction of light that is transmitted through a transparent material depends on the losses incurred by absorption and reflection, $R + A + T = 1$.

Refraction is the changing of speed of light upon transmission of light through a different medium, caused by polarization of the electrons in the material due to light photons transmitted through a material, making photons lose some of their energy. Refractive index n measures how much the light is slowed down in a material with respect to its velocity in vacuum. Scattering (Rayleigh scattering) happens when photon interacts with the electron orbiting around an atom and is deflected without any change in photon energy. Scattering reduces light intensity in the main direction by radiating part of the incident energy in all directions. Scattering is more pronounced for photons with low photon energies, i.e., blue color is scattered more than other colors in the visible spectrum making sky look blue.

2.4.1 Absorption of CDs

Although absorption and emission events are the most important interaction of light with CDs, the surface-enhanced Raman spectroscopy (SERS) has been also proposed to be exploited in this field, mostly in CDs/metal nanoparticle nanocomposites.^{93–96}

Naturally, optical properties of CDs are highly dependent on the synthetic method, where different synthetic strategy could lead to different absorption and emission behavior.⁹⁷ Anyway, common drastically simplified depictions have been proposed in this field. CDs typically exhibit strong absorption at 200–400 nm (due to C=C bonds) of $\pi-\pi^*$ transition and of $n-\pi^*$ transition (due C=O and C=N bonds) and absorption characteristics are varied with the content of surface groups, size of aromatic domains, nitrogen doping in the carbonized core.⁹⁸

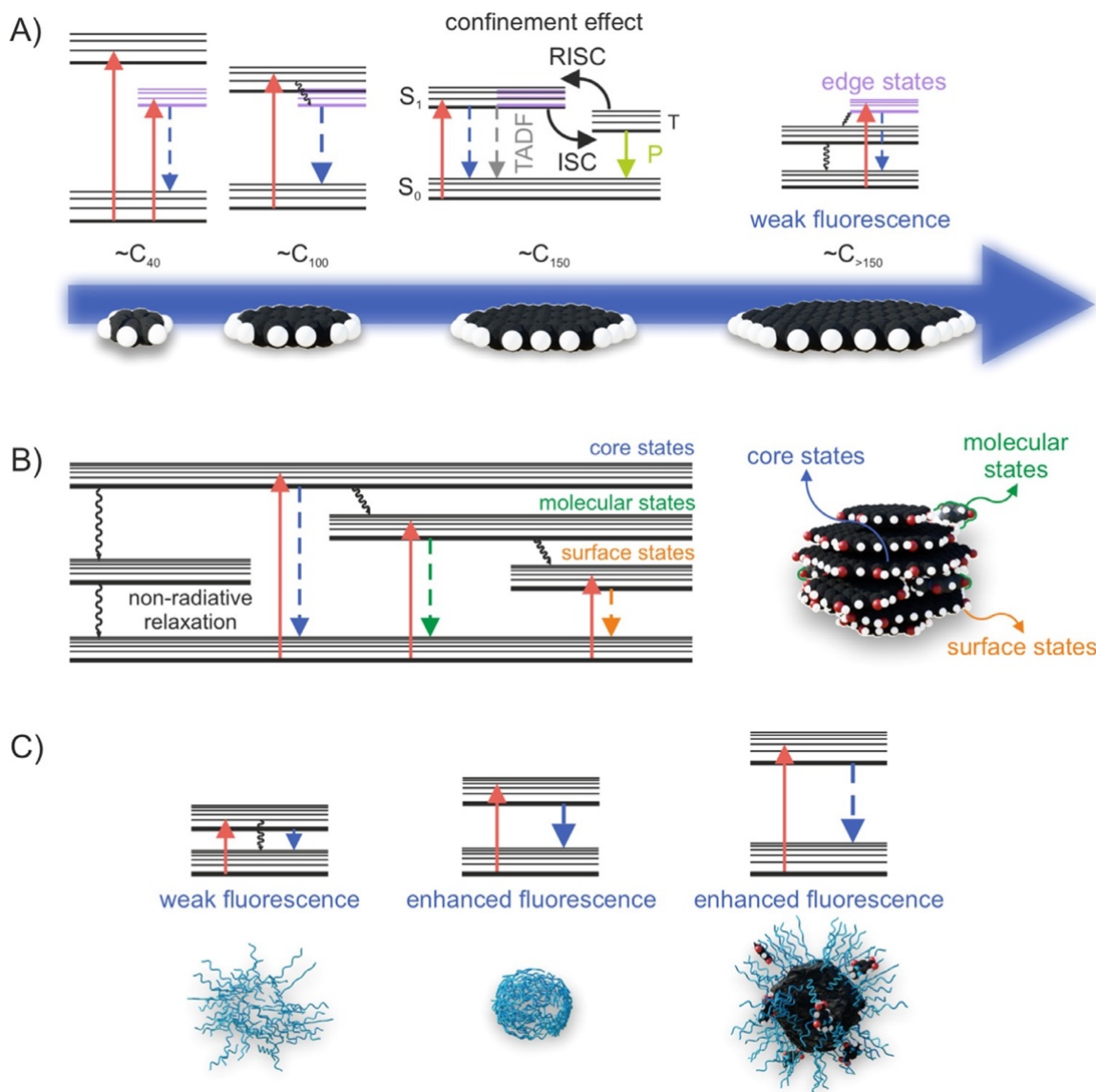


Figure 6. Possible PL mechanisms being present in CDs. (A) QCE related mainly to the size of π -conjugated domains in the CD core. (R)ISC refers to (reverse) intersystem crossing, which can lead to TADF; P refers to phosphorescence; (B) the multi-component PL typical for CNDs including the molecular PL; and (C) the CEE effect (blue lines in bottom panel represent polymers, black carbonized regions). Bold and regular horizontal lines represent electronic and vibrational energy levels, respectively. Only radiative and non-radiative decays are displayed as straight and wavy lines, respectively.³

Despite the not fully resolved structure of CDs, various phenomenological PL mechanisms have been proposed: (i) quantum confinement effect (QCE) due to aromatic core; (ii) doping effects, hybridization of the carbon backbone and surface functional groups, i.e., the defective and/or surface state PL; (iii) fluorescent molecules attached to the surface or interior of the CDs, i.e., the molecular PL (see section 2.4.3); (iv) the crosslink-enhanced emission (CEE) effect.⁸ All these mechanisms can occur in individual subclasses of CDs, and they can even manifest in a

cooperative manner. Therefore, CDs exhibit multi-center emission with three models being used to explain the PL origins of CDs, core and surface and molecular states (Figure 6).^{99,100} First, surface states are stemming from carbon hybridization and typical oxygen and nitrogen containing surface chemical groups and the corresponding electronic transitions are considered to be of low energy.^{83,101} Second, core states originate from aromatic π -conjugated sp^2 -carbon domains in CDs, which are often doped with heteroatoms; these are typically $\pi \rightarrow \pi^*$ transition.¹⁰² Third, molecular states are due to formation of molecular species in CDs samples and their corresponding transitions are typically of $n \rightarrow \pi^*$ or $\pi \rightarrow \pi^*$ character.¹⁰³

The significant dependence of PL on the synthesis temperature of the CDs can be shown on the example, where IPCA molecules and oligomers were found to dominate in the range of about 100–150 °C, whereas further heating led to carbonization and embedding of molecular PL clusters into the carbon core.¹⁰⁴

The optical properties of GQDs are mainly ruled by the size of π -conjugated domains, i.e., QCE, and surface/edge effects.^{64,65} This means the smaller the particle is, the fluorescence is more shifted to the blue part of visible spectrum, because the electronic energy levels are more distant for smaller particles. Contrary to GQDs, the intrinsic state luminescence and the QCE are their main PL mechanism of the CNDs.^{80,105} The optical properties of CPDs mainly originate from CEE effect, which make the relationship between structure and performance of CPDs more controllable.^{2,3,8}

2.4.2 Emission of CDs

Several reviews covering the topic of PL of carbon nanostructures were published.^{8,45,77,79,106} The fluorescence decay in CDs is often multicomponent, suggesting multiple decay pathways.⁹⁹ And these centers are not necessarily radiative and one or more of the pathways can often be related to non-radiative low energy levels, called trap states.¹⁰⁷ In general, the PL of CDs is tunable, meaning that the easy functionalization and diversity of CDs allow tailoring the final energy of the emitted light. For example, when surface states actively participate in the PL of CDs,¹⁰⁸ the intrinsic PL can be reduced by non-radiative decay into these defect surface states and a red shift in emission wavelengths can be observed.⁸ The emission spectra of moieties containing $-\text{COOH}$ and $-\text{NH}_2$ groups can also be affected by protonation state by modulating pH.^{64,79} The emission wavelength can also be tuned by the type, concentration and position of heteroatoms,^{64,109–114} where graphitic N doping was

shown to cause a red shift of the fluorescence of CQDs,¹⁰⁹ while pyridinic or pyrrolic nitrogens to cause usually a smaller red shift.¹¹² Nevertheless, the situation is not always clear.³ Pyridinic nitrogen was also observed to cause a blue shifted emission with respect to pristine GQD.^{114–116} Both red and blue shifts introducing pyrrolic or pyridinic nitrogens were obtained using hybrid^{112,115–117} or range separated functional.^{80,109,113,114,118} Theoretical calculations can help systematically investigate tunable PL properties of GQDs. For example, the effect of plethora potentially interesting structural features, e.g., different impact of armchair vs. zigzag edges, doping, defects in structure, edge-oxidation, and vacancies, was investigated.¹¹⁵

Quantum yield (QY) is an important characterization for CDs because of their potential to be used as imaging agents in biological samples. Extensive review on this topic stressed the importance of choice of precursors and synthetic approach on the efficiency of QY.⁷⁸ CDs suffer from the difficulty in producing high QY and long wavelength (>500 nm) emissive products, which are considered as a major disadvantage of CDs.¹¹⁹ One of the highest QY 93.3% was reported for CDs with emission at a short wavelength (417 nm),¹²⁰ probably because of the beneficial doping with N heteroatoms. The N-doping often enhances fluorescent QY of CNDs,^{79,121,122} and positive increase of QY was also observed after the heteroatom doping of CDs with boron, where QY could surpass 80 %.¹²³

Although fluorescence is the main radiative de-excitation pathway in CDs, significant ISC in the core states was observed, and thus the CDs can exhibit both fluorescence and phosphorescence.¹²⁴ Ultralong-lifetime (1.46 and 1.39 s) phosphorescence at room-temperature for CDs prepared from phosphoric acid with either ethanolamine or ethylenediamine was witnessed, which was visible for the naked eye for up to 10 s.^{125,126} This phosphorescence was only observed in the solid state and quenched in solution and the presence of phosphorus in the inner structure was the important factor for long-time emission. Nevertheless, the stabilization of triplet state, achieving the possible occurrence of phosphorescence in CDs, was not only demonstrated by the phosphorus doping,^{127,128} but also by nitrogen doping,¹²⁹ or formation of hydrogen-bonded (H-bonded) matrices.¹³⁰ Another phenomenon in relation to the triplet excitons, TADF, has been also recently associated with CDs,^{131–133} e.g., in aqueous solution by confining the fluorine and nitrogen co-doped CDs in silica nanoparticles.¹³⁴

One of the most fascinating features of CDs is the excitation-dependent PL. This effect can be attributed to their complex structures and selective excitations of individual structural features.³ As

each layer in CNDs can have different composition, they can be selectively excited independently under different conditions and the resulting fluorescence is then dependent on which fragment was excited and which internal conversion takes place prior to fluorescence.

2.4.3 Molecular fluorophores in CDs

Potential ambiguities can occur in the experimental structural characterization of CDs (high-resolution X-ray photoelectron spectroscopy, Fourier transformed infrared spectroscopy, transmission electron spectroscopy, ...), because the same signals can also be generated by molecular compounds such as citrazinic acid (CZA), a 2-pyridone derivative containing pyridinic nitrogen, as well as IPCA containing nitrogen in a pyrrolic coordination.^{3,135,136} The presence of MFs makes the PL of CDs more comprehensive. Their presence was experimentally identified in samples of bottom-up synthesized blue-emissive CDs.¹³⁷ The comprehensiveness is even more pronounced as structurally, MFs can be present in the interior of CDs,¹³⁸ covalently bonded^{139,140} or non-covalently attached¹⁴¹ to the CNDs shell.¹⁴²

The real presence and contribution of MFs to PL was demonstrated by photobleaching of the CNDs synthesized under mild conditions after exposure to the UV radiation.⁸⁰ Also, the highly intense molecular state PL signal was generated not only by CD solutions filtered through dialysis bags, but also by the solution outside the dialysis bags, indicating that the PL centers of the free molecules that passed from the bag and those incorporated in the CD were identical.⁸⁰ Finally, MFs exhibit an intense excitation-independent emission and single-exponential PL decay.¹³⁵

The typical MFs originates from citric acid are citrazinic acid (CZA),⁵⁹ and its derivatives. Besides CZA, 1-(2-aminoethyl)-5-oxo-1,2,3,5-tetrahydroimidazo[1,2-a]pyridine-7-carboxylic acid (ATPCA),¹⁴³ methylenesuccinic acid,¹⁴⁴ 5-oxo-3,5-dihydro-2H-thiazolo[3,2-a]-pyridine-3,7-dicarboxylic acid (TPDCA),¹⁴⁵ 5-oxo-3,5-dihydro-2H-thiazolo[3,2-a]pyridine-7-carboxylic acid (TPCA),¹⁴⁵ IPCA,¹³⁷ green fluorophore 4-hydroxy-1H-pyrrolo[3,4-c]pyridine-1,3,6(2H,5H)-trione (HPPT),¹⁴⁶ were the most reported MFs (Figure 7). However, it is very likely that the list does not end here and more MFs contributing to CDs PL are being produced.

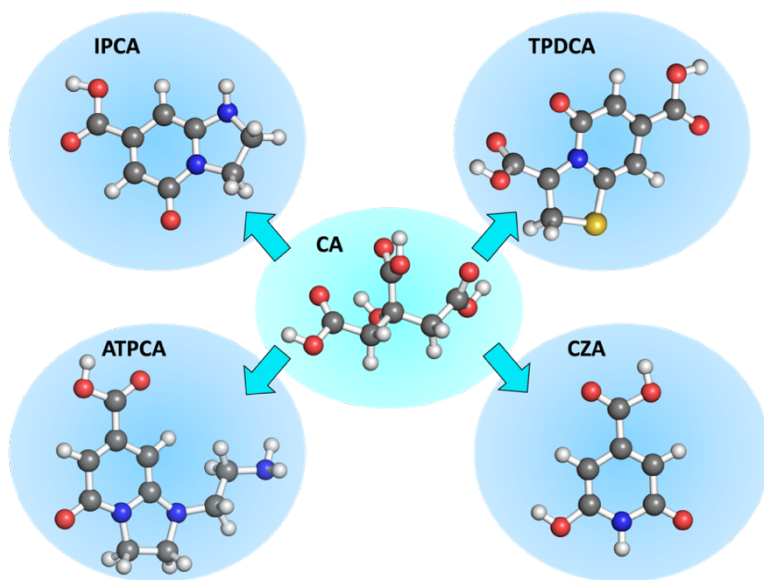


Figure 7. Typical MFs that are present in the final supernatant of preparation of CDs starting from citric acid as one of the precursors.

3 Methods

Recent progress in the field of theoretical chemistry hand-in-hand with an increase in the computer power enabled description of very complex systems including, e.g., nanomaterials. In this work, DFT, MM, QM/MM calculations and MD simulations were mostly used, hence these methods are more examined in this chapter 3.

3.1 Density functional theory

The field of density functional theory (DFT) has made tremendous progress since the 1990s, primarily due to the attractive possibility of high quality computations at low computational cost. Also, the correlated methods scale poorly with the size of the system as they are based on $4N$ -dimensional many-electron wavefunction. Additionally, the correlated methods require high angular momentum basis functions to describe electron-electron correlations,¹⁴⁷ while DFT is based on the one-electron density and depends on three spatial coordinates and one spin coordinate only. Moreover, high angular momentum functions are less important as the wavefunction is not explicitly calculated, thus the choice of only modest basis sets is sufficient.

If not stated otherwise, the information about DFT for this text has been adapted based on the great book, which is serving as the support content for the European Summer School of Quantum chemistry.¹⁴⁸

The central quantity in DFT is an electron density $\rho(\mathbf{r}_1)$. The electronic density trivially determines the number of electrons N and may be obtained from the known wave function by integration (Equation 2):

$$\rho(\mathbf{r}_1) = N \int |\Psi(\mathbf{x}_1, \mathbf{x}_2, \dots, \mathbf{x}_N)|^2 ds_1 d\mathbf{x}_2 \dots d\mathbf{x}_N \quad (2),$$

where $\Psi(\mathbf{x}_1, \mathbf{x}_2, \dots, \mathbf{x}_N)$ refers to N -electronic wavefunction.

The rigorous proof of the statement that the electronic density could be expressed as the functional of the electronic density has not been provided till 1960s. Thenceforth the proof by Hohenberg and Kohn serves as a pillar of DFT methods. The first Hohenberg-Kohn theorem¹⁴⁹ proves that the electron density determines the external potential (due to the nuclei) up to an additive constant. Hence, the electron density determines Hamiltonian \hat{H} , the wavefunction and

any other characteristics of the system. The second Hohenberg-Kohn theorem establishes a variational principle based on the electronic density (Equation 3):

$$\langle \tilde{\Psi} | \hat{H} | \tilde{\Psi} \rangle = \int \tilde{\rho}(\mathbf{r}) v(\mathbf{r}) d\mathbf{r} + F[\tilde{\rho}] = E[\tilde{\rho}] \geq E[\rho] \quad (3),$$

where $\tilde{\rho}$ refers to an approximate density, v to external potential, F is a universal potential. Thus, the exact electron density minimizes the exact energy expression.

In DFT, the electronic energy is expressed as a functional of the electron density (Equation 4):

$$E[\rho] = T[\rho(\mathbf{r})] + E_{ee}[\rho(\mathbf{r})] + E_{Ne}[\rho(\mathbf{r})] + E_{XC}[\rho(\mathbf{r})] \quad (4).$$

The classical electron-electron repulsion energy $E_{ee}[\rho]$ and the nuclear-electron attraction energy $E_{Ne}[\rho]$ can be written exactly in terms of the electronic density. The early ideas of describing kinetic energy (Equation 5) as functional by Thomas¹⁵⁰ failed due large errors:

$$T[\rho(\mathbf{r})] = C_T \int \rho^{5/3}(\mathbf{r}) d\mathbf{r} \quad (5).$$

The bad representation of the functional $T[\rho]$ is solved by introducing the orbitals and Slater determinant into the DFT problem — we are looking for the solution using Kohn-Sham (KS) theory.¹⁵¹ Moreover, besides the fact that some part of $T[\rho]$ is not fully included in the KS equations, a molecular binding cannot also be predicted, unless the exchange-correlation energy functional $E_{XC}[\rho]$ is known. It is the fundamental difficulty in DFT, finding the way how to properly cover the E_{XC} , which includes exchange, correlation, and a small kinetic energy component. Many approximations to $E_{XC}[\rho]$ have been proposed (See Equations 6–9), i.e., the local density approximation (LDA, Equation 6), generalized gradient approximations (GGA, Equation 7), meta-GGAs (Equation 8), hybrid functionals (Equation 9), meta-hybrids, double hybrids.

$$E_{XC} = \int F(\rho) d\mathbf{r} \quad (6)$$

$$E_{XC} = \int F(\rho, \nabla\rho) d\mathbf{r} \quad (7)$$

$$E_{XC} = \int F(\rho, \nabla\rho, \nabla^2\rho) d\mathbf{r} \quad (8)$$

$$E_{XC} = \int F(\rho, \nabla\rho) d\mathbf{r} + \xi E_X^0 \quad (9)$$

LDA functionals are widely applied in periodic metallic systems, however, they tend to drastically overbind molecules. *GGA functionals* generate surprisingly good results, e.g., they provide quite reasonable ionization potentials, electron affinities, atomization energies, bond lengths, on the other hand, they underestimate chemical reaction barriers (very likely due self-interaction) and nuclear magnetic resonance shielding constants. They deliver quite reasonable values of local excitations, nevertheless, they cannot comprehend Rydberg and charge-transfer (CT) excitations and they considerably underestimate them. The family of ‘Minnesota’ functionals provide notable improvements in the specific areas that they have been developed for. Such development is associated with sometimes too many semi-empirical parameters included in a specific functional (M06-2X,¹⁵² M06-L,¹⁵³ etc.) *Hybrid functionals* improve the description of ionization potentials, electron affinities atomization energies, bond lengths over the GGA functionals. Reaction barriers are still underestimated (except specifically parametrized functionals for kinetics like MPW1K¹⁵⁴) and nuclear magnetic resonance shielding provide even less accurate results than GGA. Although the local excitations are still reasonable calculated with hybrid functionals; CT and Rydberg excitations may still be significantly wrong. It is because, although short-range properties are well-described in hybrid functionals, an inadequate description of long-range exchange interactions is present. For better description of CT and Rydberg excitations, range-separation or Coulomb-attenuation must be present and their trick stems in splitting the electron-electron repulsion operator using the error function (Equation 10), e.g., in CAM-B3LYP^{155,156} (Equation 11) LC- ω PBE,¹⁵⁷ LRC- ω PBEh.¹⁵⁸

$$\frac{1}{r_{12}} = \frac{\text{erf}(\mu r_{12})}{r_{12}} + \frac{1 - \text{erf}(\mu r_{12})}{r_{12}} = \text{LR} + \text{SR} \quad (10),$$

where the parameter μ controls the attenuation.

$$\begin{aligned} E_{\text{XC}}^{\text{CAM-B3LYP}} &= E_{\text{X}}^{\text{LR}} + E_{\text{X}}^{\text{SR}}[\text{Becke88}] + E_{\text{C}}^{\text{B3LYP}} \\ E_{\text{C}}^{\text{B3LYP}} &= 0.81E_{\text{C}}^{\text{LYP}} + 0.19E_{\text{C}}^{\text{VWN}} \end{aligned} \quad (11)$$

Another functional used in this work is ω B97X-D.¹⁵⁹ It is a long-range corrected hybrid functional, and it is an extension of ω B97X¹⁶⁰ (Equation 12) with the included empirical dispersion:

$$E_{XC}^{\omega B97X} = a E_X^{SR-HF} + b E_X^{SR-B97} + E_X^{LR-HF} + E_C^{B97} \quad (12),$$

where E_X^{SR-HF} is the short-range Hartree-Fock exchange energy, E_X^{SR-B97} is the short-range exchange energy from B97 functional,¹⁶¹ E_X^{LR-HF} is the short-range Hartree-Fock exchange energy and E_C^{B97} is the correlation energy from B97 functional.

3.1.1 Calculation of excited states

Time-independent DFT can be applied only to the lowest state of a given space-spin symmetry. For calculations of the optical properties (excitation energies, absorption spectra, emission of light) of many-body systems, time-dependent density functional theory (TD-DFT) is necessary.¹⁶²⁻¹⁶⁴ Runge-Gross theorem,¹⁶⁵ a time-analogue to Hohenberg-Kohn theorem, states that the exact time-dependent density determines the time-dependent potential up to a spatially constant, time-dependent function, and hence the time-dependent wavefunction up to a time-dependent phase factor. The existence of a variational principle is achieved by the variation of the action integral with respect to the density, as the total energy is no longer a conserved quantity. A set of time-dependent KS equations are then derived based on a time-dependent non-interaction reference system.¹⁴⁸ In other words, the trick is in replacing the real interacting many-body electronic system by a non-interacting system with the same electron density. Overall, TD-DFT offers a favorable trade-off between cost and accuracy and is relatively easy to use due to its mostly ‘black-box’ nature.¹⁶⁶⁻¹⁶⁸ Nevertheless, it shall be stressed out again that TD-DFT is strongly dependent on the quality of exchange-correlation functional. Moreover, TD-DFT is also sensitive on the quality of description of the surrounding medium.

The extensive review on TD-DFT benchmarking pinpointed the most accurate or adequate exchange-correlation functional(s) for TD-DFT calculations of singlet-singlet electronic transitions considering the most common linear response (LR) formalism.¹⁶⁹ They summarized that increasing the amount of exact exchange in the exchange-correlation functionals tends to increase the predicted transition energies, thus, most pure density functionals (no exact exchange) provide poor estimates of electronic transition energies. Meanwhile, traditional global hybrids (B3LYP,^{156,170} M06¹⁷¹) offer rather satisfying excited state energies, however, large errors can be

expected for states with strong CT character and Rydberg states. Range-separated hybrids or global hybrids including ca. 50 % of exact exchange are more suited for capturing of these states in the calculations, where CAM-B3LYP, ω B97X-D and M06-2X, stands as the best possible choices. B2GPLYP (belonging into double hybrid functionals) considerably improves the description of excited states with doubly excited nature.¹⁷² Moreover, the authors stated the ΔE^{ZPVE} correction term is almost insensitive to the selected basis set.¹⁶⁹ On the other hand, it has been reported that CAM-B3LYP did not outperform standard hybrids containing 22–25 % exact exchange within vertical approximation.¹⁷³ Keeping this in mind, one should carefully choose a functional based on their studied molecular systems and preferably benchmark it against other promising ones.

3.2 Molecular Mechanics

Molecular mechanics (MM), also known as force field (FF) methods, is a computational method that uses classical mechanics to model systems. It is also known as empirical potential because the interaction potential is evaluated with the potential functions containing parameters, that were parameterized empirically, either from experimental data, or using QM calculations. A few high quality publications describing the theory of MM have been used as the source of the information for this chapter.^{174–177}

The MM has been constructed based on several assumptions. First, the Born-Oppenheimer approximations is considered. Next, an atom is modelled as a sphere of a certain radius and with a partial charge in its center; and a bond is modelled as a harmonic oscillator following the Hooke's law. That is why the MM is also known as 'balls and springs' theory. Another assumption in the MM is a transferability principle. This principle is essential for utilization of MM, because it enables a set of parameters to be transferred and used for studies on some (bio)molecules, even though they were originally derived on some different small number of molecules.¹⁷⁴ Of course, one must be careful and for some specific purposes, a new different set of parameters may be needed. The transferability is enabled due to the concept of assigning an atom type to each atom in the system. Atom type contains information about the atomic number of an element, its hybridization and local environment. Despite the transferability principle, an FF should be kept as a single unit and it is not recommended to mix the FF with parameters from another FF, even though they could the same functional form. When modelling with FF methods, it shall be kept in mind that they operate the best in the area they have been parametrized for.

More approximations can be introduced, for example instead of using all-atom FFs, where every atom has its own parameters, united-atom or coarse-grained approaches may be popular options in some cases, e.g., in simulations of membranes and biomolecules.^{178–182} The different representation of a molecule of these approaches is displayed in Figure 8.

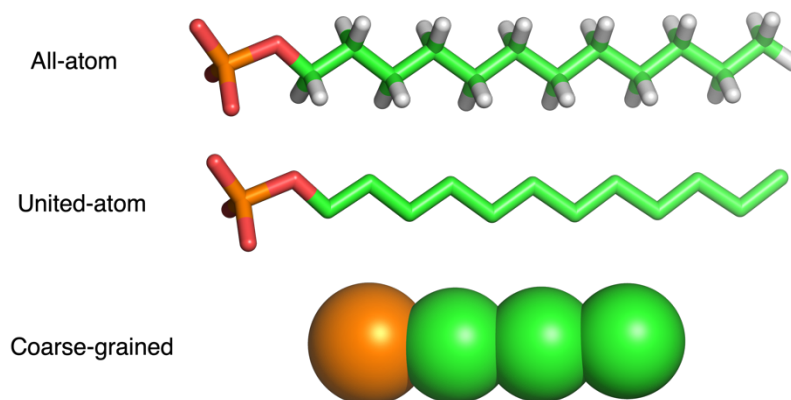


Figure 8. Three common representations of atoms and molecules for MM and MD simulations.

A total energy of a system described with MM is the function of a mutual position of nuclei and is a sum of an individual pair functions. The general form of the total energy is described in Equation 13, and generally, three bonded and two non-bonded terms are needed, i.e., bond stretching E_{bond} , angle bending E_{angle} , bond rotation E_{torsion} and non-bonded van der Waals E_{vdW} and Coulomb E_{coulomb} interactions. The form and the number of these pair functions are characteristic for each FF.

$$E_{\text{FF}} = E_{\text{bond}} + E_{\text{angle}} + E_{\text{torsion}} + E_{\text{vdW}} + E_{\text{coulomb}} + (E_{\text{polarization}} + E_{\text{other}}) \quad (13)$$

In the simplest MM calculations, the terms in the brackets are omitted, as it is not always necessary to include more power-demanding evaluation of polarization interaction $E_{\text{polarization}}$, or other more-particle interactions and crossing terms (e.g., mutual effect of a bond stretching on an angle bending; or stretch-torsion term, etc.). Simple set of equations like this allow to perform calculations on systems with thousands of atoms in a reasonable time window.

3.2.1 Amber force field example

In the next section, let me briefly present one example of the functional form of a common parm99 (Equation 14):¹⁸³

$$E_{\text{pair}} = \sum_{\text{bonds}} K_r (r - r_{\text{eq}})^2 + \sum_{\text{angles}} K_\theta (\theta - \theta_{\text{eq}})^2 + \sum_{\text{dihedrals}} \frac{V_n}{2} (1 + \cos(n\phi - \gamma)) + \sum_{i < j} \left(\frac{A_{ij}}{R^{12}} - \frac{B_{ij}}{R^6} \right) + \sum_{i < j} \left(\frac{q_i q_j}{\epsilon R} \right) \quad (14),$$

where K_r , K_θ , V_n are force constants; r and θ current values of bond lengths and angles; r_{eq} and θ_{eq} equilibrium values for bond lengths and angles; n multiplicity; ϕ torsion angle; γ phase factor (determines the point, where the torsion angle passes the minimum value); q atomic charge; ϵ relative permittivity; R current distance between i and j atoms; A_{ij} adjustable parameter responsible for short-range repulsion interactions, B_{ij} adjustable parameter responsible for dispersion (London) attraction interactions.

Bonds and angles rarely significantly deviate out of equilibrium in MM calculations. Therefore, these so-called ‘hard degree of freedom’ terms, bond stretching and angle bending, are usually expressed in the extent of the behavior close to equilibrium. For this reason, harmonic oscillator approximations or Hooke’s law formula are sufficient approaches for the description, despite their inability to describe bond breaking. The FFs being restricted only to harmonic terms are called class I FFs (Figure 9). Class II FFs (e.g., COMPASS, MMFFs) include some anharmonic effects and contain the above-mentioned explicit cross terms (cubic, quartic terms or Morse potential). Class III FFs would additionally consider chemical features like electronegativity and hyperconjugation.

The flexibility of the molecules and its corresponding conformational changes of the molecules is another important phenomenon that need to be preserved in MM simulations. Barriers to rotate the bonds of the molecules are described with the parameters for torsion angles in MM. In parm99, the functional form is expressed as a cosine series expansion. Usually, additional functional term is needed to keep sp^2 carbons in one plane and it is from out-of-plane bending term. Very commonly, this is realized using improper torsion angle, which is defined by four atoms not bonded in one (proper) 1-2-3-4 sequence.

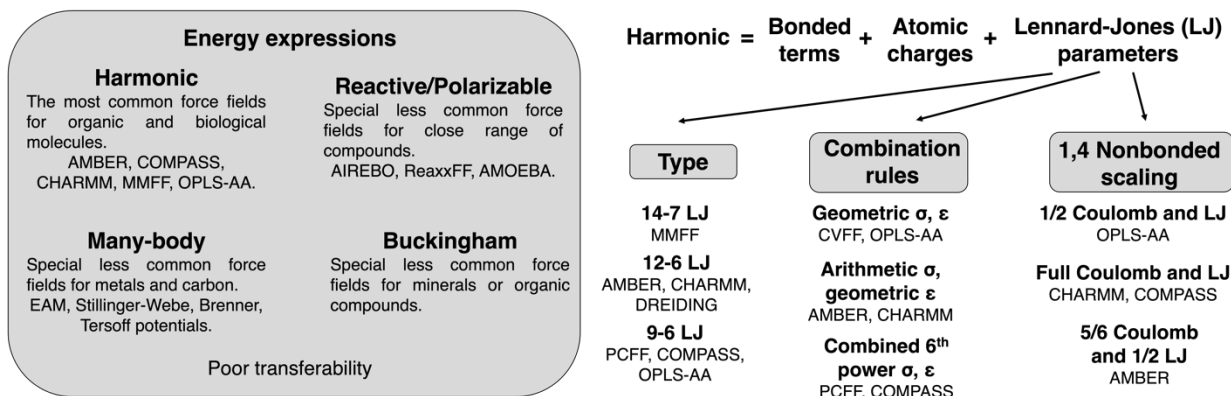


Figure 9. The overview of some typical FFs and their potential forms.

Van der Waals interaction

The exchange-repulsive and dispersion interactions between atoms must be evaluated quickly too, thus a simple, rapid, and empirical Lennard-Jones 12-6 function (LJ) is implemented for calculations of the van der Waals (vdW) potentials functions. The functional form of the LJ potential may differ in different FFs. For example, OPLS-AA¹⁸⁴ (Optimized Potentials for Liquid Simulations) FF contains collision diameter σ_{ij} (the separation, for the energy is zero) instead of r_0 (see Equation 15). It can be derived that $r_0 = 2^{1/6}\sigma$, for their difference, see Figure 10.

$$V(r) = \epsilon_{ij} \left[\left(\frac{r_{0,ij}}{R_{ij}} \right)^{12} - 2 \left(\frac{r_{0,ij}}{R_{ij}} \right)^6 \right] = 4 \epsilon_{ij} \left[\left(\frac{\sigma_{ij}}{R_{ij}} \right)^{12} - \left(\frac{\sigma_{ij}}{R_{ij}} \right)^6 \right] \quad (15)$$

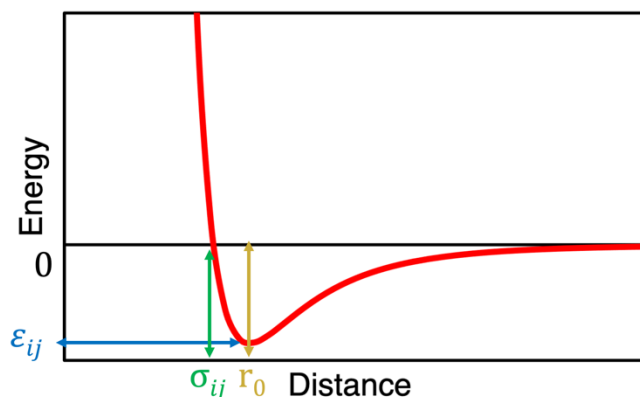


Figure 10. The Lennard-Jones potential with highlighted LJ parameters.

Generally, the rapidness of squaring r^{-6} term to obtain r^{-12} dominates over the correct implementation of the correct exponential form of the repulsive interaction. Just to name an example with no additional details, as only LJ 12-6 potential was used for my doctoral research,

Buckingham potential contains more realistic exponential potential in its expression. Moreover, the parameters for the mixed interaction in the LJ equation are determined by combining the parameters of the pure atoms using the mixing rules (see Equation 16 for the Lorentz-Berthelot combining rule). In OPLS-AA and some other FFs, the collision diameter is also calculated with the geometrical mean.¹⁸⁵

$$\begin{aligned}\sigma_{AB} &= \frac{1}{2}(\sigma_{AA} + \sigma_{BB}) \\ \epsilon_{AB} &= \sqrt{\epsilon_{AA}\epsilon_{BB}}\end{aligned}\tag{16}$$

The function describing the non-bonded interaction between two objects is the so-called additive pair potential.^{174, 175} This means that the total energy between three interaction particles (a, b, c) is a sum of pair contributions (a–b, b–c, c–a). Moreover, not all interactions between atoms are accounted for, the 1–2 and 1–3 interactions on the same molecule are omitted and 1–4 interactions are scaled. In parm99, $f_{\text{coulomb},(1-4)} = 0.5$, $f_{\text{LJ},(1-4)} = 1/1.2$.¹⁸⁶ The often used additive effective pair potential refers to the fact, that many-body contributions are effectively included in the pair potentials with the proper parametrization tricks.

Electrostatic interaction

While the description of electrostatics in *ab initio* methods is exact, the MM immensely approximates the electronic structure of a system while using some convenient approximations. Typically, the unequal distribution of charge in a molecule is represented as a fractional point charge on every atom. In the most basic approximation, they are located on the centers of the atoms, and they are called partial atomic charges (or net atomic charges). Their assignment is designed to carefully represent the true electrostatics of the systems, usually to represent the electrostatic potential of the molecule. If every atom has its assigned charge, the mutual electrostatic interaction can be easily calculated using the Coulomb's law. Again, 1–4 (coulombic) interactions are scaled by some factor in most FF, some very distant atoms are even not calculated at all. Due to the power and time demands of long-range coulombic interactions, a limiting distance from which the electrostatic interaction is not directly calculated is set. There are two most common approaches how to set a cutting distance while not causing too big errors — cut-off method¹⁸⁷ and Particle mesh Ewald (PME).^{188,189} Coulomb's law is the most common approach because with an excellent parametrization and capability to reproduce the multipole interaction

energy, but other approaches employing central multiple expansion. Such neglect of the electronic structure inherently predetermines MM for incapability of providing properties dependent upon the electronic distribution in a system.

3.3 Molecular dynamics

The quick evaluation of interaction potentials with MM is advantageously used in classical molecular dynamics (MD) simulations (henceforth referred as MD simulations). MD simulations generate trajectories specifying the time evolution of all the particles in a simulated system by calculating their velocities and positions, following the principles of classical mechanics. Trajectories are obtained by solving the differential equations in Newton's second law equation (Equation 17):

$$\begin{aligned} \mathbf{a} &= \frac{\mathbf{F}}{m} \\ \frac{d^2x}{dt^2} &= \frac{\mathbf{F}}{m} \end{aligned} \quad (17),$$

where m is the mass, \mathbf{F} the force acting on a particle i along a coordinate x .

Moving from hard sphere and square-well potentials, the MD with continuous potentials has been practiced these days. In continuous potentials methodology, the equations of motions are integrated using either a finite difference method or predictor–corrector integration methods. In finite difference methods, the integration is completed in many small-time windows ∂t . In simulations of flexible molecules, the time windows, called time-steps, should be approximately one-tenth of the time of the shortest period of motion. Among many MD algorithms using finite difference approach, all approximate the positions, velocities, accelerations (and other similar dynamic properties) as Taylor series expansion (Equation 18):

$$\begin{aligned} \mathbf{r}(t + \partial t) &= \mathbf{r}(t) + \mathbf{v}(t)\partial t + \frac{1}{2}\mathbf{a}(t)\partial t^2 + \frac{1}{6}\mathbf{b}(t)\partial t^3 + \dots \\ \mathbf{v}(t + \partial t) &= \mathbf{v}(t) + \mathbf{a}(t)\partial t + \frac{1}{2}\mathbf{b}(t)\partial t^2 + \frac{1}{6}\mathbf{c}(t)\partial t^3 + \dots \\ \mathbf{a}(t + \partial t) &= \mathbf{a}(t) + \mathbf{b}(t)\partial t + \frac{1}{2}\mathbf{c}(t)\partial t^2 + \frac{1}{6}\mathbf{d}(t)\partial t^3 + \dots \end{aligned} \quad (18),$$

where \mathbf{r} is the position, \mathbf{v} is the velocity, \mathbf{a} is the acceleration, \mathbf{b} , \mathbf{c} , \mathbf{d} is the third, fourth and fifth derivation of the position with respect to time, respectively.

The typical algorithm of MD simulation is as follows: At each time, the force acting on each particle at its current configuration is calculated as the vector sum of its interactions with other particles. The interactions are known from MM calculations. Knowing force (and assuming it is constant during the time step), we also know the acceleration and velocities of the particles, and it is possible to calculate positions and velocities at time $t+\partial t$ by combining the accelerations with velocities and positions in time t . Then, the forces at the new particle configurations are determined and the evaluation cycle continues, giving new velocities and positions at time $t+2\partial t$, and so on. Verlet algorithm (Equation 19) or its variants (velocity Verlet, leap-frog algorithm) are the widely utilized methods for integration of the Newton's equations of motion.

$$\begin{aligned}
 \mathbf{r}(t + \partial t) &= \mathbf{r}(t) + \mathbf{v}(t)\partial t + \frac{1}{2}\mathbf{a}(t)\partial t^2 + \dots \\
 \mathbf{r}(t - \partial t) &= \mathbf{r}(t) - \mathbf{v}(t)\partial t + \frac{1}{2}\mathbf{a}(t)\partial t^2 + \dots \\
 \mathbf{r}(t + \partial t) &= 2\mathbf{r}(t) - \mathbf{r}(t - \partial t) + \mathbf{a}(t)\partial t^2
 \end{aligned}
 \tag{19}$$

The disadvantage of the Verlet integration algorithm is adding small $\mathbf{a}(t)\partial t^2$ term to the difference of bigger terms $2\mathbf{r}(t) - \mathbf{r}(t - \partial t)$ which may lead to the loss of precision. Moreover, velocities are not available until the next step when the positions have been calculated. Also, the Verlet algorithm is not self-starting.

Although the MM and MD has been briefly introduced, several other points must be addressed to successfully run a MD simulation. First, the initial configuration is set either based on experimental data, from a theoretical model and/or multiple starting coordination may be designed. The initial velocities of each atom (in all-atom scheme) are assigned, for example randomly based on Maxwell-Boltzmann distribution at the temperature of interest. At this point, it is needed to deal with the problem that we can only study systems with finite numbers of particles. This problem is solved by simulating in a box with periodic boundary positions.¹⁷⁷

Before running MD, it shall also be established which ensemble is simulated, in other words, if NVT or NpT or NVE ensemble is preserved (the letters refer to which quantities are kept constant during a simulation). Realization of NpT conditions means adding one extra step to algorithms evaluating changes of positions of particles in a system., i.e., to change the volume of a simulated box. This volume is tracked, and it is another fluctuating observable in a simulation.

Furthermore, it must be selected if only approximated or true canonical ensemble is modelled. This selection is made by choice of a thermostat and barostat (Table 2), e.g., simple rescaling of all the particles velocities by factor $(T/\tau)^{1/2}$ after each integration step in the Verlet algorithm produces only the approximated canonical ensemble (T is the targeted and τ the actual temperature).

Table 2. Comparisons of the implemented thermostats commonly used in MD simulations.

Berendsen	
⊕ efficient thermalization	⊖ non-canonical ensemble
⊕ exponential relaxation (good for starts)	⊖ possible flying ice-cube effect
	⊖ very bad for small systems
Nosé-Hoover	
⊕ canonical ensemble	⊖ oscillation, decoupling
⊕ time reversible	⊖ bad for starts
⊕ appropriate for small systems	⊖ velocities included in the equations of motion
Andersen, Maxwell-Boltzmann, Langevin	
⊕ canonical ensemble	⊖ lost kinetics
⊕ exponential relaxation (good for starts)	⊖ collisions affect atomic dynamics

To conclude this chapter, it is not necessary that MM being the level of theory for the evaluation of interaction energies. The wide group of quantum dynamics enable tracing the gradual formation of bonds, etc. In quantum dynamics, we do not need to evaluate interatomic potentials, as it is based on an integration of the wavefunction in time (Car-Parrinello dynamics).

3.4 Calculations in solvents

Basically, two groups of approaches of solvent models are introduced in the theoretical calculations — explicit and implicit. In the explicit solvent models, the solute is surrounded with the solvent molecules, i.e., the coordinates of a solvent are also present in the computational input. In MD simulations, the solvent molecules have their own parameters and topologies and all the information mentioned in chapters 3.2 and 3.3 is applied to them. In QM calculations, it may be a bit problematic to use such explicit (atomistic) solvent models. The first reason is that the computational demands allow us to model only small molecular clusters and aggregates, whose properties are far from the condensed phase. Secondly, there are plenty of geometrical minima in liquids, thus, the geometry optimizations of a solute with a few molecules of water may very often relax to otherwise irrelevant minima.

In this thesis, two types of explicit water models were used in MD simulations — SPC/E¹⁹⁰ and TIP3P.¹⁹¹ They both belong to three-site nonpolarizable classical water models. This means that they have three interacting points which corresponds to the atoms of the water molecule. Each site has its own LJ parameters and a partial charge. Both these models also have rigid geometry. For the comparison of SPC/E and TIP3P models, see Table 3.

Table 3. Overview of some properties for three common solvent molecules.¹⁹²

	SPC	SPC/E	TIP3P
r(OH) [Å]	1.00	1.00	0.96
H-O-H [degree]	109.47	109.47	104.52
q(O) [e]	-0.8200	-0.8340	-0.8476
q(H) [e]	0.4100	0.417	0.4238
Dipole moment [Debye]	2.27	2.35	2.35
Relative permittivity	65	71	82
Self-diffusion [10^{-5} cm²/s]	3.85	2.49	5.19
Density maximum [° C]	-45	-41.5	-41.1

To avoid these two bottlenecks from the QM point of view, implicit models have been introduced into the market. Here, the solvent is modelled as a dielectric continuum of some properties (solvent radius, static and dynamic relative permittivity, refractive index, surface tension at interface, etc.) depending on the chemical nature of the solvent. Although plenty of different equations for implicit solvation has been suggested, self-consistent reaction field (SCRF) is the most popular choice in DFT calculations. In SCRF, additional terms are added in the Hamilton operator \hat{H} of the Schrödinger equation, defining the mutual polarization of the continuum and the solute (Equation 20):

$$(\hat{H}_{el} + V_R)\Psi = E\Psi \quad (20),$$

$$V_R = \int \frac{1}{4\pi\epsilon_0} \frac{\sigma(\mathbf{s})}{|\mathbf{r} - \mathbf{s}|} d\mathbf{s}$$

where V_R is the electrostatic potential with the charge density ρ , $\sigma(\mathbf{s})$ are the charges on the surface of the solute-solvent interface, \mathbf{s} is the position of the region on the surface, ϵ_0 is the relative permittivity of vacuum.

Thus, the solvent reacts to the electron distribution of the molecule, and it is iteratively solved during the self-consistent procedure (Figure 11). In this thesis, the contribution to the implicit solvent was based on integral equation formalism (IEF) version of the polarizable continuum

model (PCM)¹⁹³ and the universal continuum solvation model based on density (SMD).¹⁹⁴ Implicit solvents also possess some drawbacks, e.g., it is not clear how to set the border between the solute and the surrounding dielectric, i.e., how to create a cavity. And a construction of a cavity affects the results.

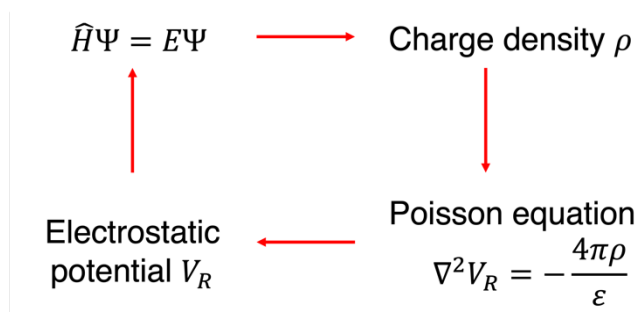


Figure 11. Scheme representing iterative SCRF cycle.

LINEAR RESPONSE

To couple the continuum model with the solute in QM calculations of the environment response in vertical (de-)excitations, two models have been proposed — linear response (LR) and state-specific (SS) models. In the LR formulation, the response of the solvent dynamic polarization to the excitation is computed from the transition density, while in the SS approach the same polarization is determined by the difference of the electron densities of the initial and final states. The LR is suitable for transitions with a small change of the electron density. For excitations involving a large density rearrangement, the LR scheme is insufficient because it does not account for the density-dependent relaxation of the solvent polarization.^{195,196} At this moment, we often employ the state-specific corrected linear response (cLR).^{197–199}

3.5 QM/MM

The combined quantum mechanical/molecular mechanical (QM/MM) approach is a popular method when it is needed to calculate big (macro)molecular compounds while still describing some regions of interest of the molecules with highly precise reliable electronic structure method. The QM/MM approach was first introduced in 1976.²⁰⁰ The entire molecular system is split into two or more regions and each region is treated with different methodologies. The small region of the molecule, where the crucial part of the process, e.g., chemical reaction, excitation, happens, is described with QM, while the rest of the molecule and surrounding explicit solvents are typically

described with MM, allowing to capture, e.g., dynamic properties (see Figure 12). All regions communicate with each other (see chapter 3.5.3).²⁰¹

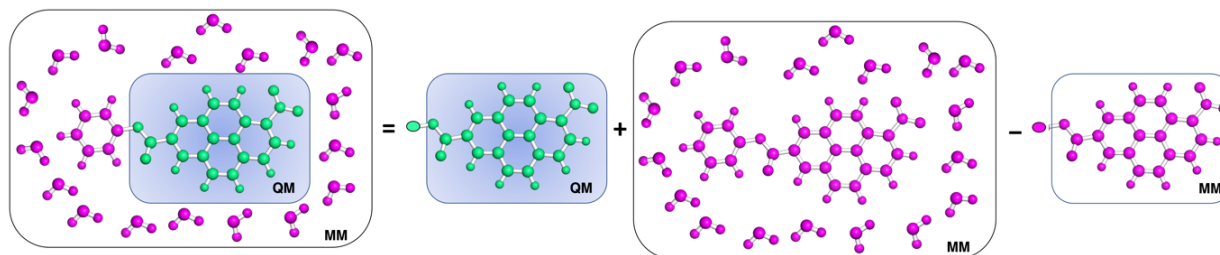


Figure 12. The schematic representation of a subtractive QM/MM scheme.

3.5.1 Additive and subtractive schemes

Let's focus on the situation with two QM/MM regions in the calculation. The total energy in QM/MM system can be evaluated using either additive, or subtractive scheme.^{201,202} In an additive scheme the total energy of the system is calculated summing the QM energy of the QM region (E_1^{QM}), the MM energy of the MM region (without the QM core, E_2^{MM}), and the interaction between both regions ($E_{1/2}^{\text{QM/MM}}$, see Equation 21):

$$E_{\text{TOTAL}}^{\text{additive}} = E_1^{\text{QM}} + E_2^{\text{MM}} + E_{1/2}^{\text{QM/MM}} \quad (21).$$

On the other hand, in the subtractive scheme, three separated calculations are performed (Equation 22):

$$E_{\text{TOTAL}}^{\text{subtractive}} = E_1^{\text{QM}} + E_{1,2}^{\text{MM}} - E_1^{\text{MM}} \quad (22),$$

where subscript refers to the system and superscript to the level of theory.²⁰²

The form of subtractive scheme directly eliminates double counting of any interaction; thus, its implementation is straightforward. On the other hand, the advantage of additive scheme is that no MM parameters are needed for atoms in the QM region.²⁰³

3.5.2 QM/MM boundaries

Although it is more or less important to implement either additive or subtractive QM/MM scheme, it is vital to properly describe the boundaries between QM/MM regions and their interaction as they dramatically affect the results. These interactions can be divided into bonded and non-bonded. The bonded interactions rise when a covalent bond extends across QM/MM

boundaries. The proper description and elimination of this bond is essential as a bad choice can meaningfully influence the observed calculated quantities. There are rules and tricks how to cut such bonds (link atom, boundary atom, localized orbitals schemes),²⁰⁴ however I have not encountered them in my QM/MM calculations, thus I am not describing them in any unnecessary detail.

3.5.3 QM/MM coupling

The description of the non-bonded interaction between QM/MM regions (known as QM/MM coupling) is crucial as well.^{201,202} The interaction between QM and MM regions is often dominated by electrostatics. Most commonly, three different levels of approximation are mentioned — mechanical, electrostatic, and polarizable embedding. Both additive and subtractive schemes may be used with mechanical, electrostatic, or polarizable embedding.

The interaction is described just at the MM level in mechanical embedding (ME), the polarization of the QM wavefunction is completely neglected.²⁰⁵ In electrostatic embedding (EE), point-charge models (typically atomic partial charges) of the surrounding atoms (region 2) are included in one-electron QM Hamiltonian of the region of importance (region 1), in other words, system 2 polarizes the QM wavefunction of system 1.²⁰⁶ This is different in polarizable embedding (PE), where there is a mutual polarization between systems 1 and 2.^{207–209} PE is the most expensive approximation out of these three embeddings, as polarizable FF and QM software with the ability to treat polarizabilities are required. Overall, EE is the most used, as it is more accurate than the ME. This sentence is valid only if the partial charges of the MM regions are not positioned too close to the QM wavefunction, leading to overestimated polarization. Also, the QM electron density shall not penetrate into the MM region.²

3.5.4 ONIOM

ONIOM^{203,210} (Our own N-layered Integrated molecular Orbital + molecular Mechanics) scheme uses the subtractive scheme to calculate the total energy of the system (Equation 23):

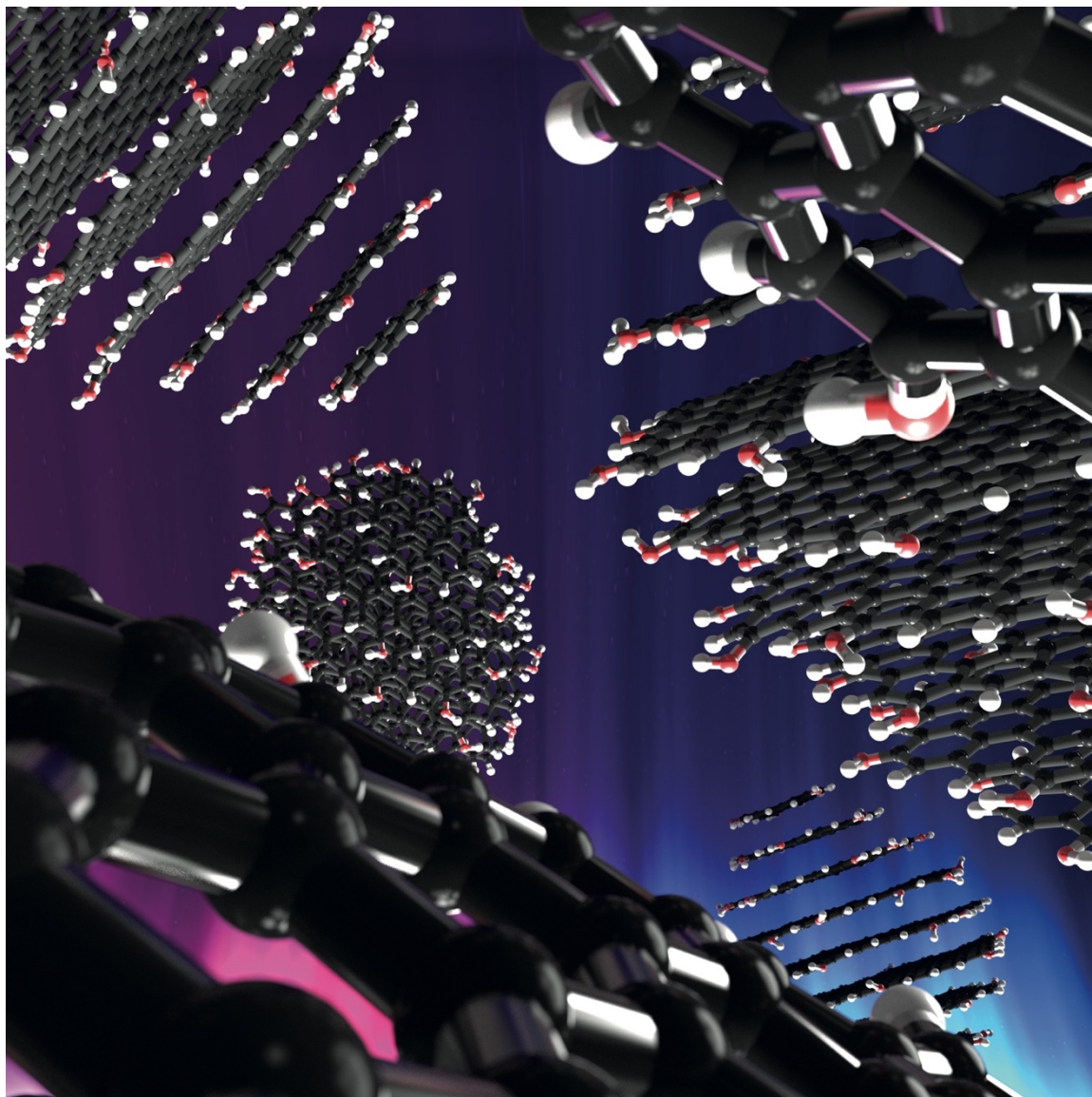
$$E_{\text{TOTAL}} = E_{\text{model}}^{\text{QM}} + E_{\text{real}}^{\text{MM}} - E_{\text{model}}^{\text{MM}} \quad (23),$$

where *model* refers to the small QM region and *real* to the entire modelled system.

Technically, the subtractive ONIOM approach requires accurate parameters for all atoms, including link atoms, because an MM calculation of the QM region is also necessary to avoid

double counting. The main advantage of the subtractive QM/MM coupling scheme is that no communication is required between the quantum chemistry and molecular mechanics routines. A major disadvantage is that an FF is required also for the QM subsystem. Additionally, the FF shall be sufficiently flexible to describe the effect of chemical changes if a reaction occurs.²¹¹

4 Structural dynamics of carbon dots in water and *N,N*-dimethylformamide probed by all-atom molecular dynamics simulations*



* Published as: Paloncýová, M.; Langer, M.; Otyepka, M. Structural Dynamics of Carbon Dots in Water and *N,N*-Dimethylformamide Probed by All-Atom Molecular Dynamics Simulations. *J. Chem. Theory Comput.* 2018, 14 (4), 2076–2083.

In my research, I have paid particular attention to CDs. My research in this field started in 2017, where I was involved in the pioneering project of a theoretical description of CDs.²¹² Without going into any unnecessary details, as this project was undergone during my masters studies, the main findings and implications of this study should be summarized to provide the readers more complete picture of my research of CDs. Additionally, some outcomes from this publication has been used in our subsequent studies (see chapter 6, 7, 8). In this project, we provided details on dynamics and structural organization of CQD models with the methods of classical MD simulations. Such MD simulations of real CDs have been performed for the first time in the field.

Very shortly, the complete procedure for performing MD simulations of CDs, from structure preparation, up to MD simulations in water and *N,N*-dimethylformamide was provided. First, a builder with Graphical User Interface (GUI) of a builder for generating CDs of a desired size and with various oxygen-containing surface functional groups was written as an VMD²¹³ plugin (<http://cd-builder.upol.cz>). This builder is capable of creating all the necessary GROMACS²¹⁴ input files, including coordinates and the topology (Figure 13).

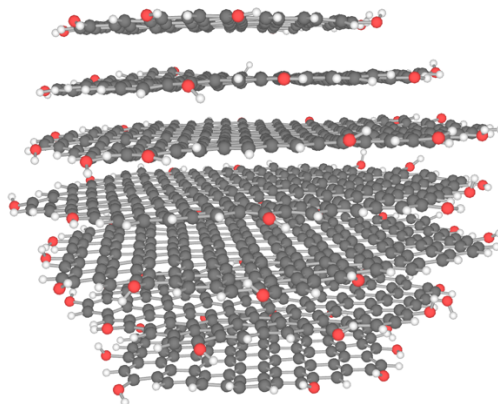


Figure 13. The structure of CD that was built with the in-house written code for generation of a full model of CDs.

The bonded and LJ parameters of MM were assigned using the transferability principle from OPLS-AA and parm99SB FFs,²¹⁵ except aromatic carbons, whose LJ have been modified to better represent graphene-like behavior.²¹⁶ The partial u charges were assigned based on the fitting the electrostatic potential either with CHELPG or RESP procedure, calculated on small models of polyaromatic hydrocarbons (PAHs) in vacuum. For each functional group, several models of

coronene and circumcoronene with various positions, various number of functional groups on the edges with the purpose of eliminating the effect of mutual positions of functional groups in bigger CD models. The models were optimized at B3LYP/6-31++G(d,p) level of theory and the electrostatic potential was calculated with HF/aug-cc-pVDZ or HF/pVDZ or HF/6-31G* level of theory. The models were further sorted by its local surrounding (armchair or zig-zag position) and partial charges assigned to the atoms of the same type were averaged. The VMD builder then automatically assigns these averaged charges to the specific atom by the script. This parametrization is aiming for the large-scale calculation of large CDs, where single RESP procedure is not available.

Nowadays, with this user-friendly protocol for running MD simulations of CDs, it is possible to study specific interaction of CDs (of desired sizes, type of functional groups and their coverage) in miscellaneous environments, e.g., in water, in the vicinity of complex biomolecules, and shed light on problems not reachable by experiments.²¹⁷ Additionally, we showed that a mutual rotation of graphitic layers in CDs is strongly dependent on the type and coverage of functional groups on the edges. Protonated and deprotonated carboxyl groups decreased the rate of internal rotations due to formation of interlayer H-bonds (Figure 14). Excess of deprotonated carboxyl, and carbonyl groups also led to the de-stabilization of CDs' shape. All MD simulations yielded behavior in accordance with experiments. For more information, please see the reference 212.

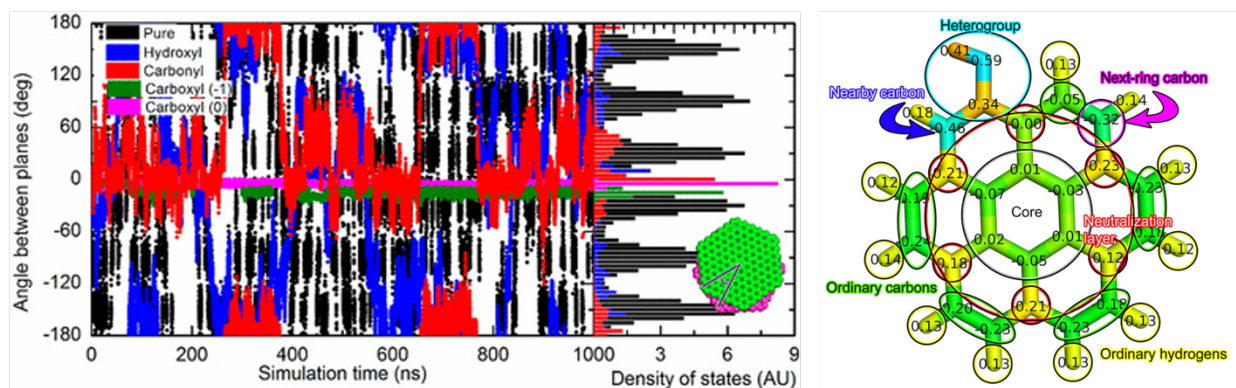
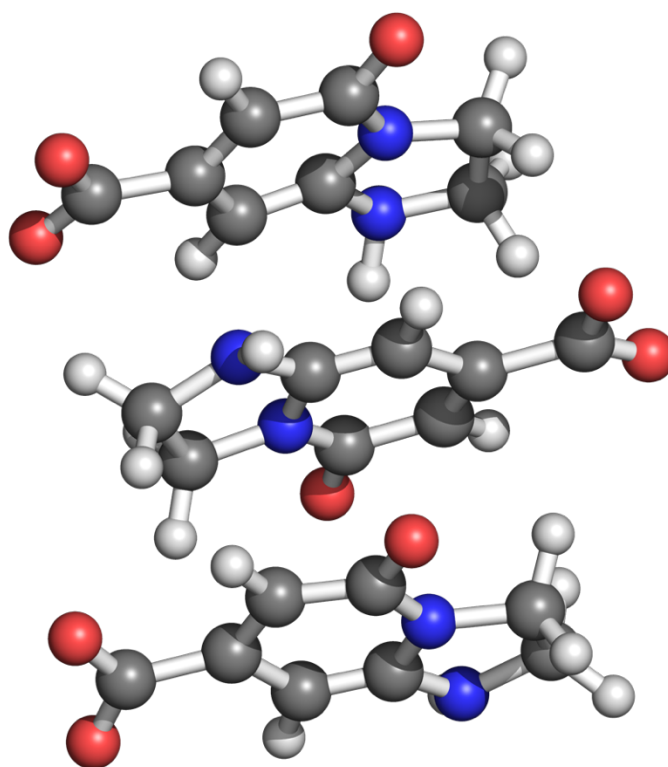


Figure 14. Left panel: Rotation of the nearest middle layers of CDs (left) and distribution of the positions (right). The inset of two CD layers shows the monitored angle. Right panel: Nomenclature of the atoms in CD layers as used for charge assignment.²¹²

5 Conformational behavior and optical properties of a fluorophore dimer as a model of luminescent centers in carbon dots[†]



[†] Published as: Siddique, F.; Langer, M.; Paloncýová, M.; Medved, M.; Otyepka, M.; Nachtigallova, D.; Lischka, H.; Aquino, A. J. A. Conformational Behavior and Optical Properties of a Fluorophore Dimer as Model of Luminescent Centers in Carbon Dots. *J. Phys. Chem. C* 2020, 124 (26), 14327–14337.

In the section 2.4.3 it was introduced that during the synthesis of CDs from citric acid and ethylenediamine, a prototypical molecular fluorophore IPCA (Figure 15) is formed. Also, it was rationalized that MFs exhibit absorption and emission in the energy regions typically reported for CDs, supporting the idea that the molecular states contribute to the PL in CDs. The optical properties of IPCA have been very briefly mentioned in the original paper reporting their synthesis, where experimentally measured absorption bands at 240, 350 nm and strong emission at 440 nm were reported.¹³⁷ Nevertheless, the insightful view on the nature of PL of IPCA molecules and changes after dimerization have been lacking in the literature. In this publication, where I mostly participated in estimating the extent of strength of dimer interaction, as a support of MD simulations and in double-checking the TD-DFT results, UV absorption and fluorescence properties of the IPCA molecule and seven stacked IPCA dimers as basic models for the fluorescent centers in CDs were analyzed using a combination of computational methods.

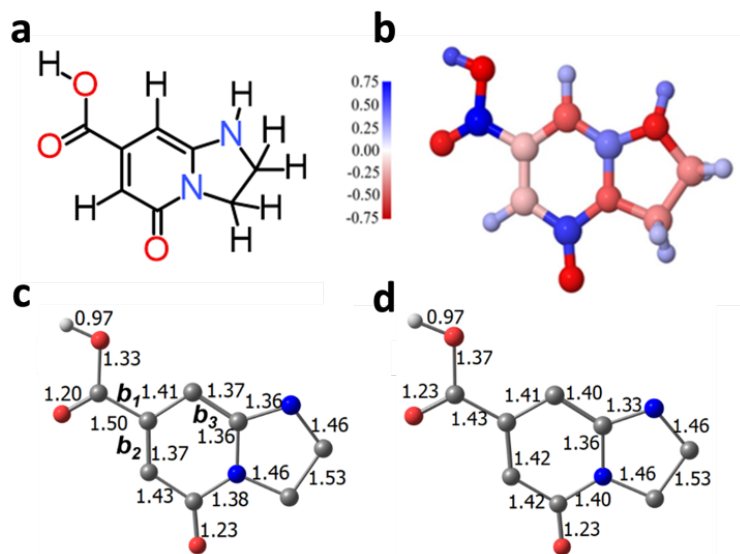


Figure 15. a) Chemical structure of IPCA. b) NPA charges for the IPCA structure in GS calculated using the CAM-B3LYP-D3 method in gas phase. c) Optimized IPCA structure in the S_0 state. d) Optimized IPCA structure in the S_1 state; both were computed for the aqueous solution with the (TD-)CAM-B3LYP-D3 level of theory. The bond lengths are in shown in Å. Only the H atoms for the carboxyl group are shown in c) and d). Reprinted with permission from 104. Copyright 2022 American Chemical Society.

First, let me focus on the calculations of optical characteristics of isolated IPCA molecule. The GS geometries were optimized with CAM-B3LYP functional always including the D3 correction for dispersion,²¹⁸ performed with the zero damping function, and using the def2-TZVP basis set.²¹⁹ Excited states were calculated with the TD-DFT methodology in gas and/or aqueous

solvent, where implicit water was introduced, i.e., the IEF-PCM¹⁹³ with a dielectric constant of $\epsilon = 78.36$ and a refractive index of $n = 1.33$ were employed. Gaussian09 program suite was used.²²⁰ Geometry optimizations were performed using equilibrium solvation for the respective state (S_0 or S_1). Vertical excitation energies (VEEs) were calculated with TD-DFT at the GS equilibrium geometry, with non-equilibrium cLR approach¹⁹⁷ with solvent equilibration for the GS. Charge transfer (qCT)²²¹ was analyzed in terms of the transition density matrix and natural transition orbitals (NTOs)²²² using the TheoDore^{223,224} software. Radiative lifetimes τ for spontaneous emission were calculated using the Einstein transition probabilities according to the formula (Equation 24):

$$\tau = \frac{c^3}{2f\Delta E_{fl}^2} \quad (24),$$

where c is the velocity of light, ΔE_{fl} is the emission energy, and f is the oscillator strength.

Table 4. VEE ΔE (eV), oscillator strength (in parentheses), character, charge transfer (qCT) for the IPCA monomer using TD-CAM-B3LYP in the gas phase and aqueous solution (PCM). Reprinted with permission from 104. Copyright 2022 American Chemical Society.

		Gas phase		PCM	
	Character	ΔE	qCT	ΔE	qCT
S_1	$\pi \rightarrow \pi^*$	3.82 (0.12)	0.26	3.67 (0.15)	0.28
S_2	$n \rightarrow \pi^*$	4.81 (0.00)	0.19	4.99 (0.00)	0.25
S_3	$n \rightarrow \pi^*$	5.14 (0.00)	0.40	5.22 (0.00)	0.34
S_4	$\pi \rightarrow \pi^*$	5.75 (0.02)	0.13	5.52 (0.00)	0.18
S_5	$\pi \rightarrow \pi^*$	5.82 (0.01)	0.10	5.89 (0.27)	0.06
S_6	$\pi \rightarrow \pi^*$	5.98 (0.16)	0.10	-	-
Emission					
S_1	$\pi \rightarrow \pi^*$	3.20 (18.8)		3.02 (16.8)	

^aRadiative lifetimes (ns) are given in parentheses. ^bExperiment 3.54 eV.¹³⁷ ^cExperiment 2.81 eV (14.1 ns).¹³⁷

Analysis of the transitions to the ten lowest excited states obtained with TD-CAM-B3LYP-D3 calculations showed that the $S_0 \rightarrow S_1$ excitation is a bright single excitation and have the VEE 3.82 eV in gas and it is red-shifted by 0.15 eV (3.67 eV) in water (Table 4). The VEE calculated in water is in a good agreement with the experimental value 3.54 eV. Interestingly, NTO analysis

describes this electronic transition to be $\pi \rightarrow \pi^*$ (Figure 16), which is not what is usually labelled in the literature for MFs in this region of energies. $S_0 \rightarrow S_{2,3}$ excitations are $n \rightarrow \pi^*$ transitions, but these are dark. The absorption spectrum of IPCA in visible region is shaped by the S_1 state, as the next bright states S_6 in gas and S_5 in water are high in energy (Table 4). The calculated emission energy in solvent is red-shifted by 0.18 eV comparing to gas (Table 4), which is again only slightly overestimated comparing to the experimental value of 2.81 eV.

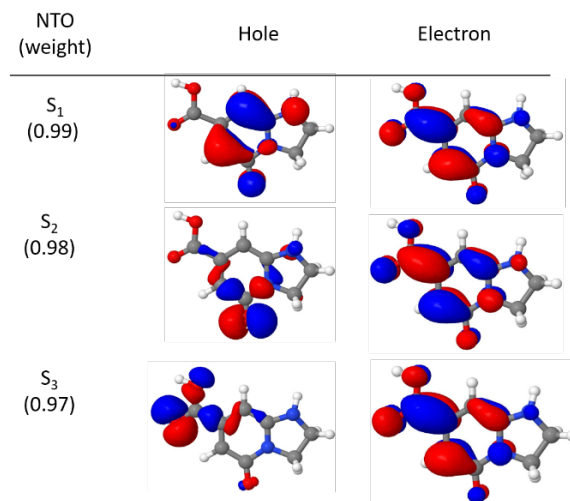


Figure 16. NTOs for the three lowest vertical singlet excitations of IPCA monomer in the gas phase. The isocontour value is 0.04 a.u. Reprinted with permission from 104. Copyright 2022 American Chemical Society.

Experimentally, the self-assembly of TPCA, a compound similar to IPCA, and the formation of TPCA stack configurations contributing to PL of respective CDs suggests that similar behavior may be estimated for IPCAs.²²⁵ Moreover, the diverse charge distribution on IPCA molecule (Figure 15b) due to the presence of the N atoms in the rings and functional groups, and plausible formation of different H-bonds because of the $-\text{COOH}$, $=\text{O}$, and $\text{N}-\text{H}$ groups make IPCA structurally comprehensive. Thus, the space for formation of interacting multimers is vast. Here, mainly due computational demands, we focused on description of IPCA dimers only. Seven different stacked IPCA dimer structures (Figure 17) were obtained with CAM-B3LYP-GD3 optimizations in aqueous solvent, starting from more configurations generated by making a full rotation of one molecule against the other in steps of 30° . Similar structures were found for the gas phase relaxations. The character of energy minima of our seven conformers was confirmed by the absence of imaginary frequencies in a harmonic vibrational analysis. The different mutual orientation of IPCAs in seven dimers caused that dimer-1, dimer-2, dimer-3 and dimer-5 formed

pronounced H-bonds in the range of 1.7–2.5 Å between the two monomers (Figure 17). Such H-bonds may help in the aggregation process leading to bigger assemblies (see chapter 6 for more detailed self-assembly study of IPCA molecules).

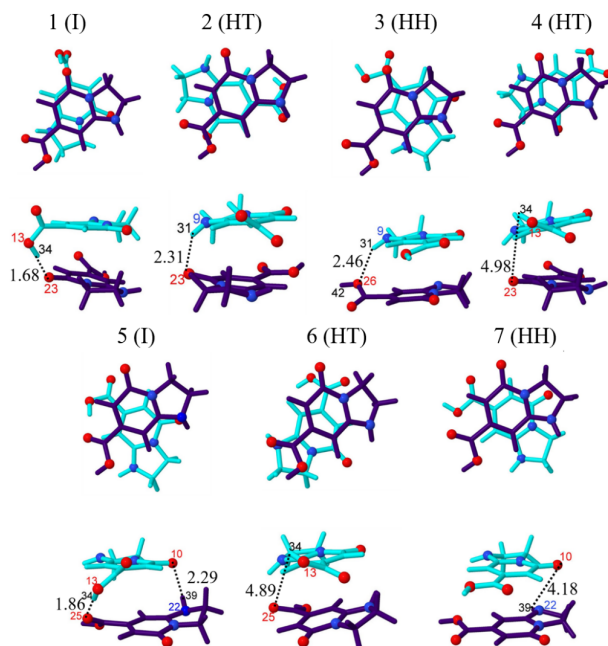


Figure 17. Top and side-views of the GS geometries of IPCA dimers 1–7 optimized using the CAM-B3LYP-D3 method with PCM. Nonbonded distances are given in Å. Reprinted with permission from 104. Copyright 2022 American Chemical Society.

The strength of interaction and thermodynamics of IPCA dimers will be described next, followed by the analysis of the optical properties. The relative stability of seven dimer structures was assessed with the interaction energies ΔE_{int} according to Equation 25 with CAM-B3LYP-GD3 in Gaussian09 and domain-based local pair natural orbital (DLPNO)²²⁶ coupled cluster CCSD(T)/cc-pVTZ^{227–229} in ORCA program package,²³⁰ both on the geometries obtained by the CAM-B3LYP-D3 calculations. TightPNO settings was applied for CC calculations and these values were corrected for the basis set superposition error (BSSE) using the counterpoise method²³¹ by computing the average of the BSSE-corrected and BSSE-uncorrected values to compensate for the overbinding when using the uncorrected values, but also for the underbinding in the case of the full counterpoise correction.²³²

$$\Delta E_{\text{int}} = E(\text{IPCA}_2) - 2E(\text{IPCA}) \quad (25),$$

where $E(\text{IPCA}_2)$ denotes the energy of the optimized dimer and $E(\text{IPCA})$ stands for the energy of the optimized monomer.

Table 5. Ground-state ΔE_{int} , ΔH_{int} and ΔG_{int} values for the dimer structures in gas phase and aqueous solution using the CAM-B3LYP-D3 method. ΔE_{int} value are given for DLPNO-CCSD(T) method only in the gas phase. All values are in kcal/mol. Reprinted with permission from 104. Copyright 2022 American Chemical Society.

No.	Interlayer H-bonds ^a	$\Delta E_{\text{int}}^{\text{b}}$			ΔH_{int}		ΔG_{int}	
		CAM-B3LYP-D3		DLPNO-CCSD(T) ^c	CAM-B3LYP-D3			
		gas	water	gas	gas	water	gas	water
1	Y	-18.5	-14.2	-14.5	-17.0	-13.0	-5.1	-2.5
2	Y	-15.5	-7.3	-12.8	-13.9	-5.8	-1.2	3.9
3	Y	-12.5	-9.5	-10.8	-11.1	-8.0	0.1	1.8
4		-12.4	-6.6	-10.0	-10.9	-5.1	0.6	4.6
5	Y	-12.2	-11.1	-9.9	-10.8	-9.6	1.9	2.0
6		-11.4	-7.7	-8.6	-10.0	-6.1	1.8	4.0
7		-11.3	-9.6	-10.1	-10.0	-8.0	1.1	2.0

^asee Figure 17; ^bcalculated with Equation 25 at the CAM-B3LYP-D3/def2-TZVP geometries; ^cthe average of the BSSE-uncorrected and BSSE-corrected values.

The most stable is dimer-1 for both gas and solvent, whose structure is almost perfectly overlapped six-membered aromatic rings and an H-bond between -COOH of first IPCA and the =O of the second IPCA (Table 5). The solvation decreased the interaction energy of dimer-1 by 4.3 kcal/mol as the solvent accessible surface in the dimer decreased in comparison to the two monomers. This trend was similar for all dimers, with the most significant decrease 8.2 kcal/mol accounted for dimer-2. DLPNO-CCSD(T) predicted the same order of interaction energies of the dimers as CAM-B3LYP-D3 calculations except for the dimer-7, which was found the fourth most stable with DLPNO-CCSD(T) calculations (Table 5), however it predicted slightly smaller interaction energies comparing, e.g., ΔE_{int} -14.5 kcal/mol of the most stable dimer-1 is smaller by 4.0 kcal/mol.

Additionally, interaction enthalpies (ΔH_{int}) and Gibbs free energies of interaction (ΔG_{int}) were calculated for the gas phase in analogy to Equation 25 using the standard harmonic oscillator/rigid rotator/ideal gas approximation. For solution, Gibbs free energy values were obtained by computing all necessary terms from the PCM calculations and a correction term $RT \cdot \ln(1/22.4)$ was added for the change of the reference state from ideal gas to solution.²³³ ΔH_{int} values only slightly decreased in the range of 1.2 to 1.6 kcal/mol comparing to ΔE_{int} (Table 5). On the other hand, Gibbs free energies changed significantly as the dimerization is accompanied by an entropy decrease related mainly to partial loss of translational and rotational freedom upon the

complexation. While ΔG values significantly reduced (Table 5), dimer-1 still manifested the most stable structure and indicated the spontaneous dimerization of IPCAs under ambient conditions.

Next, MD simulations of IPCA dimers in their GS in explicit aqueous solvent were undergone. Knowing that MD simulations sample the conformational space well, this methodology may be used to study the self-assembly and co-existence of CDs with IPCA in the bigger models (see chapter 6). The IPCA was parametrized for the generalized Amber force field (GAFF).²³⁴ The electrostatic potential of IPCA was calculated in Gaussian09 at HF/6-31G* level on geometries optimized with the same level of theory and RESP partial charges¹⁸³ were assigned by antechamber²³⁵ from AMBER software package.²³⁶ Orientation of the monomer dipole moment and its value of 6.91 Debye derived from MM partial charges agrees well with that of calculated at the CAM-B3LYP level (6.90 Debye) providing a good description of electrostatic distribution. In MD, two IPCA molecules were placed in a simulation box of dimensions $3.0 \times 3.0 \times 3.0 \text{ nm}^3$. For simulations in the water environment, the TIP3P explicit water model was used.¹⁹¹ The runs were performed in GROMACS 5.1 for 20 ns at 303 K, with 2 fs time step with LINCS constraints²³⁷ on all bonds. Coulombic interactions were treated with particle-mesh Ewald summation¹⁸⁹ at 1.4 nm while van der Waals interactions started to be switched off at 1.0 nm and fully switched off at 1.4 nm. For vacuum simulations NVT conditions were preserved, where the temperature was kept at 303 K with Nose-Hoover thermostat.^{238,239} The simulations in water were executed under NpT conditions, where additional Parrinello-Rahman barostat²⁴⁰ kept pressure of 1 atm.

The brief MM optimizations of the CAM-B3LYP-D3 dimer geometries negligibly changed their structural arrangement, as was evaluated with root-mean-square deviation (RMSD) values smaller than 0.02 nm (Figure 18). Only intermolecular H-bond distances were slightly underestimated (see side view of the dimer-1 and dimer-5 in Figure 18). This suggests that the parametrized FF may provide reasonable sampling of conformational space.

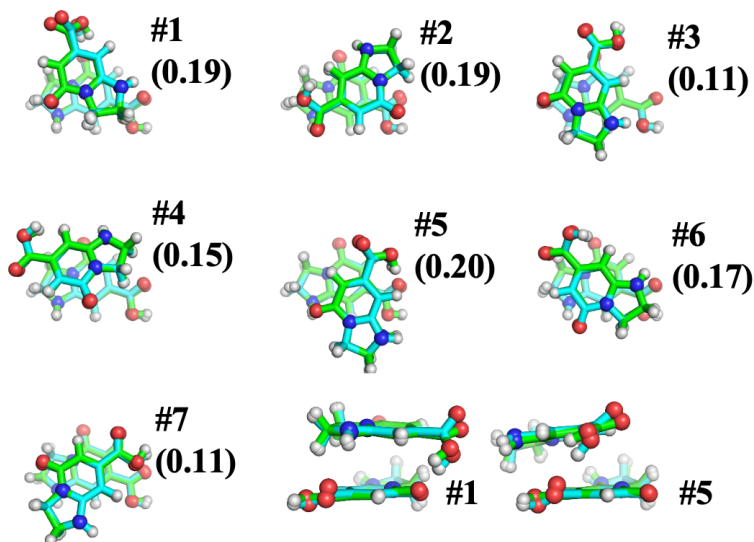


Figure 18. QM structures (cyan) and MM minimized structures (green) are almost identical (RMSD between QM and MM structures are shown in brackets in Å). Side view of structures #1 and #5 (right bottom) shows the difference in intermolecular H-bond interaction site. Reprinted with permission from 104. Copyright 2022 American Chemical Society.

Although these MD simulations demonstrated that IPCA dimers were stable in both gas and water, the tendency to dissociate to monomers was also revealed. The openings and closing of dimeric structure appeared frequently in the gas phase, while only two opening/closing movements were observed in water within the 20 ns simulation time (Figure 19a). Nevertheless, it can be stated that stacking arrangement is stable and the most populated center-of-mass (COM) distance 3.8 and 3.6 Å in the gas phase and aqueous solvent, respectively, collected within 20 ns runs (Figure 19b), were in a fair agreement, considering the temperature effects in MD simulations, with the distance range of 3.2–3.7 Å for CAM-B3LYP-D3 optimized structures. Moreover, the MD simulations showed the huge rotational flexibility of the two IPCA molecules in a dimer with respect to each other (Figure 19c). It can be seen that the distribution of angles was broader for simulations in gas, however, the histogram of angles between two IPCAs in the dimer showed that the dimer-2, the most stable structure based on the MM optimization and separated by only 1–3 kcal/mol from dimer-1 at the QM level, was the most populated (Figure 19c). The rotations occurred on short time scales, with a mean rotation time (mean time of transfer between -60° and $+60^\circ$ or vice versa) of 106 ps in the gas phase and 282 ps in water, respectively.

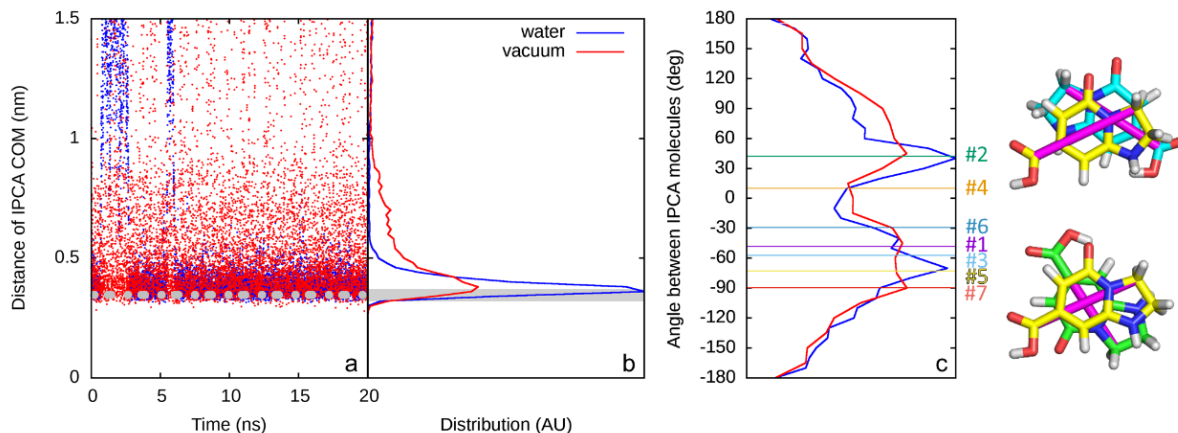


Figure 19. a) Time evolution of the distance of IPCAs COM. b) Distribution of the distances between IPCAs COM in vacuum (red) and water (blue); the distribution of COM distances in QM structures is shown as grey region. c) Histogram of angles between two molecular vectors (shown in magenta in IPCA structures). Angles corresponding to QM are shown in thin lines. Sample structures of major peaks at -70° (green) and $+45^\circ$ (cyan) are shown. Reprinted with permission from 104. Copyright 2022 American Chemical Society.

Excellent agreement with spectroscopic data was observed for excitation and emission of IPCA molecule calculated with TD-CAM-B3LYP-D3/def2-TZVP level (*vide ante*), supporting the validity of this theoretical approach. As the analysis of interaction energies and the estimations of thermodynamic values pointed on the stability of dimeric structures, their optical properties of IPCA after dimerization will be described next, with the stress on calculations in implicit PCM water. For the results of the PL of the dimers in gas, please visit the ref¹⁰⁴.

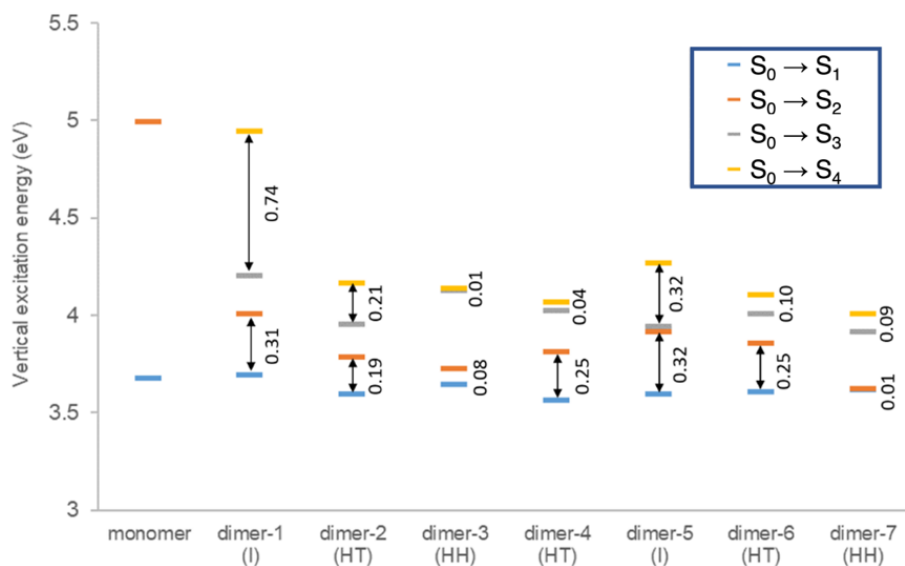


Figure 20. The VEEs (eV) for the lowest excited states of the IPCA monomer and dimers in water calculated at the TD-CAM-B3LYP-D3/def2-TZVP/cLR level of theory. Energy splitting is given in eV. Reprinted with permission from 104. Copyright 2022 American Chemical Society.

Table 6. VEEs ΔE (eV), oscillator strength (in parentheses), character, charge transfer (qCT) for the IPCA dimers using TD-CAM-B3LYP-D3 in the gas phase and aqueous solution (PCM). The character of the transition is based on the character of the hole and particle orbitals (see Table 7) for the individual monomer in the dimer. Reprinted with permission from 104. Copyright 2022 American Chemical Society.

		dimer-1				dimer-2				
		Gas phase		PCM		Gas phase		PCM		
No.	Character	ΔE	qCT	ΔE	qCT	Character	ΔE	qCT	ΔE	qCT
1	$\pi \rightarrow \pi^*$	3.62 (0.04)	0.41	3.69 (0.10)	0.13	$\pi \rightarrow \pi^*$	3.64 (0.06)	0.13	3.59 (0.08)	0.07
2	$\pi \rightarrow \pi^*$	3.92 (0.04)	0.57	4.00 (0.10)	0.55	$\pi \rightarrow \pi^*$	3.83 (0.07)	0.14	3.78 (0.12)	0.12
3	$\pi \rightarrow \pi^*$	4.32 (0.11)	0.03	4.20 (0.07)	0.35	$\pi \rightarrow \pi^*$	4.18 (0.03)	0.83	3.95 (0.03)	0.89
4	$n \rightarrow \pi^*$	5.05 (0.00)	0.02	4.94 (0.01)	0.91	$\pi \rightarrow \pi^*$	4.45 (0.02)	0.85	4.16 (0.02)	0.88
5	$n \rightarrow \pi^*$	5.27 (0.00)	0.06	5.19 (0.01)	0.03	$n \rightarrow \pi^*$	4.94 (0.00)	0.01	5.05 (0.00)	0.01
		dimer-3				dimer-4				
		Gas phase		PCM		Gas phase		PCM		
1	$\pi \rightarrow \pi^*$	3.78 (0.07)	0.05	3.64 (0.11)	0.02	$\pi \rightarrow \pi^*$	3.67 (0.04)	0.02	3.56 (0.04)	0.02
2	$\pi \rightarrow \pi^*$	3.84 (0.08)	0.03	3.72 (0.10)	0.02	$\pi \rightarrow \pi^*$	3.93 (0.14)	0.01	3.81 (0.19)	0.01
3	$\pi \rightarrow \pi^*$	4.23 (0.01)	0.93	4.12 (0.00)	0.98	$\pi \rightarrow \pi^*$	4.27 (0.00)	0.96	4.02 (0.00)	0.97
4	$\pi \rightarrow \pi^*$	4.56 (0.00)	0.96	4.13 (0.01)	0.96	$\pi \rightarrow \pi^*$	4.68 (0.00)	0.97	4.06 (0.00)	0.97
5	$n \rightarrow \pi^*$	4.81 (0.00)	0.01	5.01 (0.00)	0.00	$n \rightarrow \pi^*$	4.93 (0.00)	0.01	4.97 (0.00)	0.01
		dimer-5				dimer-6				
		Gas phase		PCM		Gas phase		PCM		
1	$\pi \rightarrow \pi^*$	3.62 (0.08)	0.03	3.59 (0.10)	0.05	$\pi \rightarrow \pi^*$	3.54 (0.04)	0.09	3.60 (0.07)	0.05
2	$\pi \rightarrow \pi^*$	4.15 (0.11)	0.10	3.91 (0.10)	0.12	$\pi \rightarrow \pi^*$	3.92 (0.12)	0.10	3.85 (0.16)	0.04
3	$\pi \rightarrow \pi^*$	4.36 (0.00)	0.94	3.94 (0.04)	0.86	$\pi \rightarrow \pi^*$	4.19 (0.01)	0.88	4.00 (0.00)	0.96
4	$\pi \rightarrow \pi^*$	4.56 (0.01)	0.89	4.26 (0.03)	0.94	$\pi \rightarrow \pi^*$	4.48 (0.01)	0.87	4.10 (0.01)	0.94
5	$n \rightarrow \pi^*$	4.71 (0.00)	0.00	4.98 (0.00)	0.00	$n \rightarrow \pi^*$	4.74 (0.00)	0.02	4.97 (0.00)	0.00
		dimer-7								
		Gas phase		PCM						
1	$\pi \rightarrow \pi^*$	3.71 (0.05)	0.07	3.61 (0.12)	0.08					
2	$\pi \rightarrow \pi^*$	3.87 (0.12)	0.10	3.62 (0.07)	0.05					
3	$\pi \rightarrow \pi^*$	4.22 (0.02)	0.88	3.91 (0.03)	0.92					
4	$\pi \rightarrow \pi^*$	4.56 (0.00)	0.92	4.00 (0.03)	0.91					
5	$n \rightarrow \pi^*$	4.71 (0.00)	0.01	4.99 (0.00)	0.00					

Table 7. NTOs for the vertical transitions of the five lowest singlet excitations for the seven ground-state dimer structures. The isocontour value is 0.04 a.u. For each state the NTO with the largest weight, the weight and the assignment are given. Reprinted with permission from 104. Copyright 2022 American Chemical Society.

Dimer-1 NTO	Hole	Electron	Dimer-2 NTO	Hole	Electron
1-S ₁ 0.987 $\pi \rightarrow \pi^*$			2-S ₁ 0.971 $\pi \rightarrow \pi^*$		
1-S ₂ 0.991 $\pi \rightarrow \pi^*$			2-S ₂ 0.984 $\pi \rightarrow \pi^*$		
1-S ₃ 0.965 $\pi \rightarrow \pi^*$			2-S ₃ 0.963 $\pi \rightarrow \pi^*$		
1-S ₄ 0.939 $n \rightarrow \pi^*$			2-S ₄ 0.992 $\pi \rightarrow \pi^*$		
1-S ₅ 0.805 $n \rightarrow \pi^*$			2-S ₅ 0.956 $n \rightarrow \pi^*$		
Dimer-3 NTO	Hole	Electron	Dimer-4 NTO	Hole	Electron
3-S ₁ 0.983 $\pi \rightarrow \pi^*$			4-S ₁ 0.884 $\pi \rightarrow \pi^*$		
3-S ₂ 0.983 $\pi \rightarrow \pi^*$			4-S ₂ 0.883 $\pi \rightarrow \pi^*$		
3-S ₃ 0.997 $\pi \rightarrow \pi^*$			4-S ₃ 0.998 $\pi \rightarrow \pi^*$		
3-S ₄ 0.997 $\pi \rightarrow \pi^*$			4-S ₄ 0.998 $\pi \rightarrow \pi^*$		
3-S ₅ 0.983 $n \rightarrow \pi^*$			4-S ₅ 0.947 $n \rightarrow \pi^*$		
Dimer-5 NTO	Hole	Electron	Dimer-6 NTO	Hole	Electron
5-S ₁ 0.984 $\pi \rightarrow \pi^*$			6-S ₁ 0.958 $\pi \rightarrow \pi^*$		

5-S ₂ 0.952 $\pi \rightarrow \pi^*$			6-S ₂ 0.888 $\pi \rightarrow \pi^*$		
5-S ₃ 0.962 $\pi \rightarrow \pi^*$			6-S ₃ 0.967 $\pi \rightarrow \pi^*$		
5-S ₄ 0.985 $\pi \rightarrow \pi^*$			6-S ₄ 0.991 $\pi \rightarrow \pi^*$		
5-S ₅ 0.993 $n \rightarrow \pi^*$			6-S ₅ 0.988 $n \rightarrow \pi^*$		
Dimer-7 NTO	Hole	Electron			
7-S ₁ 0.957 $\pi \rightarrow \pi^*$					
7-S ₂ 0.901 $\pi \rightarrow \pi^*$					
7-S ₃ 0.972 $\pi \rightarrow \pi^*$					
7-S ₄ 0.995 $\pi \rightarrow \pi^*$					
7-S ₅ 0.989 $n \rightarrow \pi^*$					

The first two excited states for all dimers can be characterized by an excitonic splitting of the molecule $S_0 \rightarrow S_1$ transition (Figure 20). These are different for the seven dimers, as they strongly depend on the relative orientation of the IPCA molecules. Taking into consideration many populated states with MD simulations, the PL may be quite diverse. In solvent, the smallest splitting was observed for dimer-7 and dimer-3 (0.01 eV and 0.08 eV), the highest was observed dimer-5 (0.32 eV). The S_1 states of most dimers are lowered by ~ 0.2 eV compared to the single IPCA molecule S_1 state in the water solvent (Table 6).

Interlayer charge transfer (CT) excitations may be interesting as in general they could be more sensitive to the changes in the environment. For the first two $S_0 \rightarrow S_{1-2}$ electronic transitions, only NTOs for $S_0 \rightarrow S_1$ transitions in dimer-1 demonstrated that the electron is transferred from

a π -orbital delocalized over both monomers to a π^* orbital localized only on one of the monomers (Table 7). The NTOs of S_1 state for the other dimer showed that the transition is a local excitation realized within the π -orbital space of one monomer only. For the higher excited state S_{3-5} other CT transitions could be found, e.g., S_3 state of dimer-5, but these states are dark as their calculated oscillator strength is close to zero (Table 6). The character of first $S_0 \rightarrow S_{1-4}$ is $\pi \rightarrow \pi^*$ transition except dark S_4 state of dimer-1. Thus, the UV absorption spectrum of the IPCA spectrum is dominated by $\pi \rightarrow \pi^*$ transitions, which gives a new picture for the assignment of lumiphore bands in CDs by stressing the importance of $\pi \rightarrow \pi^*$ excitations not only in the CD core but also in the CD shell containing molecular luminophores, in contrast to previous analyses,¹⁰³ which reported $n \rightarrow \pi^*$ transitions.

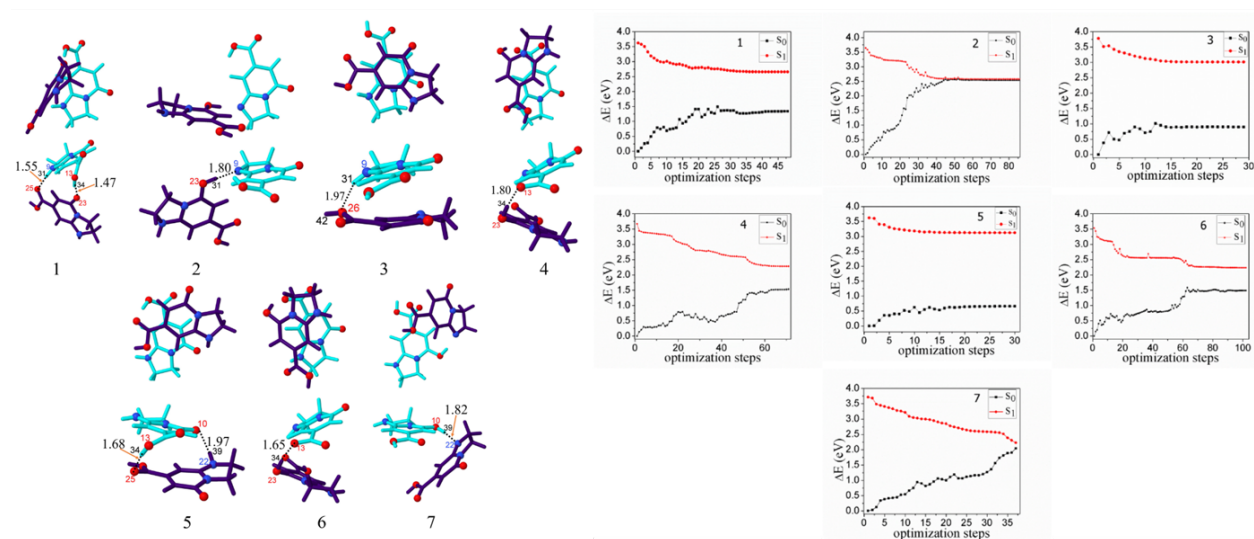
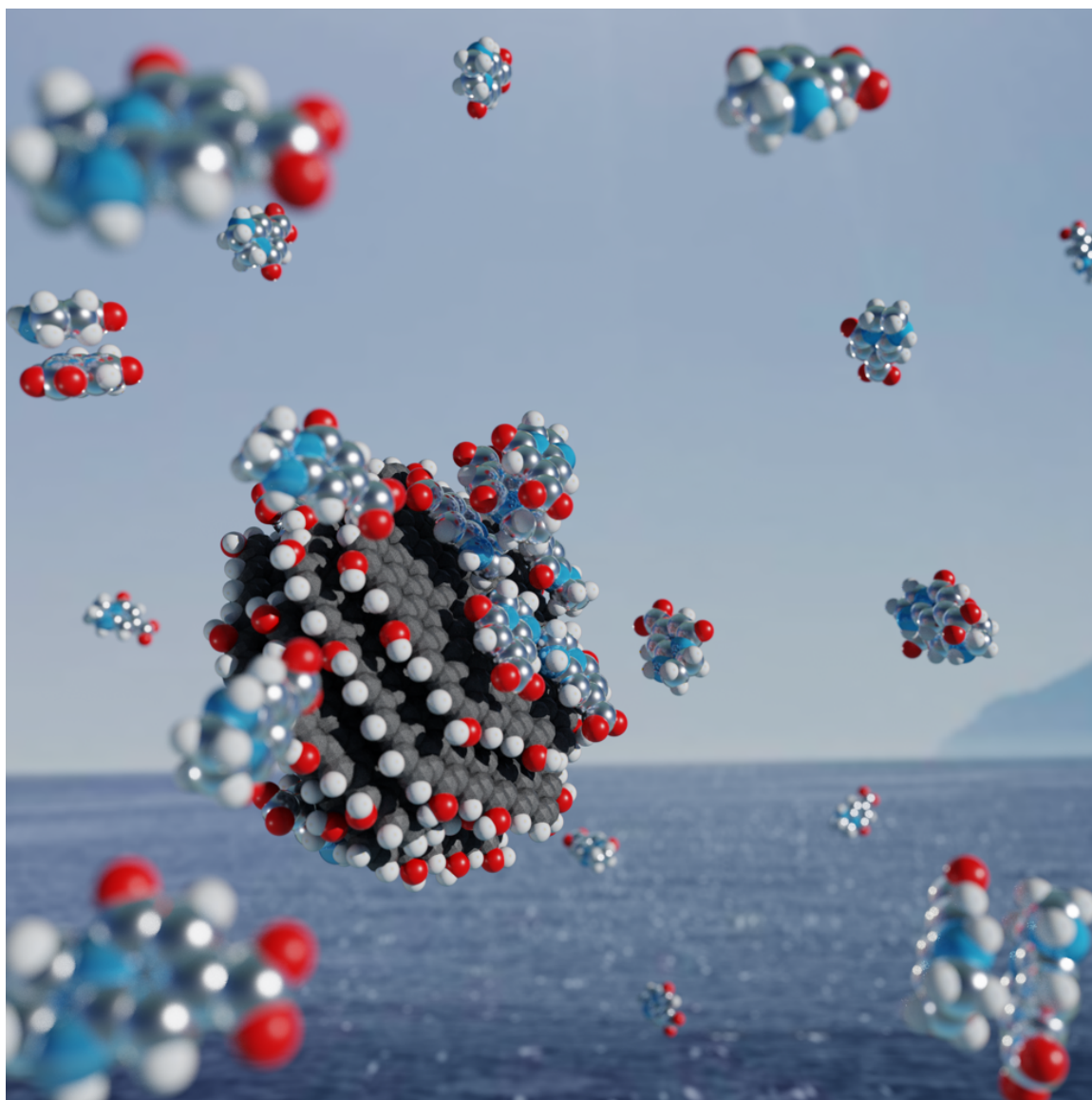


Figure 21. Left panel: Dimer structures in the gas phase after partial optimization in S_1 ; distances are in Å. The structures are taken at the endpoints of the optimization curves shown in the right panel. Right panel: Potential energy curves for S_0 and S_1 states during the geometry optimization steps for S_1 of the IPCA dimer for structures dimers-1-7 in gas phase. Reprinted with permission from 104. Copyright 2022 American Chemical Society.

In the analysis of the emission of the dimers, the highly interesting possibility of dimer opening and the occurrence of conical intersection between S_0 and S_1 could be anticipated. This would lead to the rapid internal conversion to the GS and quenching of the fluorescence. The optimizations pathways for the S_1 state in gas phase indicated such S_1/S_0 intersections for dimer-2 and dimer-7 and structurally, these dimeric structures are open with more pronounced CT (Figure 21). On contrary, the large S_1/S_0 energy gaps were witnessed for dimer-3 and dimer-5. Such opening of the IPCA dimers was not found in the calculations in aqueous solvent. The vertical

emission energy in water of the four dimers demonstrated either almost no shift comparing to single IPCA molecule, or a red-shift 0.31 eV or large red-shift of ~ 0.9 eV suggesting interesting photodynamical behavior with respect to both internal conversion and fluorescence emission behavior.

6 Molecular Fluorophores Self-Organize into C-Dot Seeds and Incorporate into C-Dot Structures[‡]



[‡] Published as: Langer, M.; Paloncýová, M.; Medved', M.; Otyepka, M. Molecular Fluorophores Self-Organize into C-Dot Seeds and Incorporate into C-Dot Structures. *J. Phys. Chem. Lett.* 2020, 11 (19), 8252–8258.

The break of the stacked IPCA dimer arrangement in its S_1 geometry minimum in gas settled the foundation for the investigation if the dramatic change of PL due to the opening of the stacked IPCA dimer is plausible in real CDs samples. Although the break of stacking pattern was already found unlikely in water, the organization of MFs in the vicinity of CDs is not known. MFs may still occupy some specific local conformations with CDs, where similarities with behavior in gas may be observed. Therefore, the mutual arrangement of IPCA/CDs had to be addressed. There are also three other reasons behind this publication. First, the aggregates of MFs and assemblies of PAHs exhibit PL properties similar to those reported for CDs. It is highly challenging for experimental techniques to provide the structural features of such assemblies. On the contrary, MD simulations can apprehend the complexity and dynamics of the MF assemblies and provide the proper sampling of the phase space (see chapter 5). Third motivation is the idea that MFs may form the seeds of CDs for carbonization process during CD growth.

Here, classical all-atom MD simulations delivered the insight how two protonated forms of IPCA, i.e., neutral and anionic, self-assemble and interact with graphitic units of CDs (Figure 22). Only non-covalent bonds between CD and IPCA were considered here.

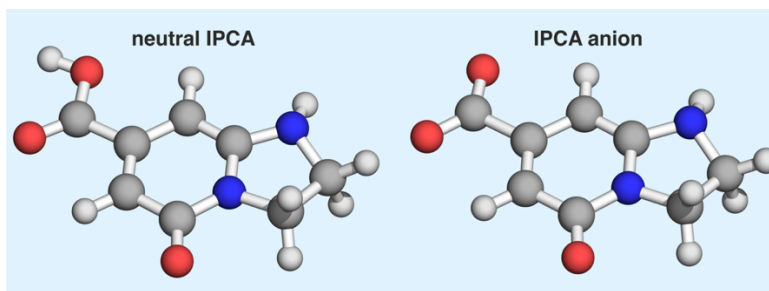


Figure 22. The molecular structures of neutral IPCA(0) and anionic IPCA(-1).

Methodologically, GAFF (for IPCA) and parm99 (for PAHs) FFs were used for description of the interaction potentials in our MD simulations; LJ parameters of aromatic carbons in CDs were, again, refined based on the study of ammonia adsorption on the basal plane of graphite.²¹⁶ All simulations were performed in SPC/E water model. Several different model systems were investigated, their list is summarized in Table 8. All structures and topologies of CDs functionalized on the edges by 30% with -OH groups, as well as PAHs, were generated using the CD Builder (see chapter 4). In the calculations of anionic IPCAs, the simulation box was neutralized using the Na^+ ions.²⁴¹

All MD computational details may be found in the ref ²⁴². Here, I would like to briefly summarize that productive MD simulations were performed in GROMACS 5.0 software package under NpT conditions with a 2 fs time step. Temperature was kept constant at 300 K with the V-rescale thermostat²⁴³ with a 0.1 ps scaling constant, pressure was kept at 1 bar with the isotropic Berendsen barostat,²⁴⁴ and the time constant for pressure relaxation was set to 2.0 ps. Electrostatic interactions were treated by means of the PME method with a real-space cutoff of 1.0 nm; the same cutoff was applied for van der Waals interactions. Periodic boundary conditions were applied in all three dimensions. Moreover, alternative set of simulations were also carried out for 4 studied systems (see asterisks in Table 8) at temperature of 473 K and pressure 15.5 bar to mimic the synthetic conditions during carbonization of CDs.

Table 8. Composition of simulation boxes with numbers of PAH layers, number of IPCAs and water molecules. Reprinted with permission from 242. Copyright 2022 American Chemical Society.

	System	CD	Largest layer edge size (#rings)	IPCA (-1)	IPCA (0)	Water	Box dimensions (nm)	Simulation length (ns)
IPCA (-1)	A	None*	0	50	0	10894	7.4 × 7.0 × 6.7	200
	B	4 layers	6	20	0	7302	6.1 × 6.1 × 6.1	200
	C	9 layers	6	10	0	10753	7.4 × 7.0 × 6.7	200
	D	6 layers*	6	15	0	8360	6.5 × 6.5 × 6.5	200
	E	5 layers	3	5	0	3870	5.0 × 5.0 × 5.0	100
IPCA (0)	F	None*	0	0	50	10929	7.4 × 7.0 × 6.7	200
	G	4 layers	6	0	20	7309	6.2 × 6.2 × 6.2	200
	H	9 layers	6	0	10	10766	7.4 × 7.0 × 6.7	200
	I	6 layers*	6	0	15	8360	6.5 × 6.5 × 6.5	200
	J	5 layers	3	0	5	3870	5.0 × 5.0 × 5.0	100
PAH	K	9 layers	6	0	0	8280	6.5 × 6.5 × 6.5	200
	L	5 layers	3	0	0	3910	5.0 × 5.0 × 5.0	100

* These simulations were also performed at temperature 473 K and pressure 15.5 bar.

The quality of the chosen FF was proven by the good agreement of interaction energies ΔE_{int} calculated with the MM potential on minimized MM geometries with DLPNO-CCSD(T), i.e., the mean error -1.5 kcal/mol and mean unsigned error 2.4 kcal/mol (Table 9) of the MM potential comparing to DLPNO-CCSD(T). Interaction energies were calculated following the Equation 26 and MM values were calculated in GROMACS on geometries obtained after steepest descent energy minimization of IPCA dimer structures in the gas phase. DLPNO-CCSD(T)/TightPNO²²⁶ energies of stacked dimers were taken from our previous calculations,¹⁰⁴ the H-bonded dimer was

calculated in the same manner, and ω B97x-D/6-31++G(d,p)¹⁵⁹ energies were calculated on the same geometries.

$$\Delta E_{\text{stab}} = E(\text{AB})_{\text{AB}} - E(\text{A})_{\text{A}} - E(\text{B})_{\text{B}} \quad (26)$$

Table 9. MM was calculated with the same parameters as used in the MD simulation; DLPNO-CCSD(T)(TightPNO)/cc-pVTZ energies are those from chapter 5; and ω B97x-D/6-31++G(d,p) interaction energies ΔE_{int} for the dimer IPCA(0) structures in the GS calculated in the gas phase. Ground state Δ ZPVE (zero point vibration energy), ΔH_{corr} , $T\Delta S$ for the dimerization of IPCAs(0),¹⁰⁴ were calculated for two different temperature and pressure conditions (A: 293.15 K, 1.0 atm; B: 473.15 K, 15.3 atm). All values are in kcal/mol. Reprinted with permission from 242. Copyright 2022 American Chemical Society.

.No.	ΔE_{stab}			ω B97x-D/6-31++G(d,p) ^c							
	MM ^a	DLPNO-CCSD(T) ^c	ω B97x-D ^c	Δ ZPVE + ΔE_{corr} + ΔH_{corr}		$T\Delta S$		$\Delta\Delta(G_{\text{solv}})$		ΔG_{solv} ^d	
				A	B	A	B	A	B	A	B
1	-13.0	-14.5 ^b	-20.2	0.3	0.1	-16.2	-23.4	-4.4	-4.1	-2.4	5.0
2	-15.3	-12.8 ^b	-17.2	0.3	0.2	-15.4	-22.0	-7.4	-7.8	-4.4	1.6
3	-13.0	-10.8 ^b	-14.8	-1.1	-1.8	-17.5	-26.1	-2.2	-0.7	3.4	12.8
4	-12.3	-10.0 ^b	-14.0	-0.5	-0.8	-15.7	-22.8	-3.3	-3.0	1.9	9.0
5	-8.5	-9.9 ^b	-13.2	0.1	0.0	-15.6	-22.3	-2.2	-2.9	3.5	9.5
6	-13.4	-8.6 ^b	-13.1	-0.5	-0.8	-16.6	-24.2	-3.5	-3.2	4.1	11.6
7	-12.0	-10.1 ^b	-13.0	0.0	0.0	-13.7	-19.1	-3.6	-4.9	0.1	4.2
8	-14.3	-24.3	-17.6	0.1	-0.4	-15.0	-21.9	-8.4	-9.4	-17.5	-12.2

^a Calculated on MM optimized geometries.

^b These values were taken from the reference.¹⁰⁴

^c Calculated using CAM-B3LYP/def2-TZVP/GD3 geometries.

^d The ΔG_{solv} value was obtained as the sum of the DLPNO-CCSD(T) electronic energy and all other contributions evaluated at the DFT level.

A. IPCA-IPCA assembly

The MD simulations at ambient conditions revealed the fast and spontaneous formation of stacked self-assemblies of both protonated forms of IPCA within a few nanoseconds (system A Figure 23). Because anionic IPCAs electrostatically repulse other anionic IPCAs due to their deprotonated $-\text{COO}^-$ groups, the neutral IPCAs formed more stable stacks and those were assembled in much longer fibrils interacting via π - π stacking interactions comparing to anionic IPCA, as it is displayed in the clustering analysis, that was done using the customized code (Figure 24).²⁴⁵ Besides the extensive stacking, the IPCA(0) stacks also formed H-bonds with the IPCA(0) molecules of the neighboring stack (Figure 26f). The MD simulations at temperature of 473 K and

pressure 15.5 bar, being the synthetic conditions during one preparation procedure of CDs, the IPCAs clustered less (Figure 24e, f). Nonetheless, the IPCA stacks were still formed at these synthetic conditions (Figure 24d), confirming the idea that IPCAs could act like seeds for CDs growth.

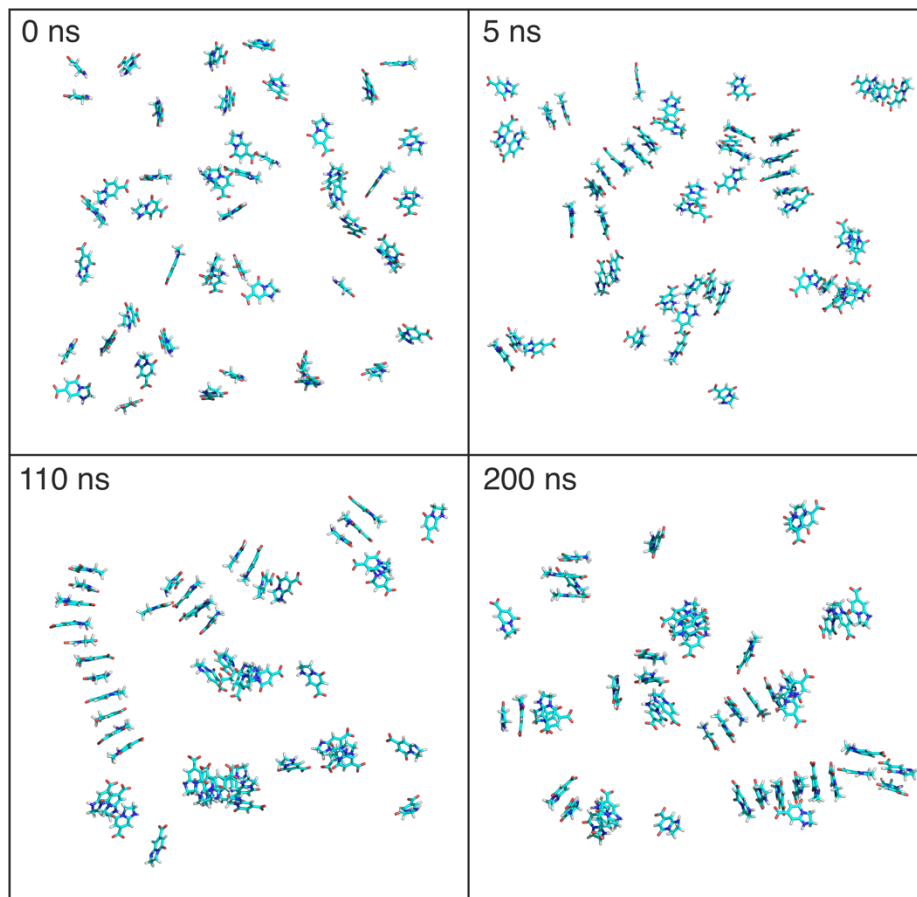


Figure 23. Evolution of self-assemblies of IPCA anions (system A in Table 9) in time. Coloring scheme: cyan-carbon; red-oxygen; blue-nitrogen; white-hydrogens. Water and ions were omitted for clarity. Reprinted with permission from 242. Copyright 2022 American Chemical Society.

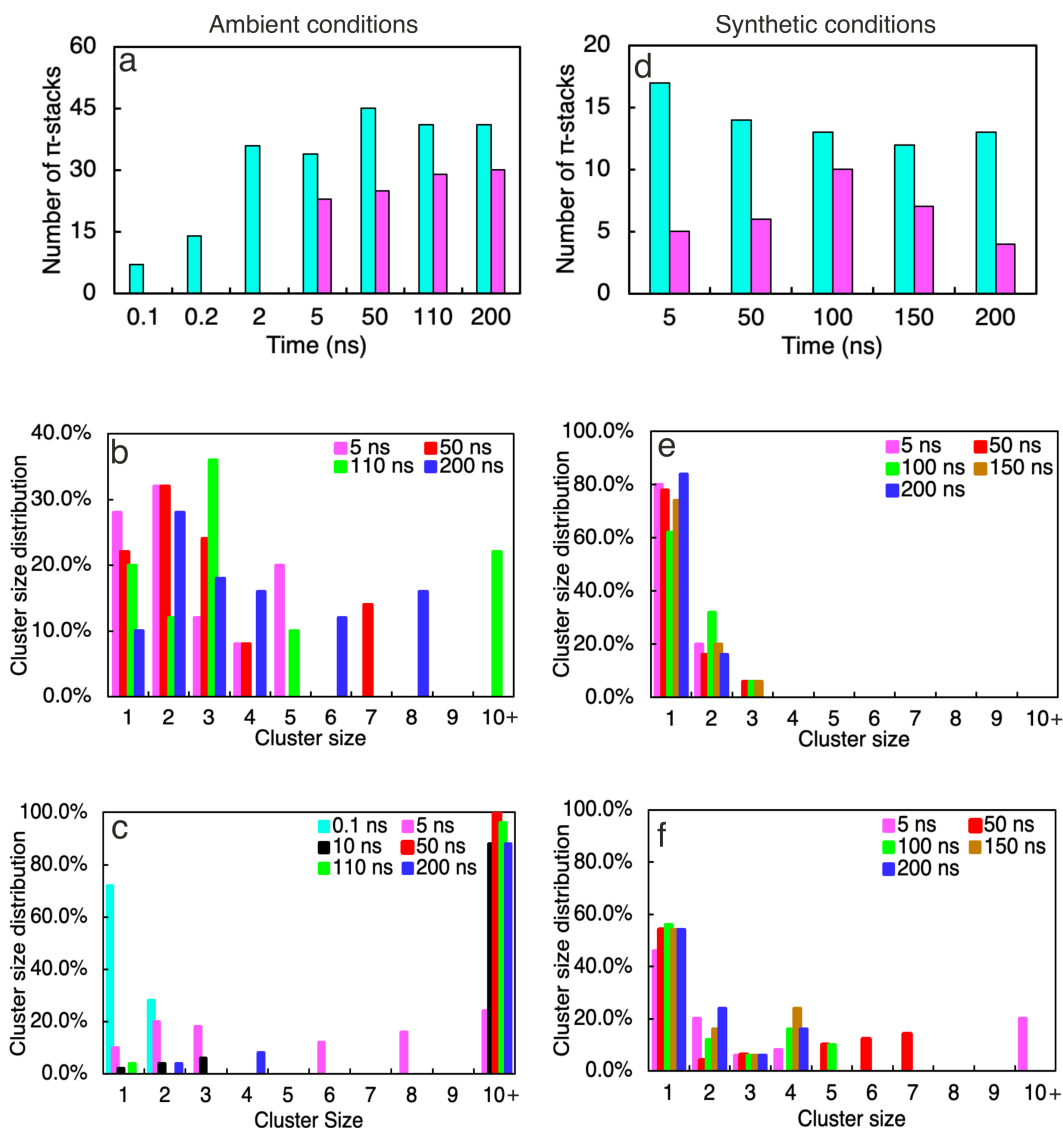


Figure 24. (a, d) Number of π -stacks of neutral (cyan, system A) and deprotonated (magenta, system F) IPCA molecules collected at different times of MD simulations simulated at (a) 300 K and 1 bar; and (d) at 473 K and 15.5 bar, revealing the tendency of IPCA molecules to be self-assembled in water. Clustering analysis of (b) deprotonated IPCAs (300 K, 1 bar), (c) neutral IPCAs (300 K, 1 bar), (e) deprotonated IPCAs (473 K, 15.5 bar), (f) neutral IPCAs (473 K and 15.5 bar) analyzed for selected simulation times show the number of IPCAs that preferentially formed the clusters. Cluster size distribution refers to how many IPCAs of the total number are in the particular stack. Reprinted with permission from 242. Copyright 2022 American Chemical Society.

The stronger affinity of neutral IPCAs comparing to anionic IPCAs was supported by potential of mean forces (PMF) profiles (Figure 25, see green and red curves). These biased MD simulations (constraining the distances of COMs) clearly quantified the tendency of IPCA molecules to stack, with the π - π stacking interlayer distance ~ 0.34 nm, which is close to the (002) facet of graphitic structures. Although the interaction ~ 3.8 kcal/mol for IPCA(0) stacks holds the

stacks together, these systems are highly dynamical. Dissociation and reassociation events were observed in IPCA multimers; dimers were formed either from two molecules or by the disintegration of larger stacks; and they either aggregated into longer stacks or dissolved back into two molecules. Despite the electrostatic repulsion of anionic IPCA molecules, the π - π stacking was preserved by the orientation of the charged carboxyl group in the neighboring stacks facing the opposite direction (Figure 26d) and/or by stabilization with the Na^+ counterions.

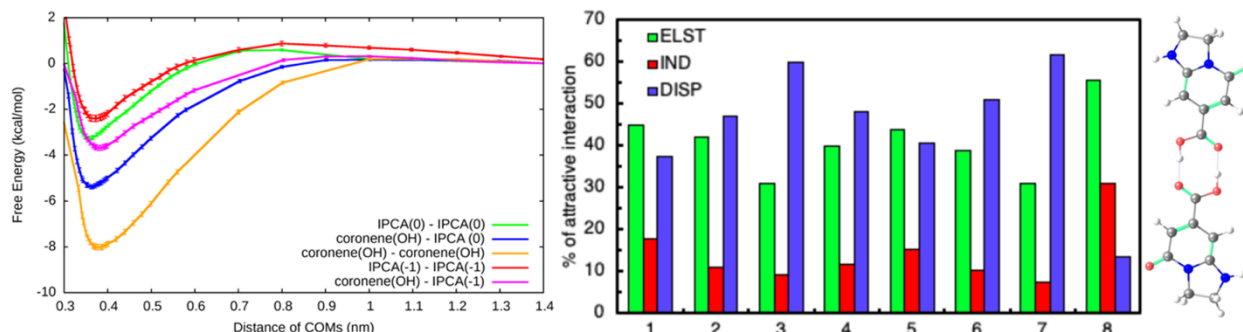


Figure 25. Left panel displays PMF along the distance of centers of masses (COMs) for IPCA(0) dimer (green), IPCA(0) on OH-coronene (blue), two OH-coronenes (orange), IPCA(-1) dimer (red) and IPCA(-1) on OH-coronene (magenta). Right panel displays SAPT0 percentual contribution to the attractive interaction energy components, i.e., electrostatics (ELST), induction (IND) and dispersion (DISP) for IPCA dimers. The quasi-planar H-bonded dimer represents structure labeled as 8, the structures of other dimers were taken from the reference.¹⁰⁴ Reprinted with permission from 242. Copyright 2022 American Chemical Society.

The nature of the interaction between seven stacked IPCA(0) dimers (see chapter 5) and one H-bonded IPCA(0) dimer (structure in Figure 25) was further elucidated with symmetry-adapted perturbation theory (SAPT)²⁴⁶ calculations in the PSI4²⁴⁷ code. The SAPT²⁴⁶ approach at the zeroth-order fluctuation potential approximation (SAPT0) in combination with the aug-cc-pVDZ basis set was used for decomposition of the interaction energy for IPCA(0) dimers in the gas phase using the CAM-B3LYP/def2-TZVP/GD3^{155,156,218} geometries of stacked dimers. Geometry of a quasi-planar H-bonded dimer (labeled as 8) was obtained at the same level of theory. The SAPT0 calculations showed that all studied stacked dimers were predominantly stabilized by dispersion and electrostatics, where the main contribution was dependent on the mutual orientation of the molecules (see Figure 25, right panel). The quasi-planar H-bonded dimer-8 was mostly stabilized by electrostatics.

Additionally, free energies ΔG (Equation 27) and enthalpies ΔH of dimerization evaluated at ambient (298.15 K; 1 atm) and synthetic (473.15 K; 15.3 atm) condition revealed an increase in the $T\Delta S$ term by ~ 5.6 kcal/mol for the synthetic conditions (Table 9), which indicated the decrease

of IPCA stacking at synthetic conditions. On the other hand, the ~ 0.3 kcal/mol difference of average value of ΔH (over all dimers) for both conditions reveals that enthalpy is not behind the dissociation of dimers. Free energies ΔG and enthalpies ΔH of dimerization were calculated in the gas phase and water (SMD implicit water model¹⁹⁴) at the ω B97x-D/6-31++G(d,p) level of theory in Gaussian16.²⁴⁸ Structures of IPCA(0) dimers were taken from the reference¹⁰⁴ (CAM-B3LYP/def2-TZVP/GD3).

$$\Delta G_{solv} = \Delta E + \Delta ZPVE + \Delta E_{corr} + \Delta H_{corr} - T\Delta S + \Delta\Delta(G_{solv}) \quad (27),$$

where ΔE is the electronic energy, $\Delta ZPVE$ is the zero-point vibrational energy, ΔE_{corr} is thermal energy correction, ΔH_{corr} is the thermal correction to enthalpy, ΔS is entropy and $\Delta\Delta(G_{solv})$ was calculated as $[\Delta G(\text{gas}) - \Delta G(\text{solvent})]$.

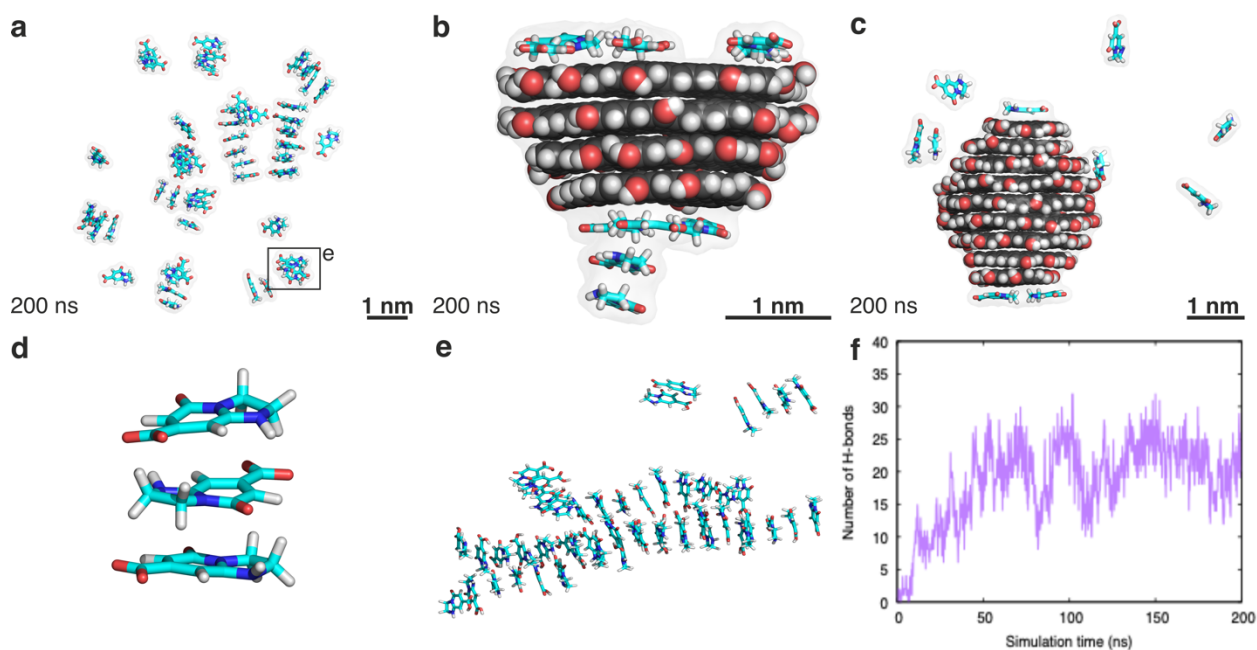


Figure 26. Snapshots taken from MD simulations (at 200 ns) of (a) system **A** (in Table 9) showing self-assemblies of IPCA anions; (b) System **B** showing that IPCA anions can self-assemble and also stack on an accessible surface of a CD fragment (shown by darker colors), forming an ad-layer on the CD; (c) System **C** showing that IPCA can also interact with a spherical CD. (d) Inset taken from panel (a) showing an example of IPCA trimer. (e) Self-assembled structure of system **F** collected at 200 ns. (f) Evolution of the number of H-bonds between in system **F**. Coloring scheme: cyan, black-carbon; red-oxygen; blue-nitrogen; white-hydrogens. Water and Na^+ are omitted for clarity. Reprinted with permission from 242. Copyright 2022 American Chemical Society.

B. IPCA-PAHs assembly

Our MD simulations of IPCAs with CD units, either with half-spherical (systems **B**, **G**) or spherical CD (systems **C**, **H**) revealed that IPCAs interact with graphitic layers of CDs either by π - π stacking on the solvent exposed accessible aromatic surface (IPCA anions created typically one or two or three adlayers on the outer CD layer) and/or by formation of H-bonds with –OH groups on the edges of CDs, creating mixed nanoparticles (Figure 26b, c). Nevertheless, the H-bonded complexes of IPCA with CDs were unstable and quickly broke apart in few ns. Both protonated and deprotonated IPCAs were able to create adlayers internally stabilized by a H-bonding network, with an arrangement of layers similar to that in ordinary graphitic CDs (shown on system **I** in Figure 27). These layers stacked on each other in order to regain the spherical shape, which is displayed on radius of gyration (R_g). R_g varied during the first ~20 ns, afterwards it remained constant and similar in all dimensions, suggesting a spherical shape (shown on system **J** in Figure 28). Additionally, the interlayer spacing ~0.34 nm was still resembling graphitic layering (shown on systems **D**, **K**, Figure 29). Hence, the assembly process leads to the formation of CDs with graphitic structure that are hardly distinguishable from PAH CDs in terms of their density profile. The stacking of IPCAs onto the PAHs was further corroborated with the PMF calculations from MD simulations (Figure 25, see blue and pink curves). While the depth of energy minimum in IPCA dimer correspond to ~3.8 kcal/mol, IPCA(0) on coronene interacts with 5.5 kcal/mol and two coronenes stack with a 8.2 kcal/mol energy gain (Figure 25, see orange curve).

The MD simulations also suggested that IPCA molecules can also incorporate into the structure of CDs (Figure 27, Figure 28). All these observations imply that MFs may be confined inside and as such, the unwanted non-radiative emission due to dimer opening is not very likely. The close distance of MFs and CDs should be kept in mind in a discussion of mechanism of their PL. Therefore, all the PL centers, core, surface, and molecular states may co-operate, and energy and charge transfer pathways may be enabled.

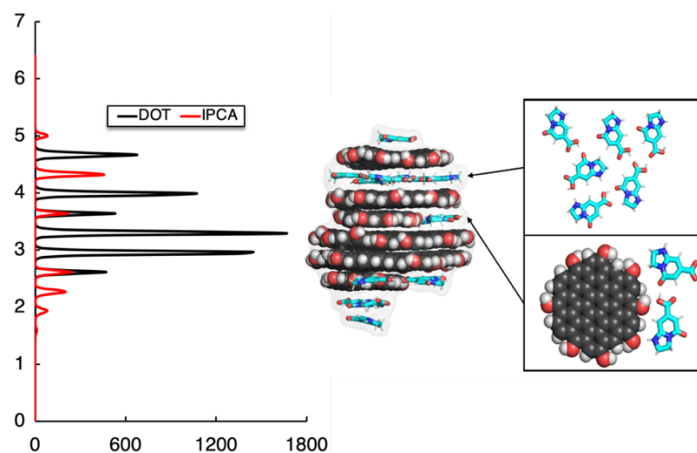


Figure 27. Density profile of studied system **I** collected over 100 ns simulation time and the molecular arrangement of IPCAs(0) in this structure. PAH layers are represented by spheres, IPCAs are represented with sticks. Coloring scheme: cyan, black-carbon; red-oxygen; blue-nitrogen; white-hydrogens. Reprinted with permission from 242. Copyright 2022 American Chemical Society.

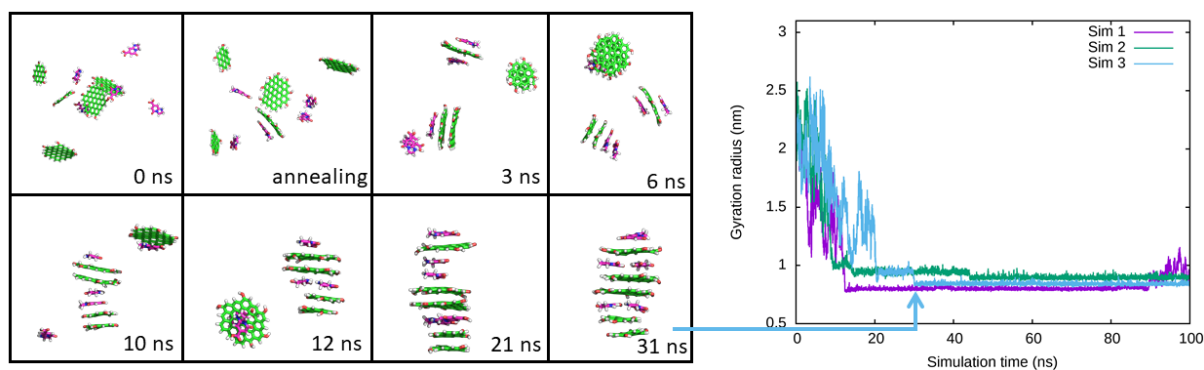


Figure 28. Snapshots taken from self-assembly of system **J** and time evolution of radii of gyration (R_g). Increase in R_g for Sim 1 after ~ 90 ns is caused by detaching of one IPCA molecule into the solution. Coloring scheme: green/magenta-carbon; red-oxygen; blue-nitrogen; white-hydrogens. Water was omitted for clarity. Reprinted with permission from 242. Copyright 2022 American Chemical Society.

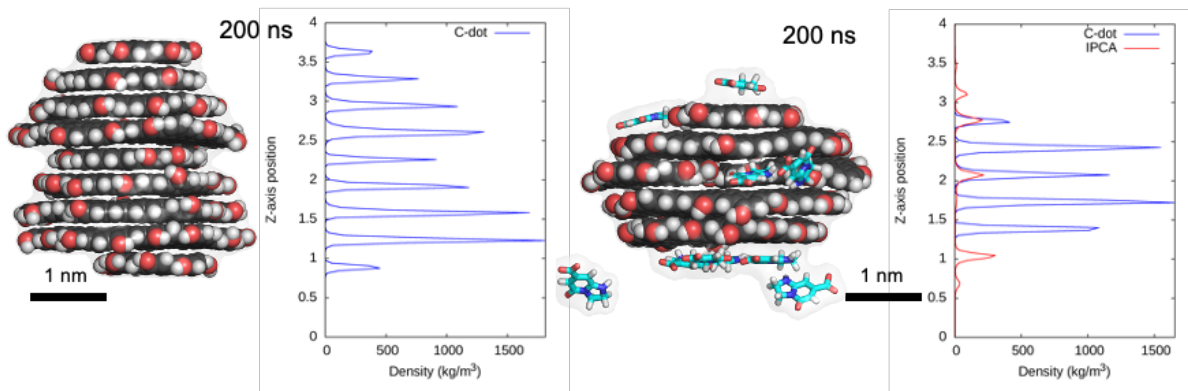
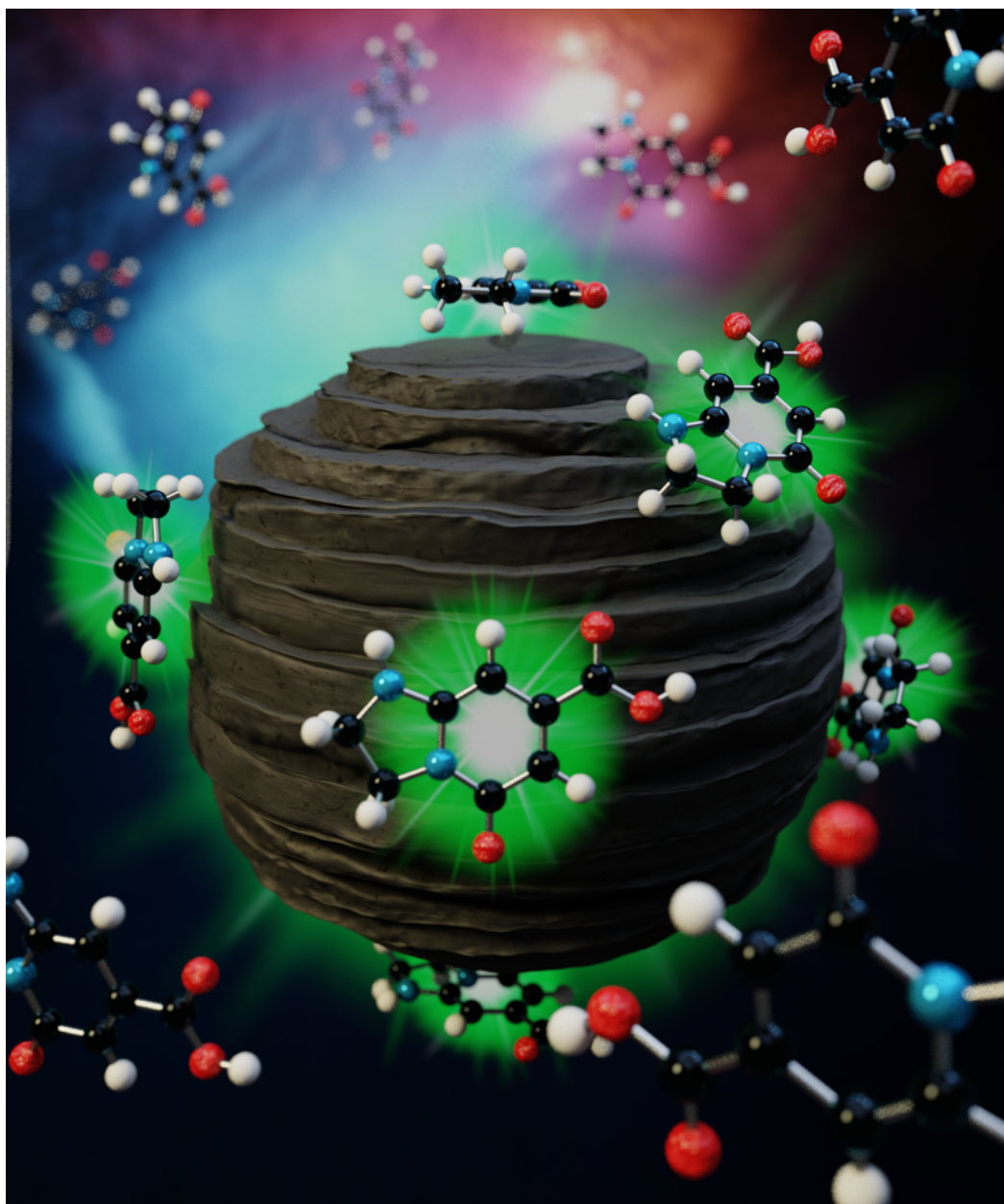


Figure 29. Snapshots of self-assembled CD of system **K** ($R_g = 1.16$ nm) and system **D** ($R_g = 1.08$ nm) and their corresponding density profiles. PAH layers are represented by spheres (carbon-black; oxygen-red; hydrogen-white) and IPCA by sticks (carbon-cyan; nitrogen-blue). Water is omitted for clarity. Reprinted with permission from 242. Copyright 2022 American Chemical Society.

7 Contribution of the Molecular Fluorophore IPCA to Excitation-Independent Photoluminescence of Carbon Dots[§]



[§] Published as: Langer, M.; Hrivnák, T.; Medved', M.; Otyepka, M. Contribution of the Molecular Fluorophore IPCA to Excitation-Independent Photoluminescence of Carbon Dots. *J. Phys. Chem. C* 2021, 125 (22), 12140–12148.

In the previous sections, optical properties of IPCA molecule and stacked dimers in gas and water have been well characterized. Nevertheless, the situation in real CDs is still much more comprehensive. In the self-assembly study of IPCA molecules with the CD units, it was witnessed that IPCA may occupy several different positions with respect to CD and to each other (see chapter 6). Similarly, multicenter structural model of CDs whose PL depends on stacking effects and the distance between luminescent centers was also suggested experimentally.¹³⁸ Thus, an interesting question arises: "To what extent does the incorporation of IPCAs into specific positions in CD matrices affect their absorption and emission? Could citric acid-based PL CDs thus strongly depend on changes in the electronic structure of MFs induced by specific interactions with the local environment in the CD?" To answer this question, optical properties of IPCAs in the heterogeneous environment of CQDs (henceforth referred as CDs) must be investigated by theoretical calculations.

The sizes of real CD/MF systems are commonly 2–8 nm (see chapter 2.2), making them too large to be studied using accurate QM methods. Thus, the choice of affordable hybrid QM/MM methodology with electrostatic embedding (QM/MM/EE) in ONIOM allowed us to study the PL of a CD-embedded IPCA molecules on the reliable CD structural models (over thirteen hundred atoms, not counting the waters) obtained from MD simulations. The choice of border separating QM and MM regions was intuitive and straightforward. One IPCA molecule or IPCA dimer were in the QM region, the rest of IPCAs and the surrounding water molecules were in the MM region. TD-CAM-B3LYP method was used to describe the QM region and calculate excitation energies and emissions in all cases.

A. Validation of the QM/MM Approach

First, the ability of TD-CAM-B3LYP level of theory to describe relevant vertical electronic transitions was confirmed by comparison with gas-phase CC2 calculations (calculated using Turbomole 6.3,²⁴⁹ TMOLEX 4.1²⁵⁰) with the same def2-TZVP functional (on QM/MM/EE optimized geometries, *vide ante*). The excitation and emission energies of IPCA(0) were 0.07 eV and 0.04 eV higher, respectively, than the CC2 energies (green and violet bars Figure 30b, c). Next, the validity of TD-CAM-B3LYP/MM/EE was demonstrated by careful benchmarking by comparing the vertical $S_0 \rightarrow S_1$ and $S_1 \rightarrow S_0$ electronic transitions against TD- ω B97X-D/MM/EE, TD-CAM-B3LYP/MM/PE accounting for solvent molecule polarization,^{251,252}

TD-CAM-B3LYP/def2-TZVP/SMD(cLR)¹⁹⁴ and experimental data.¹³⁷ Smaller hydrated IPCA(0) (Figure 30a) and IPCA(-1) molecules (no CD fragments) were chosen as a model for benchmarking. Focusing on IPCA(0) here, small bars for gas calculations pointed on small impact of indirect (i.e., structural) solvent effects on the VEE and emission energies. On contrary, polarization of the GS and ES electronic wavefunctions by the solvent, i.e., inclusion of direct (i.e., polarization) solvent effects, in QM/MM/EE (using ONIOM in Gaussian16) and QM/MM/PE (using OpenMolcas,²⁵³ Dalton 2019^{254,255}) calculations resulted in a large spread of excitation and emission energies (blue and red bars Figure 30b, c).

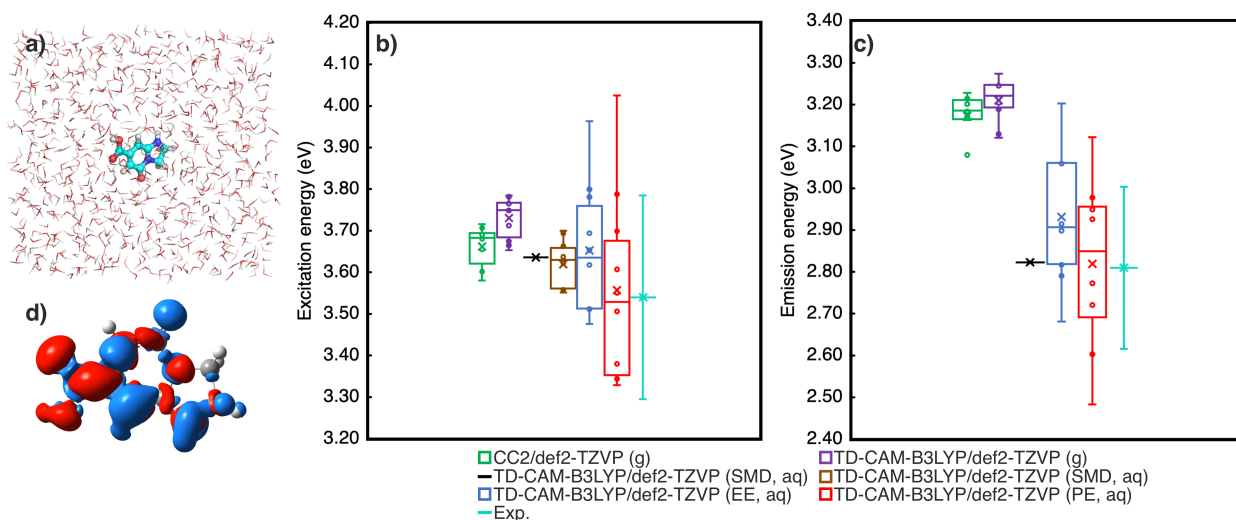


Figure 30. (a) The neutral form of IPCA solvated with explicit water molecules. Color scheme: cyan - carbon; blue - nitrogen; red - oxygen; white - hydrogen. (b) Excitation energies to the first excited electronic state (S_1) of IPCA(0) and (c) emission energies from this state calculated at various levels of theory in gas (g) and water (aq), shown using box and whisker representations (inclusive median; crosses indicate means and circles indicate calculated points). EE (PE) denotes the QM/MM approach with electrostatic (polarizable) embedding, SMD denotes QM calculations with the implicit solvent model (the black mark represents the result obtained using the optimum CAM-B3LYP/SMD geometry; the results represented with bars were calculated using the geometries extracted from MD simulations). The experimental values and their spreads are derived from the maxima and full-width-in-half-maximum (FWHM) of the published absorption and emission spectra (measured in water).¹³⁷ (d) Electron density difference plot for the $S_0 \rightarrow S_1$ transition of hydrated IPCA(0) calculated at the TD-CAM-B3LYP/def2-TZVP level of theory in implicit SMD water model (isovalue = 0.001 a.u.; decrease/increase of the density is in blue/red). Reprinted with permission from 256. Copyright 2022 American Chemical Society.

Interestingly, TD-CAM-B3LYP/SMD calculations performed on the same geometries as the QM/MM calculations predicted small VEE variance (brown bar in Figure 30) suggesting that the specific H-bonded interactions and solvent-shell structural features considered in the QM/MM methodologies contributed significantly to the observed VEE variance. Because of the dynamic

nature of the solution, averaging of optical properties can be expected in ensembles, thus the following results focus mainly on mean values. Additionally, the SMD calculations in water predicted that the VEEs in solution are red-shifted by 0.09 eV relative to the gas-phase values, in keeping with the results previously obtained using the IEF-PCM.¹⁰⁴

The benchmarking also revealed that different range-separated hybrid, ω B97X-D demonstrated very similar results to those obtained by CAM-B3LYP (see Table 10).

Table 10. Comparison of vertical excitation and emission energies calculated with two different methods using the def2-TZVP basis set in gas on the same QM/MM/EE geometries. Comparison of vertical excitation and emission energies calculated with TD-CAM-B3LYP/MM/EE and TD- ω B97X-D/MM/EE for hydrated IPCA(0). Reprinted with permission from 256. Copyright 2022 American Chemical Society.

	VEEs (eV)				Vertical emission energies (eV)			
	Gas		Explicit water (QM/MM/EE)		Gas		Explicit water (QM/MM/EE)	
	CAM-B3LYP	ω B97X-D	CAM-B3LYP	ω B97X-D	CAM-B3LYP	ω B97X-D	CAM-B3LYP	ω B97X-D
1	3.66	3.68	3.51	3.53	3.20	3.22	2.79	2.82
2	3.75	3.76	3.80	3.82	3.13	3.15	3.07	3.08
3	3.77	3.78	3.62	3.64	3.25	3.27	2.91	2.94
4	3.78	3.80	3.96	3.98	3.27	3.29	3.20	3.33
5	3.75	3.77	3.69	3.71	3.23	3.25	3.06	3.08
6	3.71	3.73	3.51	3.53	3.22	3.24	2.82	2.86
7	3.78	3.80	3.78	3.80	3.25	3.27	3.06	3.08
8	3.77	3.78	3.65	3.76	3.12	3.14	2.82	2.84
9	3.65	3.67	3.51	3.53	3.25	3.27	2.90	2.93
10	3.67	3.69	3.48	3.50	3.19	3.21	2.68	2.72
Average	3.73	3.75	3.65	3.68	3.21	3.23	2.93	2.97

Now, TD-CAM-B3LYP/MM/EE, TD-CAM-B3LYP/MM/PE, TD-CAM-B3LYP/def2-TZVP/SMD(cLR), and experimental data are compared. All three consistently predicted the $S_0 \rightarrow S_1$ electronic excitation, involving a similar set of molecular orbitals (Figure 31). The electronic transitions in CDs around 340 nm are believed to be $n-\pi^*$ transitions. Here reported $\pi-\pi^*$ character could be ascribed to more efficient delocalization of the electronic density owing to the presence of the imidazole ring.¹³⁶ The differences between the averaged VEEs of EE, PE, SMD ranged from 0.01 to 0.09 eV (Figure 30b, Table 11), and the good agreement was also observed for averaged vertical emission energies (differences by 0.00–0.11 eV, Figure 30c, Table 11). Moreover, all three methods yielded $S_1 \rightarrow S_0$ transition energies in fair agreement with the experimental value 2.81 eV.¹³⁷

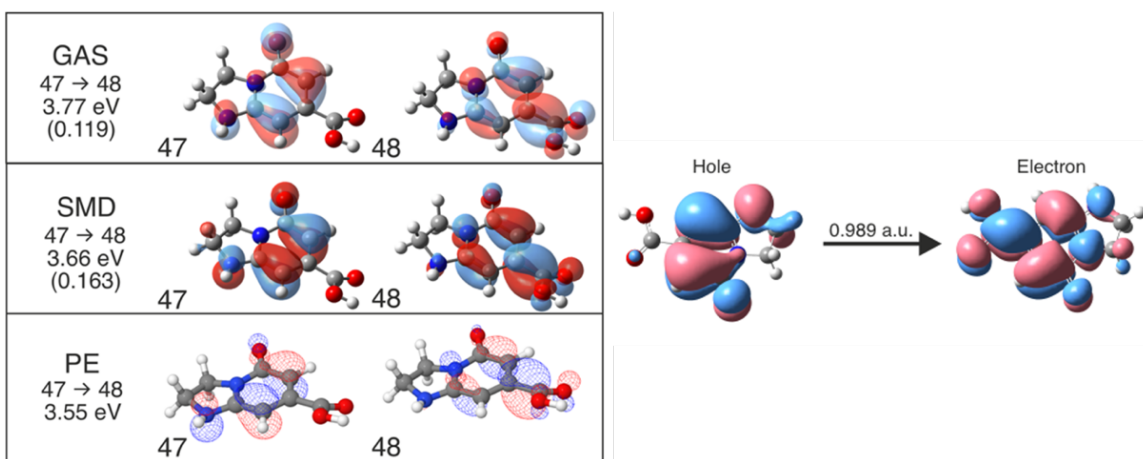


Figure 31. Left panel displays molecular orbitals involved in the $S_0 \rightarrow S_1$ excitation displayed for a representative structure of hydrated IPCA(0) calculated on the same geometries in the gas phase and by implicit SMD and QM/MM/PE approaches, together with the corresponding excitation energy (in eV) and oscillator strength. Right panel shows NTOs for $S_0 \rightarrow S_1$ vertical transition of an IPCA molecule in water (SMD solvent). The isocontour value is 0.02 a.u. Reprinted with permission from 256. Copyright 2022 American Chemical Society.

Table 11. Pair differences between the mean excitation (emission) energies (in eV) obtained by the QM/MM/EE, QM/MM/PE and QM/SMD methods for hydrated IPCA(0).²⁵⁶

	IPCA(0)					
	EE	PE	SMD	EE	PE	SMD
Mean $S_0 \rightarrow S_1$ energy (Oscillator strength)	3.65 (0.11)	3.56 (0.14)	3.64 (0.16)			
Mean $S_1 \rightarrow S_0$ energy				2.93	2.82	2.82
	Excitation to S_1^a			Emission from S_1^b		
	EE-PE	EE-SMD	PE-SMD	EE-PE	EE-SMD	PE-SMD
Difference (eV)	0.09	0.01	-0.08	0.11	0.11	0.00

^a 10, 10 and 1 structures for EE, PE and SMD, respectively; ^b 10, 8 and 1 structures for EE, PE and SMD, respectively.

Comparison of theoretical VEEs and emission energies with experimentally determined absorption and emission maxima should be done cautiously, as the former ignores the vibronic coupling effects. Nevertheless, we calculated the absorption-fluorescence crossing points (AFCPs)^{257,258} of hydrated IPCA at the TD-CAM-B3LYP/def2-TZVP/SMD level, finding an excellent match between the calculated (396 nm) and experimental (397 nm) values.¹³⁷ The evaluation of 0–0 energies (difference between the adiabatic ES and GS energies corrected for the zero-point vibrational energies (ZPVE) of the two states), enables direct comparisons between theoretical and experimental values, the latter being taken as the AFCPs.

To sum up this benchmarking section, the appropriateness of the choice of QM/MM/EE approach for the analysis of electronic transitions of IPCA(0) in protic environments was proved.

B. Behavior of IPCA in various CD models

Next, the effect of modulation of PL characteristics of IPCA(0) by its embedding in CD matrix was probed by calculations of the absorption and emission spectra of IPCA(0) in several various structural arrangements within CD models (Table 12, Figure 32). These arrangements were identified in MD simulations (AMBER11 package, GROMACS 5.0) of the co-assembly of IPCA molecules and CD fragments with OH-passivated edges (see chapter 6).

Table 12. List of studied self-assembled IPCA-CD systems calculated with QM/MM/EE.²⁵⁶

System	Appearance	Note
i	Figure 32a	IPCA(0) molecule embedded in CD and water exposed
ii	Figure 32b	IPCA H-bonded dimer embedded in CD and water exposed (dimer or molecule in QM region)
iii	Figure 32c	IPCA(0) in a layer formed from H-bonded IPCAs embedded in CD and water exposed (dimer or molecule in QM region)
iv	Figure 32d	IPCA(0) molecule embedded in a central void
v	Figure 32e	Stacked IPCA(0) dimer embedded in a central void
vi	Figure 32f	Two H-bonded stacked IPCA(0) dimers embedded in CD and water exposed (one of molecules or dimer in QM region)

After minimization and short equilibration, 2.5 ns long MD simulations of CD fragments, i.e., PAH-like structures, and IPCAs described with parm99SB and GAFF were performed using sander in the AMBER11 suite²⁵⁹ to sample the conformational space and choose representative snapshots for our model structures of QM/MM calculations. The representative snapshots were centered using PTRAJ (version 12.0)²⁶⁰ and later translated with the in-house script to produce the ONIOM input files of IPCA/CD structures for QM/MM/EE calculations, including all the parameters needed for the description of the MM region.

In these QM/MM calculations, (TD-)DFT methodology at CAM-B3LYP/def2-TZVP/GD3 level of theory was used for the description of electronic states in the QM region, the same FF as in our MD simulations (see chapter 6) were used in the MM region. In the QM/MM optimizations of the S_1 state, the same QM region as in the GS optimizations was considered and the energy contributions from the environment ($E_{\text{low, real}}^* - E_{\text{low, model}}^*$) were approximated by the GS energy assuming that the electronic excitation is localized in the model (QM) region.²¹⁰ For more computational details, please refer to reference 256.

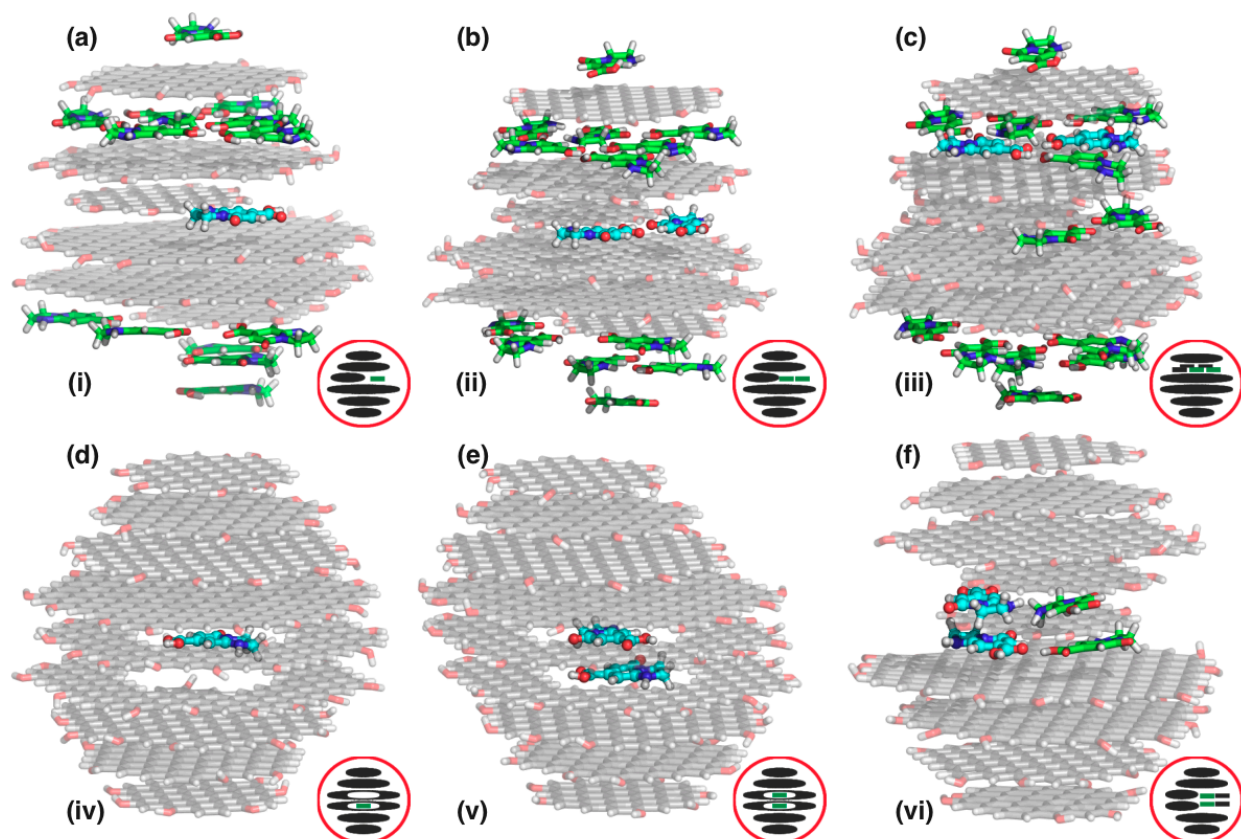
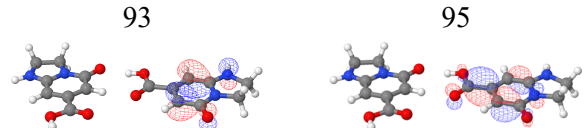
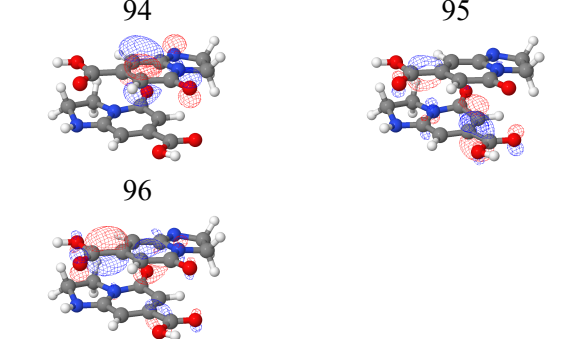
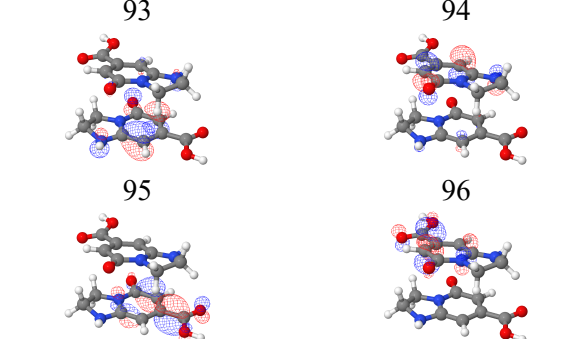


Figure 32. IPCA(0) model systems used in QM/MM/EE calculations. (a) IPCA molecule embedded in CD and partly exposed to water, (b) H-bonded and water-exposed dimer embedded in a CD, (c) water-exposed dimer in a layer of H-bonded IPCA molecules embedded in a CD, (d) monomer embedded in a central void, (e) stacked dimer embedded in a central void, (f) two H-bonded and water-exposed stacked dimers embedded in a CD. IPCA molecules in QM regions are shown using ball-and-stick representations, while those in MM regions are shown in stick form. Color scheme: cyan, green, and grey-carbon; blue-nitrogen; red-oxygen; white-hydrogen. For clarity, water is not shown. Pictograms indicate the approximate positioning of the IPCA molecules of interest (represented as green bars) in the CDs (represented as circles) and the nature of their interactions with other IPCA molecules (represented as black bars). Reprinted with permission from 256. Copyright 2022 American Chemical Society.

In all the studied configurations, the first bright vertical excitations were $\pi \rightarrow \pi^*$ transitions, as can be seen for the exemplar dimeric structures in Table 13. This is consistent with the calculations for hydrated IPCA(0) molecule. Moreover, in systems (i) and (iv) with only IPCA monomer in the center of focus, the $S_0 \rightarrow S_1$ excitation was bright, similarly to IPCA(0). For systems (ii), (iii) and (v), both $S_0 \rightarrow S_{1,2}$ excitations were bright and in system (vi), only $S_0 \rightarrow S_2$ electronic transition was much brighter than $S_0 \rightarrow S_1$ transition.

Table 13. Molecular orbitals involved in an excitation displayed for a representative structure of a system **(ii)**, system **(v)**, system **(vi)** calculated on the QM/MM/EE geometries; the transition of electron with the involved molecular orbitals and excitation energy (in eV) with its oscillator strength.²⁵⁶

System	Molecular orbitals	Transition	Excitation energy (eV) (Oscillator strength)
ii	 <p>93 95</p>	93 → 95 (0.692)	3.69
v	 <p>94 95</p> <p>96</p>	94 → 95 (0.555) 94 → 96 (-0.411)	3.45
vi	 <p>93 94</p> <p>95 96</p>	93 → 95 (0.455) 93 → 96 (-0.152) 94 → 95 (0.494) 94 → 96 (0.132)	3.45

Now, let me present the shifts and changes in VEEs and emission energies for every system one-by-one. In system **(i)** with IPCA molecule only partly exposed to the surrounding explicit water molecules, the averaged value value of $S_0 \rightarrow S_1$ excitation energy was not altered (3.65 eV average) and $S_1 \rightarrow S_0$ emission energies was slightly blue-shifted (3.12 eV) compared to nonembedded hydrated IPCA(0) results (Figure 33). For this system **(i)**, the variation of excitation and emission energies is also displayed in (Figure 34), showing quite a big range of excitation (3.52–3.74 eV) and emission (2.96–3.25 eV) energies. Because the variation of VEEs and emission energies was still highest for hydrated IPCA(0), it can be suggested that solvent-shell interactions are responsible for this.

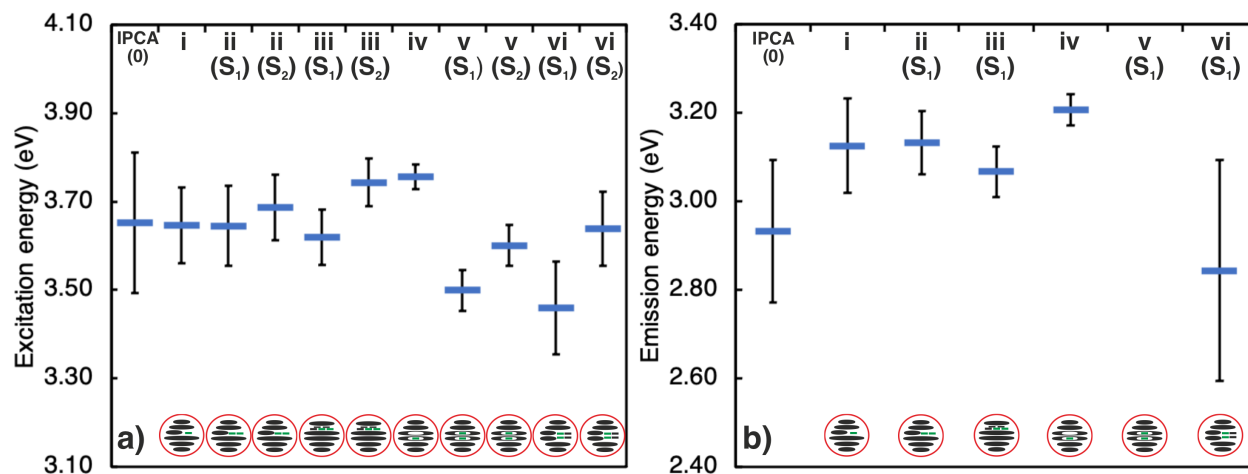


Figure 33. The means and standard deviations of the (a) VEEs and (b) emission energies of the studied IPCA(0)-CD systems based on multiple snapshots collected from MD simulations. The pictograms show the approximate positioning of the IPCA molecule(s) in the CD. The CD is represented as a disc and the IPCA molecules are represented as bars; green bars represent the IPCA molecules whose optical properties were investigated. The IPCA(0) labels show the mean excitation and emission energies of hydrated IPCA(0). Reprinted with permission from 256. Copyright 2022 American Chemical Society.

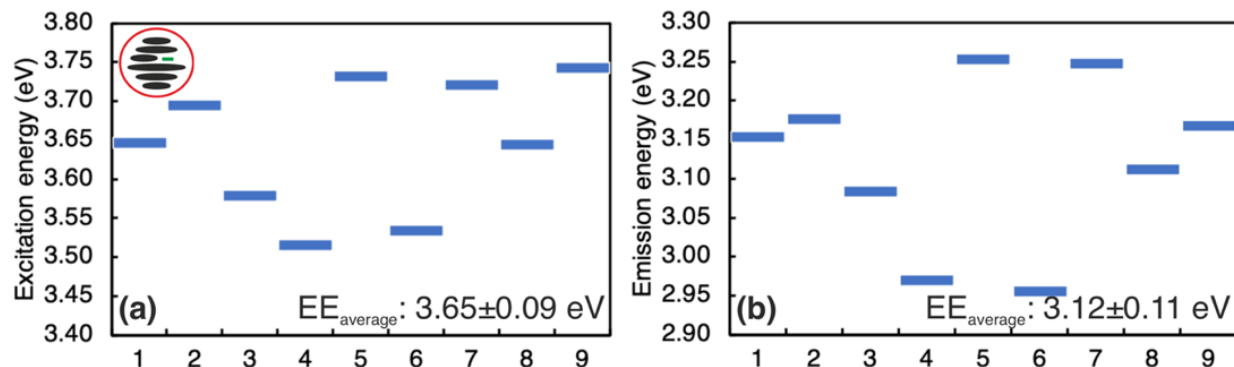


Figure 34. (a) $S_0 \rightarrow S_1$ excitation energies and (b) $S_1 \rightarrow S_0$ emission energies of system (i) calculated with QM/MM/EE methodology for more structures sampled with MD simulations. Reprinted with permission from 256. Copyright 2022 American Chemical Society.

Similarly as in system (i), the S_1 energy was almost identical to that for hydrated IPCA(0) in the case of a system (ii) containing two neighboring coplanar H-bonded IPCA molecules (Figure 33). Including two H-bonded IPCAs in QM region of the QM/MM/EE calculations caused the blue-shift of the Kasha emission energy approximately by 0.20 eV. In system (iii), the calculated H-bonded IPCA(0) dimer lies in the layer fully composed of IPCA molecules. The H-bonded interactions and confinement between two OH-PAH layers negligibly affected $S_0 \rightarrow S_1$ VEE, however, the PL was blue-shifted by 0.14 eV (Figure 33). IPCA in system (iv) does not have any water exposed IPCA, because it is trapped inside the central void in CD matrix. Interestingly, this

affected by S_1 excitation and emission energies, where blue-shift by 0.11 eV and 0.28 eV were observed for both energies, respectively (Figure 33). Despite this, the location of the stacked dimer in this central void in CD matrix, studied as system (v), resulted in a red shift of $S_0 \rightarrow S_1$ VEE by 0.15 eV in comparison to hydrated IPCA(0). Another difference was the brightness of the $S_0 \rightarrow S_1$ transition, where none of the first three ESs were very bright, as exciton splitting of the monomer's $\pi \rightarrow \pi^*$ transition was observed for the stacked dimers. Lastly, the effects of all the mentioned contributions, i.e., H-bonds, stacking and water exposition in IPCA dimer, on excitation and emission of IPCAs were investigated in system (vi). The red-shift by 0.19 eV was observed for $\pi \rightarrow \pi^*$ $S_0 \rightarrow S_1$ transition, however, this state is dark. The standard deviation of calculated emission energies of system (vi) may imply that biggest structural changes that may have occurred in this system comparing to systems (i)-(v).

One may suggest that simplification of the calculations by considering only one IPCA in the QM region instead of both IPCAs in the QM/MM/EE calculations of the systems with IPCA dimers may speed-up the simulation while still obtaining the same qualitative description. Our calculations revealed that the description of the second IPCA just by MM in QM/MM is not adequate. Significantly different results were seen for system (ii) when only one IPCA molecule was included in the QM region, where the $S_0 \rightarrow S_1$ excitation energy was strongly red-shifted and the PL remained almost unchanged comparing to hydrated IPCA(0) (Figure 35a,b). Similar contrasting results were witnessed for system (vi), where small shifts were observed for the $S_0 \rightarrow S_1$ VEEs, depending on the number of IPCA(0) molecules included in the QM region. The large differences can be explained by the fact that the EE model only includes electrostatic and (partially) delocalization intermolecular interactions.

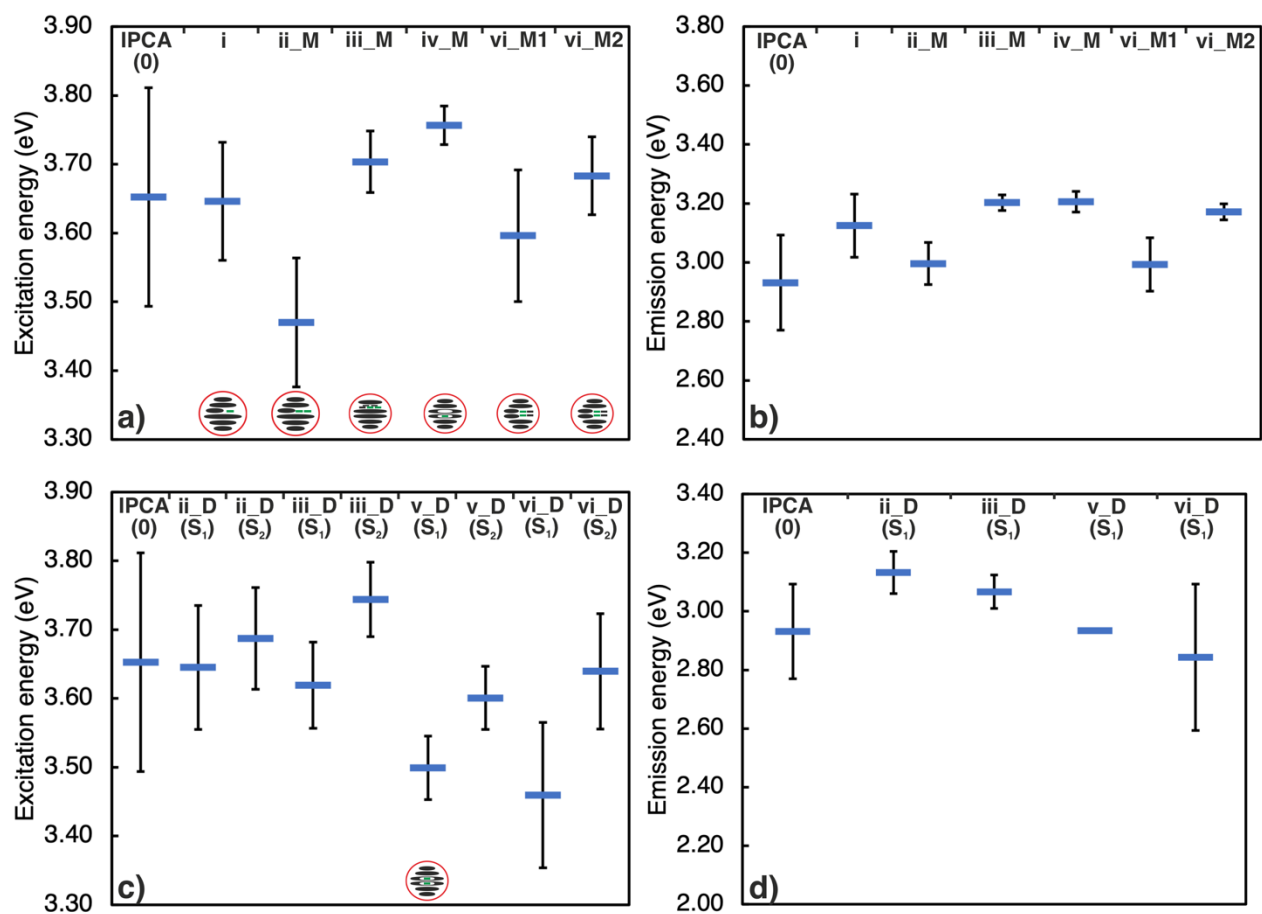


Figure 35. Mean and standard deviations of (a, c) excitation and (b, d) emission energies of the studied IPCA(0)-CD systems based on multiple snapshots collected from MD simulations. IPCA molecules and dimers described in QM region are label as “_M” and “_D”, respectively. The pictograms show the approximate positioning of the IPCA molecule(s) in the CD. The CD is represented as a disc and the IPCA molecules are represented as bars; green bars represent the IPCA molecules whose optical properties were investigated. The IPCA(0) labels show the mean excitation and emission energies of hydrated IPCA(0). Reprinted with permission from 256. Copyright 2022 American Chemical Society.

Lastly, we also simulated the PL spectra of IPCA molecules embedded in various CD models based on the computed excitation and emission energies and their corresponding oscillator strengths (Figure 36a–f). Before the construction of excitation-emission maps and comparisons with real experimental data, few considerations had to be done based on the quality of the TD-DFT methodology and vibronic effects of the solvent. First, inhomogeneous broadening effects were approximated by broadening the calculated excitation and emission peaks by applying a FWHM parameter of 0.4 eV. Second, we found out that TD-CAM-B3LYP/MM/EE overestimated the experimental excitation and emission maxima by roughly 0.11 and 0.12 eV for hydrated IPCA(0) due to neglect of solvent polarization effects in QM/MM/EE approach. Thus, all our simulated

spectra were red-shifted, applying the approximation that the environmental effects would be similar in all the studied cases. With these approximations, the emission spectra for systems (i)-(vi) simulated for excitation energies 300–380 nm were in an agreement with the reported emission energies, where they varied between 400 and 480 nm depending the position of the IPCA(0) molecules within the CD matrix (Figure 36a–f). Moreover, they all exhibited rather broad excitation-independent emission peaks, which is also consistent with the conclusions of general emission of MFs. The intensity of PL was strongly dependent on the arrangement of the embedded IPCAs with dimeric H-bonded structures surrounded by carbon fragments (systems (ii) and (iii)), exhibited more intense PL than individual IPCA molecules (systems (i) and (iv)) and stacked IPCA dimers (systems (v) and (vi)).

Finally, the excitation-emission maps (Figure 37a) were constructed by averaging the simulated spectra in Figure 36a–f, employing another approximation that systems (i)-(vi) are equally abundant in real samples, which may not necessarily be true in real CDs samples. Despite all the assumptions, our simulated excitation-emission map is in a good agreement with the experimental one (Figure 37b),²⁶¹ as our simulated signals are only slightly blue-shifted.

To illustrate more the roles of individual structures, partial excitation-emission maps were plotted (Figure 37c–f) and most importantly, it can be seen that the emission of the stacked structures was red-shifted (Figure 37f), suggesting that these structures may be more abundant in real samples as the agreement of the emission wavelengths in the excitation-emission map is closer to the experimental map. Preferential formation of such structures during our MD simulations is demonstrated in Figure 38.

In summary, the nature of arrangements of IPCA inside a CD was found to significantly affect the PL intensity and excitation-emission Stokes shifts of IPCAs. Moreover, the good agreement between the calculated and experimental excitation-emission maps of these MF-embedded CD systems indicated that MFs are the main source of broad excitation-independent emission in CDs.

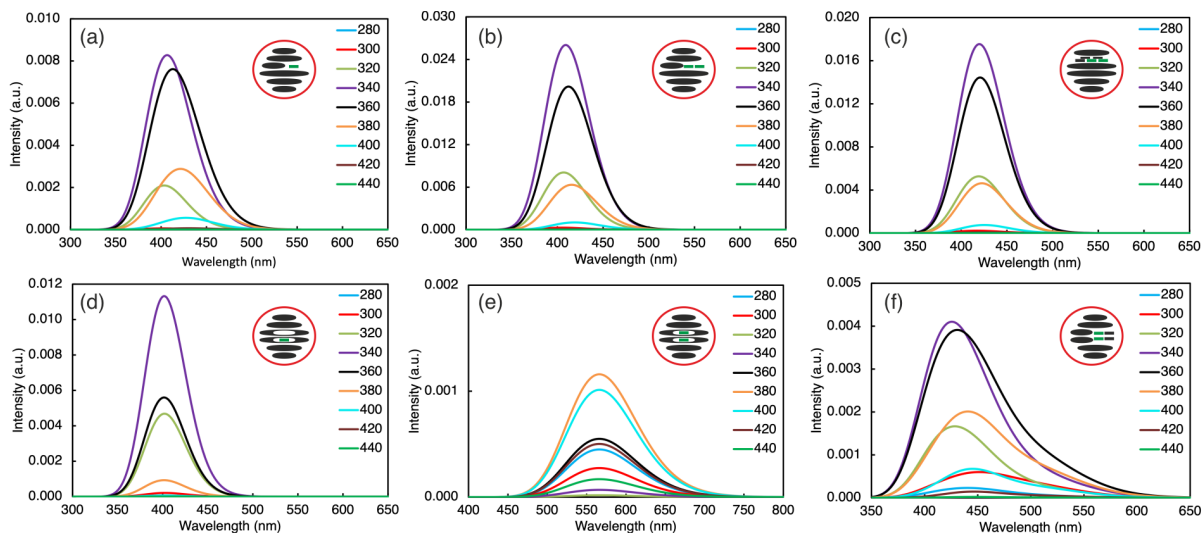


Figure 36. (a-f) Simulated emission spectra of the six studied IPCA/CD systems for different excitation wavelengths. Spectra for different excitation wavelengths were obtained by weighting the corresponding emission spectrum by the oscillator strength in the absorption spectrum at each of the probed wavelengths. Reprinted with permission from 256. Copyright 2022 American Chemical Society.

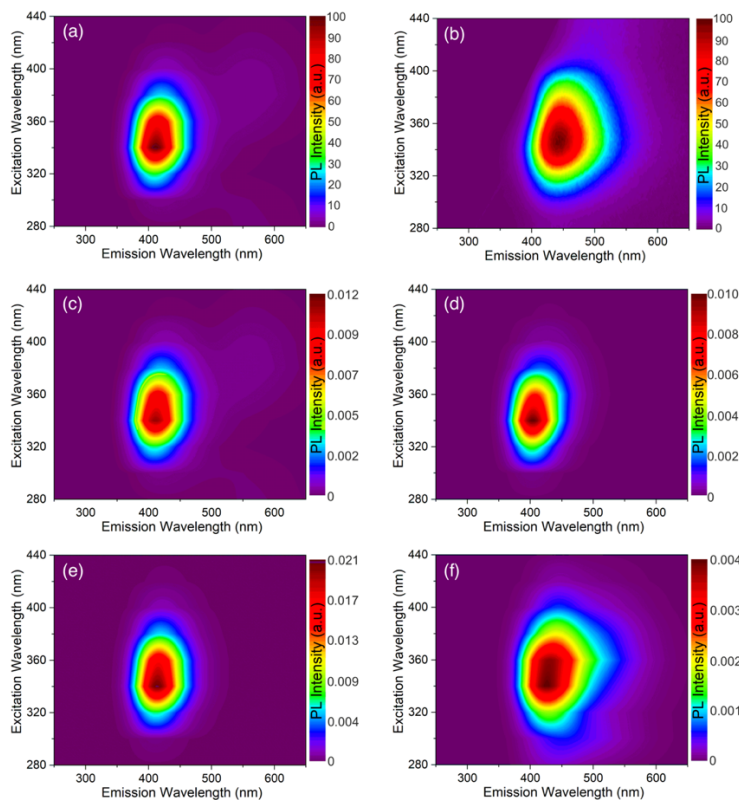


Figure 37. (a) Calculated and (b) experimental excitation-emission maps. The calculated excitation-emission map was constructed from the spectra presented in Figure 36a-f. (b) Experimental excitation-emission map for MF-containing CDs taken from ref. 261. Partial excitation-emission maps of (a) systems (i)-(vi); (b) monomeric systems (i) and (iv); (c) H-bonded systems (ii) and (iii); and stacked system (vi). Reprinted with permission from 256. Copyright 2022 American Chemical Society.

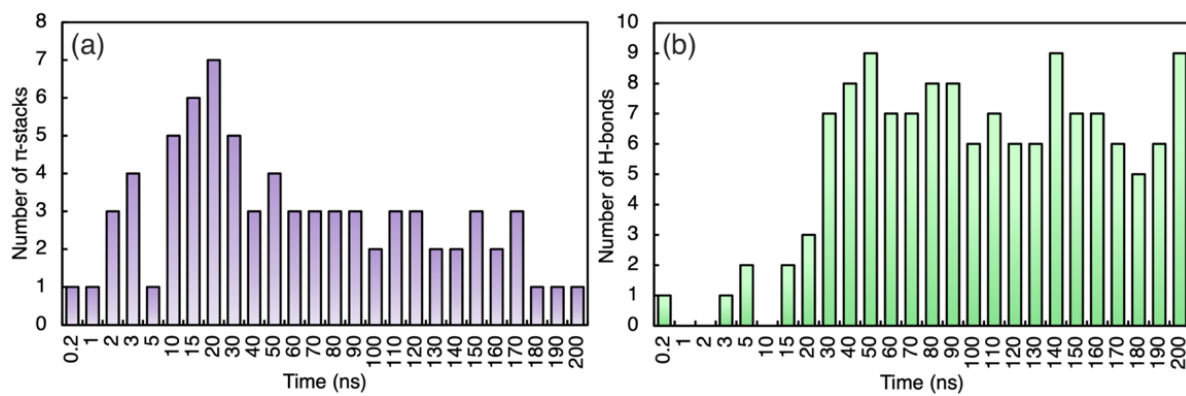
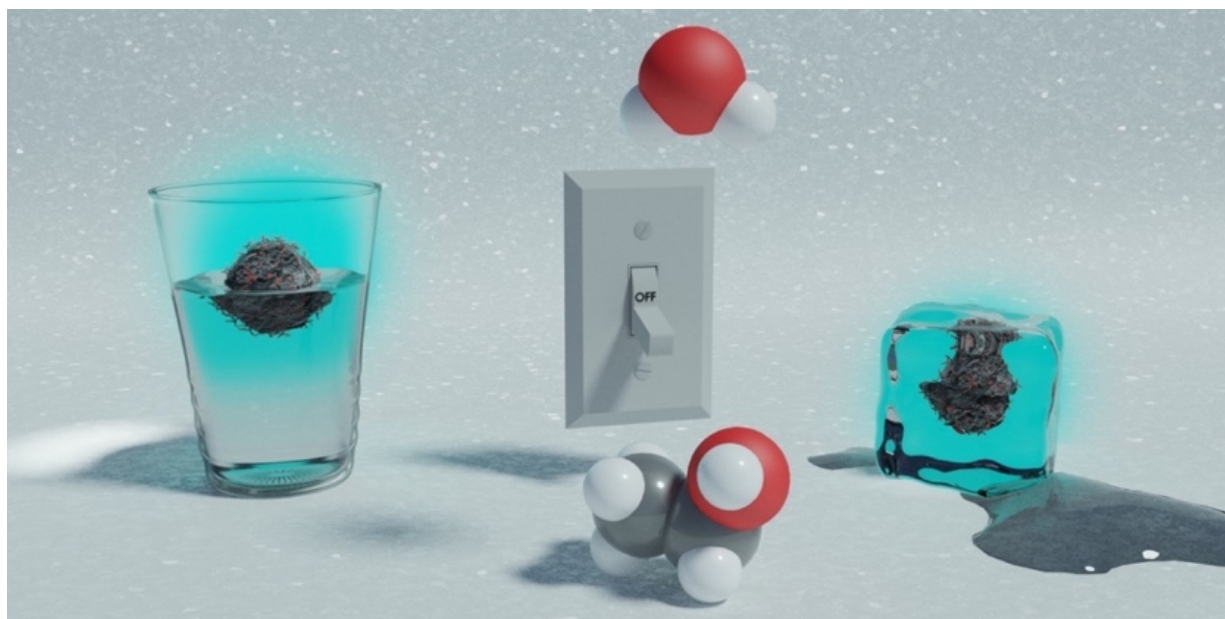


Figure 38. (a) Formation of (a) π -stacks of IPCA(0) molecules and (b) H-bonds between IPCA(0)-IPCA(0) molecules in MD simulations that led to formation of systems (ii) and (iii). Please note that there are two H-bonds donor and acceptor sites in one IPCA molecule. Reprinted with permission from 256. Copyright 2022 American Chemical Society.

8 Carbon Dots Detect Water-to-Ice Phase Transition and Act as Alcohol Sensors via Fluorescence Turn-Off/On Mechanism**



** Published as: Kalytchuk, S.; Zdražil, L.; Bad'ura, Z.; Medved', M.; Langer, M.; Paloncýová, M.; Zoppellaro, G.; Kershaw, S. V.; Rogach, A. L.; Otyepka, M.; et al. Carbon Dots Detect Water-to-Ice Phase Transition and Act as Alcohol Sensors via Fluorescence Turn-Off/On Mechanism. ACS Nano 2021, 15 (4), 6582–6593.

The above chapters have shown that different computational methodologies have been implemented and benchmarked, and that several different properties and phenomena have been targeted and described. Therefore, we can currently closely collaborate with experimentalists to elucidate conundrums posed by the nature. Nowadays, with our expertise and skills, we can either support experimental data or provide the insights hardly achievable solely with a laboratory work. Here, the combination of MD simulations and DFT calculations of electron affinities and ionization energies were helpful in explanation of mechanism behind the quenching of CDs fluorescence after phase-transition.²⁶¹

With the use of experimental techniques light-induced electron paramagnetic resonance (LEPR), transmission electron microscopy (TEM), atomic force microscopy (AFM), X-ray photoelectron spectroscopy (XPS) analysis, Fourier transform infrared (FTIR) measurements, UV/Vis absorption spectroscopy, steady-state and time resolved PL spectroscopy (PL emission, PL excitation, and PL decay measurements), the material was fully characterized. Water-soluble CDs with a mean size of 4.8 nm were made from citric acid and ethylenediamine in an autoclave being annealed at 200 °C for 5 hours. It has been shown that IPCA is also formed as a side-product besides CDs in this type of synthesis. Without providing any experimental details, the PL turn-off/on behavior of aqueous CDs allowing the reversible monitoring of the water–ice phase transition was reported.²⁶¹ It was discovered that the bright PL also originates from MFs present on the CD surface and this channel was quenched by changing the liquid aqueous environment to solid phase (ice) primarily by the activation of nonradiative relaxation channels. Moreover, control sample prepared in a way to not produce any MFs but only CDs displayed PL from core/surface states and this PL channel was not quenched after phase transition. It was also carefully ensured that this quenching was not simply due to the chemical degradation of CDs because more freezing/melting cycles revealed the full reversibility of the PL quenching in these CDs. Interestingly, the PL was not quenched when adding small concentration of primary alcohols to the solution. Here, all-atom MD simulations were introduced to help discover the mechanism behind this.

Table 14. Composition of MD simulation boxes with number of PAH layers, charged and uncharged IPCA molecules, water, and ethanol molecules. Reprinted with permission from 261. Copyright 2022 American Chemical Society.

	#PAH layer	#IPCA		#water	#ethanol	Simulation time (ns)
		(-1)	(0)			
CD	9		50	8277	642	400
CD/IPCA	6		15	7797	100	150
	6	15		7779	100	150

Methodologically, IPCA molecules were described by a GAFF similarly as in our other publications (see chapter 6). Structures of CDs were also created with CD builder (see chapter 4),²¹² where 30% of -OH groups were on edges of individual PAH layers. CDs were parameterized in an parm99 with refinement on aromatic carbons.²¹⁶ Three models were created in simulated (Table 14). TEM images showed that the CDs were monodispersed, and size ranged 3–7 nm, the AFM line scans also revealed their height range 1.7–5.4 nm. Thus, in the first model, spherical CD with the diameter 2.9 nm was modelled with 50 IPCA molecules solvated by water and ethanol (642 molecules). In the other two models, we represented CD by only 6-layered model opposed to 9-layered system to offer more accessible surface for adsorption of IPCA (15 neutral or anionic molecules in the simulation box) and ethanol (100 molecules). The systems were solvated with different concentrations of ethanol,^{262,263} SPC/E water model,¹⁹⁰ ions.²⁴¹ After minimization with steepest descent algorithm, MD simulations were performed under NpT conditions. Pressure was kept at 1 bar with the isotropic Berendsen barostat;²⁴⁴ the time constant for pressure relaxation was set to 2.0 ps; v-rescale thermostat²⁴³ was used to keep the temperature at 300 K with a 0.1 ps scaling constant. Bonds involving hydrogens were constrained with the LINCS algorithm,²³⁷ thus 2 fs time step was used. Particle-mesh Ewald (PME)¹⁸⁹ was used for treating the electrostatic interactions with a real-space cutoff of 1.0 nm, the same cutoff was applied for van der Waals interactions. The periodic boundary conditions were applied in all three dimensions. MD simulations were performed by GROMACS 4.5.1 and 5.0 versions.

MD simulations revealed that the ethanol concentration is significantly higher in proximity to the CD with respect to that in the more distant bulk solvent (Figure 39a). Therefore, the suppression of quenching induced by freezing could be attributed to a change of relative permittivity caused by the high tendency of alcohol to increase its concentration at the CD/solvent interface. The normalized density maps also displayed that IPCAs are non-covalently bound to CDs surface

solvent (Figure 39b). Thus, the shell, involving IPCA, is sensitive to electrostatic interactions with solvent molecules and its electronic behavior is tuned by solvent polarity (relative permittivity) and solvent-shell chemical interactions (H-bonding interactions with diverse strengths).

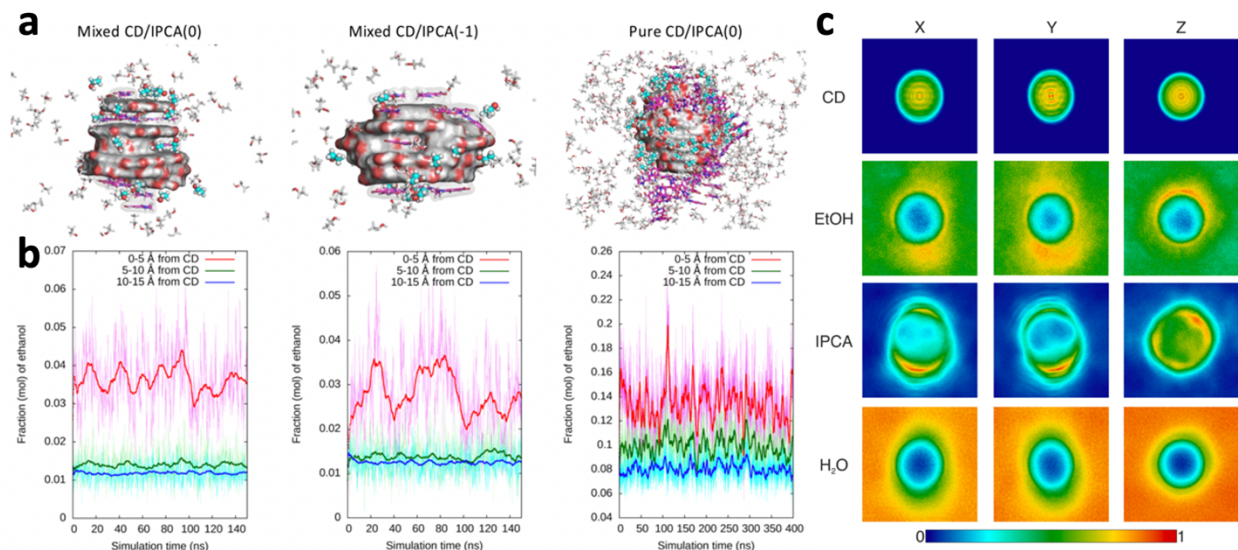


Figure 39. (a) Snapshots from MD simulations showing ethanol molecules concentrated on CDs' surface. PAH layers at the surface are shown in grey/red, IPCAs as magenta sticks, ethanol molecules in the bulk of solution as white sticks, while ethanol molecules within 5 Å of PAH layers as cyan balls. Other color coding: hydrogen-white, oxygen-red, nitrogen-blue. Water is omitted for clarity. (b) Evolution of molar fraction of ethanol within certain distance of a closest atom of PAH layer highlighting the increased fraction of ethanol in proximity of CD. (c) Normalized density maps of pure CD/IPCA(0) model, displaying the preferential spots where CD, IPCA, ethanol (EtOH) and H₂O prefer to reside during 400 ns of the MD simulation. Cross-sections along three perpendicular x, y, z directions of view. Coloring scheme: the normalized density increases from blue to red color. Reprinted with permission from 261. Copyright 2022 American Chemical Society.

The core-shell structure of these anisotropic CDs with the hydrophobic center and hydrophilic shell offers the generation of exciton under the light irradiation, and charge transfer (CT) processes may occur if the lowest unoccupied molecular orbital (LUMO) of the donor is energetically higher than the LUMO of the acceptor, creating a spatially separated e⁻/h⁺ pair. DFT calculations supported light-induced electron paramagnetic resonance (LEPR) measurements and helped creating theoretic kinetic model, which assumed the formation of charge-separated CD core-shell trap states which are in equilibrium with the photoexcited exciplex. The location of the photoexcited donor D* at the CD shell was suggested based on the absorption region (maximum located at 341 nm) and available theoretically calculated data.¹⁰⁹ Also, the nature of [D⁺···A⁻] state was deciphered even if the detailed analysis is limited due to sizes and complexity of the studied

CDs. It was stated that the LUMO of the core can act as an electron acceptor in the $[D^+ \cdots A^-]$ state, because it is below the LUMO of the shell, which was supported by our DFT theoretical calculations of electron affinities and ionization energies (Table 15, Table 16) on the small *ad-hoc* models displayed in Figure 40. The geometries of the model structures representing carbon core, hydrophilic CD surface, and IPCA were optimized at the CAM-B3LYP/6-31G(d)/CPCM level (coronene) or taken from references.^{104,109} Vertical ionization energies and electron affinities of model were then calculated at the CAM-B3LYP¹⁵⁵/aug-cc-pVTZ^{229,264,265}/CPCM^{266,267} level of theory. All DFT calculations were performed with the Gaussian16 program.

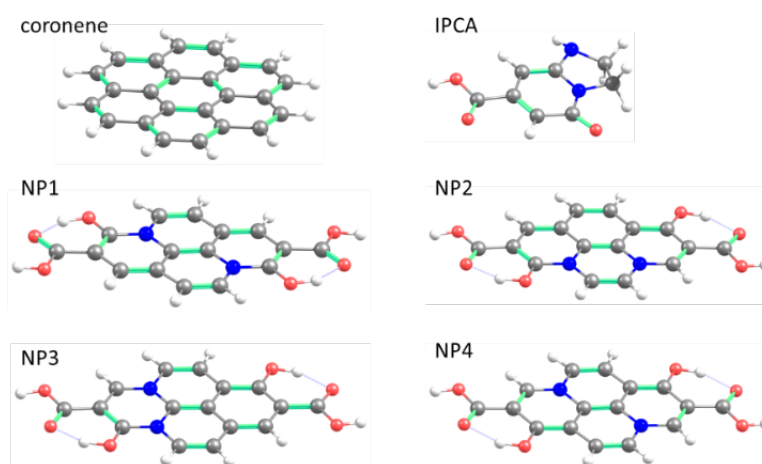


Figure 40. Structures of model species representing carbon core (coronene), hydrophilic surface (NP1-NP4), and IPCA molecule. The structure of coronene was optimized at the CAM-B3LYP/6-31G(d)/CPCM(water) level of theory, the structures of NP1-NP4 and IPCA were taken from 109 and 104, respectively. Reprinted with permission from 261. Copyright 2022 American Chemical Society.

Table 15. Vertical ionization potentials (IE) and electron affinities (EA) (in kcal/mol) of model species representing carbon core (coronene), hydrophilic surface (NP1-NP4), and IPCA (see structures in Figure 40) calculated at the CAM-B3LYP/aug-cc-pVTZ/CPCM level of theory using the geometries optimized at the CAM-B3LYP/6-31G(d)/CPCM (coronene) or taken from literature: ref. 109 and ref. 104. Reprinted with permission from 261. Copyright 2022 American Chemical Society.

Environment	Water		Ice ^a		Differences		
	System	IE	EA	IE	EA	Δ IE	Δ EA
coronene		136.7	44.0	136.5	44.3	-0.2	0.3
NP1		96.1	45.1	95.8	45.4	-0.3	0.3
NP2		91.7	53.0	91.4	53.2	-0.3	0.2
NP3		90.4	60.3	90.1	60.6	-0.3	0.3
NP4		89.3	52.2	89.1	52.5	-0.2	0.3
IPCA		134.1	51.5	133.8	51.8	-0.3	0.3

^aIce was treated within the CPCM model by the change of relative permittivity of water from 78.4 to 171.0.

Table 16. Estimated relative energies (ΔE_{CT}) of the $[D^+ \dots A^-]$ state (with respect to the GS) computed as the difference of IE of a donor and EA of an acceptor ($IE(D) - EA(A)$) taken from Table 15. Reprinted with permission from 261. Copyright 2022 American Chemical Society.

Donor	Acceptor	ΔE_{CT} (kcal/mol)		ΔE_{CT} (eV)	
		Water	Ice	Water	Ice
NP1	coronene	52.1	51.5	2.26	2.23
NP2	coronene	47.7	47.1	2.07	2.04
NP3	coronene	46.4	45.8	2.01	1.99
NP4	coronene	45.3	44.8	1.96	1.94
IPCA	coronene	90.1	89.5	3.91	3.88
NP1	IPCA	44.6	44.0	1.93	1.91
coronene	NP1	91.6	91.1	3.97	3.95

These values also suggest that competitive CT process on the CD shell may also be possible, whereas the electron transfer from the core to surface was found to be energetically more demanding and thus less probable.

The ultimate output of this work is the possibility to detect very low concentrations of small primary alcohols, which can be used as a diagnostic tool for early-stage lung cancer screening based on exhaled breath condensate.

9 Conclusion

This PhD thesis focused on the investigation of the contribution of MF called IPCA to the PL properties of CDs. While writing our review paper on understanding the PL of CDs using computational methods, we came across experimental data showing that in certain types of syntheses, MFs affect the resulting PL of CDs. In our search for whether the experimental data reporting PL of MFs, especially IPCA, are supported by theoretical computations, we did not find any. This is the reason why I dedicated my research time mostly to a theoretical description of CDs&MF systems and the goal of this thesis was to retell our results deciphering the importance of the IPCA in PL of CDs.

IPCA molecule has a large variability in charge distribution due to the presence of heteroatoms. The fact that IPCA could also form H-bonds due to $-\text{COOH}$, $-\text{N}-\text{H}$ and $-\text{C}=\text{O}$ groups makes the situation very complex. These properties result in existence of several energetically stable rotational conformers of IPCA dimers and multimers, and these can serve as basic models for the fluorescent centers in CDs.

One of our interesting findings was the demonstration of the dominance of $\pi \rightarrow \pi^*$ transitions for the explanation of the absorption spectra of IPCA molecule and IPCA dimers. Typically reported $n \rightarrow \pi^*$ excitations were also observed but these do not play any role for the explanation of the absorption spectrum due to their zero oscillator strength. This gives a new picture for the assignment of luminophore bands in CDs by stressing the importance of $\pi \rightarrow \pi^*$ excitations not only in the CD core but also in the CD shell containing MFs.

Quite interestingly, a certain pathway for PL quenching was illustrated. The break of the stacked IPCA dimer arrangement during the geometry relaxations of the S_1 state in gas phase calculations suggested radiationless conversion to the GS because of intersection pathways of S_1/S_0 electronic states. Although this happened exclusively in the gas, much bigger sampling of configuration space was needed to find out if we can observe such behavior in real CDs. With this intention, our classical MD simulations revealed that IPCA&CDs systems can form non-covalent complexes in solvent, which shall be stable in real samples. IPCAs not only rapidly self-assembled into stacked structures in water, possibly forming seeds for growth of CDs during their synthesis, and interacted with the accessible aromatic carbons in CDs, but they also incorporated into CD matrix. Due to these spatial restrictions, we believe that the quenching of PL will not be very likely

in the CD matrix, but it should not be dismissed in our considerations, since it is a source for unwanted fluorescence quenching.

This MD study also helped us to generate initial structures for QM/MM calculations, which helped us to observe that the environment of the IPCA molecules and the nature and localization of their embedding within CD matrix were found to significantly affect their PL intensity and excitation-emission Stokes shifts. Eventually, the good agreement between the calculated and experimental excitation-emission maps of embedded IPCA&CD systems indicated that MFs are the main source of broad excitation-independent emission in CDs. Moreover, we reported that stacking of IPCA dimers could cause higher red-shifts of emission in comparison with isolated IPCA molecule and/or H-bonded IPCA systems. This agrees with the common knowledge of emission of MFs while providing essential insight hardly accessible with experimental techniques.

Finally, our MD simulations and DFT calculations supported experimental data in the explanation why the bright PL attributable to IPCA present on the CD surface was quenched by liquid-to-solid phase transition of water, but not-quenched after addition of small alcohols. MD simulations revealed the increase of concentration of alcohol in the vicinity of the CD shell, stressing the importance of CD/solvent interface interactions. Additionally, our *ad-hoc* model and DFT calculations of vertical IEs and EAs proved the feasibility of the formation of charge-separated CD core-shell trap states, i.e., the states that explain our PL quenching process.

In this doctoral thesis, I presented only the scientific story of my involvement in the field of CDs. Nonetheless, I also investigated other nanosystems. Just very shortly, all-atom classical MD simulations were performed alongside experimental work to elucidate that GCN/Ag nanohybrid, i.e., silver covalently bound to cyanographene, strongly interacted with a simplified model of bacterial membrane, generating a significant perturbation of its structure.²⁶⁸ Additionally, Monte Carlo ray-tracing simulation (MCRTS) identified the loss caused by non-unity PL QY being the most significant contribution to the overall efficiency loss of internal optical quantum efficiency η_{int} for solar concentrating in Bi-doped $\text{Cs}_2\text{Ag}_{0.4}\text{Na}_{0.6}\text{InCl}_6$ double-perovskite nanocrystals.²⁶⁹ MCRTS also allowed to estimate the efficiency of 39.4 % for 2,500 cm^2 luminescent solar concentrator with hypothetical unity QY, which could not have been evaluated only with experiments. All-atom MD simulations can also be used to accurately describe interfacial behavior of electrolytes in systems containing carbon allotropes. In our study, we accounted essential polarization effects in the MD simulations and demonstrated different structuring of potassium

halides at the graphene surface.²⁷⁰ The findings shall be relevant for supercapacitor applications and understanding the resting state of graphene as an electrode material. Finally, another potentially interesting material with the usage in electronics and sensing was predicted using our all-atom MD simulations.²⁷¹ This material was made from alternating coronene and perfluorocoronene molecules and the simulations revealed that it could self-assemble into stacks in environments of different humidity. If these alternating layers were connected with a stretchable linker, they could form ultrastretchable and possibly electrically conducting nanofibers.

10 References

- (1) Bottari, G.; Torres, T. A New Dimension for Low-Dimensional Carbon Nanostructures. *Chem* **2017**, *3* (1), 21–24.
- (2) Liu, J.; Li, R.; Yang, B. Carbon Dots: A New Type of Carbon-Based Nanomaterial with Wide Applications. *ACS Cent. Sci.* **2020**, *6* (12), 2179–2195.
- (3) Langer, M.; Paloncýová, M.; Medved', M.; Pykal, M.; Nachtigallová, D.; Shi, B.; Aquino, A. J. A.; Lischka, H.; Otyepka, M. Progress and Challenges in Understanding of Photoluminescence Properties of Carbon Dots Based on Theoretical Computations. *Appl. Mater. Today.* **2021**, *22*, 100924.
- (4) Khairol Anuar, N. K.; Tan, H. L.; Lim, Y. P.; So'aib, M. S.; Abu Bakar, N. F. A Review on Multifunctional Carbon-Dots Synthesized From Biomass Waste: Design/Fabrication, Characterization and Applications. *Front. Energy Res.* **2021**, *9*, 67.
- (5) Jorns, M.; Pappas, D.; Tagmatarchis, N.; Kelarakis, A. A Review of Fluorescent Carbon Dots, Their Synthesis, Physical and Chemical Characteristics, and Applications. *Nanomaterials (Basel)* **2021**, *11* (6), 1448.
- (6) Kurian, M.; Paul, A. Recent Trends in the Use of Green Sources for Carbon Dot Synthesis—A Short Review. *Carbon Trends* **2021**, *3*, 100032.
- (7) Sharma, A.; Das, J. Small Molecules Derived Carbon Dots: Synthesis and Applications in Sensing, Catalysis, Imaging, and Biomedicine. *J. Nanobiotechnology* **2019**, *17*, 92.
- (8) Zhu, S.; Song, Y.; Zhao, X.; Shao, J.; Zhang, J.; Yang, B. The Photoluminescence Mechanism in Carbon Dots (Graphene Quantum Dots, Carbon Nanodots, and Polymer Dots): Current State and Future Perspective. *Nano Res.* **2015**, *8* (2), 355–381.
- (9) Mintz, K. J.; Bartoli, M.; Rovere, M.; Zhou, Y.; Hettiarachchi, S. D.; Paudyal, S.; Chen, J.; Domena, J. B.; Liyanage, P. Y.; Sampson, R.; et al. A Deep Investigation into the Structure of Carbon Dots. *Carbon N. Y.* **2021**, *173*, 433–447.
- (10) Luo, H.; Lari, L.; Kim, H.; Herou, S.; Tanase, L. C.; Lazarov, V. K.; Titirici, M. M. Structural Evolution of Carbon Dots during Low Temperature Pyrolysis. *Nanoscale* **2022**, *14* (3), 910–918.
- (11) Chan, M. H.; Chen, B. G.; Ngo, L. T.; Huang, W. T.; Li, C. H.; Liu, R. S.; Hsiao, M. Natural Carbon Nanodots: Toxicity Assessment and Theranostic Biological Application. *Pharmaceutics* **2021**, *13* (11), 1874.
- (12) Havrdova, M.; Hola, K.; Skopalik, J.; Tomankova, K.; Petr, M.; Cepe, K.; Polakova, K.; Tucek, J.; Bourlinos, A. B.; Zboril, R. Toxicity of Carbon Dots – Effect of Surface Functionalization on the Cell Viability, Reactive Oxygen Species Generation and Cell Cycle. *Carbon N. Y.* **2016**, *99*, 238–

- 248.
- (13) Molaei, M. J. Principles, Mechanisms, and Application of Carbon Quantum Dots in Sensors: A Review. *Anal. Methods* **2020**, *12* (10), 1266–1287.
 - (14) Baker, S. N.; Baker, G. A. Luminescent Carbon Nanodots: Emergent Nanolights. *Angew. Chemie - Int. Ed.* **2010**, *49* (38), 6726–6744.
 - (15) Essner, J. B.; Baker, G. A. The Emerging Roles of Carbon Dots in Solar Photovoltaics: A Critical Review. *Environ. Sci.: Nano.* **2017**, *4*, 1216-1263.
 - (16) Li, X.; Rui, M.; Song, J.; Shen, Z.; Zeng, H. Carbon and Graphene Quantum Dots for Optoelectronic and Energy Devices: A Review. *Adv. Funct. Mater.* **2015**, *25* (31), 4929–4947.
 - (17) Wang, Y.; Zhu, Y.; Yu, S.; Jiang, C. Fluorescent Carbon Dots: Rational Synthesis, Tunable Optical Properties and Analytical Applications. *RSC Adv.* **2017**, *7*, 40973-40989.
 - (18) Fernando, K. A. S.; Sahu, S.; Liu, Y.; Lewis, W. K.; Gulians, E. A.; Jafariyan, A.; Wang, P.; Bunker, C. E.; Sun, Y. P. Carbon Quantum Dots and Applications in Photocatalytic Energy Conversion. *ACS Appl. Mater. Interfaces* **2015**, *7* (16), 8363–8376.
 - (19) Wu, Z. L.; Liu, Z. X.; Yuan, Y. H. Carbon Dots: Materials, Synthesis, Properties and Approaches to Long-Wavelength and Multicolor Emission. *J. Mater. Chem. B* **2017**, *5* (21), 3794–3809.
 - (20) Semeniuk, M.; Yi, Z.; Poursorkhabi, V.; Tjong, J.; Jaffer, S.; Lu, Z. H.; Sain, M. Future Perspectives and Review on Organic Carbon Dots in Electronic Applications. *ACS Nano* **2019**, *13* (6), 6224–6255.
 - (21) Qu, D.; Sun, Z. The Formation Mechanism and Fluorophores of Carbon Dots Synthesized: Via a Bottom-up Route. *Mater. Chem. Front.* **2020**, *4*, 400-420.
 - (22) Xu, X.; Ray, R.; Gu, Y.; Ploehn, H. J.; Gearheart, L.; Raker, K.; Scrivens, W. A. Electrophoretic Analysis and Purification of Fluorescent Single-Walled Carbon Nanotube Fragments. *J. Am. Chem. Soc.* **2004**, *126* (40), 12736–12737.
 - (23) Sun, Y. P.; Zhou, B.; Lin, Y.; Wang, W.; Fernando, K. a S.; Pathak, P.; Mezziani, M. J.; Harruff, B. a.; Wang, X.; Wang, H.; et al. Quantum-Sized Carbon Dots for Bright and Colorful Photoluminescence. *J. Am. Chem. Soc.* **2006**, *128* (24), 7756–7757.
 - (24) Dong, Y.; Chen, C.; Zheng, X.; Gao, L.; Cui, Z.; Yang, H.; Guo, C.; Chi, Y.; Li, C. M. One-Step and High Yield Simultaneous Preparation of Single- and Multi-Layer Graphene Quantum Dots from CX-72 Carbon Black. *J. Mater. Chem.* **2012**, *22* (18), 8764–8766.
 - (25) Li, Y.; Hu, Y.; Zhao, Y.; Shi, G.; Deng, L.; Hou, Y.; Qu, L. An Electrochemical Avenue to Green-Luminescent Graphene Quantum Dots as Potential Electron-Acceptors for Photovoltaics. *Adv. Mater.* **2011**, *23* (6), 776–780.
 - (26) Xue, Q.; Huang, H.; Wang, L.; Chen, Z.; Wu, M.; Li, Z.; Pan, D. Nearly Monodisperse Graphene

- Quantum Dots Fabricated by Amine-Assisted Cutting and Ultrafiltration. *Nanoscale* **2013**, *5* (24), 12098–12103.
- (27) Calabro, R. L.; Yang, D. S.; Kim, D. Y. Liquid-Phase Laser Ablation Synthesis of Graphene Quantum Dots from Carbon Nano-Onions: Comparison with Chemical Oxidation. *J. Colloid Interface Sci.* **2018**, *527*, 132–140.
- (28) Xu, J.; Sahu, S.; Cao, L.; Anilkumar, P.; Tackett, K. N.; Qian, H.; Bunker, C. E.; Gulians, E. A.; Parenzan, A.; Sun, Y.-P. Carbon Nanoparticles as Chromophores for Photon Harvesting and Photoconversion. *ChemPhysChem* **2011**, *12* (18), 3604–3608.
- (29) Lee, J.; Kim, K.; Park, W. I.; Kim, B. H.; Park, J. H.; Kim, T. H.; Bong, S.; Kim, C. H.; Chae, G.; Jun, M.; et al. Uniform Graphene Quantum Dots Patterned from Self-Assembled Silica Nanodots. *Nano Lett.* **2012**, *12* (12), 6078–6083.
- (30) Ponomarenko, L. A.; Schedin, F.; Katsnelson, M. I.; Yang, R.; Hill, E. W.; Novoselov, K. S.; Geim, A. K. Chaotic Dirac Billiard in Graphene Quantum Dots. *Science* (80-.). **2008**, *320* (5874), 356–358.
- (31) Weng, Y.; Li, Z.; Peng, L.; Zhang, W.; Chen, G. Fabrication of Carbon Quantum Dots with Nano-Defined Position and Pattern in One Step via Sugar-Electron-Beam Writing. *Nanoscale* **2017**, *9* (48), 19263–19270.
- (32) Isaacoff, B. P.; Brown, K. A. Progress in Top-Down Control of Bottom-Up Assembly. *Nano Lett.* **2017**, *17* (11), 6508–6510.
- (33) Zhou, J.; Booker, C.; Li, R.; Zhou, X.; Sham, T. K.; Sun, X.; Ding, Z. An Electrochemical Avenue to Blue Luminescent Nanocrystals from Multiwalled Carbon Nanotubes (MWCNTs). *J. Am. Chem. Soc.* **2007**, *129* (4), 744–745.
- (34) Ray, S. C.; Saha, A.; Jana, N. R.; Sarkar, R. Fluorescent Carbon Nanoparticles: Synthesis, Characterization, and Bioimaging Application. *J. Phys. Chem. C* **2009**, *113* (43), 18546–18551.
- (35) Liu, M.; Xu, Y.; Niu, F.; Gooding, J. J.; Liu, J. Carbon Quantum Dots Directly Generated from Electrochemical Oxidation of Graphite Electrodes in Alkaline Alcohols and the Applications for Specific Ferric Ion Detection and Cell Imaging. *Analyst* **2016**, *141* (9), 2657–2664.
- (36) Nguyen, V.; Yan, L.; Si, J.; Hou, X. Femtosecond Laser-Induced Size Reduction of Carbon Nanodots in Solution: Effect of Laser Fluence, Spot Size, and Irradiation Time. *J. Appl. Phys.* **2015**, *117* (8), 084304.
- (37) Dang, H.; Huang, L. K.; Zhang, Y.; Wang, C. F.; Chen, S. Large-Scale Ultrasonic Fabrication of White Fluorescent Carbon Dots. *Ind. Eng. Chem. Res.* **2016**, *55* (18), 5335–5341.
- (38) Zhang, B.; Liu, C. Y.; Liu, Y. A Novel One-Step Approach to Synthesize Fluorescent Carbon Nanoparticles. *Eur. J. Inorg. Chem.* **2010**, *2010* (28), 4411–4414.

- (39) Zeng, Q.; Shao, D.; He, X.; Ren, Z.; Ji, W.; Shan, C.; Qu, S.; Li, J.; Chen, L.; Li, Q. Carbon Dots as a Trackable Drug Delivery Carrier for Localized Cancer Therapy in Vivo. *J. Mater. Chem. B* **2016**, *4* (30), 5119–5126.
- (40) Wan, J. Y.; Yang, Z.; Liu, Z. G.; Wang, H. X. Ionic Liquid-Assisted Thermal Decomposition Synthesis of Carbon Dots and Graphene-like Carbon Sheets for Optoelectronic Application. *RSC Adv.* **2016**, *6* (66), 61292–61300.
- (41) Fong, J. F. Y.; Chin, S. F.; Ng, S. M. A Unique “Turn-on” Fluorescence Signalling Strategy for Highly Specific Detection of Ascorbic Acid Using Carbon Dots as Sensing Probe. *Biosens. Bioelectron.* **2016**, *85*, 844–852.
- (42) Qian, Z.; Shan, X.; Chai, L.; Ma, J.; Chen, J.; Feng, H. Si-Doped Carbon Quantum Dots: A Facile and General Preparation Strategy, Bioimaging Application, and Multifunctional Sensor. *ACS Appl. Mater. Interfaces* **2014**, *6* (9), 6797–6805.
- (43) Li, H.; He, X.; Liu, Y.; Huang, H.; Lian, S.; Lee, S. T.; Kang, Z. One-Step Ultrasonic Synthesis of Water-Soluble Carbon Nanoparticles with Excellent Photoluminescent Properties. *Carbon N. Y.* **2011**, *49* (2), 605–609.
- (44) Wang, J.; Wei, J.; Su, S.; Qiu, J. Novel Fluorescence Resonance Energy Transfer Optical Sensors for Vitamin B12 Detection Using Thermally Reduced Carbon Dots. *New J. Chem.* **2014**, *39* (1), 501–507.
- (45) Liu, M. L.; Chen, B. Bin; Li, C. M.; Huang, C. Z. Carbon Dots: Synthesis, Formation Mechanism, Fluorescence Origin and Sensing Applications. *Green Chem.* **2019**, *21*, 449–471.
- (46) Misra, S. K.; Srivastava, I.; Tripathi, I.; Daza, E.; Ostadhossein, F.; Pan, D. Macromolecularly Caged Carbon Nanoparticles for Intracellular Trafficking via Switchable Photoluminescence. *J. Am. Chem. Soc.* **2017**, *139* (5), 1746–1749.
- (47) Rizzo, C.; Arcudi, F.; Dordević, L.; Dintcheva, N. T.; Noto, R.; D’Anna, F.; Prato, M. Nitrogen-Doped Carbon Nanodots-Ionogels: Preparation, Characterization, and Radical Scavenging Activity. *ACS Nano* **2018**, *12* (2), 1296–1305.
- (48) Xu, X.; Zhang, K.; Zhao, L.; Li, C.; Bu, W.; Shen, Y.; Gu, Z.; Chang, B.; Zheng, C.; Lin, C.; et al. Aspirin-Based Carbon Dots, a Good Biocompatibility of Material Applied for Bioimaging and Anti-Inflammation. *ACS Appl. Mater. Interfaces* **2016**, *8* (48), 32706–32716.
- (49) Shen, C. L.; Lou, Q.; Liu, K. K.; Dong, L.; Shan, C. X. Chemiluminescent Carbon Dots: Synthesis, Properties, and Applications. *Nano Today* **2020**, *35*, 100954.
- (50) Kim, T. H.; Sirdarta, J. P.; Zhang, Q.; Eftekhari, E.; St. John, J.; Kennedy, D.; Cock, I. E.; Li, Q. Selective Toxicity of Hydroxyl-Rich Carbon Nanodots for Cancer Research. *Nano Res.* **2018**, *11* (4), 2204–2216.

- (51) Mei, S.; Liu, X.; Zhang, W.; Liu, R.; Zheng, L.; Guo, R.; Tian, P. High-Bandwidth White-Light System Combining a Micro-LED with Perovskite Quantum Dots for Visible Light Communication. *ACS Appl. Mater. Interfaces* **2018**, *10* (6), 5641–5648.
- (52) Zhou, Z.; Tian, P.; Liu, X.; Mei, S.; Zhou, D.; Li, D.; Jing, P.; Zhang, W.; Guo, R.; Qu, S.; et al. Hydrogen Peroxide-Treated Carbon Dot Phosphor with a Bathochromic-Shifted, Aggregation-Enhanced Emission for Light-Emitting Devices and Visible Light Communication. *Adv. Sci.* **2018**, *5* (8), 1800369.
- (53) Tetsuka, H.; Nagoya, A.; Fukusumi, T.; Matsui, T. Molecularly Designed, Nitrogen-Functionalized Graphene Quantum Dots for Optoelectronic Devices. *Adv. Mater.* **2016**, *28* (23), 4632–4638.
- (54) Arcudi, F.; Strauss, V.; Đorđević, L.; Cadranel, A.; Guldi, D. M.; Prato, M. Porphyrin Antennas on Carbon Nanodots: Excited State Energy and Electron Transduction. *Angew. Chemie - Int. Ed.* **2017**, *56* (40), 12097–12101.
- (55) Liu, J.; Liu, Y.; Liu, N.; Han, Y.; Zhang, X.; Huang, H.; Lifshitz, Y.; Lee, S.; Zhong, J.; Kang, Z. Metal-Free Efficient Photocatalyst for Stable Visible Water Splitting via a Two-Electron Pathway. *Science (80-.)*. **2015**, *347* (6225), 970–974.
- (56) Shan, X.; Chai, L.; Ma, J.; Qian, Z.; Chen, J.; Feng, H. B-Doped Carbon Quantum Dots as a Sensitive Fluorescence Probe for Hydrogen Peroxide and Glucose Detection. *Analyst* **2014**, *139* (10), 2322–2325.
- (57) Zhang, M.; Hu, L.; Wang, H.; Song, Y.; Liu, Y.; Li, H.; Shao, M.; Huang, H.; Kang, Z. One-Step Hydrothermal Synthesis of Chiral Carbon Dots and Their Effects on Mung Bean Plant Growth. *Nanoscale* **2018**, *10* (26), 12734–12742.
- (58) Guo, J.; Li, H.; Ling, L.; Li, G.; Cheng, R.; Lu, X.; Xie, A. Q.; Li, Q.; Wang, C. F.; Chen, S. Green Synthesis of Carbon Dots toward Anti-Counterfeiting. *ACS Sustain. Chem. Eng.* **2020**, *8* (3), 1566–1572.
- (59) Sciortino, A.; Mauro, N.; Buscarino, G.; Sciortino, L.; Popescu, R.; Schneider, R.; Giammona, G.; Gerthsen, D.; Cannas, M.; Messina, F. β -C₃N₄ Nanocrystals: Carbon Dots with Extraordinary Morphological, Structural, and Optical Homogeneity. *Chem. Mater.* **2018**, *30* (5), 1695–1700.
- (60) Zhou, J.; Yang, Y.; Zhang, C. Y. A Low-Temperature Solid-Phase Method to Synthesize Highly Fluorescent Carbon Nitride Dots with Tunable Emission. *Chem. Commun.* **2013**, *49* (77), 8605–8607.
- (61) Rong, M.; Song, X.; Zhao, T.; Yao, Q.; Wang, Y.; Chen, X. Synthesis of Highly Fluorescent P,O-g-C₃N₄ Nanodots for the Label-Free Detection of Cu²⁺ and Acetylcholinesterase Activity. *J. Mater. Chem. C* **2015**, *3* (41), 10916–10924.
- (62) Cayuela, A.; Soriano, M. L.; Carrillo-Carrión, C.; Valcárcel, M. Semiconductor and Carbon-Based

- Fluorescent Nanodots: The Need for Consistency. *Chem. Commun.* **2016**, 52 (7), 1311–1326.
- (63) Xia, C.; Zhu, S.; Feng, T.; Yang, M.; Yang, B. Evolution and Synthesis of Carbon Dots: From Carbon Dots to Carbonized Polymer Dots. *Adv. Sci.* **2019**, 6 (23), 1901316.
- (64) Jin, S. H.; Kim, D. H.; Jun, G. H.; Hong, S. H.; Jeon, S. Tuning the Photoluminescence of Graphene Quantum Dots through the Charge Transfer Effect of Functional Groups. *ACS Nano* **2013**, 7 (2), 1239–1245.
- (65) Sun, H.; Wu, L.; Wei, W.; Qu, X. Recent Advances in Graphene Quantum Dots for Sensing. *Mater. Today* **2013**, 16 (11), 433–442.
- (66) Kang, S.; Jeong, Y. K.; Jung, K. H.; Son, Y.; Choi, S. C.; An, G. S.; Han, H.; Kim, K. M. Simple Preparation of Graphene Quantum Dots with Controllable Surface States from Graphite. *RSC Adv.* **2019**, 9 (66), 38447–38453.
- (67) Pillar-Little, T.; Kim, D. Y. Differentiating the Impact of Nitrogen Chemical States on Optical Properties of Nitrogen-Doped Graphene Quantum Dots. *RSC Adv.* **2017**, 7 (76), 48263–48267.
- (68) Qu, D.; Zheng, M.; Zhang, L.; Zhao, H.; Xie, Z.; Jing, X.; Haddad, R. E.; Fan, H.; Sun, Z. Formation Mechanism and Optimization of Highly Luminescent N-Doped Graphene Quantum Dots. *Sci. Rep.* **2014**, 4 (1), 5294.
- (69) Zhou, Y.; Sharma, S. K.; Peng, Z.; Leblanc, R. M. Polymers in Carbon Dots: A Review. *Polymers.* **2017**, 9 (2), 67.
- (70) Bourlinos, A. B.; Stassinopoulos, A.; Anglos, D.; Zboril, R.; Karakassides, M.; Giannelis, E. P. Surface Functionalized Carbogenic Quantum Dots. *Small* **2008**, 4 (4), 455–458.
- (71) Hill, S. A.; Benito-Alifonso, D.; Morgan, D. J.; Davis, S. A.; Berry, M.; Galan, M. C. Three-Minute Synthesis of sp³ Nanocrystalline Carbon Dots as Non-Toxic Fluorescent Platforms for Intracellular Delivery. *Nanoscale* **2016**, 8 (44), 18630–18634.
- (72) Holá, K.; Bourlinos, A. B.; Kozák, O.; Berka, K.; Šišková, K. M.; Havrdova, M.; Tuček, J.; Šafářová, K.; Otyepka, M.; Giannelis, E. P.; et al. Photoluminescence Effects of Graphitic Core Size and Surface Functional Groups in Carbon Dots: COO⁻ Induced Red-Shift Emission. *Carbon N. Y.* **2014**, 70, 279–286.
- (73) Siddique, A. B.; Pramanick, A. K.; Chatterjee, S.; Ray, M. Amorphous Carbon Dots and Their Remarkable Ability to Detect 2,4,6-Trinitrophenol. *Sci. Rep.* **2018**, 8 (1), 9770.
- (74) Sun, X.; Brückner, C.; Lei, Y. One-Pot and Ultrafast Synthesis of Nitrogen and Phosphorus Co-Doped Carbon Dots Possessing Bright Dual Wavelength Fluorescence Emission. *Nanoscale* **2015**, 7 (41), 17278–17282.
- (75) Sciortino, A.; Cayuela, A.; Soriano, M. L.; Gelardi, F. M.; Cannas, M.; Valcárcel, M.; Messina, F. Different Natures of Surface Electronic Transitions of Carbon Nanoparticles. *Phys. Chem. Chem.*

- Phys.* **2017**, *19* (34), 22670–22677.
- (76) Chu, K. W.; Lee, S. L.; Chang, C. J.; Liu, L. Recent Progress of Carbon Dot Precursors and Photocatalysis Applications. *Polymers (Basel)*. **2019**, *11* (4), 689.
- (77) Holá, K.; Zhang, Y.; Wang, Y.; Giannelis, E. P.; Zbořil, R.; Rogach, A. L. Carbon Dots - Emerging Light Emitters for Bioimaging, Cancer Therapy and Optoelectronics. *Nano Today* **2014**, *9* (5), 590–603.
- (78) Mintz, K. J.; Zhou, Y.; Leblanc, R. M. Recent Development of Carbon Quantum Dots Regarding Their Optical Properties, Photoluminescence Mechanism, and Core Structure. *Nanoscale* **2019**, *11*, 4634-4652.
- (79) Kozák, O.; Sudolská, M.; Pramanik, G.; Cígler, P.; Otyepka, M.; Zbořil, R. Photoluminescent Carbon Nanostructures. *Chem. Mater.* **2016**, *28* (12), 4085–4128.
- (80) Shamsipur, M.; Barati, A.; Taherpour, A. A.; Jamshidi, M. Resolving the Multiple Emission Centers in Carbon Dots: From Fluorophore Molecular States to Aromatic Domain States and Carbon-Core States. *J. Phys. Chem. Lett.* **2018**, *9* (15), 4189–4198.
- (81) Kuo, W.-S.; Chang, C.-Y.; Huang, K.-S.; Liu, J.-C.; Shao, Y.-T.; Yang, C.-H.; Wu, P.-C. Amino-Functionalized Nitrogen-Doped Graphene-Quantum-Dot-Based Nanomaterials with Nitrogen and Amino-Functionalized Group Content Dependence for Highly Efficient Two-Photon Bioimaging. *Int. J. Mol. Sci.* **2020**, *21* (8), 2939.
- (82) Zhu, S.; Shao, J.; Song, Y.; Zhao, X.; Du, J.; Wang, L.; Wang, H.; Zhang, K.; Zhang, J.; Yang, B. Investigating the Surface State of Graphene Quantum Dots. *Nanoscale* **2015**, *7* (17), 7927–7933.
- (83) Sweetman, M. J.; Hickey, S. M.; Brooks, D. A.; Hayball, J. D.; Plush, S. E. A Practical Guide to Prepare and Synthetically Modify Graphene Quantum Dots. *Adv. Funct. Mater.* **2019**, *29* (14), 1808740.
- (84) Yan, F.; Jiang, Y.; Sun, X.; Bai, Z.; Zhang, Y.; Zhou, X. Surface Modification and Chemical Functionalization of Carbon Dots: A Review. *Microchim. Acta* **2018**, *185*, 424.
- (85) Liu, S.; Zhao, N.; Cheng, Z.; Liu, H. Amino-Functionalized Green Fluorescent Carbon Dots as Surface Energy Transfer Biosensors for Hyaluronidase. *Nanoscale* **2015**, *7* (15), 6836–6842.
- (86) Xia, C.; Tao, S.; Zhu, S.; Song, Y.; Feng, T.; Zeng, Q.; Liu, J.; Yang, B. Hydrothermal Addition Polymerization for Ultrahigh-Yield Carbonized Polymer Dots with Room Temperature Phosphorescence via Nanocomposite. *Chem. - A Eur. J.* **2018**, *24* (44), 11303–11308.
- (87) Tao, S.; Zhu, S.; Feng, T.; Xia, C.; Song, Y.; Yang, B. The Polymeric Characteristics and Photoluminescence Mechanism in Polymer Carbon Dots: A Review. *Mater. Today Chem.* **2017**, *6*, 13–25.
- (88) Tao, S.; Song, Y.; Zhu, S.; Shao, J.; Yang, B. A New Type of Polymer Carbon Dots with High

- Quantum Yield: From Synthesis to Investigation on Fluorescence Mechanism. *Polymer (Guildf)*. **2017**, *116*, 472–478.
- (89) Song, Y.; Zhu, S.; Shao, J.; Yang, B. Polymer Carbon Dots-a Highlight Reviewing Their Unique Structure, Bright Emission and Probable Photoluminescence Mechanism. *J. Polym. Sci. Part A Polym. Chem.* **2017**, *55* (4), 610–615.
- (90) Guenther, R. D.; Steel, D. G. *Encyclopedia of modern optics*; Elsevier: Amsterdam, 2018.
- (91) Tseng, H. W.; Shen, J. Y.; Kuo, T. Y.; Tu, T. S.; Chen, Y. A.; Demchenko, A. P.; Chou, P. T. Excited-State Intramolecular Proton-Transfer Reaction Demonstrating Anti-Kasha Behavior. *Chem. Sci.* **2015**, *7* (1), 655–665.
- (92) Zu, F.; Yan, F.; Bai, Z.; Xu, J.; Wang, Y.; Huang, Y.; Zhou, X. The Quenching of the Fluorescence of Carbon Dots: A Review on Mechanisms and Applications. *Microchim. Acta* **2017**, *184* (7), 1899–1914.
- (93) Liang, X.; Li, N.; Zhang, R.; Yin, P.; Zhang, C.; Yang, N.; Liang, K.; Kong, B. Carbon-Based SERS Biosensor: From Substrate Design to Sensing and Bioapplication. *NPG Asia Mater.* **2021**, *13* (1), 8.
- (94) Bhunia, S. K.; Zeiri, L.; Manna, J.; Nandi, S.; Jelinek, R. Carbon-Dot/Silver-Nanoparticle Flexible SERS-Active Films. *ACS Appl. Mater. Interfaces* **2016**, *8* (38), 25637–25643.
- (95) Panyathip, R.; Sucharitakul, S.; Phaduangdhitidhada, S.; Ngamjarurojana, A.; Kumnorkaew, P.; Chooon, S. Surface Enhanced Raman Scattering in Graphene Quantum Dots Grown via Electrochemical Process. *Molecules* **2021**, *26* (18).
- (96) Oliveira, E. G. d. L.; de Oliveira, H. P.; Gomes, A. S. L. Metal Nanoparticles/Carbon Dots Nanocomposites for SERS Devices: Trends and Perspectives. *SN Appl. Sci.* **2020**, *2* (9), 1491.
- (97) Khayal, A.; Dawane, V.; Amin, M. A.; Tirth, V.; Yadav, V. K.; Algahtani, A.; Khan, S. H.; Islam, S.; Yadav, K. K.; Jeon, B. H. Advances in the Methods for the Synthesis of Carbon Dots and Their Emerging Applications. *Polymers (Basel)* **2021**, *13* (18), 3190.
- (98) Singhal, P.; Vats, B. G.; Pulhani, V. Origin of Solvent and Excitation Dependent Emission in Newly Synthesized Amphiphilic Carbon Dots. *J. Lumin.* **2022**, *244*, 118742.
- (99) Wang, W.; Wang, B.; Embrechts, H.; Damm, C.; Cadranel, A.; Strauss, V.; Distaso, M.; Hinterberger, V.; Guldi, D. M.; Peukert, W. Shedding Light on the Effective Fluorophore Structure of High Fluorescence Quantum Yield Carbon Nanodots. *RSC Adv.* **2017**, *7* (40), 24771–24780.
- (100) Ding, H.; Li, X. H.; Chen, X. B.; Wei, J. S.; Li, X. B.; Xiong, H. M. Surface States of Carbon Dots and Their Influences on Luminescence. *J. Appl. Phys.* **2020**, *127* (23), 231101.
- (101) Wang, L.; Zhu, S.-J.; Wang, H.-Y.; Qu, S.-N.; Zhang, Y.-L.; Zhang, J.-H.; Chen, Q.-D.; Xu, H.-L.; Han, W.; Yang, B.; et al. Common Origin of Green Luminescence in Carbon Nanodots and Graphene Quantum Dots. *ACS Nano* **2014**, *8* (3), 2541–2547.

- (102) Shi, B.; Nachtigallová, D.; Aquino, A. J. A.; Machado, F. B. C.; Lischka, H. Excited States and Excitonic Interactions in Prototypic Polycyclic Aromatic Hydrocarbon Dimers as Models for Graphitic Interactions in Carbon Dots. *Phys. Chem. Chem. Phys.* **2019**, *21* (18), 9077–9088.
- (103) Schneider, J.; Reckmeier, C. J.; Xiong, Y.; Von Seckendorff, M.; Susha, A. S.; Kasak, P.; Rogach, A. L. Molecular Fluorescence in Citric Acid-Based Carbon Dots. *J. Phys. Chem. C* **2017**, *121* (3), 2014–2022.
- (104) Siddique, F.; Langer, M.; Palonciová, M.; Medved, M.; Otyepka, M.; Nachtigallová, D.; Lischka, H.; Aquino, A. J. A. Conformational Behavior and Optical Properties of a Fluorophore Dimer as Model of Luminescent Centers in Carbon Dots. *J. Phys. Chem. C* **2020**, *124* (26), 14327–14337.
- (105) Yoon, H.; Chang, Y. H.; Song, S. H.; Lee, E.-S.; Jin, S. H.; Park, C.; Lee, J.; Kim, B. H.; Kang, H. J.; Kim, Y.-H.; et al. Intrinsic Photoluminescence Emission from Subdomained Graphene Quantum Dots. *Adv. Mater.* **2016**, *28* (26), 5255–5261.
- (106) Hai, X.; Feng, J.; Chen, X.; Wang, J. Tuning the Optical Properties of Graphene Quantum Dots for Biosensing and Bioimaging. *J. Mater. Chem. B* **2018**, *6* (20), 3219–3234.
- (107) Xu, Q.; Zhou, Q.; Hua, Z.; Xue, Q.; Zhang, C.; Wang, X.; Pan, D.; Xiao, M. Single-Particle Spectroscopic Measurements of Fluorescent Graphene Quantum Dots. *ACS Nano* **2013**, *7* (12), 10654–10661.
- (108) Zdrzil, L.; Zahradnicek, R.; Mohan, R.; Sedlacek, P.; Nejd, L.; Schmiedova, V.; Pospisil, J.; Horak, M.; Weiter, M.; Zmeskal, O.; et al. Preparation of Graphene Quantum Dots through Liquid Phase Exfoliation Method. *J. Lumin.* **2018**, *204*, 203–208.
- (109) Holá, K.; Sudolská, M.; Kalytchuk, S.; Nachtigallová, D.; Rogach, A. L.; Otyepka, M.; Zbořil, R. Graphitic Nitrogen Triggers Red Fluorescence in Carbon Dots. *ACS Nano* **2017**, *11* (12), 12402–12410.
- (110) Kundelev, E. V.; Tepliakov, N. V.; Leonov, M. Y.; Maslov, V. G.; Baranov, A. V.; Fedorov, A. V.; Rukhlenko, I. D.; Rogach, A. L. Amino Functionalization of Carbon Dots Leads to Red Emission Enhancement. *J. Phys. Chem. Lett.* **2019**, *10* (17), 5111–5116.
- (111) Wang, J.; Cao, S.; Ding, Y.; Ma, F.; Lu, W.; Sun, M. Theoretical Investigations of Optical Origins of Fluorescent Graphene Quantum Dots. *Sci. Rep.* **2016**, *6* (1), 24850.
- (112) Lu, S.; Cong, R.; Zhu, S.; Zhao, X.; Liu, J.; S.tse, J.; Meng, S.; Yang, B. pH-Dependent Synthesis of Novel Structure-Controllable Polymer-Carbon NanoDots with High Acidophilic Luminescence and Super Carbon Dots Assembly for White Light-Emitting Diodes. *ACS Appl. Mater. Interfaces* **2016**, *8* (6), 4062–4068.
- (113) Sarkar, S.; Sudolská, M.; Dubecký, M.; Reckmeier, C. J.; Rogach, A. L.; Zbořil, R.; Otyepka, M. Graphitic Nitrogen Doping in Carbon Dots Causes Red-Shifted Absorption. *J. Phys. Chem. C* **2016**,

- 120 (2), 1303–1308.
- (114) Sudolská, M.; Otyepka, M. Exact Roles of Individual Chemical Forms of Nitrogen in the Photoluminescent Properties of Nitrogen-Doped Carbon Dots. *Appl. Mater. Today* **2017**, *7*, 190–200.
- (115) Sk, M. A.; Ananthanarayanan, A.; Huang, L.; Lim, K. H.; Chen, P. Revealing the Tunable Photoluminescence Properties of Graphene Quantum Dots. *J. Mater. Chem. C* **2014**, *2* (34), 6954–6960.
- (116) Niu, X.; Li, Y.; Shu, H.; Wang, J. Revealing the Underlying Absorption and Emission Mechanism of Nitrogen Doped Graphene Quantum Dots. *Nanoscale* **2016**, *8* (46), 19376–19382.
- (117) Feng, J.; Dong, H.; Pang, B.; Shao, F.; Zhang, C.; Yu, L.; Dong, L. Theoretical Study on the Optical and Electronic Properties of Graphene Quantum Dots Doped with Heteroatoms. *Phys. Chem. Chem. Phys.* **2018**, *20* (22), 15244–15252.
- (118) Strauss, V.; Margraf, J. T.; Dolle, C.; Butz, B.; Nacken, T. J.; Walter, J.; Bauer, W.; Peukert, W.; Spiecker, E.; Clark, T.; et al. Carbon Nanodots: Toward a Comprehensive Understanding of Their Photoluminescence. *J. Am. Chem. Soc.* **2014**, *136* (49), 17308–17316.
- (119) Khan, W. U.; Wang, D.; Zhang, W.; Tang, Z.; Ma, X.; Ding, X.; Du, S.; Wang, Y. High Quantum Yield Green-Emitting Carbon Dots for Fe(III) Detection, Biocompatible Fluorescent Ink and Cellular Imaging. *Sci. Reports* **2017**, *7* (1), 14866.
- (120) Zheng, C.; An, X.; Gong, J. Novel pH Sensitive N-Doped Carbon Dots with Both Long Fluorescence Lifetime and High Quantum Yield. *RSC Adv.* **2015**, *5* (41), 32319–32322.
- (121) Yuan, Y. H.; Liu, Z. X.; Li, R. S.; Zou, H. Y.; Lin, M.; Liu, H.; Huang, C. Z. Synthesis of Nitrogen-Doping Carbon Dots with Different Photoluminescence Properties by Controlling the Surface States. *Nanoscale* **2016**, *8* (12), 6770–6776.
- (122) Wang, J.; Zhang, P.; Huang, C.; Liu, G.; Leung, K. C. F.; Wang, Y. X. J. High Performance Photoluminescent Carbon Dots for in Vitro and in Vivo Bioimaging: Effect of Nitrogen Doping Ratios. *Langmuir* **2015**, *31* (29), 8063–8073.
- (123) Choi, Y.; Kang, B.; Lee, J.; Kim, S.; Kim, G. T.; Kang, H.; Lee, B. R.; Kim, H.; Shim, S. H.; Lee, G.; et al. Integrative Approach toward Uncovering the Origin of Photoluminescence in Dual Heteroatom-Doped Carbon Nanodots. *Chem. Mater.* **2016**, *28* (19), 6840–6847.
- (124) Mueller, M. L.; Yan, X.; McGuire, J. A.; Li, L. S. Triplet States and Electronic Relaxation in Photoexcited Graphene Quantum Dots. *Nano Lett.* **2010**, *10* (7), 2679–2682.
- (125) Jiang, K.; Wang, Y.; Gao, X.; Cai, C.; Lin, H. Facile, Quick, and Gram-Scale Synthesis of Ultralong-Lifetime Room-Temperature-Phosphorescent Carbon Dots by Microwave Irradiation. *Angew. Chemie Int. Ed.* **2018**, *57* (21), 6216–6220.

- (126) Jiang, K.; Wang, Y.; Cai, C.; Lin, H. Conversion of Carbon Dots from Fluorescence to Ultralong Room-Temperature Phosphorescence by Heating for Security Applications. *Adv. Mater.* **2018**, *30* (26), 1800783.
- (127) Sun, Y.; Liu, S.; Sun, L.; Wu, S.; Hu, G.; Pang, X.; Smith, A. T.; Hu, C.; Zeng, S.; Wang, W.; et al. Ultralong Lifetime and Efficient Room Temperature Phosphorescent Carbon Dots through Multi-Confinement Structure Design. *Nat. Commun.* **2020**, *11* (1), 5591.
- (128) Tang, G.; Wang, C.; Zhang, K.; Wang, Y.; Yang, B. Deep-Blue Room-Temperature Phosphorescent Carbon Dots/Silica Microparticles from a Single Raw Material. *Langmuir* **2021**, *37* (45), 13187–13193.
- (129) Gao, Y.; Han, H.; Lu, W.; Jiao, Y.; Liu, Y.; Gong, X.; Xian, M.; Shuang, S.; Dong, C. Matrix-Free and Highly Efficient Room-Temperature Phosphorescence of Nitrogen-Doped Carbon Dots. *Langmuir* **2018**, *34* (43), 12845–12852.
- (130) Li, Q.; Zhou, M.; Yang, M.; Yang, Q.; Zhang, Z.; Shi, J. Induction of Long-Lived Room Temperature Phosphorescence of Carbon Dots by Water in Hydrogen-Bonded Matrices. *Nat. Commun.* **2018**, *9* (1), 734.
- (131) He, J.; He, Y.; Chen, Y.; Zhang, X.; Hu, C.; Zhuang, J.; Lei, B.; Liu, Y. Construction and Multifunctional Applications of Carbon Dots/PVA Nanofibers with Phosphorescence and Thermally Activated Delayed Fluorescence. *Chem. Eng. J.* **2018**, *347*, 505–513.
- (132) Jiang, K.; Wang, Y.; Cai, C.; Lin, H. Activating Room Temperature Long Afterglow of Carbon Dots via Covalent Fixation. *Chem. Mater.* **2017**, *29* (11), 4866–4873.
- (133) Liu, J.; Wang, N.; Yu, Y.; Yan, Y.; Zhang, H.; Li, J.; Yu, J. Carbon Dots in Zeolites: A New Class of Thermally Activated Delayed Fluorescence Materials with Ultralong Lifetimes. *Sci. Adv.* **2017**, *3* (5), 1603171.
- (134) Mo, L.; Xu, X.; Liu, Z.; Liu, H.; Lei, B.; Zhuang, J.; Guo, Z.; Liu, Y.; Hu, C. Visible-Light Excitable Thermally Activated Delayed Fluorescence in Aqueous Solution from F, N-Doped Carbon Dots Confined in Silica Nanoparticles. *Chem. Eng. J.* **2021**, *426*, 130728.
- (135) Xiong, Y.; Schneider, J.; Ushakova, E. V.; Rogach, A. L. Influence of Molecular Fluorophores on the Research Field of Chemically Synthesized Carbon Dots. *Nano Today* **2018**, *23*, 124–139.
- (136) Cappai, A.; Melis, C.; Stagi, L.; Ricci, P. C.; Mocci, F.; Carbonaro, C. M. Insight into the Molecular Model in Carbon Dots through Experimental and Theoretical Analysis of Citrazinic Acid in Aqueous Solution. *J. Phys. Chem. C* **2021**, *125* (8), 4836–4845.
- (137) Song, Y.; Zhu, S.; Zhang, S.; Fu, Y.; Wang, L.; Zhao, X.; Yang, B. Investigation from Chemical Structure to Photoluminescent Mechanism: A Type of Carbon Dots from the Pyrolysis of Citric Acid and an Amine. *J. Mater. Chem. C* **2015**, *3* (23), 5976–5984.

- (138) Stepanidenko, E. A.; Arefina, I. A.; Khavlyuk, P. D.; Dubavik, A.; Bogdanov, K. V.; Bondarenko, D. P.; Cherevkov, S. A.; Kundelev, E. V.; Fedorov, A. V.; Baranov, A. V.; et al. Influence of the Solvent Environment on Luminescent Centers within Carbon Dots. *Nanoscale* **2020**, *12* (2), 602–609.
- (139) Wang, T.; Wang, A.; Wang, R.; Liu, Z.; Sun, Y.; Shan, G.; Chen, Y.; Liu, Y. Carbon Dots with Molecular Fluorescence and Their Application as a “Turn-off” Fluorescent Probe for Ferricyanide Detection. *Sci. Rep.* **2019**, *9* (1), 10723.
- (140) Starukhin, A. N.; Nelson, D. K.; Eurov, D. A.; Kurdyukov, D. A.; Golubev, V. G. Manifestation of Fluorophore Segmental Motion in Carbon Dots in Steady-State Fluorescence Experiments. *Phys. Chem. Chem. Phys.* **2020**, *22* (16), 8401–8408.
- (141) Righetto, M.; Privitera, A.; Fortunati, I.; Mosconi, D.; Zerbetto, M.; Curri, M. L.; Corricelli, M.; Moretto, A.; Agnoli, S.; Franco, L.; et al. Spectroscopic Insights into Carbon Dot Systems. *J. Phys. Chem. Lett.* **2017**, *8* (10), 2236–2242.
- (142) Righetto, M.; Carraro, F.; Privitera, A.; Marafon, G.; Moretto, A.; Ferrante, C. The Elusive Nature of Carbon Nanodot Fluorescence: An Unconventional Perspective. *J. Phys. Chem. C* **2020**, *124* (40), 22314–22320.
- (143) Liu, X.; Li, H. B.; Shi, L.; Meng, X.; Wang, Y.; Chen, X.; Xu, H.; Zhang, W.; Fang, X.; Ding, T. Structure and Photoluminescence Evolution of Nanodots during Pyrolysis of Citric Acid: From Molecular Nanoclusters to Carbogenic Nanoparticles. *J. Mater. Chem. C* **2017**, *5* (39), 10302–10312.
- (144) Khan, S.; Sharma, A.; Ghoshal, S.; Jain, S.; Hazra, M. K.; Nandi, C. K. Small Molecular Organic Nanocrystals Resemble Carbon Nanodots in Terms of Their Properties. *Chem. Sci.* **2017**, *9* (1), 175–180.
- (145) Shi, L.; Yang, J. H.; Zeng, H. B.; Chen, Y. M.; Yang, S. C.; Wu, C.; Zeng, H.; Yoshihito, O.; Zhang, Q. Carbon Dots with High Fluorescence Quantum Yield: The Fluorescence Originates from Organic Fluorophores. *Nanoscale* **2016**, *8* (30), 14374–14378.
- (146) Kasprzyk, W.; Świergosz, T.; Bednarz, S.; Walas, K.; Bashmakova, N. V.; Bogdał, D. Luminescence Phenomena of Carbon Dots Derived from Citric Acid and Urea – a Molecular Insight. *Nanoscale* **2018**, *10* (29), 13889–13894.
- (147) Kutzelnigg, W.; Morgan, J. D. Rates of Convergence of the Partial-wave Expansions of Atomic Correlation Energies. *J. Chem. Phys.* **1998**, *96* (6), 4484.
- (148) Reine, S.; Saue, T. (2019). *European summerschool in Quantum Chemistry*. ESQC.
- (149) Hohenberg, P.; Kohn, W. Inhomogeneous Electron Gas. *Phys. Rev.* **1964**, *136* (3B), B864.
- (150) Thomas, L. H. The Calculation of Atomic Fields. *Math. Proc. Cambridge Philos. Soc.* **1927**, *23* (5),

- 542–548.
- (151) Kohn, W.; Sham, L. J. Self-Consistent Equations Including Exchange and Correlation Effects. *Phys. Rev.* **1965**, *140* (4A), A1133.
- (152) Zhao, Y.; Schultz, N. E.; Truhlar, D. G. Design of Density Functionals by Combining the Method of Constraint Satisfaction with Parametrization for Thermochemistry, Thermochemical Kinetics, and Noncovalent Interactions. *J. Chem. Theory Comput.* **2006**, *2* (2), 364–382.
- (153) Zhao, Y.; Truhlar, D. G. A New Local Density Functional for Main-Group Thermochemistry, Transition Metal Bonding, Thermochemical Kinetics, and Noncovalent Interactions. *J. Chem. Phys.* **2006**, *125* (19), 194101.
- (154) Lynch, B. J.; Fast, P. L.; Harris, M.; Truhlar, D. G. Adiabatic Connection for Kinetics. *J. Phys. Chem. A* **2000**, *104* (21), 4813–4815.
- (155) Yanai, T.; Tew, D. P.; Handy, N. C. A New Hybrid Exchange-Correlation Functional Using the Coulomb-Attenuating Method (CAM-B3LYP). *Chem. Phys. Lett.* **2004**, *393* (1–3), 51–57.
- (156) Becke, A. D. Density-Functional Thermochemistry. III. The Role of Exact Exchange. *J. Chem. Phys.* **1993**, *98* (7), 5648–5652.
- (157) Vydrov, O. A.; Scuseria, G. E. Assessment of a Long-Range Corrected Hybrid Functional. *J. Chem. Phys.* **2006**, *125* (23), 234109.
- (158) Rohrdanz, M. A.; Martins, K. M.; Herbert, J. M. A Long-Range-Corrected Density Functional That Performs Well for Both Ground-State Properties and Time-Dependent Density Functional Theory Excitation Energies, Including Charge-Transfer Excited States. *J. Chem. Phys.* **2009**, *130* (5), 054112.
- (159) Chai, J. Da; Head-Gordon, M. Long-Range Corrected Hybrid Density Functionals with Damped Atom-Atom Dispersion Corrections. *Phys. Chem. Chem. Phys.* **2008**, *10* (44), 6615–6620.
- (160) Chai, J. Da; Head-Gordon, M. Systematic Optimization of Long-Range Corrected Hybrid Density Functionals. *J. Chem. Phys.* **2008**, *128* (8), 084106.
- (161) Becke, A. D. Density-Functional Thermochemistry. V. Systematic Optimization of Exchange-Correlation Functionals. *J. Chem. Phys.* **1998**, *107* (20), 8554.
- (162) Marques, M. A. L., Ullrich, C. A., Nogueira, F., Rubio, A., Burke, K., Gross, E. K. U. (2006). *Time-dependent density functional theory* (1st ed., Ser. Lecture Notes in Physics). Springer Nature.
- (163) Burke, K. Perspective on Density Functional Theory. *J. Chem. Phys.* **2012**, *136* (15), 150901.
- (164) Casida, M. E. Time-Dependent Density-Functional Theory for Molecules and Molecular Solids. *J. Mol. Struct. THEOCHEM* **2009**, *914* (1–3), 3–18.
- (165) Runge, E.; Gross, E. K. U. Density-Functional Theory for Time-Dependent Systems. *Phys. Rev. Lett.* **1984**, *52* (12), 997.

- (166) Brémond, E.; Savarese, M.; Adamo, C.; Jacquemin, D. Accuracy of TD-DFT Geometries: A Fresh Look. *J. Chem. Theory Comput.* **2018**, *14* (7), 3715–3727.
- (167) Jacquemin, D.; Perpète, E. A.; Scuseria, G. E.; Ciofini, I.; Adamo, C. TD-DFT Performance for the Visible Absorption Spectra of Organic Dyes: Conventional versus Long-Range Hybrids. *J. Chem. Theory Comput.* **2007**, *4* (1), 123–135.
- (168) Guido, C. A.; Jacquemin, D.; Adamo, C.; Mennucci, B. On the TD-DFT Accuracy in Determining Single and Double Bonds in Excited-State Structures of Organic Molecules. *J. Phys. Chem. A* **2010**, *114* (51), 13402–13410.
- (169) Laurent, A. D.; Jacquemin, D. TD-DFT Benchmarks: A Review. *Int. J. Quantum Chem.* **2013**, *113* (17), 2019–2039.
- (170) Stephens, P. J.; Devlin, F. J.; Chabalowski, C. F.; Frisch, M. J. Ab Initio Calculation of Vibrational Absorption and Circular Dichroism Spectra Using Density Functional Force Fields. *J. Phys. Chem.* **1994**, *98* (45), 11623–11627.
- (171) Zhao, Y.; Truhlar, D. G.; Zhao, Y.; Truhlar, D. G. The M06 Suite of Density Functionals for Main Group Thermochemistry, Thermochemical Kinetics, Noncovalent Interactions, Excited States, and Transition Elements: Two New Functionals and Systematic Testing of Four M06-Class Functionals and 12 Other Functionals. *Theor. Chem. Accounts 2007 1201* **2007**, *120* (1), 215–241.
- (172) Grimme, S.; Neese, F. Double-Hybrid Density Functional Theory for Excited Electronic States of Molecules. *J. Chem. Phys.* **2007**, *127* (15), 154116.
- (173) Jacquemin, D.; Wathélet, V.; Perpète, E. A.; Adamo, C. Extensive TD-DFT Benchmark: Singlet-Excited States of Organic Molecules. *J. Chem. Theory Comput.* **2009**, *5* (9), 2420–2435.
- (174) Leach, A. R. (2001). *Molecular modelling: Principles and applications*. Prentice Hall.
- (175) Jensen, J. H. (2017). *Molecular modeling basics*. CRC Press.
- (176) Vanommeslaeghe, K.; Guvench, O.; MacKerell, A. D.; Jr. Molecular Mechanics. *Curr. Pharm. Des.* **2014**, *20* (20), 3281–3292.
- (177) Nezbeda, I., Kotrla, M., Kolafa, J. (2003). *Úvod do počítačových simulací: Metody Monte Carlo A Molekulární Dynamiky*. Karolinum.
- (178) Noid, W. G. Perspective: Coarse-Grained Models for Biomolecular Systems. *J. Chem. Phys.* **2013**, *139* (9), 090901.
- (179) Bradley, R.; Radhakrishnan, R. Coarse-Grained Models for Protein-Cell Membrane Interactions. *Polymers (Basel)*. **2013**, *5* (3), 890.
- (180) Kmiecik, S.; Gront, D.; Kolinski, M.; Wieteska, L.; Dawid, A. E.; Kolinski, A. Coarse-Grained Protein Models and Their Applications. *Chem. Rev.* **2016**, *116* (14), 7898–7936.
- (181) Takada, S. Coarse-Grained Molecular Simulations of Large Biomolecules. *Curr. Opin. Struct. Biol.*

- 2012**, 22 (2), 130–137.
- (182) Kukol, A. Lipid Models for United-Atom Molecular Dynamics Simulations of Proteins. *J. Chem. Theory Comput.* **2009**, 5 (3), 615–626.
- (183) Wang, J.; Cieplak, P.; Kollman, P. A. How Well Does a Restrained Electrostatic Potential (RESP) Model Perform in Calculating Conformational Energies of Organic and Biological Molecules? *J. Comput. Chem.* **2000**, 21 (12), 1049–1074.
- (184) Jorgensen, W. L.; Maxwell, D. S.; Tirado-Rives, J. Development and Testing of the OLPS All-Atom Force Field on Conformational Energetics and Properties of Organic Liquids. *J. Am. Chem. Soc.* **1996**, 118 (15), 11225–11236.
- (185) Li, P.; Merz, K. M. Metal Ion Modeling Using Classical Mechanics. *Chem. Rev.* **2017**, 117 (3), 1564–1686.
- (186) Cornell, W. D.; Cieplak, P.; Bayly, C. I.; Kollman, P. a.; Kollmann, P. A. Application of RESP Charges To Calculate Conformational Energies, Hydrogen Bond Energies, and Free Energies of Solvation. *J. Am. Chem. Soc.* **1993**, 115 (7), 9620–9631.
- (187) van Gunsteren, W. F.; Berendsen, H. J. C. Computer Simulation of Molecular Dynamics: Methodology, Applications, and Perspectives in Chemistry. *Angew. Chemie Int. Ed. English* **1990**, 29 (9), 992–1023.
- (188) Toukmaji, A. Y.; Board, J. A. Ewald Summation Techniques in Perspective: A Survey. *Comput. Phys. Commun.* **1996**, 95 (2–3), 73–92.
- (189) Darden, T.; York, D.; Pedersen, L. Particle Mesh Ewald: An $N \cdot \log(N)$ Method for Ewald Sums in Large Systems. *J. Chem. Phys.* **1993**, 98 (12), 10089–10092.
- (190) Berendsen, H. J. C.; Grigera, J. R.; Straatsma, T. P. The Missing Term in Effective Pair Potentials. *J. Phys. Chem.* **1987**, 91 (24), 6269–6271.
- (191) Jorgensen, W. L.; Chandrasekhar, J.; Madura, J. D.; Impey, R. W.; Klein, M. L. Comparison of Simple Potential Functions for Simulating Liquid Water. *J. Chem. Phys.* **1983**, 79 (2), 926–935.
- (192) https://water.lsbu.ac.uk/water/water_models.html (visited March 18, 2022)
- (193) Tomasi, J.; Mennucci, B.; Cammi, R. Quantum Mechanical Continuum Solvation Models. *Chem. Rev.* **2005**, 105 (8), 2999–3093.
- (194) Marenich, A. V.; Cramer, C. J.; Truhlar, D. G. Universal Solvation Model Based on Solute Electron Density and on a Continuum Model of the Solvent Defined by the Bulk Dielectric Constant and Atomic Surface Tensions. *J. Phys. Chem. B* **2009**, 113 (18), 6378–6396.
- (195) Guido, C. A.; Jacquemin, D.; Adamo, C.; Mennucci, B. Electronic Excitations in Solution: The Interplay between State Specific Approaches and a Time-Dependent Density Functional Theory Description. *J. Chem. Theory Comput.* **2015**, 11 (12), 5782–5790.

- (196) Zuehlsdorff, T. J.; Hine, N. D. M.; Spencer, J. S.; Harrison, N. M.; Riley, D. J.; Haynes, P. D. Linear-Scaling Time-Dependent Density-Functional Theory in the Linear Response Formalism. *J. Chem. Phys.* **2013**, *139* (6), 064104.
- (197) Caricato, M.; Mennucci, B.; Tomasi, J.; Ingrosso, F.; Cammi, R.; Corni, S.; Scalmani, G. Formation and Relaxation of Excited States in Solution: A New Time Dependent Polarizable Continuum Model Based on Time Dependent Density Functional Theory. *J. Chem. Phys.* **2006**, *124* (12), 124520.
- (198) Cammi, R.; Corni, S.; Mennucci, B.; Tomasi, J. Electronic Excitation Energies of Molecules in Solution: State Specific and Linear Response Methods for Nonequilibrium Continuum Solvation Models. *J. Chem. Phys.* **2005**, *122* (10), 104513.
- (199) Bussy, A.; Hutter, J. First-Principles Correction Scheme for Linear-Response Time-Dependent Density Functional Theory Calculations of Core Electronic States. *J. Chem. Phys.* **2021**, *155* (3), 034108.
- (200) Warshel, A.; Levitt, M. Theoretical Studies of Enzymic Reactions: Dielectric, Electrostatic and Steric Stabilization of the Carbonium Ion in the Reaction of Lysozyme. *J. Mol. Biol.* **1976**, *103* (2), 227–249.
- (201) Banáš, P.; Jurečka, P.; Walter, N. G.; Šponer, J.; Otyepka, M. Theoretical Studies of RNA Catalysis: Hybrid QM/MM Methods and Their Comparison with MD and QM. *Methods* **2009**, *49* (2), 202–216.
- (202) Cao, L.; Ryde, U. On the Difference between Additive and Subtractive QM/MM Calculations. *Front. Chem.* **2018**, *6*, 89.
- (203) Svensson, M.; Humbel, S.; Froese, R. D. J.; Matsubara, T.; Sieber, S.; Morokuma, K. ONIOM: A Multilayered Integrated MO + MM Method for Geometry Optimizations and Single Point Energy Predictions. A Test for Diels–Alder Reactions and Pt(P(t-Bu)₃)₂ + H₂ Oxidative Addition. *J. Phys. Chem.* **1996**, *100* (50), 19357–19363.
- (204) Senn, H. M.; Thiel, W. QM/MM Methods for Biomolecular Systems. *Angew. Chemie Int. Ed.* **2009**, *48* (7), 1198–1229.
- (205) Maseras, F.; Morokuma, K. IMOMM: A New Integrated Ab Initio + Molecular Mechanics Geometry Optimization Scheme of Equilibrium Structures and Transition States. *J. Comput. Chem.* **1995**, *16* (9), 1170–1179.
- (206) Singh, U. C.; Kollman, P. A. A Combined Ab Initio Quantum Mechanical and Molecular Mechanical Method for Carrying out Simulations on Complex Molecular Systems: Applications to the CH₃Cl + Cl⁻ Exchange Reaction and Gas Phase Protonation of Polyethers. *J. Comput. Chem.* **1986**, *7* (6), 718–730.
- (207) Söderhjelm, P.; Husberg, C.; Strambi, A.; Olivucci, M.; Ryde, U. Protein Influence on Electronic

- Spectra Modeled by Multipoles and Polarizabilities. *J. Chem. Theory Comput.* **2009**, *5* (3), 649–658.
- (208) Bondanza, M.; Nottoli, M.; Cupellini, L.; Lipparini, F.; Mennucci, B. Polarizable Embedding QM/MM: The Future Gold Standard for Complex (Bio)Systems? *Phys. Chem. Chem. Phys.* **2020**, *22* (26), 14433–14448.
- (209) List, N. H.; Olsen, J. M. H.; Kongsted, J. Excited States in Large Molecular Systems through Polarizable Embedding. *Phys. Chem. Chem. Phys.* **2016**, *18*, 20234–20250.
- (210) Chung, L. W.; Sameera, W. M. C.; Ramozzi, R.; Page, A. J.; Hatanaka, M.; Petrova, G. P.; Harris, T. V.; Li, X.; Ke, Z.; Liu, F.; et al. The ONIOM Method and Its Applications. *Chem. Rev.* **2015**, *115* (12), 5678–5796.
- (211) Monticelli, L., Salonen, E.; Groenhof, G. (2013). Introduction to QM/MM Simulations. In *Biomolecular simulations: Methods and protocols*. Humana Press.
- (212) Palonc'ová, M.; Langer, M.; Otyepka, M. Structural Dynamics of Carbon Dots in Water and *N, N*-Dimethylformamide Probed by All-Atom Molecular Dynamics Simulations. *J. Chem. Theory Comput.* **2018**, *14* (4), 2076–2083.
- (213) Humphrey, W.; Dalke, A.; Schulten, K. VMD - Visual Molecular Dynamics. *J. Molec. Graph.* **1996**, *14*, 33–38.
- (214) Van Der Spoel, D.; Lindahl, E.; Hess, B.; Groenhof, G.; Mark, A. E.; Berendsen, H. J. C. GROMACS: Fast, Flexible, and Free. *J. Comput. Chem.* **2005**, *26* (16), 1701–1718.
- (215) Hornak, V.; Abel, R.; Okur, A.; Strockbine, B.; Roitberg, A.; Simmerling, C. Comparison of Multiple Amber Force Fields and Development of Improved Protein Backbone Parameters. *Proteins: Struct. Funct. Genet.* **2006**, *65* (3), 712–725.
- (216) Cheng, A.; Steele, W. a. Computer Simulation of Ammonia on Graphite. I. Low Temperature Structure of Monolayer and Bilayer Films. *J. Chem. Phys.* **1990**, *92* (6), 3858.
- (217) Erimban, S.; Daschakraborty, S. Permeation Pathway of Two Hydrophobic Carbon Nanoparticles across a Lipid Bilayer. *J. Chem. Sci.* **2021**, *133* (4), 105.
- (218) Grimme, S.; Antony, J.; Ehrlich, S.; Krieg, H. A Consistent and Accurate Ab Initio Parametrization of Density Functional Dispersion Correction (DFT-D) for the 94 Elements H-Pu. *J. Chem. Phys.* **2010**, *132* (15), 154104.
- (219) Weigend, F.; Ahlrichs, R. Balanced Basis Sets of Split Valence, Triple Zeta Valence and Quadruple Zeta Valence Quality for H to Rn: Design and Assessment of Accuracy. *Phys. Chem. Chem. Phys.* **2005**, *7* (18), 3297–3305.
- (220) Frisch, M. J.; Trucks, G. W.; Schlegel, H. B.; Scuseria, G. E.; Robb, M. A.; Cheeseman, J. R.; Montgomery, Jr., J. A.; Vreven, T.; Kudin, K. N.; Burant, J. C.; et al. Gaussian09 Revision C.01

- Gaussian, Inc.: Wallingford CT, 2013.
- (221) Plasser, F.; Lischka, H. Analysis of Excitonic and Charge Transfer Interactions from Quantum Chemical Calculations. *J. Chem. Theory Comput.* **2012**, *8* (8), 2777–2789.
- (222) Martin, R. L. Natural Transition Orbitals. *J. Chem. Phys.* **2003**, *118* (11), 4775.
- (223) Plasser, F.; Wormit, M.; Dreuw, A. New Tools for the Systematic Analysis and Visualization of Electronic Excitations. I. Formalism. *J. Chem. Phys.* **2014**, *141* (2), 024106.
- (224) Plasser, F. TheoDORE: A Toolbox for a Detailed and Automated Analysis of Electronic Excited State Computations. *J. Chem. Phys.* **2020**, *152* (8), 084108.
- (225) Zhang, J.; Yang, L.; Yuan, Y.; Jiang, J.; Yu, S. H. One-Pot Gram-Scale Synthesis of Nitrogen and Sulfur Embedded Organic Dots with Distinctive Fluorescence Behaviors in Free and Aggregated States. *Chem. Mater.* **2016**, *28* (12), 4367–4374.
- (226) Riplinger, C.; Pinski, P.; Becker, U.; Valeev, E. F.; Neese, F. Sparse Maps - A Systematic Infrastructure for Reduced-Scaling Electronic Structure Methods. II. Linear Scaling Domain Based Pair Natural Orbital Coupled Cluster Theory. *J. Chem. Phys.* **2016**, *144* (2), 024109.
- (227) Purvis, G. D.; Bartlett, R. J. A Full Coupled-cluster Singles and Doubles Model: The Inclusion of Disconnected Triples. *J. Chem. Phys.* **1998**, *76* (4), 1910.
- (228) Raghavachari, K.; Trucks, G. W.; Pople, J. A.; Head-Gordon, M. A Fifth-Order Perturbation Comparison of Electron Correlation Theories. *Chem. Phys. Lett.* **1989**, *157* (6), 479–483.
- (229) Dunning, T. H. Gaussian Basis Sets for Use in Correlated Molecular Calculations. I. The Atoms Boron through Neon and Hydrogen. *J. Chem. Phys.* **1998**, *90* (2), 1007.
- (230) Neese, F. The ORCA Program System. *Wiley Interdiscip. Rev. Comput. Mol. Sci.* **2012**, *2* (1), 73–78.
- (231) Boys, S. F.; Bernardi, F. The Calculation of Small Molecular Interactions by the Differences of Separate Total Energies. Some Procedures with Reduced Errors. *Mol. Phys.* **1970**, *19* (4), 553–566.
- (232) Burns, L. A.; Marshall, M. S.; Sherrill, C. D. Comparing Counterpoise-Corrected, Uncorrected, and Averaged Binding Energies for Benchmarking Noncovalent Interactions. *J. Chem. Theory Comput.* **2014**, *10* (1), 49–57.
- (233) Cieplak, P.; Kollman, P. A. Calculation of the Free Energy of Association of Nucleic Acid Bases in Vacuo and Water Solution. *J. Am. Chem. Soc.* **1988**, *110* (12), 3734–3739.
- (234) Wang, J.; Wolf, R. M.; Caldwell, J. W.; Kollman, P. A.; Case, D. A. Development and Testing of a General Amber Force Field. *J. Comput. Chem.* **2004**, *25* (9), 1157–1174.
- (235) Wang, J.; Wang, W.; Kollman, P. A.; Case, D. A. Automatic Atom Type and Bond Type Perception in Molecular Mechanical Calculations. *J. Mol. Graph. Model.* **2006**, *25* (2), 247–260.
- (236) Case, D. A.; Cheatham, T. E.; Darden, T.; Gohlke, H.; Luo, R.; Merz, K. M.; Onufriev, A.;

- Simmerling, C.; Wang, B.; Woods, R. J. The Amber Biomolecular Simulation Programs. *J. Comput. Chem.* **2005**, *26* (16), 1668–1688.
- (237) Hess, B.; Bekker, H.; Berendsen, H. J. C.; Fraaije, J. G. E. M. LINCS: A Linear Constraint Solver for Molecular Simulations. *J. Comput. Chem.* **1997**, *18* (12), 1463–1472.
- (238) Nosé, S. A Unified Formulation of the Constant Temperature Molecular Dynamics Methods. *J. Chem. Phys.* **1984**, *81* (1), 511–519.
- (239) Hoover, W. G. Canonical Dynamics: Equilibrium Phase-Space Distributions. *Phys. Rev. A* **1985**, *31* (3), 1695–1697.
- (240) Parrinello, M.; Rahman, A. Polymorphic Transitions in Single Crystals: A New Molecular Dynamics Method. *J. Appl. Phys.* **1981**, *52* (12), 7182–7190.
- (241) Åqvist, J. Ion-Water Interaction Potentials Derived from Free Energy Perturbation Simulations. *J. Phys. Chem.* **1990**, *94* (21), 8021–8024.
- (242) Langer, M.; Paloncýová, M.; Medved', M.; Otyepka, M. Molecular Fluorophores Self-Organize into C-Dot Seeds and Incorporate into C-Dot Structures. *J. Phys. Chem. Lett.* **2020**, *11* (19), 8252–8258.
- (243) Bussi, G.; Donadio, D.; Parrinello, M. Canonical Sampling through Velocity Rescaling. *J. Chem. Phys.* **2007**, *126* (1), 014101.
- (244) Berendsen, H. J. C.; Postma, J. P. M.; van Gunsteren, W. F.; DiNola, A.; Haak, J. R. Molecular Dynamics with Coupling to an External Bath. *J. Chem. Phys.* **1984**, *81* (8), 3684–3690.
- (245) Mlýnský, V.; Kührová, P.; Kühn, T.; Otyepka, M.; Bussi, G.; Banáš, P.; Šponer, J. Fine-Tuning of the AMBER RNA Force Field with a New Term Adjusting Interactions of Terminal Nucleotides. *J. Chem. Theory Comput.* **2020**, *16* (6), 3936–3946.
- (246) Jeziorski, B.; Moszynski, R.; Szalewicz, K. Perturbation Theory Approach to Intermolecular Potential Energy Surfaces of van Der Waals Complexes. *Chem. Rev.* **1994**, *94* (7), 1887–1930.
- (247) Parrish, R. M.; Burns, L. A.; Smith, D. G. A.; Simmonett, A. C.; DePrince, A. E.; Hohenstein, E. G.; Bozkaya, U.; Sokolov, A. Y.; Di Remigio, R.; Richard, R. M.; et al. Psi4 1.1: An Open-Source Electronic Structure Program Emphasizing Automation, Advanced Libraries, and Interoperability. *J. Chem. Theory Comput.* **2017**, *13* (7), 3185–3197.
- (248) Frisch, M. J.; Trucks, G. W.; Schlegel, H. B.; Scuseria, G. E.; Robb, M. A.; Cheeseman, J. R.; Scalmani, G.; Barone, V.; Petersson, G. A.; Nakatsuji, H.; et al. Gaussian16 Revision B.01. Gaussian, Inc.: Wallingford, CT, 2016.
- (249) Furche, F.; Ahlrichs, R.; Hättig, C.; Klopper, W.; Sierka, M.; Weigend, F. Turbomole. *Wiley Interdiscip. Rev. Comput. Mol. Sci.* **2014**, *4* (2), 91–100.
- (250) Steffen, C.; Thomas, K.; Huniar, U.; Hellweg, A.; Rubner, O.; Schroer, A. TmoleX--A Graphical User Interface for TURBOMOLE. *J. Comput. Chem.* **2010**, *31*, 2967–2970.

- (251) Olsen, J. M.; Aidas, K.; Kongsted, J. Excited States in Solution through Polarizable Embedding. *J. Chem. Theory Comput.* **2010**, *6* (12), 3721–3734.
- (252) Olsen, J. M. H.; Kongsted, J. Molecular Properties through Polarizable Embedding. *Adv. Quantum Chem.* 2011, *61*, 107–143.
- (253) Fdez. Galván, I.; Vacher, M.; Alavi, A.; Angeli, C.; Aquilante, F.; Autschbach, J.; Bao, J. J.; Bokarev, S. I.; Bogdanov, N. A.; Carlson, R. K.; et al. OpenMolcas: From Source Code to Insight. *J. Chem. Theory Comput.* **2019**, *15* (11), 5925–5964.
- (254) Aidas, K.; Angeli, C.; Bak, K. L.; Bakken, V.; Bast, R.; Boman, L.; Christiansen, O.; Cimiraglia, R.; Coriani, S.; Dahle, P.; et al. The Dalton Quantum Chemistry Program System. *Wiley Interdiscip. Rev. Comput. Mol. Sci.* **2014**, *4* (3), 269–284.
- (255) Dalton, a Molecular Electronic Structure Program, Release Dalton 2019. Alpha (2019). <http://daltonprogram.org> (accessed May 7, 2021).
- (256) Langer, M.; Hrivnák, T.; Medved', M.; Otyepka, M. Contribution of the Molecular Fluorophore IPCA to Excitation-Independent Photoluminescence of Carbon Dots. *J. Phys. Chem. C* **2021**, *125* (22), 12140–12148.
- (257) Jacquemin, D.; Duchemin, I.; Blase, X. 0-0 Energies Using Hybrid Schemes: Benchmarks of TD-DFT, CIS(D), ADC(2), CC2, and BSE/GW Formalisms for 80 Real-Life Compounds. *J. Chem. Theory Comput.* **2015**, *11* (11), 5340–5359.
- (258) Loos, P.; Jacquemin, D. Evaluating 0–0 Energies with Theoretical Tools: A Short Review. *ChemPhotoChem* **2019**, *3* (9), 684–696.
- (259) Case, D. A.; Darden, T. A.; Cheatham, T. E., 3rd.; Simmerling, C. L.; Wang, J.; Duke, R. E.; Luo, R.; Walker, R. C.; Zhang, W.; Merz, K. M.; et al. AMBER 11, University of California, San Francisco. 2010.
- (260) Roe, D. R.; Cheatham, T. E. PTRAJ and CPPTRAJ: Software for Processing and Analysis of Molecular Dynamics Trajectory Data. *J. Chem. Theory Comput.* **2013**, *9* (7), 3084–3095.
- (261) Kalytchuk, S.; Zdražil, L.; Bad'ura, Z.; Medved', M.; Langer, M.; Palonc'ová, M.; Zoppellaro, G.; Kershaw, S. V.; Rogach, A. L.; Otyepka, M.; et al. Carbon Dots Detect Water-to-Ice Phase Transition and Act as Alcohol Sensors via Fluorescence Turn-Off/On Mechanism. *ACS Nano* **2021**, *15* (4), 6582–6593.
- (262) Caleman, C.; Hong, M.; Costa, L. T.; Maaren, P. J. Van; Hub, J. S. Force Field Benchmark of Organic Liquids: Density, Enthalpy of Vaporization, Heat Capacities, Surface Tension, Compressibility, Expansion Coefficient and Dielectric Constant *J. Chem. Theory Comput.* **2012**, *8* (1), 61–74.
- (263) van der Spoel, D.; van Maaren, P. J.; Caleman, C. GROMACS Molecule & Liquid Database.

- Bioinformatics* **2012**, *28* (5), 752–753.
- (264) Kendall, R. A.; Dunning, T. H.; Harrison, R. J. Electron Affinities of the First-row Atoms Revisited. Systematic Basis Sets and Wave Functions. *J. Chem. Phys.* **1998**, *96* (9), 6796.
- (265) Woon, D. E.; Dunning, T. H. Gaussian Basis Sets for Use in Correlated Molecular Calculations. IV. Calculation of Static Electrical Response Properties. *J. Chem. Phys.* **1998**, *100* (4), 2975.
- (266) Barone, V.; Cossi, M. Quantum Calculation of Molecular Energies and Energy Gradients in Solution by a Conductor Solvent Model. *J. Phys. Chem. A* **1998**, *102* (11), 1995–2001.
- (267) Cossi, M.; Rega, N.; Scalmani, G.; Barone, V. Energies, Structures, and Electronic Properties of Molecules in Solution with the C-PCM Solvation Model. *J. Comput. Chem.* **2003**, *24* (6), 669–681.
- (268) Panáček, D.; Hochvaldová, L.; Bakandritsos, A.; Malina, T.; Langer, M.; Belza, J.; Martinčová, J.; Večeřová, R.; Lazar, P.; Poláková, K.; et al. Silver Covalently Bound to Cyanographene Overcomes Bacterial Resistance to Silver Nanoparticles and Antibiotics. *Adv. Sci.* **2021**, *8* (12), 2003090.
- (269) Zdražil, L.; Kalytchuk, S.; Langer, M.; Ahmad, R.; Pospíšil, J.; Zmeškal, O.; Altomare, M.; Osvet, A.; Zbořil, R.; Schmuki, P.; et al. Transparent and Low-Loss Luminescent Solar Concentrators Based on Self-Trapped Exciton Emission in Lead-Free Double Perovskite Nanocrystals. *ACS Appl. Energy Mater.* **2021**, *4* (7), 6445–6453.
- (270) Pykal, M.; Langer, M.; Blahová Prudilová, B.; Banáš, P.; Otyepka, M. Ion Interactions across Graphene in Electrolyte Aqueous Solutions. *J. Phys. Chem. C* **2019**, *123* (15), 9799–9806.
- (271) Han, Y.; Langer, M.; Medved', M.; Otyepka, M.; Král, P. Stretch-Healable Molecular Nanofibers. *Adv. Theory Simulations* **2020**, *3* (10), 2000094.

List of publications

1. Paloncýová, M.; Langer, M.; Otyepka, M. Structural Dynamics of Carbon Dots in Water and *N, N* - Dimethylformamide Probed by All-Atom Molecular Dynamics Simulations. *J. Chem. Theory Comput.* 2018, *14*, 2076–2083.
2. Pykal, M.; Langer, M.; Blahová Prudilová, B.; Banáš, P.; Otyepka, M. Ion Interactions across Graphene in Electrolyte Aqueous Solutions. *J. Phys. Chem. C* 2019, *123*, 9799–9806.
3. Siddique, F.; Langer, M.; Paloncýová, M.; Medved', M.; Otyepka, M.; Nachtigallová, D.; Lischka, H.; Aquino, A. J. A. Conformational Behavior and Optical Properties of a Fluorophore Dimer as Model of Luminescent Centers in Carbon Dots. *J. Phys. Chem. C* 2020, *124*, 14327–14337.
4. Langer, M.; Paloncýová, M.; Medved', M.; Otyepka, M. Molecular Fluorophores Self-Organize into C-Dot Seeds and Incorporate into C-Dot Structures. *J. Phys. Chem. Lett.* 2020, *11*, 8252–8258.
5. Han, Y.; Langer, M.; Medved', M.; Otyepka, M.; Král, P. Stretch-Healable Molecular Nanofibers. *Adv. Theory Simulations* 2020, *3*, 2000094.
6. Langer, M.; Paloncýová, M.; Medved', M.; Pykal, M.; Nachtigallová, D.; Shi, B.; Aquino, A. J. A.; Lischka, H.; Otyepka, M. Progress and Challenges in Understanding of Photoluminescence Properties of Carbon Dots Based on Theoretical Computations. *Appl. Mater. Today*. 2021, *22*, 100924.
7. Kalytchuk, S.; Zdražil, L.; Bad'ura, Z.; Medved', M.; Langer, M.; Paloncýová, M.; Zoppellaro, G.; Kershaw, S. V.; Rogach, A. L.; Otyepka, M.; Zbořil, R. Carbon Dots Detect Water-to-Ice Phase Transition and Act as Alcohol Sensors via Fluorescence Turn-Off/On Mechanism. *ACS Nano* 2021, *15*, 6582–6593.
8. Panáček, D.; Hochvaldová, L.; Bakandritsos, A.; Malina, T.; Langer, M.; Belza, J.; Martincová, J.; Večeřová, R.; Lazar, P.; Poláková, K.; Kolařík, J.; Válková, L.; Kolář, M.; Otyepka, M.; Panáček, D.; Zbořil, R. Silver Covalently Bound to Cyanographene Overcomes Bacterial Resistance to Silver Nanoparticles and Antibiotics. *Adv. Sci.* 2021, *8*, 2003090.
9. Zdražil, L.; Kalytchuk, S.; Langer, M.; Ahmad, R.; Pospisil, J.; Zmeškal, O.; Altomare, M.; Osvet, A.; Zbořil, R.; Schmuki, P.; Brabec, C.; Otyepka, M.; Kment, S. Transparent and Low-Loss Luminescent Solar Concentrators Based on Self-Trapped Exciton Emission in Lead-Free Double Perovskite Nanocrystals. *ACS Appl. Energy Mater.* 2021, *4*, 6445–6453.
10. Langer, M.; Hrivnák, T.; Medved', M.; Otyepka, M. Contribution of the Molecular Fluorophore IPCA to Excitation-Independent Photoluminescence of Carbon Dots. *J. Phys. Chem. C* 2021, *125*, 12140–12148.

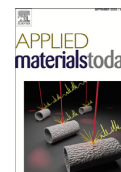
Appendix A: Progress and challenges in understanding of photoluminescence properties of carbon dots based on theoretical computations



ELSEVIER

Contents lists available at ScienceDirect

Applied Materials Today

journal homepage: www.elsevier.com/locate/apmt

Progress and challenges in understanding of photoluminescence properties of carbon dots based on theoretical computations

Michal Langer^{a,b}, Markéta Paloncýová^a, Miroslav Medved^a, Martin Pykal^a, Dana Nachtigallová^{a,c}, Baimei Shi^d, Adélia J.A. Aquino^{d,e}, Hans Lischka^{d,f}, Michal Otyepka^{a,*}

^a Regional Centre of Advanced Technologies and Materials, Faculty of Science, Palacký University Olomouc, Šlechtitelů 27, Olomouc 783 71, Czech Republic

^b Department of Physical Chemistry, Faculty of Science, Palacký University Olomouc, 17. listopadu 12, Olomouc 711 46, Czech Republic

^c The Czech Academy of Sciences, Institute of Organic Chemistry and Biochemistry v.v.i., Prague 6 166 10, Czech Republic

^d School of Pharmaceutical Science and Technology, Tianjin University, Tianjin 300072, China

^e Department of Mechanical Engineering, Texas Tech University, Lubbock, TX 79409, USA

^f Department of Chemistry and Biochemistry, Texas Tech University Lubbock, TX 79409-1061, USA

ARTICLE INFO

Article history:

Received 27 October 2020

Revised 1 December 2020

Accepted 21 December 2020

Keywords:

Carbon dots

Structure

Absorption

Photoluminescence

Theoretical calculations

ABSTRACT

Carbon dots (CDs), including graphene quantum dots, carbon nanodots, carbon quantum dots, and carbonized polymer dots, belong to extensively studied nanomaterials with a very broad application potential resulting from their bright photoluminescence (PL), high (photo)stability, low toxicity and great biocompatibility. However, the design of CDs with tailored properties is still hampered by a fairly limited understanding of the CD PL, which stems from their rather complex structure and variability of the PL centers. Theoretical calculations provide valuable insights into the nature of the excited states and the source of PL. In this review, we focus on state-of-the-art theoretical methods for the description of absorption and PL of CDs and their limitations, along with providing an overview of theoretical studies addressing structural models and the electronic structure of various types of CDs in the context of their overall optical properties. Besides the assessment of the current state of knowledge, we also highlight the opportunity for further advancements in the field.

© 2020 Elsevier Ltd. All rights reserved.

1. Introduction

1.1. Discovery and definition of carbon dots

Nanosized carbon-based materials, such as fullerenes, nanotubes, and graphene, have attracted attention of scientists owing to their unique physicochemical properties often very different from those of the original bulk material. In 2004, Xu *et al.* [1] started to write a new exciting chapter on carbon nanostructures by separating a mixture of weakly fluorescent carbon nanoparticles from single-walled carbon nanotubes obtained from arc-discharge soot. Since then, carbon dots (CDs), as these carbon-based fluorescent nanoparticles (with at least one dimension smaller than 10 nm) are nowadays referred to, have expanded into a large class of metal-free nanomaterials with significant and tuneable photoluminescence (PL). Other unique properties, in particular, non/low-toxicity, biocompatibility, dispersibility in a wide range of solvents, biodegradability, low-cost, facile and scalable synthesis, predispose CDs for plethora of environment-

friendly applications in biomedical imaging and sensing [2–4], cancer therapy [5], or theranostics [6], anti-counterfeiting [7], light-emitting devices [8–11], optoelectronic devices [12–15], photocatalysis [16] and functional materials [17,18].

1.2. Synthesis of CDs

In general, the CDs can be prepared by employing either top-down or bottom-up approaches [12]. The top-down methods usually require harsh conditions (strong oxidants, concentrated acids, and high temperatures) or severe physical techniques (laser ablation, arc discharge and nanolithography) to cut, decompose and/or exfoliate bulk carbonaceous materials (e.g., graphite, graphene oxide, activated carbon, soot, carbon nanotubes) into carbon nanoparticles [19–27]. On the other hand, the bottom-up strategies such as stepwise organic synthesis, hydrothermal/solvothermal synthesis, and chemical vapor deposition and microwave-assisted treatments can utilize a large variety of simple organic precursors [28,29]. The optimization of reagents and reaction conditions yielded CDs with significantly enhanced PL quantum yields (QYs) which were mainly attributed to heteroatom doping effects, surface functionalities, and, last but not least, the presence of molecular fluorophores

* Corresponding author.

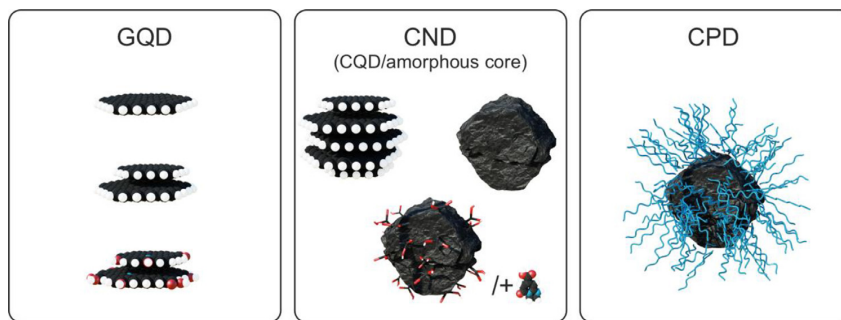


Fig. 1. CDs can be classified into three major groups; graphene quantum dots (GQDs), carbon nanodots (CNDs) with either graphitic inner structure (CQDs) or with the amorphous one, and carbonized polymer dots (CPDs). During the synthesis of CNDs, molecular fluorophores can be found in the final fluorescent product (displayed as IPCA in bottom right of the middle panel).

(MFs). One of the most frequently used precursors for the bottom-up syntheses is citric acid (CA), which was shown to react with various nitrogen-containing organic reagents such as 1,2-diamines, urea, amino acids, etc. forming highly fluorescent CDs (with QYs up to 86 %) [29–33].

1.3. Classification of CDs

Because of the diversity of available preparation methods, CDs nowadays represent a large family of fluorescent 0D carbon materials that can be classified according to the carbon core structure, which can be either crystalline or amorphous, surface functionalities, and performance features into several sub-groups including graphene quantum dots (GQDs), carbon nanodots (CNDs), carbon quantum dots (CQDs), and carbonized polymer dots (CPDs) (Fig. 1) [28,34,35]. The GQDs are typically prepared from graphene/graphite or other graphitic materials by top-down synthetic approaches [36–38] and exhibit strong PL [39–41]. They consist of a single layer or few layers of graphene which are usually functionalized by chemical groups on the edge [37]. The shape of GQDs is often oblate with the lateral diameter typically <20 nm, although some can be as large as 60 nm [40]. The PL of GQDs is mainly ruled by quantum confinement and edge effects [37,42]. Contrary to GQDs, the CQDs (often considered to be a special case of CNDs) and CNDs are always quasi-spherical with the diameter up to 10 nm [38]. In CQDs, the carbon core possesses graphitic crystalline structure and the surface is functionalized by oxygen/nitrogen groups, which show intrinsic state PL and the quantum confinement effect (QCE) [43], and thus the PL wavelength can be tuned by the CQDs' size and the functionalization of the surface [44,45]. On the other hand, amorphous CNDs are mostly prepared by bottom-up synthetic strategies, and their core exhibits high carbonization degree without obvious crystal structure or polymer features. The edges of the amorphous carbon core domains often doped by heteroatoms are passivated by surface functional groups. Contrary to CQDs, the PL of CNDs is not dominated by the QCE of the particle size [46,47]. In addition, MFs as a remnant of the condensation phase of the synthesis can be covalently bound or non-covalently attached to both CQDs and amorphous CNDs. As a result of incomplete carbonization process, the CPDs exhibit hybrid polymer/carbon structure, in which carbonized fragments are incorporated into a polymer matrix [28]. Consequently, the CPDs possess not only the features of CNDs but also inherit important polymeric properties [48,49]. The CPDs can exhibit extraordinary PL QYs, which are attributed to the multicenter fluorophore structure and special PL mechanism [50–52]. It should also be noted that the CPDs are distinguished from polymer dots (PDs), which lack the cross-linking of carbonized

nanoparticles with polymer network structure [53]. CDs with well-defined homogeneous structures such as triangular CDs with narrow size distributions [54], crystalline C_3N CDs [55], and chiral CDs [56–58] have also been reported. Importantly, composite materials containing CDs incorporated in polymers (e.g., polyvinyl alcohol), metal-organic frameworks, or inorganic (e.g., zeolites) host matrices exhibiting room temperature phosphorescence (RTP) and/or delayed fluorescence have been designed [45,59–63].

1.4. Scope of the review

Many excellent reviews have been written on synthesis, characterizations, PL mechanisms and applications of CDs [12,15,33,60,64–69]. Although some of them include also theoretical models [70], a comprehensive survey of quantum mechanics (QM) and/or molecular mechanics (MM) approaches and models applied in the field of CDs is missing. In the current review, we (i) briefly summarize the experimental evidence on the structure and PL properties of individual classes of CDs referring the reader to more comprehensive reviews, (ii) describe state-of-the-art theoretical methods for description of absorption and fluorescence of CDs, (iii) provide an overview of theoretical studies addressing the structural models and electronic structure of CDs in the context of PL, and (iv) outline perspectives for future computational studies in the field of CDs.

2. Experimental data on structure and photoluminescence properties of CDs

2.1. Structural characterization of CDs

A detailed structural information about systems of interest is a crucial aspect for any theoretical investigation. In this regard, CDs are indeed a challenging target not only because of inherent ill-defined core and surface structures, but also due to a dependence of their final structure on the reaction conditions. In fact, different types of CDs can be synthesized from the same precursors depending on the ratio of reagents, temperature and pH [47,71]. In addition, as pointed out by Rogach and coworkers [72], potential ambiguities can occur in the structural characterisation of CDs when employing techniques commonly applied in other areas of the material science such as high-resolution X-ray photoelectron spectroscopy (HR-XPS), Fourier transformed infrared spectroscopy (FTIR), transmission electron spectroscopy (TEM), atomic force microscopy (AFM), and X-ray diffraction (XRD). For example, HR-XPS signals of substitutional nitrogen functionalities are usually presented as a proof of the nitrogen doping in CDs; however, the same signals can also be generated by molecular compounds such as

citrazinic acid (CZA), a 2-pyridone derivative containing pyridinic nitrogen, as well as 5-oxo-1,2,3,5-tetrahydroimidazo[1,2-a]pyridine-7-carboxylic acid (IPCA) containing nitrogen in a pyrrolic coordination. Similar issues arise in the interpretation of FTIR spectra used for identification of surface functionalities on CDs, which can also be present in MFs. Clearly, combined theoretical and experimental efforts are necessary to gather various types of data, so that reliable structural models of CDs could be established based on their consistent interpretation, as shown, e.g., for N-doping of graphene [73]. In what follows, we describe in more detail commonly accepted views on structural features of individual classes of CDs that can serve as a base for designing pertinent theoretical models of CDs or at least their structural subunits.

2.1.1. Graphene quantum dots

GQDs are sub-100 nm anisotropic nanoparticles consisting of either a single layer or a few layers of (doped) graphene with nitrogen or oxygen functional groups covalently attached to the edges [74]. The lateral dimensions typically vary from 2 to 40 nm or sometimes even bigger CDs may be synthesized [40], while the thickness ranges from 1.3 to 8 nm [75–78]. Although the core of GQDs is relatively well defined, consisting of sp^2 hybridized carbons or heteroatoms, the overall structure of the final GQD product is often dependent on the synthetic precursors and conditions [79]. Adapting the conditions, one can prepare pure GQDs [80], GQDs with specific (hexagonal or triangular) shape [54,81], single-, double- or multi-heteroatom doped GQDs [82], or GQDs with different functional groups [83,84]. In the case of doped GQDs, pyridinic, pyrrolic and graphitic nitrogen atoms are often embedded in the GQD lattice as revealed by HR-XPS [85–89].

Functional groups in GQDs typically involve electron donating groups such as $-NH_2$, $-OH$, $-OR$, $-OCOR$, or electron withdrawing groups including $-X$, $-CHO$, $=O$, $-COOR$, $-COOH$, $-CN$, $-NH_3^+$, $-NO_2$ [90–92]. Besides these common functional groups, the occurrence of bulkier groups such as *o*-phenylenediamine, diamionaphthalene and azo- moieties in GQDs was also reported [13]. Overall, owing to versatility of the potential functional groups on the edges, the observed changes in optical spectra of GQDs can be related to the existence of push-pull structures due to the presence of electron donor ($-NH_2$) and electron acceptor ($-COOH$) groups on the edge [13,93]. Depending on the synthesis, the microstructure of GQDs might not be perfect and defect-free, especially if they are prepared by top-down methods [94]. The study of pure GQDs using surface enhanced Raman spectroscopy (SERS) revealed large defects on the edges, sp^3 -like defects and disorders on the basal planes [95]. It was also described that presence of epoxy- groups on basal planes of GQDs makes them more prone to be attacked by some chemical reagents [96]. The existence of free edges on GQDs can be considered as another defect in GQDs structure, where free zigzag edges are carbene-like, with a triplet ground state [97]. Finally, although it is usually not easy to analyze, it can be expected that the GQDs, especially those prepared by top-down approaches, can contain various types of vacancies [94]. The defects and vacancies can dramatically affect the electronic structure of GQDs. For example, the QCE mainly related to the size of sp^2 -hybridized carbon domains can be altered by the increasing content of oxygen due to the increase of the number of defects that can result in creation of several smaller mutually separated π -conjugated domains which can act as the PL centers [34].

2.1.2. Carbon nanodots

CNDs are commonly described as spherical nanoparticles smaller than 10 nm [64,98,99] composed of an sp^2 -hybridized carbon core and a shell passivated by functionalized sp^3 carbon atoms [47,100,101]. The CNDs core is usually 2–4 nm in size [102–104] and can be either structurally disordered (amorphous) or have

a crystalline structure, which is mostly graphitic (CQDs) [62,105–110], although carbon nitride C_3N_4 cores have also been reported [111–114]. The lattice spacing in the CQDs core was found to be ~ 0.330 , ~ 0.208 , 0.194 , 0.186 , ~ 0.210 nm which agrees well with (002), (102), (104), (105), (100) diffraction planes of sp^2 graphitic carbon, respectively [115–120]. Similarly to GQDs, the CNDs can be doped with nitrogen (pyrrolic, pyridinic, graphitic), phosphorus (P-O binding), sulphur (C-S-C units) and boron (B-C, B-N, B-O bonding) [120–129]. Depending on the synthetic procedure, the shell contains various oxygen- or nitrogen-containing functional groups, typically the polar $-CHO$, $=O$, $-COOH$, $-OH$, $-CONR_2$ or $-NH_2$ groups [130,131]. These functionalities conduct interactions with the surrounding and thus significantly affect the dispersibility of CNDs in solvents and the pH-dependency (protonation of carboxylic and other acidic groups, pyridine and pyrrolic nitrogens, etc.) of optical properties of CDs [132], which are essential features for the sensing applications based on the ability of CDs to interact with specific chemical species. In addition, because of this complexity, many subsequent chemical covalent and non-covalent surface functionalization pathways, e.g., copolymerization and sulfonation reactions, amidic coupling, and esterification, can occur in CNDs systems [130].

In 2015, MFs as highly fluorescent ingredients were identified in samples of bottom-up synthesized blue-emissive CDs [29]. Since then, their structural arrangement and the role in PL of CDs have been heavily discussed and, from an experimental point of view, summarized in very recent reviews [33,72]. Structurally, MFs can be present in the interior of CDs [133], covalently bonded [134,135] or non-covalently attached [136] to the CNDs shell [137]. Starting typically from CA, CZA [138] and its derivatives have been identified as the main structural MF motifs responsible for the blue emission of CDs. Besides CZA, 1-(2-aminoethyl)-5-oxo-1,2,3,5-tetrahydroimidazo[1,2-a]pyridine-7-carboxylic acid (ATPCA) [139], methylenesuccinic acid (MA) [140], 5-oxo-3,5-dihydro-2H-thiazolo[3,2-a]-pyridine-3,7-dicarboxylic acid (TPDCA) [141], 5-oxo-3,5-dihydro-2H-thiazolo[3,2-a]pyridine-7-carboxylic acid (TPCA) [142], IPCA [29], green fluorophore 4-hydroxy-1H-pyrrolo[3,4-c]pyridine-1,3,6(2H,5H)-trione (HPPT) [143], N-(2-hydroxyethyl)-2-oxo-1-vinyl-6-(vinylamino)-1,2-dihydropyridine-4-carboxamide (NVDPA) [144] were the most reported MFs (Fig. 2). Nevertheless, there is still plenty of room for deeper investigation into the chemical nature of molecular intermediates that are formed during syntheses of CDs. There are very likely more MFs contributing to CDs PL being produced, e.g., as side products during synthesis of CDs from carbohydrates [145]. Importantly, it was also shown that MFs tend to form J-type (a head-to-tail arrangement of dimers) and H-type (dimers in a face-to-face sandwich-type arrangement interacting via π - π stacking) aggregates [146–148].

2.1.3. Carbonized polymer dots

CPD is a hybrid structure composed of a majority of organic polymer chains and probably a small fraction of an “inorganic” carbon core. One important parameter to evaluate the structure of CPDs is the carbonization degree, where CPDs can be regarded as CDs of low carbonization degree or fluorescent non-conjugated polymer nanoparticles with high crosslink degree. Some oligomers, polymers, and cross-linked polymers are the main components in these dots. Due to their structure, CPDs may not inherit all properties of CDs, such as, quantum size effect, stability against photobleaching, etc. [49]. Nevertheless, it is hard to clearly describe the specific chemical structure of CPDs due to their polydispersity and irregular chemical compositions. The polydispersity originates in the randomness of events during the preparation steps. Quick hydrothermal and microwave assisted condensations of monomers are the most common ways for CPDs fabrication. CPDs can also be prepared from the monomers or non-conjugated polymers by con-

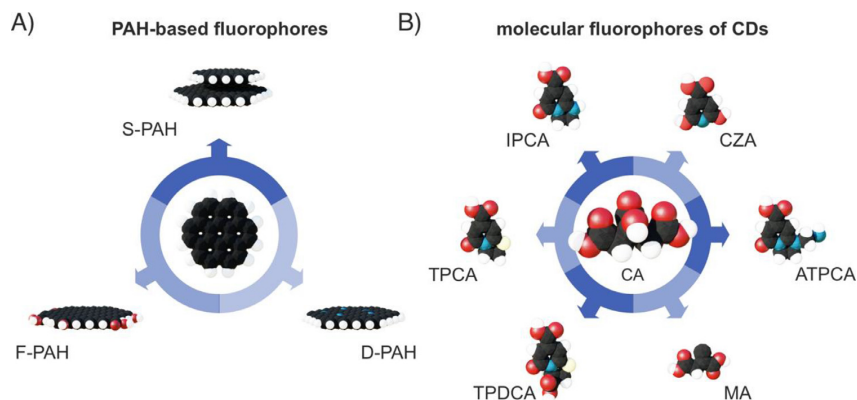


Fig. 2. The commonly reported (A) PAH-based fluorophores and (B) some typical molecular fluorophores present in the final products of the CDs synthesis. S-PAH: stacked PAHs; F-PAH: functionalized PAHs; D-PAH: doped PAHs; CA: citric acid; IPCA: 5-oxo-1,2,3,5-tetrahydroimidazo[1,2-a]pyridine-7-carboxylic acid; CZA: citrazinic acid; ATPCA: 1-(2-aminoethyl)-5-oxo-1,2,3,5-tetrahydroimidazo [1,2-a]pyridine-7-carboxylic acid; MA: methylenesuccinic acid; TPDCa: 5-oxo-3,5-dihydro-2H-thiazolo[3,2-a]pyridine-3,7-dicarboxylic acid; TPCA: 5-oxo-3,5-dihydro-2H-thiazolo[3,2-a]pyridine-7-carboxylic acid. Carbons are represented in black, hydrogens white, oxygens red and nitrogens in blue balls.

densation, crosslinking, assembling, or slightly carbonization processes. According to differences in raw materials, CPDs could be further classified into two classes, including the one prepared from a small molecule precursor and the one from a polymer precursor (polymers with/without small molecules). Many polymer-like features are also reflected in CPDs, such as the abundant reactive functional groups, the polydispersity of products, the highly crosslinked network structure [48]. The favorable building blocks for these bottom-up synthetic methods are molecules with multiple $-\text{COOH}$, $-\text{OH}$, or $-\text{NH}_2$ groups, such as CA, glucose, amino acids [29,49]. The presence of these functional groups is essential for the proper internal organization of CPDs and these $\text{C}=\text{O}$, $\text{C}=\text{C}$ bonds with large numbers of residual hydroxyl groups are commonly found in their IR spectra [149]. Other suitable precursors for CPDs are linear or branched water soluble polymers [150], biomass [151], polyvinyl alcohol [152], etc. A simple and green route to synthesize water-soluble and nitrogen-doped polymer-like carbonaceous nanospheres with a uniform size of ~ 70 nm on a large scale through hydrothermal treatment of cocoon silk in water was reported as well [153].

2.2. Photoluminescence properties

2.2.1. Phenomenological insights into PL

Despite the not fully resolved structure of CDs, various phenomenological PL mechanisms have been proposed based on a strong experimental evidence with a support of simplified theoretical models (see also Fig. 3): (i) QCE related mainly to the size of π -conjugated domains in the CD core; (ii) the defective and/or surface state PL, which is determined by doping effects, hybridization of the carbon backbone and surface functional groups; (iii) the molecular PL, which is imprinted solely by fluorescent molecules attached to the surface and/or interior of the CDs; and (iv) the crosslink-enhanced emission (CEE) effect [34]. In addition, owing to small singlet-triplet energy splitting (ΔE_{S-T}) in CDs, the involvement of triplet states can lead to long-time PL processes such as (v) thermally activated delayed fluorescence (TADF) and (vi) phosphorescence (P; see Fig. 3A for a detailed schematics) [15,60,61,114]. In principle, all these mechanisms can occur in individual CD subclasses and can take place in a cooperative manner, what makes the interpretation of PL characteristics such as QYs, (multi-)exponential PL decay, sensitivity to photo-bleaching and environmental effects an extremely challenging task. Several

reviews covering the topic of PL of carbon nanostructures were published [15,34,38,60,101,154,155], therefore we survey here only briefly the major experimental observations. We focus first on single sheets of QDs demonstrating the PL principles, followed by more complex CNDs and CPDs.

2.2.2. Graphene quantum dots PL

Unlike pristine graphene, the QGDs as small finite size graphene fragments exhibit a non-zero band gap rendering unique optical and electronic properties. Owing to the size diversity, possible heteroatom doping, surface functionalization and presence of various types of defects, PL of QGDs can range from UV, through visible up to near-IR region and exhibit different PL characteristics (QY, PL decay, sensitivity to the surrounding, etc.).

PL of QGDs is mostly governed by core states in the conjugated π -domains and the QCE. Similar to other semiconducting quantum dots (QDs) of nanometer scale, the QGD edges influence the electronic structure of the conjugated sp^2 domain. Due to light atoms, QGDs have larger band gap than other similarly sized semiconducting inorganic QDs [34]. The band gap of the core states decreases with the increasing QGD size, and a red shift of the emission band occurs, up to the point where the effect of shape and edge dominates over QGD size [41]. Analysis of the concentration dependence of PL of small polycyclic aromatic hydrocarbons (PAH) dispersed in poly(methyl methacrylate) (PMMA) revealed that the band gap in QGDs can also be reduced by stacking effects that can lead to self-trapping of excitons and excimer formation in the PAH network [156]. Also, efficient intersystem crossing (ISC) related to low ΔE_{S-T} values in the core states was observed, and thus the QGDs can exhibit TADF and phosphorescence [157]. The former results from a reversible S-T transition, in which the long-living triplet excitons (due to a spin-forbidden $T_1 \rightarrow S_0$ transition and small ΔE_{S-T}) undergo the reverse ISC (RISC) leading to delayed fluorescence from the S_1 state with lifetimes prolonged by few orders of magnitude compared to ordinary fluorescence. In the case of low-efficient RISC and provided that the triplet excitons are not deactivated non-radiatively, the spin-forbidden $T_1 \rightarrow S_0$ transition accompanied with photon emission (phosphorescence) occurs on much slower timescales (typically microseconds).

Apart from the intrinsic emission from the QGD core, surface states actively participate in the PL [78]. After excitation, intrinsic PL can be reduced by non-radiative decay into these surface states and a red shift in emission wavelengths can be observed

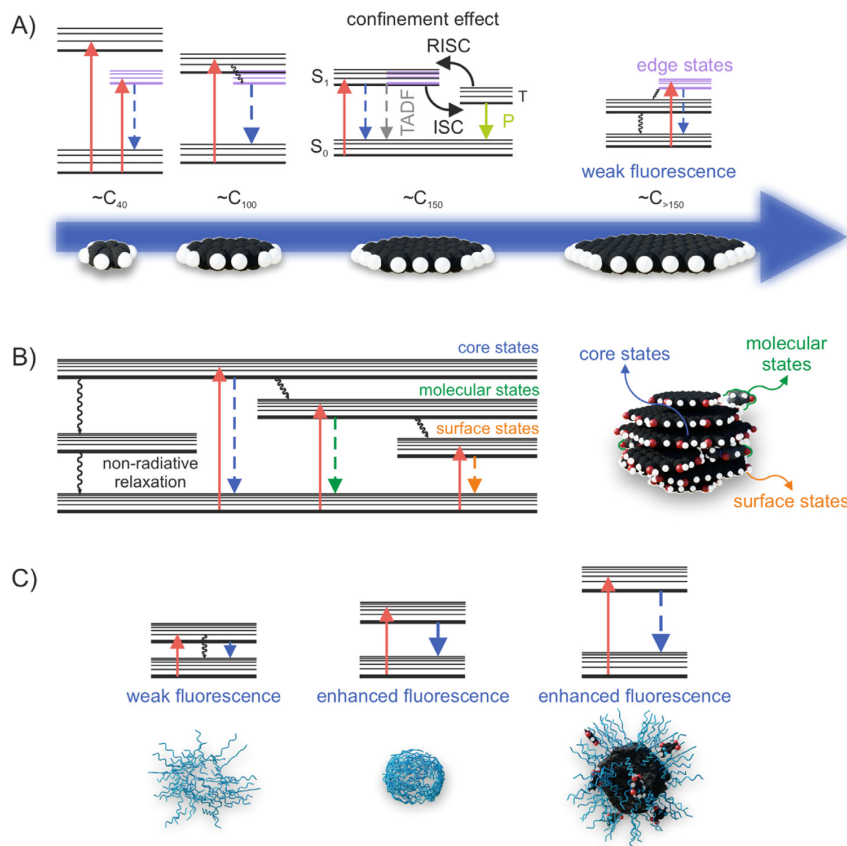


Fig. 3. Possible PL mechanisms being present in CDs. (A) the quantum confinement effect (QCE) related mainly to the size of π -conjugated domains in the CD core. (R)ISC refers to (reverse) intersystem crossing, which can lead to thermally activated delayed fluorescence (TADF); P refers to phosphorescence; (B) the multi-component PL typical for CNDs including the molecular PL; and (C) the crosslink-enhanced emission (CEE) effect (blue lines in bottom panel represent polymers, black carbonized regions). Bold and regular horizontal lines represent electronic and vibrational energy levels, respectively. Only radiative and non-radiative decays are displayed as straight and wavy lines, respectively.

[34]. The emission spectra of moieties containing $-\text{COOH}$ and $-\text{NH}_2$ groups can also be affected by protonation state by modulating pH [37,101]. Such dependence of PL properties on the surface chemistry gives us the possibility to tune the PL characteristics by changing the surface groups.

2.2.3. Carbon nanodots PL

One of the most fascinating features of CNDs is their common excitation-dependent PL that can be attributed to their complex structures and selective excitations of individual structural features. Not only intrinsic or surface emission of single GQD is present, but CND layered structure allows selective excitation of each differently sized layer with specific chemical composition.

Consistently with QCE, a red shift of the core PL with increasing CND size was usually observed [34,158]. This can be explained in terms of sizes of individual layers. However, an opposite trend was also observed, where either PL wavelength did not correlate with the CND size, or increasing the size caused a blue shift [159]. The individual layers are made of imperfect graphene-like sheets (GQDs) and thus the actual PL may not be dependent on the CND diameter, but on the size of the conjugated sp^2 matrix. Therefore, one need not see a perfect size-emission wavelength dependence in such complex structures such as CNDs.

Surface states play a dominant role in PL of CNDs. Although the excitation can affect electrons in the intrinsic band of the sp^2

domains, emission occurs mostly after relaxation to the surface states [34,160]. As the surface of CNDs is often oxidized, higher amount of O functional groups on the surface can create more surface defects and therefore bring a red shift in the emission spectra based on the same principle as in the case of simple GQDs. Such a shift is dependent on the amount of surface functional groups [102]. Moreover, some O- and N-containing functional groups can (de)protonate in response to a change of pH of the environment. The pH dependence of PL is a widely reported phenomenon for oxygenated GQDs and change of pH may end up in quenching of PL [161–163].

Fluorescence decay in CNDs is often multicomponent, suggesting multiple decay pathways [164]. Apart from multiple absorption and emission centers, one or more of the pathways are often related to non-radiative low energy levels, called trap states [75]. Their origin is not fully resolved, but it is hypothesized that they come from surface states and/or defects arising from imperfect passivation of the CND surface [34,75,154,155,165,166]. The surface passivation can thus not only modulate the wavelength of the emission, but also hinder or reduce the radiative decay.

Doping of CNDs with N is the most common because it can be easily achieved by synthesis using N-containing precursors. The emission wavelength can be tuned by the type, concentration and position of heteroatoms [87]. Both red and blue shifts caused by individual N forms were observed [101], which can be attributed

to a dependency of this effect on N type and position. For example, graphitic N-doping was shown to cause a red shift the fluorescence of CQDs [87]. The N-doping often significantly enhances fluorescent QY of CNDs, which is another very useful advantage of introducing heteroatoms into the CDs structure [101].

2.2.4. Molecular state PL

Experimental evidence of an intense excitation-independent long-lived component in PL spectra of some CNDs prepared by bottom-up synthetic procedures indicated the presence of molecular PL centers similar to common organic fluorescent dyes [29,47,72,167]. The enhancement of the PL component observed under mild reaction conditions and attributed to low-molecular mass structures was in line with the proposed mechanism of the formation of CNDs from molecular precursors, according to which the condensation phase is followed by carbonization, and the latter can be suppressed by using shorter reaction time and/or lower temperature [47]. Undesirable PL photobleaching of the CNDs synthesized under mild conditions after exposure to the UV radiation further corroborated the presence of MFs [47]. Importantly, it was observed that the highly intense molecular state PL signal was generated not only by CD solutions filtered through dialysis bags, but also by the solution outside the dialysis bags, indicating that the PL centers of the free molecules that passed from the bag and those incorporated in the CD structure (on the surface and/or in the CD interior) were identical [47]. Although it is tempting to attribute the PL signal of the solution of MFs to individual (solvated) molecules, several studies in past years supported the idea of MFs closely interacting with CD structure, possibly directly incorporated inside [72,146].

2.2.5. PL of CPDs

Besides abovementioned mechanisms common for CNDs, CPDs PL possess additional PL features related to the CEE effect. Simply speaking, polymer chains surrounding the carbonized core can contain potential PL centers, e.g., secondary or tertiary amine groups. Without being constrained in CPDs, such centers exhibit weak fluorescence (Fig. 3C), because of strong non-radiative vibrational relaxation [168]. On the other hand, if they are spatially constrained in CPDs, the vibrational relaxation is suppressed, which significantly increases the PL intensity, which differs from MFs that exhibit PL even without spatial confinement.

To sum up, given the structural diversity of CDs and the complexity of PL mechanism, there is an urgent need for reliable multi-scale theoretical models developed by using state-of-the-art computational tools. It also needs to be mentioned that the diversity of applied (not always adequate) methods makes the mutual comparison of available theoretical data as well as their confrontation with experiment very difficult. A consistent computational protocol relying on best available theoretical methods tailored and tested for specific problems reflecting the multi-scale character of the structure and (photo)chemistry of CDs would be highly welcome.

3. Theoretical methods for the description of optical absorption and emission processes in CDs

3.1. Ground state electronic structure of PAHs

The popular systems to model CDs are PAHs of medium or larger sizes with different shapes, including polyacenes, circumacenes and periacenes. Depending on the size and molecular structure, the ground state (GS) wavefunctions of PAHs may possess biradicaloid (open-shell) character and/or sizeable contribution of double excited electronic configurations. A characteristic feature of these situations is the presence of several resonance structures

whose contributions to the GS wavefunction increase with the increasing size of the systems [169–172]. A useful classification tool is given by Clar's rule [173,174] stating that for benzenoid PAHs the structure with more aromatic sextets possesses higher aromatic stabilization energy. Thus, the structure with the valence bond structure with more Clar's sextet rings, although gaining radical character, can become equally or more stable than a closed shell structure. This can be exemplified by resonance structures of heptacene (Fig. 4A). The closed-shell electronic configuration (Kekulé structure) exists only if one Clar's sextet is present, while two or more Clar's sextets can coexist only with the structure with a biradical character. Starting with heptacene the latter resonance structures are more stabilized than the closed-shell structure, resulting in the radical character and reactivity of higher member of acenes [169,171].

Fig. 4B (see also Ref. [176]) illustrates another example in which doping with heteroatoms can introduce the radical character in PAHs electronic structure. The most stable resonance structure of pristine pyrene is the Kekulé structure with two Clar's sextets. N-doping in graphitic positions, in which the N-atom contributes with two electrons to the π -space, changes the character of the electronic structures depending on their mutual position. The Kekulé structure is obtained for pyr-graphitic-1 as for pyrene but no Clar's sextet can be formed. The same situation is observed also for pyr-graphitic-2. This configuration is in resonance with the structure containing one Clar's sextet but at the expense of biradicaloid character. On the contrary, in pyr-graphitic-3 neither Kekulé structure no Clar's sextet can exist without biradicaloid character. Other examples of the biradicaloid character of the GS wavefunctions which appears upon functionalization of PAHs are documented in Refs. [177–179]. With increasing size of the systems, the energy gap between the occupied and virtual orbitals is stepwise reduced and also the excited state (ES) configurations can contribute increasingly to the originally closed-shell GS wavefunction. Importantly, the biradicaloid character and doubly excited configurations do not only affect the GS but also ESs and should be carefully considered when selecting an adequate computational method.

3.2. Strategy for computations of electronic excitation and emission processes

Computational modeling of ESs behavior of CD, in particular their PL properties, is based on several steps displayed in Fig. 5 with the focus on singlet electronic states.

The interpretation of CD optical spectra starts with the characterization of absorption spectra, i.e., the characterization of electronic transitions starting from the GS, of excitation energies and oscillator strengths. Prediction of the luminescence properties relies on the validity of Kasha's rule stating that the molecule preferentially emits photon from the lowest ES of a given multiplicity [180]. In other words, the emission wavelength of MF is independent of the excitation energy. Kasha's rule can be explained by competing non-radiative relaxations via internal conversion from higher ESs (S_2 in Fig. 5) to the S_1 state with direct radiative emission from a higher ES. The former processes occur usually at significantly shorter timescales and lead to a population of the S_1 state first, from which then the radiative emission occurs. The theoretical characterization of PL thus includes finding the geometry of the S_1 energy minimum and, in the simplest case, determination of the vertical $S_1 \rightarrow S_0$ emission energy and radiative decay probability. More sophisticated methods include the nuclear motion explicitly, as mentioned below. The PL $S_1 \rightarrow S_0$ competes with non-radiative internal conversion to S_0 , which appears most prominently, but not only, at the crossings of S_1 and S_0 states (Fig. 5). Another

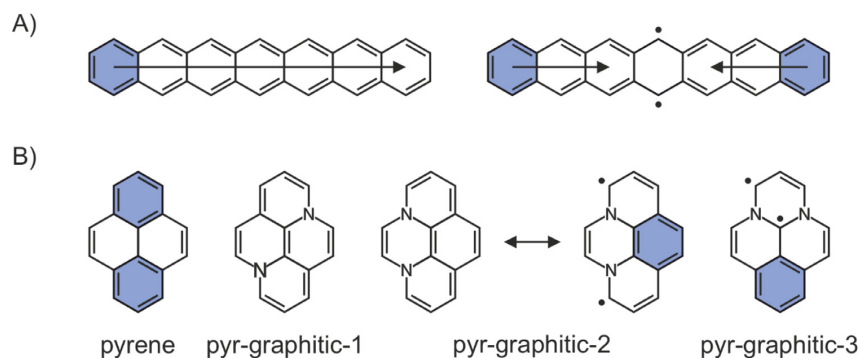


Fig. 4. Resonance structures of (A) heptacene and (B) nitrogen doped pyrene in graphitic positions. The arrows in heptacene structures indicate the movement of the Clar's sextet along the heptacene structure. The Clar's sextet refers to six π -electrons localized in a single benzene-like ring separated from adjacent rings by formal CC single bonds; no neighboring benzene-like molecules can share π -electrons simultaneously to form their own sextets, i.e. no neighboring Clar's sextet can be drawn [175]. Black dots represent radicals. Reprinted with permission from ref [176]. Copyright 2020 the Royal Society of Chemistry.

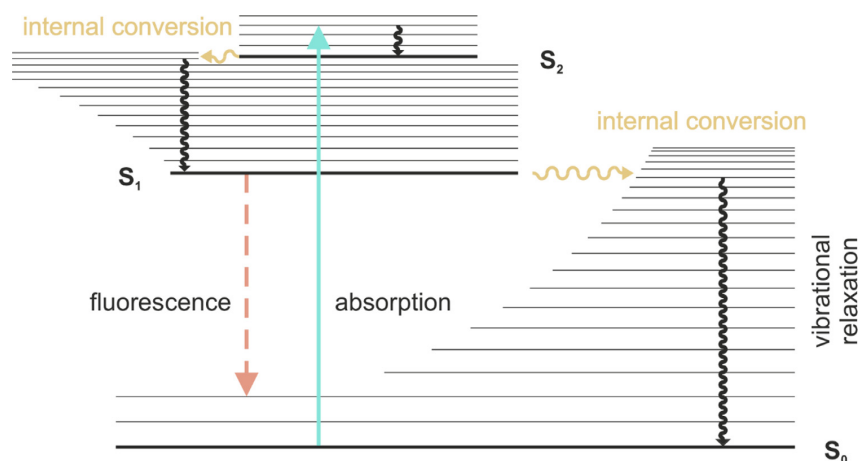


Fig. 5. Selected radiative (straight vertical lines) and non-radiative (wavy lines) processes involving electronic (bold horizontal lines) and vibrational (regular horizontal lines) states. Singlet states are shown only. **Note:** Thick lines represent zero-point vibration energies (ZPVE) levels.

non-radiative process competing with fluorescence (not shown in Fig. 5) is the ISC to a triplet state.

A correct characterization of spectra requires a balanced treatment of all relevant ESs and the GS along the ESs channels, including states silent in the absorption spectra since they can significantly influence the PL properties via non-radiative transitions. The complexity of PL spectra character can be further increased by a possible formation of dimers, trimers or higher aggregates.

3.3. Classification of computational methods

Computational tools applied in the field of CDs range from highly accurate QM methods suitable for detailed characterization of the electronic structure and optical properties of small and medium-size fluorophores, through computationally more efficient but still reliable QM approaches based on density functional theory (DFT) [181,182] enabling to study larger systems (typically hundreds atoms), and semiempirical (SE) methods, see Fig. 6. Among the SE approaches, unrestricted natural orbital-configuration interaction (UNO-CI) calculations [30], Zerner's intermediate neglect of differential overlap (ZINDO/S) [183] and PM7 [184] have been used to study the electronic structure, optical properties and/or chemical reactivity of CDs [185–188]. More advanced density-functional-based tight binding (DFTB) method [189–191], the semiempirical

QM method defined within the DFT framework, uses smaller number of empirical parameters compared to other SE methods and scales 2–3 times faster compared to DFT methods. DFTB method can be classified as a tight-binding method parametrized from DFT calculations [192]. DFTB approach in combination with MD simulation has been successfully used to model the mechanism and kinetics of single-walled carbon nanotube (SWNT) nucleation using metal-carbide nanoparticles as precursors [193] and the formation of graphene [194] from acetylene via radical mechanism. Finally, MM (also termed empirical or empirical potential method) can handle hundreds or thousands of atoms but it does not provide any insight into electronic structure of the model system. It can be efficiently used to study conformational behavior and classical molecular dynamics (MD) of large systems including CDs models [195,196]. Both QM and MM methods can also be combined to study complex molecular systems in hybrid/multiscale molecular models (e.g., QM/MM), which divide the subjected systems into parts/layers, which can be treated at various levels of computational chemistry.

3.3.1. QM methods

The QM methods evaluate electronic structure of molecular systems in terms of wavefunction or electron density and can be applied for calculations of both GS and ESs. They can be classified ac-

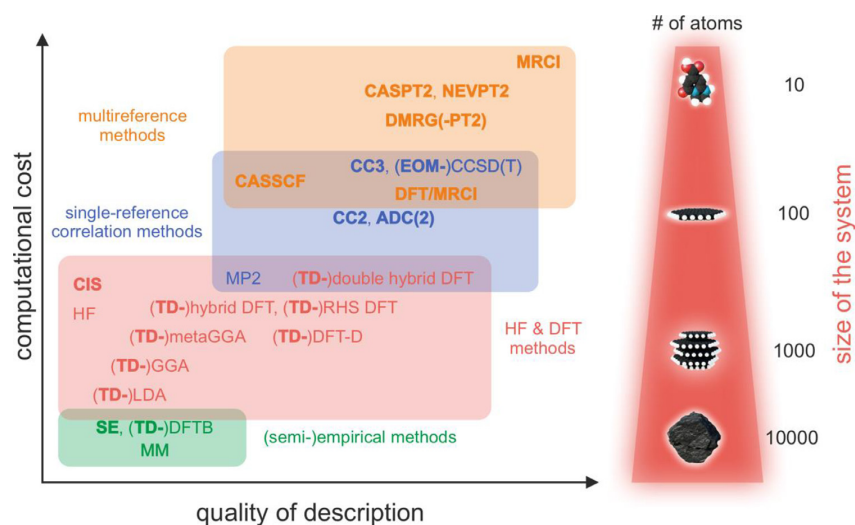


Fig. 6. Overview of commonly used computational methods for the description of structure and optoelectronic properties of CDs. The methods are horizontally placed according to their quality of electronic structure description and vertically according to their computational cost. The right panel shows size of system for which these methods can be approximately applied. All methods can provide information about structure, while methods highlighted in bold can also be used for the description of excitation/emission properties.

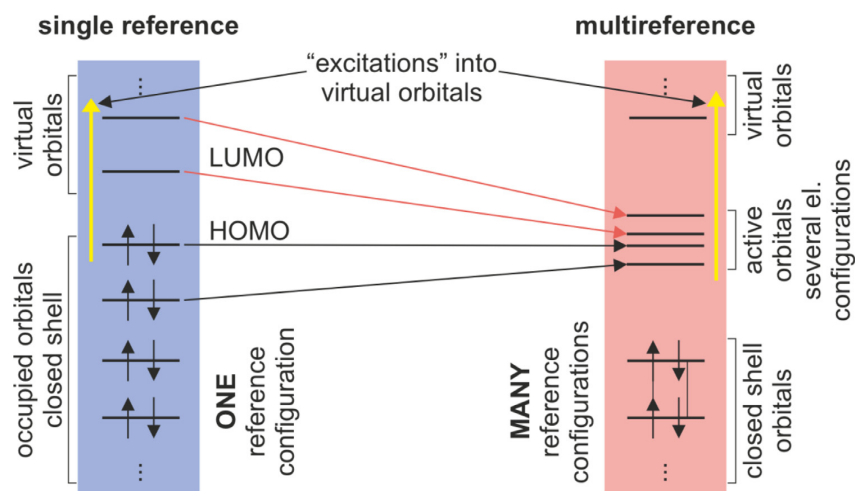


Fig. 7. Characterization and comparison of single reference versus multireference schemes.

according to the description of the wavefunction as single reference (SR) and multireference (MR). For extended reviews with focus on MR methods see Refs. [197] and [198]. The basic concepts of SR reference vs. MR theory are displayed in Fig. 7.

In the SR approach only one reference configuration, usually the Hartree-Fock (HF) determinant, is considered as a starting point. In the case of closed-shell singlet (left part of Fig. 7) the electron excitations from the reference doubly occupied into virtual orbital spaces are considered. The wavefunction is then obtained by different methods among which variational, e.g., CIS [199], or perturbational approaches, e.g. MP2 [200], are popular choices. Other methods like coupled-cluster (CC) theory can be used as well [201]. The validity of such an approach relies on the assumption that the HF determinant is a good starting point and that this electronic configuration dominates the GS wavefunction. In the MR approach, the orbitals are divided into the closed-shell, active and

virtual subspaces (right part of Fig. 7). The reference wavefunction is constructed from a set of electronic configurations in which the closed-shell and virtual orbital spaces are kept doubly-occupied and empty, respectively, while in the general case, all possible occupations within the active orbital space are allowed [202], resulting in the so-called complete active space (CAS) approach. All electronic configurations generated within the CAS can contribute to the reference wavefunction. The total wavefunction is then formed by excitations out of the above reference wavefunction. The higher-order correlation effects are accounted for in the subsequent treatment, e.g., using perturbation theory in CASPT2 method [203,204], the widely used method to describe ESs of small and medium sized systems or MR configuration interaction (MRCI). These MR methods are generally applicable and can reliably describe bond breaking processes or biradicaloid systems as discussed in Fig. 4.

As an alternative to wavefunction-based approaches, DFT methods have become very popular due to their excellent trade-off between accuracy and cost. In DFT, the electronic energy is expressed as a functional of the GS electron density. Owing to the unknown exact form of the exchange-correlation functional (XCF), a plethora of DFT methods is available nowadays [205], and novel XCFs are still under development. Although it is not straightforward to assess the quality of a particular XCF, there is a clear evidence that the accuracy of provided results systematically increases with improving the physical content of XCFs. The increase of an overall quality of XCFs can therefore be expressed in the form of a metaphorical Jacob's five-rank ladder introduced by Perdew [206] starting with XCFs based on the local density approximation (LDA) as the lowest rank and ending with so-called double hybrid XCFs at the top rank. Range-separated hybrid (RSH) functionals, e.g., LC-BLYP, ω B97X-D, LC- ω HPBE and CAM-B3LYP [207–210], represent a very important extension of hybrid XCFs constituting the 4th rank of the Jacob's ladder as they have been successfully used for studies of extended π -conjugated systems as well as ES calculations [211]. RSH functionals include an increasing fraction of the exact exchange when the interelectronic distance increases, thus significantly improving the description of charge-transfer (CT) transitions [212]. In the context of investigations of CDs, it is worth noting that the standard functionals, including hybrid XCFs such as B3LYP and PBE0, fail to properly describe dispersion interactions. Therefore, various flavors of DFT-based methods including dispersion corrections have been developed. According to the treatment of the dispersion, they can be classified in a ladder-like manner [213] analogous to the Perdew's ladder of XCFs. It should be noted that inclusion of dispersion interaction is required for correct description of noncovalent complexes and some models of CDs based, e.g., on stacked PAHs.

The most popular method to describe the ESs of CDs is DFT-based linear-response time-dependent density functional theory (TDDFT) [214] approach due to its favorable cost-performance ratio. A reliable use of such approach requires a careful benchmarking, as discussed in the recent study of Grotjahn and Kaupp [215]. Major difficulties in the TDDFT approach result from its incapability to properly describe polyradicaloid character of the GS wavefunction, the failure to include doubly ESs [216] due to the adiabatic approximation of the time-dependent correlation-exchange potential and, in several cases, to correctly describe the ES ordering of PAHs [171,217,218]. These problems could be only partially fixed by introducing modifications in the DFT functionals [219–223]. In particular, considerable improvement of the ordering of ESs in PAHs has been achieved with the inclusion of long-range effects [224], as exemplified by comparison of results obtained with standard B3LYP functional [225,226], and its extension by the TD-Coulomb attenuating method-B3LYP (TD-CAM-B3LYP) [210]. Despite of that, the TDDFT approach has proven to provide useful information on the optical spectra in good agreement with more sophisticated methods and with experiment for several PAHs.

An alternative approach among the SR methods which reasonably scales with the size of the system is the wave-function based approach CC method, the second-order approximate coupled-cluster (CC2) [227], the algebraic diagrammatic construction to second order (ADC(2)) [228], and its variants [229], which provide reliable results and a well-balanced description of the ESs of relatively large PAH systems [224,230]. However, they are also not capable of describing doubly-ESs as explained in Ref. [231]. Even more accurate description of electron correlation taking into account the effect of triple excitations can be obtained by using the third-order coupled-cluster (CC3) [232] or equation-of-motion (EOM)-CCSD(T) methods [233].

The MR approach significantly improves the reliability of the ES calculations. The popular CASSCF/CASPT2 method has been used

for these purposes [172,234]. Its use is, however, limited due to rapidly increasing computational demands with the molecular size. An alternative, cost-effective multi-reference method based on perturbation theory, the n -electron valence state perturbation theory to the second order (NEVPT2) [235,236] can be used. This method does not significantly exceed the computational expense of SR methods, still providing reliable results of excitations energies of PAHs [224,237]. A number of promising strategies have emerged recently, among which the density matrix renormalization group (DMRG) [238] is probably the most popular and already used for the ES calculations of CD models [239–243]. An interesting alternative approach is the density functional theory/multireference configuration interaction (DFT/MRCI) method [244], a parametrized approach which treats the dynamic electron correlation and multi-reference character of the states at DFT and MRCI levels, respectively [245–247]. As shown in the literature [224,244,248], this approach correctly describes the ordering of the ESs with calculated excited energies in an excellent agreement with experiment.

Fig. 8 illustrates the performance of SR (TD-B3LYP, CAM-TD-B3LYP and spin-opposite scaled second-order algebraic diagrammatic construction (SOS-ADC(2)) and MR (DFT/MRCI and NEVPT2) methods to compute the first bright ES for a series of pyrene- and coronene-based PAHs [224]. Since all states have the same character, resulting from the combination of HOMO–1/LUMO and HOMO/LUMO+1 transitions, all methods give a similar monotonic decrease of excitation energies with increasing number of fused benzene rings, showing a good performance of SR methods in this particular case. Extrapolated values to infinite number of carbon atoms give good agreement with experimental absorption peaks for the three lowest bright states gives of a GQD with 168 carbon atoms [249].

The evaluation of emission spectra includes finding of the minima of the S_1 state (following Kasha's rule). The vertical $S_1 \rightarrow S_0$ emission energies (Fig. 5) can be obtained with the SR approaches for most cases. These methods have, indeed, been recently used to explain unusually large Stokes shifts observed in the emission spectra of CDs by emission from excimer aggregates formed by stacking rather than from the monomer emission [250].

3.3.2. Treatment of environmental and dynamical effects

The optical properties of CD fluorophores can be significantly affected by their environment, being the fluorophore's neighborhood within the CD and/or solvent. Methodologically, the environmental effects can be modeled by either implicit or explicit approaches. In the former, the solute molecule (i.e., a fluorophore) treated at the QM level occupies a cavity created in a homogeneous polarizable medium (continuum) which is described by relative permittivity and refractive index. The polarization interaction between the continuum and the solute needs to be evaluated iteratively, leading to the so-called self-consistent reaction field (SCRF) models. Several SCRF models have been implemented, differing in the construction of the cavity, the treatment of the electrostatic solute–continuum interactions, the inclusion of non-electrostatic contributions, etc. Popular models include the family of polarizable continuum models (PCM) [251], the solvation model based on density (SMD) [252], and the conductor-like screening model (COSMO) [253]. The main limitations of the continuum models lie in their inability to accurately describe specific interactions, such as hydrogen bonds, and more complex solvation shells. Importantly, the combination of TDDFT with the SCRF models in calculations of optical properties necessitates a careful treatment of the equilibration of the cavity charges with respect to the GS and ES electron densities [254]. In particular, in the case of absorption we need to comply with so-called *non-equilibrium regime* meaning that the slow components (arising from translations and rotations of the solvent molecules) are not equilibrated with the solute upon the excita-

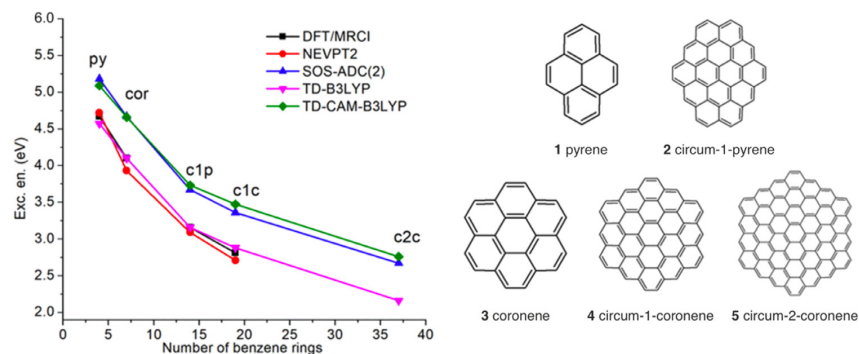


Fig. 8. The vertical excitation energies of the first bright ESs for pyrene (py), circum-1-pyrene (c1p), coronene (cor), circum-1-coronene (c1c) and circum-2-coronene (c2c) as a function of the number of benzene rings calculated with various methods. Reprinted with permission from ref [224]. Copyright 2019 AIP Publishing.

tion. On the other hand, to describe the emission we need to first *equilibrate* the cavity charges with the ES density (in the optimized ES geometry) and then apply the non-equilibrium setup to describe the vertical de-excitation. In both cases, the linear-response TDDFT approach in which the transition densities are used to determine the changes of the cavity charges upon the excitation can be applied [255]. However, the using of transition densities instead of state densities can introduce substantial errors, and therefore the state-specific approaches based on the one-particle TDDFT density matrix such as perturbative corrected linear response (cLR) [256], or vertical excitation method (VEM) [257] should preferably be used.

Whereas the implicit models can be efficiently used to describe the fluorophore-solvent interactions, they are not suitable for description of the heterogeneous environment of fluorophores embedded in CDs. Here, the surrounding molecules or CD subunits need to be considered explicitly. As the number of atoms increases rapidly with the system size, one needs to rely on an MM description of the whole system or combined QM/MM approaches, in which the part of interest (e.g., fluorophore) is treated at the QM level while the surrounding is described by MM.

The MM potential can also be used in classical all-atom MD simulations which offer important insights into the conformational dynamics of CDs. MD tracks positions of all atoms (usually also including solvent molecules) in time and provides unique and very fine in time (femtosecond) and in space (atomic) resolutions simultaneously. For example, MD simulations were performed to study dynamics and stability of CD models in water and *N,N*-dimethylformamide [196]. Very recently, incorporation of MFs (IPCA) into CD model structures was addressed by MD providing detailed insights into the mechanism of CDs formation [195]. Moreover, MD simulations can serve to provide an ensemble of conformational states that can be further treated by applying the QM methods for the “high-level” region while its surrounding can be described by a computationally less demanding “low-level” approach employing the ONIOM method with electrostatic or polarizable embedding approaches [258–260], as used for example in the studies of wild-type green fluorescent protein [261] and photo-switchable molecules in membranes [262].

3.4. Analysis of spectra

The excitation and emission energies, oscillator strengths and characterizations of the electronic transition are nowadays directly obtained from ES calculations using most available methods. However, these characteristics often do not provide all information necessary for a direct interpretation of experimental data. In order to resolve observed spectral bands, a treatment capable of vibrational

resolution (vibronic coupling) needs to be considered. Several approaches have been developed based on the assumption that the spectral band shape is determined by the GS nuclear-geometry distribution using the Franck-Condon approach [263–265], wave packet dynamics [266], path integral MD [267], and the nuclear ensemble approach [268,269].

The characterization important for understanding of ES phenomena needs to be completed by the analysis of ESs. For this purpose, the formalisms based on the transition density matrices, directly connected with physical observables independent of the wavefunction model [270–272] have been proposed. Among those, the natural transition orbitals (NTOs) provide a convenient way to give a compact representation of the orbitals involved in the transition [270,273]. Fig. 9A shows the NTOs calculated for the pyrene S_1 ES and the geometry differences between optimized geometries in the S_0 and S_1 states. The NTO plots in Fig. 9A show that the S_1 state consists of a combination of two electronic configurations. The NTOs, in particular bonding orbital contribution in the electron NTO of the first configuration, explain the shortening of the central CC bond of pyrene and the lengthening of the connected C–C bonds in the S_1 minimum.

4. Understanding CDs properties from theoretical studies

4.1. Modeling structure of CDs/Structural models of CDs

The trade-off between the accuracy and computational demands of theoretical approaches described in the previous section naturally puts limitations on theoretical models used to investigate the structure and optical properties of CDs. On the one hand, small models (usually containing less than 100 atoms) including single molecules (e.g., graphene fragments, doped and/or functionalized PAHs, and MFs) and small molecular aggregates (e.g., few layered PAHs, dimers or trimers of MFs) can be described by advanced quantum chemistry methods at high accuracy (Fig. 6). Although these models suffer from ignoring the structural complexity of CDs (see Section 2.1), they often provide very useful insights into the electronic structure of CDs or at least their structural components. In particular, they are indispensable for investigation of QGDs, because many important relationships can be revealed from the size and shape dependence of the properties of graphene-like fragments. The small models are also highly adequate for description of MFs, which are either non-covalently or covalently bonded to CDs and thus behave to a large extent as separated subunits, although very recent studies indicated their tendency to aggregate and/or co-assemble with PAH-like structures [195]. On the other hand, large structural models can cover many features of CDs, but their size heavily limits the available armament of compu-

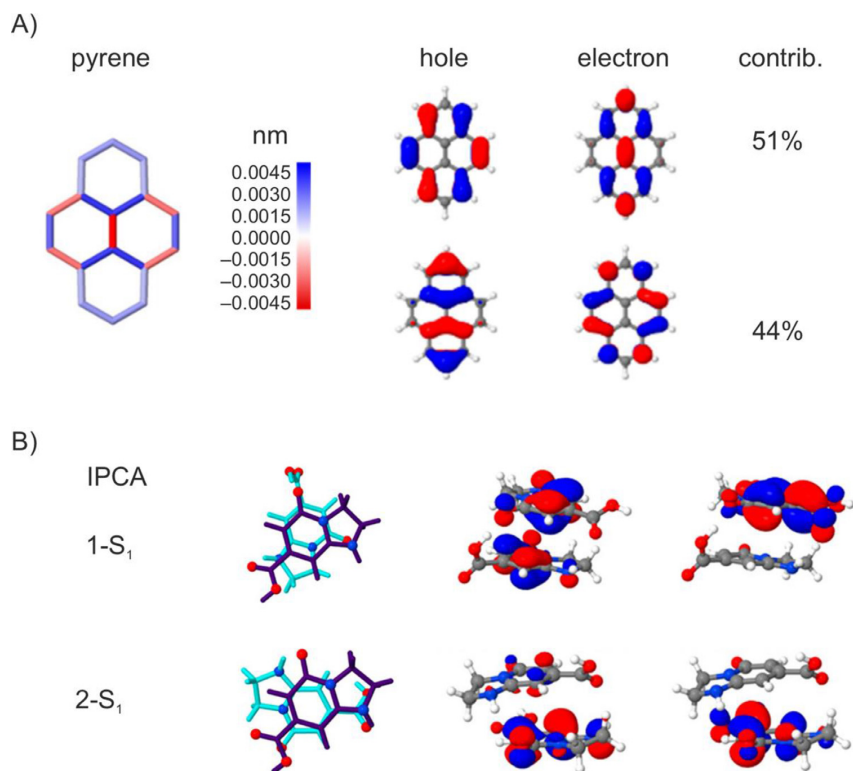


Fig. 9. A) Geometry differences (nm) between S_1 and S_0 states of pyrene and NTOs for the $S_1 \rightarrow S_0$ transition. Reprinted with permission from [250]. Copyright 2019 American Chemical Society. B) Structure of IPCA dimers and corresponding NTOs for $S_1 \rightarrow S_0$ transition. Reprinted with permission from [274]. Copyright 2020 American Chemical Society.

tational chemistry methods, due to enormous computational costs, and thus we are forced to turn to more approximate SE, MM and QM/MM approaches. In this section, we survey the structural models applied in theoretical studies of CDs and their subunits starting with single molecules, then we describe multilayer models and aggregates, and finally we discuss models addressing the amorphous nature of some CD cores and polymeric structure of an outer shell of CPDs.

4.1.1. Polyaromatic hydrocarbons (PAHs)

In general, PAHs represent a very diverse family of compounds differing by the size, shape and edge-arrangement (Fig. 10). Typically, they consist of 6-membered fused aromatic rings (so called alternant PAHs), but structures containing larger or smaller rings are also not uncommon [275]. The structure of small PAHs such as pyrene, coronene, circum-1-pyrene and circum-1-coronene, circum-2-coronene as small finite-size models of graphene and GQDs has been thoroughly surveyed in literature [276], and therefore here we only briefly summarize the features relevant to their optical properties. These models have also been used in methodological studies focused on benchmarking cheaper computational approaches by more rigorous methods in the context of calculation of optical properties of CDs core [250,277].

As discussed in Section 3, the character of the GS can be understood in terms of the Glidewell-Lloyd rule [278,279] and its particular case for benzenoid species formulated earlier by Clar [175], as also shown for alternant PAHs by Yeh *et al.* [280] Their findings also supported the observations that the radical character of PAHs

increases with increasing system size [281]. Moreover, the topology of the rings does matter; for instance, in the class of PAHs consisting of six-membered rings, coronene displays a stable singlet GS while triangulene and acenes exhibit strong (poly)radical character [280]. Also, stronger radical character was demonstrated for one-dimensional zigzag structures in comparison to armchair edges, although non-radical character up to structures with twenty aromatic rings was revealed [280]. Owing to the quasi-degenerate character of their GS wavefunctions, commonly used DFT methods may not be the best choice, and multi-reference approaches should be preferably adopted for calculations of large PAHs [169,170,172].

Larger single layer PAHs as model structures of CDs have been employed rather rarely [282]. Some interestingly shaped models of GQDs, i.e., not the common hexagonal ones, were studied due to their interesting tunability for specific purposes. Calculations on triangular and squared GQDs were studied with DFT methods, where triangular structure consisted of 4, 10, and 19 fused benzene rings functionalized with electron-donating hydroxyl groups or electron-withdrawing carboxyl groups or without functionalization, the square-like structure consisted of 4, 9, 10, 19 and 20 fused benzene rings [54]. Finally, a systematic study on a large variety of GQDs (~400 systems) of various sizes, shapes, topologies and edges has been performed to explore their linear and nonlinear optical properties, utilizing the strengths of both semiempirical and first-principles methods [283]. All models were passivated with hydrogen, and it was concluded that among the circular, triangular, stripe, and random shaped GQDs, those with inequivalent sublattice atoms always possess lower HOMO-LUMO gap (HLG), broad-

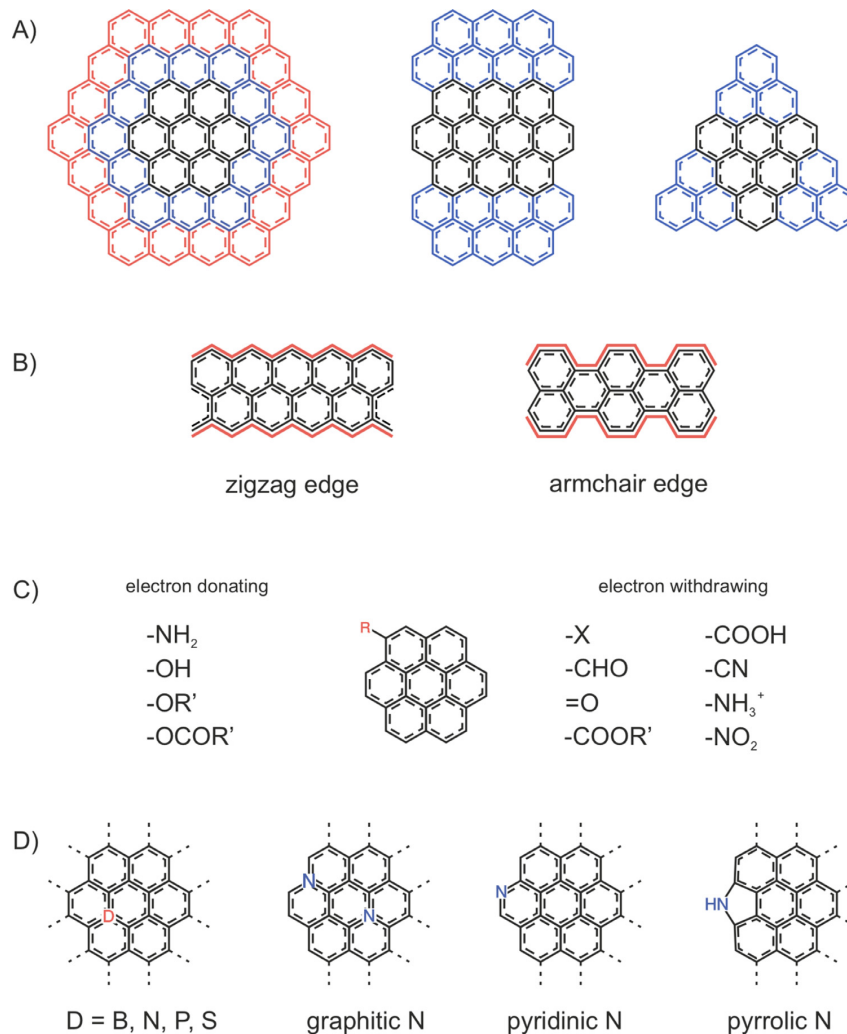


Fig. 10. Polyaromatic hydrocarbons (PAHs) can be sorted based on their: (A) - shape (hexagonal, squared, triangular). Coloring represents systematic extension of the structures. (B) - edge organization (zigzag or armchair). (C) - presence of particular functional groups. (D) - doping elements and their positions (graphitic, pyridinic, pyrrolic).

band absorption, and high nonlinear optical coefficients. Also, a majority of the GQDs with interesting linear and nonlinear optical properties had zigzag edges. Furthermore, it was also found that among the different GQD shapes, circular GQDs were the most stable ones, ribbon-like GQDs were the least stable and it was reported that systems with a smaller number of edge atoms are easier to be formed. Investigations of thermal stability of fully hydrogenated triangular and hexagonal PAHs employing classical MD simulations demonstrated that these PAHs are able to retain their planarity for simulated temperatures up to 1500 K, starting to degrade into amorphous nanocarbon for temperatures above 3000 K [284].

In one of the earliest studies Sk *et al.* [285] systematically investigated tunable PL properties of GQDs using DFT and TDDFT calculations. From a structural point of view, they covered wealth of potentially interesting structural features, e.g., different impact of armchair vs. zigzag edges, doping, defects in structure, edge-oxidation, and vacancies. They constructed many different models based on single-layer small PAHs as well as large benzenoid structures. Interesting but probably less realistic models consisting of

small sp^2 clusters joined by either sp^2 or sp^3 carbons were also used in their calculations to test the hypothesis that synthesized GQDs are mostly composed of isolated sp^2 clusters, which dictate the PL properties of GQD.

Although the PAH models made solely of carbon and hydrogen atoms are pertinent for understanding the structural features of GQDs, they are not suitable for describing the core structure of other classes of CDs (see Section 2.1), where doping and functionalization effects need to be taken into account. The properties of such modified structures are altered, and the degree of change is dependent not only on a chemical nature of dopant/functional groups, but also on their position in a structure, concentration, doping level, etc., as will be discussed later.

4.1.2. Oxygen functionalization

As O-containing functional groups are very common in synthesized CDs, the role of O-functionalization in PL properties of CDs has been studied, starting with small PAH models. In one of the earlier studies of systems with 7 and 12 aromatic rings and with four types of oxygen functional groups (i.e. $-\text{OH}$, $\text{C}-\text{O}-$

C, =O and –COOH), it was revealed that edge and basal functional groups induced structural deformation of otherwise perfectly planar structures, leading to presence of trap states in PL spectra [161]. Next, Sudolská *et al.* analyzed structures and absorption spectra of single-layered as well as multilayer (up to three layers) O-functionalized PAH models to capture interlayer physical phenomena such as the effects of stacking, excitonic coupling, and/or interlayer CT [211]. Pyrene and coronene functionalized by –OH, –COOH (including deprotonated forms), and C–O–C groups were used as one-layer building blocks. Later on, Feng *et al.* [286] calculated the HLG for differently sized PAHs (C₂₄, C₃₂, C₄₂ and C₁₃₂) containing O-functional groups thus extending the previously considered set to –CHO and –OCH₃ groups. It was found that that geometry distortions of the basal plane of PAHs due to functionalization were the dominating factor for tuning the HLG. DFT calculations revealed that –COOH functionalized PAH models were thermodynamically stable and hexagonal clusters with armchair edges had the highest stability among all hexagonal/triangular armchair/zigzag models. Also, it was observed that stability increased with the increasing number of carboxyl groups [287]. Larger models representing O-functionalized GQDs with C₁₃₂, C₁₆₈, C₁₇₀ atoms were also considered [288]. The effect of hydroxylation on PL properties of GQDs was studied on coronene, ovalene and circumcoronene [289]. It was demonstrated that a distortion caused by the –OH functionalization led to activation of electronic transitions which were symmetry forbidden in the flat arrangement, and that the distortion had an impact on the optical band-gap [289].

The effects of functionalization by a wide spectrum of substituents (–NH₂, –OH, –F, –CHO, –COCH₃, –COOH, –CH₃, –H) on electronic and optical properties of GQDs, represented by a circumcoronene monomer, were systematically investigated by employing a combined approach of DFT, GW approximation [290], and the Bethe–Salpeter equation (BSE) [291,292]. These works revealed that the functional groups containing a carbon–oxygen double bond (C=O) and –NH₂ groups were the most effective in tuning the optical properties of GQDs. Oxygen functionalized PAHs with stoichiometry C₁₆₀H₃₀O₁₅ were used to study the effects of vacancies and curvature. It was shown that the vacancies can significantly influence the structure and properties of CDs [94].

4.1.3. Nitrogen functionalization and doping

To elucidate the nature of the absorptive properties of CNDs, Sheardy *et al.* [293] very recently performed TDDFT calculations for twelve model structures, addressing also the oxygen and nitrogen functionalization/doping effects on their structure. Various types of defects in the CND aromatic structure were also considered in this study. Whereas the structures with only edge functional groups and structures with graphitic nitrogens in the lattice were fairly planar, the remaining structures with disruptive internal functional groups showed notable deviations from planarity [293]. The nitrogen functionalization of CDs surface was also studied using single layer PAH models of amino –NH₂ functionalized pyrene, perylene, hexabenzocoronene and one molecule having 41 aromatic rings [37,294,295]. It was shown that GQDs with edges fully covered by –NH₂ groups were very distorted from their planar geometry, thus decreasing their symmetry. To elucidate an influence of graphitic N-doping on CD absorption and fluorescence, the electronic and optical properties of computationally tractable models, i.e., pyrene and coronene molecules functionalized by –COOH groups, were evaluated [87]. Lu *et al.* considered a single layer O-functionalized N-doped (pyridinic, amidic and graphitic) coronene for investigation of the PL mechanism of supersmall CNDs [163]. Sarkar *et al.* presented a comparative computational study of N-doped (graphitic core, graphitic edge, pyrrolic, pyridinic positions) and O- and/or N-functionalized CDs with models of single and

double layer pyrene- and coronene-like molecules [296]. Sudolská *et al.* employed single and double layer models of N-doped pyrene-like molecules with –NH₂, pyridinic and pyrrolic moieties in order to mimic the chromophore diversity [297]. Here, the Boltzmann averaging of different suggested models was applied to simulate the absorption spectra of real samples (Fig. 11). It was based on the thermodynamically driven probability of formation of a particular isomer within one class (e.g., aminopyrenes) of possible functionalization of the edges and doping, and the final absorption and emission spectra were constructed as the sum of the individual isomers' spectra scaled by their Boltzmann populations (oscillator strength values of electronic transitions in a particular isomer *i* were weighted by the respective Boltzmann population). Furthermore, Fig. 11 shows that the calculated absorption and emission spectra of –NH₂ functionalized PAHs can provide insights into a role of functionalization on experimental absorption and emission spectra of CDs.

A detailed investigation of graphitic and pyridinic doping addressing the effects of the number and positions of nitrogen atoms in pyrene models using also high level methods (including DLPNO-CCSD(T) and DFT/MRCI) was recently reported by Shao *et al.* [176]. Their thorough analysis employing also qualitative tools (the valence bond theory, Clar's rule, HOMA index for assessing the aromaticity, etc.) enabled to rationalize relative stabilities of different isomers, and also respective shifts in the UV spectra. A strong biradical character was found for structures with two nitrogen atoms located in the same sublattice where no Kekulé structure could be constructed. It was demonstrated that increasing the interatomic distance between the N atoms enhanced the stability of the doped structures, and the isomers with N atoms located in different sublattices appeared to be preferred. Other set of small PAHs (aza-pyracylene, aza-benzoanthracene derivative, aza-pyrene, azaperylene, corannulene, and some N-containing corannulene derivatives) served as models for DFT calculations addressing the role of aromatic domains in the PL of CDs [47].

4.1.4. Other doping and co-doping

Single-layered larger PAH models were used to investigate the effects of B and/or N doping on the reactivity, aromaticity and absorption spectra of graphene and O-functionalized carbon clusters mimicking GQDs [299]. The models were based on C₇₆H₂₂ containing 28 benzene rings with hydrogen terminated edges which were (co-)doped with up to three boron and/or nitrogen atoms and functionalized by –OH and –COOH groups. Wang *et al.* [300] studied the impact of nitrogen and sulfur edge (co-)doping on HLGs, considering small C₄₂ PAHs as suitable CD models. In particular, three doping types were considered, i.e., nitrogen doped CDs (pyridinic nitrogen without hydrogen, pyrrolic nitrogen with hydrogen), sulfur doped CDs, and nitrogen and sulfur co-doped CDs. Additionally, Fan *et al.* [301] in their boron doping study revealed that the model structure and the presence of borax (Na₂B₄O₇) in solution in a proximity of B-GQDs have an impact on the resulting PL properties. The suggested structure of pure B-GQDs without borax, which is thought to be responsible for the PL, consisted of two covalently associated pyrene-like molecules. The structure stems from the association of B-GQDs by a [2+2] cycloaddition reaction over two C=B double bonds. Moreover, Feng *et al.* [302] demonstrated that the heteroatom type (B, N, O, S) and geometry configuration collectively alter the HLG of doped GQDs and geometry deformation has been identified as one of the key factors that tailor the energy gap and electronic structure of graphene materials. Smaller sized PAHs models (C₄₂) were considered as a suitable model here.

Preferential doping position in two types of graphitic carbon nitride quantum dots (g-C₃N₄; with triazine or heptazine structural motif) differed for boron, oxygen, carbon and phosphorus [303]. Whereas B preferentially replaced the internal carbon atoms in the

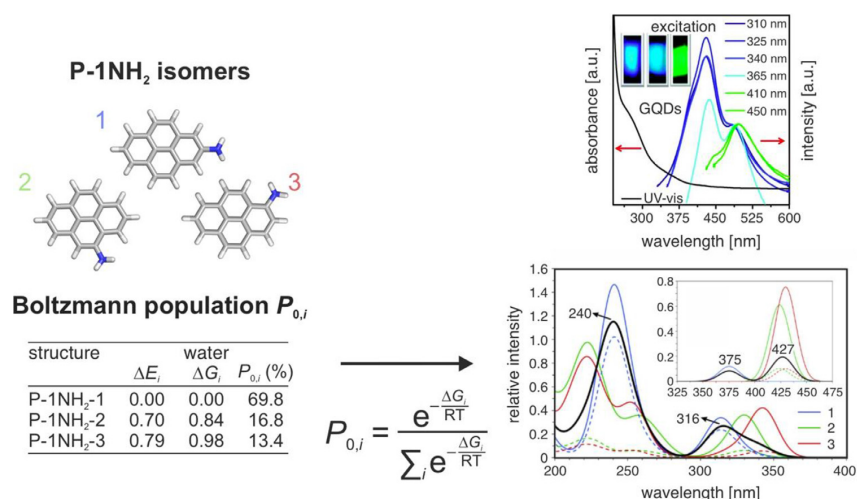


Fig. 11. Left top panel: Structures of three aminopyrene isomers considered in the Boltzmann averaging applied for simulation of absorption and fluorescence spectra (shown on right bottom panel). Left bottom panel: Relative electronic and Gibbs energies (in kcal/mol) and Boltzmann populations of isomers 1-3 ($T=298$ K, $p=1$ atm). Right top panel: Measured UV-vis absorption and PL spectra (at six different excitation wavelengths) of amino-functionalized GQDs. Reprinted with permission from [298]. Copyright 2014 Royal Society of Chemistry. Right bottom panel: Calculated absorption and fluorescence (inset) spectra of pyrene chromophores with single $-\text{NH}_2$ substitutions (full lines), their rescaled counterparts (dashed lines) and the final averaged spectrum (thick black line), in water. Isomers 1, 2, 3 are indicated by blue, green, and red lines, respectively. The absorption and fluorescence maxima wavelengths are given in nm. Reprinted with permission from [297]. Copyright 2017 Elsevier.

larger central rings of both types of $g\text{-C}_3\text{N}_4$, O and S preferred the substitutional doping at the bridge nitrogen atoms. Finally, P preferred to substitute the bridge nitrogen atom in the heptazine type $g\text{-C}_3\text{N}_4$, but interstitial two-coordinated nitrogen atoms were more favored in the triazine $g\text{-C}_3\text{N}_4$.

4.1.5. Molecular fluorophores

QM calculations indicated that typical MFs are stable in water. CZA is known to form keto and imino tautomers, but only the keto form is stable in the aqueous solution [304]. Moreover, CZA forms stable J-type hydrogen-bonded aggregates in water, mostly dimers. The possible formation of $\pi\text{-}\pi$ stacked H-type aggregates was ruled out as the calculated absorption spectra did not correlate with the experimental ones [304]. The formation of an intermediate with pyridone-like structure similar to CZA during the synthesis of CDs from CA and diamines was supported by comparing experimental and simulated FT-IR spectra [164]. Based on experimental data, geometries of doubly hydrogen-bonded dimers of MA in solution were computationally optimized and proved to be stable. Different protonated forms in solution were theoretically explored as well [140]. Being identified as one of the most pertinent MFs, IPCA molecule was proven to be planar, and its protonated form prevailing in the acidic environment was only very slightly affected by the presence of solvent [29,274]. Importantly, pK_a of the IPCA $-\text{COOH}$ group was estimated to be 2.9, and thus IPCA anion was expected to be the dominant form at neutral pH [195]. Owing to the electrostatic repulsion of the anions, the tendency of IPCA to aggregate in solution decreases from the acidic to neutral environments. Nevertheless, both IPCA forms are prone to assembling in aqueous solutions and can form even bigger clusters of IPCAs that can be incorporated into the structure of CDs [195].

4.1.6. Multimers, assemblies and interaction with complex surroundings

Although single layer models are capable to provide essential insights into various CDs properties and therefore have been used in a majority of studies, the role of stacking, aggregation and surrounding effects in (photo)chemistry of CDs

has also been investigated. As in the case of single molecules, benchmarking studies assessing the suitability of cheaper TDDFT methods against more rigorous but computationally more demanding approaches, e.g. DFT/MRCI, were performed for stacked dimers (pyrene, coronene, circum-1-pyrene, circum-1-coronene and circum-2-coronene) [248]. This study also showed that the interplanar distances for the S_1 state decreased in comparison to the corresponding GS values. These reductions were most pronounced for the pyrene dimer (~ 0.01 nm) and decreased significantly for the larger dimers.

We also contributed to this field by exploring the aggregation effects on electronic structure of functionalized and doped PAHs in several studies [89, 100, 101]. The stacking effects on the structure and absorption spectra of dimers and trimers of O-functionalized pyrene-like PAHs were investigated [211]. From the structural point of view, the stacked systems revealed slight bending at the edges with $-\text{COOH}$ and $-\text{OH}$ groups being inclined toward each other. Solvation and additional deprotonation had only a minor effect on the geometry of the stacked structures. It was also shown that the hydrogen bonding between neighboring $-\text{OH}/-\text{COOH}$ pairs had a significant stabilizing effect on the single-layer structures. Similar peak positions in the experimental and calculated absorption spectra of the two-layer systems indicated that the size of π -conjugated regions in the used models is reasonable. In a follow-up study [297], six classes of two-layer models were constructed by the stacking of two functionalized/doped molecules of the same type and their PL properties were evaluated. It was noted that multi-layer CDs can be rich in rotational conformers, which should be taken into account during the design of doped CDs in relation to their optical characteristics. Next, a bilayer model composed of amide-capped graphene ribbons helped understand the fundamental structure-property relationships [30], and besides $-\text{CONR}_2$ groups, other chemical modifications of the sp^2 network such as epoxidation, hydroxylation of a central double bond, and existence of pyridinic nitrogens at the edges of the lattice were also considered [30].

MD simulations were used to study structural features [305–308] and behavior of CDs in the vicinity of more complex molecu-

lar systems like chitosan [309], peptides [310–312], enzymes [313], DNA [314], and membranes [56,315–318]. Elvati *et al.* found that single GQDs tend to be more flexible as the size of the core increases and also that steric hinderance and tendency for formation of hydrogen bonds through carboxylic groups make them deviate from perfectly planar geometry, while functionalization with –CHO group did not lead to structural distortions of GQDs [305]. They also studied aggregation of such configurations and found out that GQDs assembled into three types of stable substructures: (i) a close stack, where two GQDs lie parallel to each other in close contact, (ii) a wide stack with a single molecular layer of water molecules separating the GQDs, and (iii) a perpendicular stack with the main plane of a GQD being orthogonal to the main planes of two or more GQDs. Gu *et al.* [307] modeled various structures based on their synthesis of $g\text{-C}_3\text{N}_4$, i.e., heavily N-doped graphene covered with =O groups and O-doped $g\text{-C}_3\text{N}_4$. It was shown that the structure with C-edges was more stable than the one with C/N edges with region of sp^2 carbons on the surface. It was also revealed that a squared structure with armchair edges was not favorable, but the hexagonal zigzag structure was stable. Finally, it was stated that the substitutional N atom gradually replaced pyrrolic or pyridinic N during the pyrolysis at high N concentrations, thus N-doped GQDs (with pyrrolic and pyridine N) transformed to carbon nitride quantum dots (with quaternary N). Suzuki *et al.* [56] found that ripples appeared at the edges of the graphene sheets as the diameter of the sheets became larger. They also observed that the chirality of substituents on the edge does matter, e.g., in permeation of molecules into membrane. In general, all these MD simulations revealed that PAHs tend to form stacked structures via $\pi\text{-}\pi$ interactions [313]. Although MD simulations with QM potentials are rather rare in the literature, DFT-MD studies of single layered –COOH functionalized PAHs (edge functionalization, because edges show better formation energies) with polyaniline (PANI) conductive polymer were carried out and they uncovered that PAHs remained flat with the most important structural changes localized at the edges [319]. These MD simulations also demonstrated a good affinity between PANI and PAH.

Theoretical calculations of real models of spherical CDs are less abundant in the literature. Real models of CNDs, i.e., those having ~2.4 nm in diameter, contain ~9,000 atoms, which is too many for accurate ab-initio and DFT methods that are currently state-of-the-art in the field of PL calculations of MFs and fluorescent materials in general (see Section 3). A few studies employing classical MD simulations were carried out to describe stability and structural features of spherical CDs [196] and some more amorphous assemblies [320]. Paloncýová *et al.* [196] employed a model of few layered pure and O-functionalized (–COOH/COO[–], –OH, =O) spherical CDs, where the role of size, chemical nature of side groups and their coverage were studied. To facilitate generating CD structures of various composition, size, coverage and positions of functional groups, an efficient tool interfacing employed MD simulation programs was presented in this study. The simulations revealed that surface O-functionalized CDs were stable in water through the formation of an inter- and intra-hydrogen bonding network. It was also demonstrated that individual layers of CDs were highly dynamical when the rate of rotation of layers with respect to each other decreased as the size of the core increased. The chemical nature of functional groups also influenced this internal dynamics, where –COOH groups interconnected the neighboring layers and decreased the rate of internal rotations. Further, it was shown that highly charged CDs, due to an excess of deprotonated carboxylic groups, caused the instability of CDs. Additionally, the simulations in DMF showed a decreased stability of pure CDs but an increased level of interlayer hydrogen bonding of the functionalized ones. Recently, Langer *et al.* [195] used MD simulations to study the self-assembly of spherical CDs and/or its fragments with IPCAs, and

its possible intercalation into CD graphitic layers (Fig. 12), providing hints about the validity of experimental results suggesting the importance of MFs in PL of CD [142,321] or even the conclusions that ~0.34 nm interlayer distance measured in TEM images is due to solely self-assembled MFs [140], because they tend to be non-covalently adsorbed on the surface of CDs interacting either by $\pi\text{-}\pi$ stacking or via hydrogen bonding network. Very recently, assemblies of molecule-like subunits of PAHs (perylene)s attached to the CD surface were studied [322], discussing the effect of different structural organization with either non-interacting monomers, or non-covalently bound dimers, or covalently bound dimers with two, three, or four carbon aliphatic linkers on PL properties. Although simulations focusing on interactions of CDs with more complex systems like biomembranes have also been performed [323], the MD simulations of CDs permeation through a membrane can be tricky, e.g., because of the large size of a membrane model necessary to properly describe the CD-membrane double-layer interface. Another issue is the convergence necessary to obtain reliable results. As an alternative, one can employ more approximate coarse-grained MD approaches, or to use advanced sampling methods to estimate the energetic barriers for penetration of CDs into the hydrophobic region of a membrane.

To sum up, classical MD simulations can provide unique views into structural features of CDs. They can also be used to select configurations of stable and potentially interesting conformers of luminescent molecules (e.g. IPCA) and nanosystems, whose PL properties can be further calculated with advanced methods [274]. Moreover, MD simulations can also be applied to model possible pathways of the formation of CDs from its precursors [195,324].

Li and coworkers showed that CQDs synthesized from 1,4,5,8-tetraminoanthraquinone and CA exhibited near infrared PL and ability to transport drugs, which can be used for tumor therapeutics [6]. They documented that the CQDs accumulated in tumors, because they were transported into cells by the large neutral amino acid transporter 1 (LAT1). A binding pose of the CQDs model in LAT1 was probed by molecular docking which is a computational technique that predicts mutual orientation of two molecules, in this case, LAT1 and functionalized PAH as a CQD model. Using a genetic algorithm for pose generation and empirical scoring function for pose scoring, the binding affinity of CQD model to LAT1 was estimated to be –2.1 kcal/mol.

Significantly less attention has been paid to even more complex systems, e.g., CDs supported on other nanomaterials, despite significant application potential of such nanocomposite hybrid systems, e.g., in photocatalysis. In the study by Sen and coworkers, it was shown that the electronic properties of CDs can be tuned by boron doping in order to achieve an optimal band alignment with TiO₂ support [325]. Theoretical calculations on TiO₂-GQD hybrid structure served well for the verification of possible C–O–Ti bonds in this hybrid as well as for the prediction of its optical spectra [326]. The calculated absorption spectra were fully consistent with the experimental absorption data and significantly different from bare TiO₂. From the point of exploring a photocatalytic activity TiO₂ in conjunction with GQDs a DFT study was performed elsewhere [327].

Covalently bonded hybrid structures of $g\text{-C}_3\text{N}_4$ and GQDs was studied for probing their light absorption, electronic, and excitonic characteristics [328]. It was shown that the relative size of the two components of this hybrid remarkably affected the absorption spectra and the electronic/excitonic structures of the hybrid. On the contrary, non-covalently modified hybrid of $g\text{-C}_3\text{N}_4$ with GQD in a stacked arrangement was explored in different study [329]. The structure of $g\text{-C}_3\text{N}_4$ was wrinkled due to the interaction with GQD, and the structure of $g\text{-C}_3\text{N}_4$ itself determined where the charge was distributed. The charge was accumulated in the region facing the cavities in $g\text{-C}_3\text{N}_4$ and depleted in the region which was

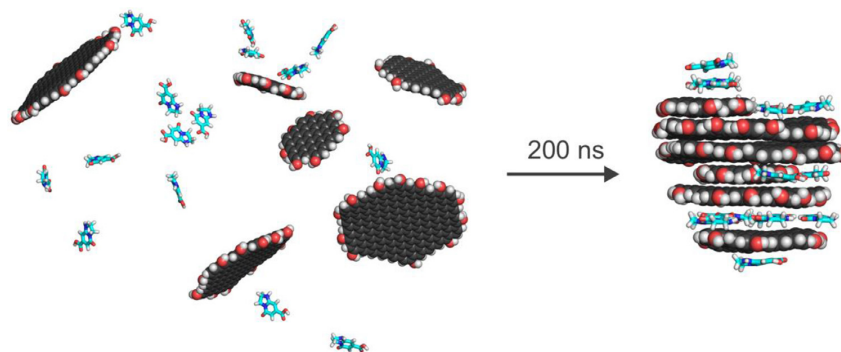


Fig. 12. Molecular dynamics simulations showed self-assembly of molecular fluorophores and functionalized PAHs in an aqueous solution, forming quasi-spherical like CDs. Coloring scheme: Carbon-black and cyan; oxygen-red; nitrogen-blue; hydrogen-white. Water is omitted for clarity. (For details see study [195].)

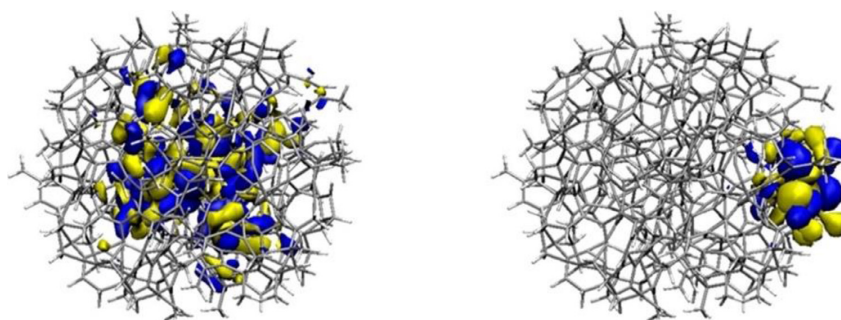


Fig. 13. Electronic calculations of 2 nm model of amorphous nanodot identified molecular orbitals, which may correspond to band-like (left) and surface states (right). Reprinted with permission from [185]. Copyright 2015 American Chemical Society.

facing the heptazine unit of $g\text{-C}_3\text{N}_4$. Studies of such systems can be carried out by utilization of plane-wave DFT calculations under periodic boundary conditions. It should be noted that studies focused on heterostructures require perfect control over properties of both systems, i.e., CDs model and the support, their mutual arrangement and adopted level of computation.

4.1.7. Amorphous CNDs

Mass density and relative content of sp^3 , sp^2 , sp carbons are the most significant structural parameters of amorphous CNDs. Margraf *et al.* [185] used SE computational methods to study hydrogen-passivated pure and N- (mostly as amine-, imine- or cyano- groups) and/or O- (mostly ether or carbonyl groups) doped amorphous carbon nanostructure models, i.e., structures that might emerge from low temperature (400–500 K) solvent-based synthetic procedures. As many as 93 structures with stoichiometry $C_wN_xO_yH_z$ ($119 < w < 128$; $0 < x < 6$; $0 < y < 3$; $1 < z < 14$) with fully saturated edges (no dangling bonds) in closed-shell singlet GSs were used for calculation of HLG and excitation energies (see Fig. 13). A general observation was that the low-density amorphous carbons feature a higher proportion of sp and sp^2 carbon atoms than high density ones. The structure of amorphous carbon nanoparticles and its stability in vacuum and water was also studied by Monte Carlo and MD simulations, DFT based machine learning techniques and Force Enhanced Atomic Refinement method (FEAR) [330–334]. In the study by dos Santos *et al.* [330] amorphous carbon (a-C) consisting almost entirely of threefold-coordinated (sp^2 -abundant) sites was considered as a model. On the five a-CN models it was shown that with the decreasing density (2.16, 2.00, 1.84, 1.79, 1.72 g/cm^3 densities) of nanoparticles the ratio of sp^2/sp^3 carbons in-

creased. The sp -hybridized carbons were also present in all five models. The structure with the highest density exhibited the highest cohesive energy per atom, indicating that this structure was the most stable. Simulations of nanoparticles in water revealed that two hydration shells were formed around the most dense structures, while for less dense configurations containing large enough cavities, clathrate-like structures were formed. Also, due to the presence of dangling bonds increasing the reactivity of the surface of such amorphous carbon nanoparticles, the electric double layer is expected to be formed around the nanoparticles. With the FEAR approach, four models of a-C with 648 atoms with densities 3.50, 2.99, 2.44 and 0.951 g/cm^3 were constructed based on the experimental data. For the highest density, a model with 96 % of sp^3 carbon bonded network was built; for the density of 2.99 g/cm^3 , the content of sp^3 carbon was 82.70 %, and the lowest density the model was mostly built from sp^2 carbons, interconnected with a small fraction of sp^3 sites. The sp carbons were abundant in all four models [334].

4.1.8. Carbonized polymer dots (CPDs)

Theoretical studies of CPDs are less frequent in literature, due to its structural complexity and ambiguity (see Section 2.1.). Val-lan *et al.* [335] introduced a structural model of CPDs prepared from CA and ethylene diamine (EDA) at low-temperature conditions with the aim to understand the role of the inner structure of CPDs in the enhancement of their blue PL. A complete characterization of their chemical structure by a broad set of experimental methods unveiled the formation of a hydrogen-bonded rigid network of short polyamide chains of about 10 monomer units. DFT calculations for a model with polymeric $[C_8H_{12}O_5N_2]_n$ units re-

vealed that the optimized structures exhibited an intricate network due to the establishment of both intra- and intermolecular hydrogen bonds.

The dependence of the HLG on the sp^2 -hybridization factor of carbon atoms in CPDs was also studied [336]. To reflect the hybrid polymer-like structure of CPDs, the applied model was composed of an amorphous core and a polymer-like structure made of sp^3 -hybridized amorphous carbon containing small sp^2 -hybridized atomic domains of various geometries (represented by a pair of coupled pyrene molecules). The internal structure of the amorphous core was not modeled. Importantly, the domains (represented by pairs of coupled polycyclic aromatic molecules) were not like stacked dimers of flat aromatic systems, because of their non-planar geometry and the proximity of the atomic layers. The best agreement with the experimental absorption and emission spectra was achieved when pyrene-sized sp^2 domains were considered, suggesting that these domains may be the prevailing structural element in CDs corresponding to the employed synthetic conditions.

4.2. Electronic structure and PL of CDs

The spectacular and not fully understood PL properties of CDs put them into the spotlight of computational methods, which can provide deep insights into electronic structure and origin of PL. In this section, we first describe the electronic structure of simple PAHs as useful models of QGDs and π -conjugated cores of CDs in general focusing on the size and shape effects. Then we discuss the impact of chemical modifications of the core and shell of CDs, i.e., doping and/or functionalization, on the optical properties of CDs. Next we review the studies devoted to the electronic structure and spectra of MFs. Possibilities to account for the impact of solvation are also considered. Finally, the aggregation effects with an emphasis on (co-)assembling of PAHs with MFs are discussed.

4.2.1. Polycyclic aromatic hydrocarbons

Due to its low computational cost, HLG is often calculated as a very rough estimate of the excitation energy of a molecule. In solid state semiconductors, HOMO corresponds to a valence band, LUMO to the conduction band, therefore HLG corresponds to a band gap.

As commonly accepted, absorption of pure PAHs is dominated by $\pi \rightarrow \pi^*$ transitions [248,282,337,338]. In agreement with experimental data, theoretical studies confirmed that the absorption maxima of small and medium sized PAHs are mostly localized in UV region [30,283]. During the PAHs excitation, transition into S_1 or S_2 state is only weakly allowed, but excitation into higher ESs, such as S_3 and S_4 is strongly allowed in numerous PAH models as revealed by TD-B3LYP [282,288,337]. This finding agrees with experimental observations [157]. This can be, however, different in smaller systems, such as pyrenes, where even S_2 was found to be involved, as shown by using TD-CAM-B3LYP [248]. Such observations can be, however, caused both by real differences in the molecules as well as by used method. Multireference methods (such as MRCI or NEVPT2) in the same study [248] predicted S_3 or S_4 as the first allowed excitation.

In PAHs, the $S_1 \rightarrow S_0$ transition has a $\pi-\pi^*$ character, as revealed by, e.g., TD-CAM-B3LYP [47] and TD-B3LYP [288]. The higher ESs stemming from previous excitation can either decay via internal conversion to lower lying states, or undergo ISC into triplet states and decay via phosphorescence [34,337]. This is favored in the case of larger PAHs that have delocalized electrons in larger area, which reduces the singlet-triplet splitting and favors the ISC [288] to triplet states laying a slightly below the corresponding singlets (Fig. 3A) [282]. Therefore, a small radiative rate constant and low QY from the S_1 state was observed for such molecules [157,288].

4.2.1.1. Role of shape/size. In experiments, the increase of PAHs size generally causes a red shift both in their absorption and PL spectra (Fig. 3A). Theoretical studies of PAHs focusing on calculations of HLG [283,286,339–341], absorption [30,248,282,283,288,342] as well as fluorescence [30,248,285,288,342] were in line with this observations using mostly single reference TDDFT methods with generalized-gradient approximation (GGA) functionals [340], hybrid B3LYP [282,285,286,288,341] or PBE0 [342] functionals, RSH functionals, such as ω B97X-D [30] or CAM-B3LYP [283], as well as DFTB [339], and MRCI or SC-NEVPT2 calculations [248]. Due to the low computational cost, TD-B3LYP/6-31G* was the most often used, agreeing well with experimental data [282,285,286,288]. The red shift of the absorption and emission maxima with the increasing layer size is consistent with a theory of the dependence of PL wavelength on the size of sp^2 domain due to QCE [34]. Sk *et al.* confirmed this hypothesis by deliberate manipulation of sp^2 domain size, dividing sp^2 layer into smaller domains by introducing sp^3 regions [285]. The wavelength shift indeed comes from π -delocalization of electrons with increasing π -conjugated domain size and QCE (Fig. 14) [285].

Apart from the size of PAHs, the shape and edges play an important role in their PL properties. For example, hexagonally shaped PAHs exhibit much larger band gap than rectangular or triangular PAHs [285]. The triangular structure was also found to be responsible for a multicolor narrow PL peak as calculated with B3LYP and experimentally measured by Yuan *et al.* [54]. The shape also affects the dependency of optical properties on the layer size. This can be observed for shapes pertinent in particular for QGDs. While extended nanoribbons acquire the properties of polyphenanthrenes or polyacenes, by increasing the radius of circular PAHs the HLG approaches zero and the properties converge to those of graphene, as observed using DFT and DFTB [339], Gerischer-Marcus theory [343] or fragment molecular oscillation [344]. In the case of similar sizes and shapes, zigzag edges induce a red shift in both absorption and emission maxima with respect to armchair edge arrangements, in agreement with sparse available experimental data [283,285].

4.2.2. Introducing heteroatoms

The elemental analysis of many QGDs, CNDs and CQDs identified significant amounts of N, O, B, S or P in various chemical forms in CD structures. Without any doubt, the presence of heteroatoms, their chemical form and abundance influence optical properties of all types of CDs. Understanding relationships between the structure and optical properties also motivated many theoretical studies. These were either focused on heteroatoms substituting carbons in the aromatic matrix, i.e., doping, or on functional groups substituting hydrogens on the edges.

4.2.2.1. Role of doping. Introducing heteroatoms (typically nitrogen, which is well structurally tolerated by the aromatic matrix) into a QGD increases the amount of possible energy levels available for internal conversion (Fig. 3). Both heteroatoms substituting carbons in the aromatic sp^2 domains and surface functional groups induce edge, surface or defect states and often cause a red shift in PL properties (Fig. 3B) [345], though not with a full consensus, as discussed below.

Due to chemical composition of precursors in bottom-up synthetic strategies, the most common doping element is nitrogen. Nitrogen is known to affect the PL properties both in terms of wavelength as well as QY [101]. The most common forms of N in QGDs are graphitic N (in QGD core substituting carbon, Fig. 10D), pyridinic N (on the edge of a 6-membered ring) and pyrrolic N (5-membered ring). However, despite the development in the field and though multiple theoretical studies were focused on the role of doping atoms, many issues still remain unresolved.

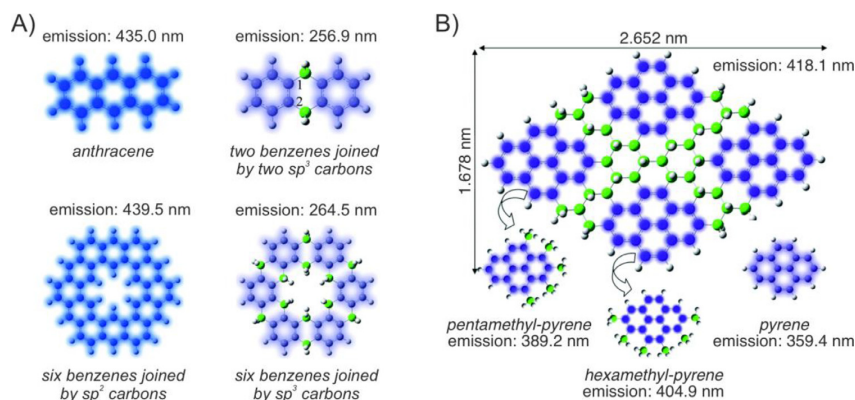


Fig. 14. (A) Role of quantum confinement effect on emission properties of GQDs. Substituting sp^2 carbons with sp^3 carbons leads to a blue shift in resulting emission wavelength. (B) The emission wavelength of GQD composed of pyrene domains is similar to the wavelength of individual sp^2 domains. Reprinted with permission from [285]. Copyright 2014 Royal Society of Chemistry.

Comparing to carbon, graphitic nitrogen contributes to the electronic structure with one extra electron. Therefore, the nature of the GS depends on the parity of number of added nitrogens leading to odd multiplicity in the case of the even number of graphitic nitrogens and *vice versa*. The excitation of GQDs doped with graphitic nitrogen has a $\pi-\pi^*$ character [176], same as in undoped PAHs. Theoretical studies of graphitic N doped systems showed a red shift of absorption maxima with respect to pristine GQDs [299,337] or functionalized coronene and pyrene [87,176,296], similar red shift was observed in the emission maxima with respect to corresponding non-doped GQD models [47,87,163,285,302] in agreement with experimental observations [87]. Interestingly, a slight blue shift upon introducing graphitic N was reported for a spherical armchair-edged GQD with 13 aromatic rings studied by B3LYP [302] as well as for -OH or -COOH substituted GQDs with 28 aromatic rings studied by CAM-B3LYP [299]. While in the first case the blue shift could arise from the armchair-edged structure, in the latter it was attributed to the local electronic changes induced by the functional groups rather than to N doping. Also contrary to experimental observations and other theoretical studies, using B3LYP, Niu *et al.* predicted no fluorescence upon introducing graphitic N into GQDs with diameters ranging from 1–5 nm [337], though a red shifted absorption was observed. In these works, hybrid B3LYP [163,285,302,337], as well as RSH CAM-B3LYP [47,299] or ω B97X-D [87,296] functionals were used. Apart from that, the role of nitrogen doping was also studied by Shao *et al.* [176] with multireference methods, such as MRCI, highlighting the role of N position and the role of double excitation. Shao *et al.* concluded that graphitic N inside GQDs red shifted the absorption, while graphitic N on GQDs edges can induce either red or blue shift.

Nitrogen substitutions of edge carbon atoms, i.e., pyridinic or pyrrolic nitrogens, cause usually a smaller red shift than the graphitic position in the GQD core in HLG [163], absorption [296] and emission spectra [47,87]. Pyrrolic nitrogen behaves similar to graphitic-edge nitrogen both causing either a blue shift [285] or red shift [297,337,346] in absorption spectra of GQDs. Niu *et al.* found that the edge doping with N preserves the π -conjugated domain of GQD and increases the oscillator strength of the $S_1 \rightarrow S_0$ transition. Together with increasing the probability of internal conversion, emission intensity of such GQDs is increased [337]. Moderately red shifted absorption was observed in the case of pyridinic nitrogen in smaller GQDs [302] and red shifted emission was predicted for pyridinic derivatives of coronulenes [47]. However, the pyridinic nitrogen was also observed to cause a blue shifted emission with respect to pristine GQD

[285,297,337] or blue shifted absorption in amino functionalized GQDs [30]. Both red and blue shifts introducing pyrrolic or pyridinic nitrogens were obtained using hybrid [163,285,302,337] or RSH functional [30,47,87,296,297] so the reason for this variability probably does not lay in the used method. Unlike in the case of graphitic N, with pyridinic N the excitation has a $n-\pi^*$ character and N contributes only with one electron to the π -system, thus shifting the absorption spectra only mildly to red, more resembling the original GQD (pyrene), as calculated by MRCI or SC-NEVPT2 [176]. Furthermore, a level of frontier orbital hybridization is found to be crucial for doping effects on optical properties. In the case of even hybridization, a blue shift of absorption and emission spectra can be expected, while uneven hybridization leads to red shift [337]. Although the direction of induced shift in the resulting spectra is still debatable, the effect of N doping is consistently concentration dependent [87,285,337].

Apart from nitrogen, boron, phosphorus or sulphur doping was also studied. Similarly to the N doping, the abundance and position of doped atoms affect PL of GQDs. It was observed that heteroatoms are actively involved in electron transitions. In general, electron-rich atoms (e.g., N, P, S) raise the HOMO energy, while electron deficient ones (e.g., B) lower the LUMO energy, thus in general inducing a red-shift in absorption/emission spectra. Indeed, the B doping into GQD core caused a red shift in absorption spectra in pristine GQD, although a blue shift in OH- or COOH-functionalized GQDs was also observed with CAM-B3LYP [299]. Both in 5- and 6-membered rings, the most profound effect was observed for S [302], remarkably reducing the HLG, as calculated by B3LYP. This was explained by a larger atomic radius and excess of electrons of S. The HLG also depends significantly on geometric deformations invoked by doping with larger atoms such as P and S, which effectively reduce the sp^2 hybridization. Also, partial edge substitution with B and N can alter the HLG in rectangular or cross-linked GQDs [340].

4.2.2.2. Functional groups. Another possible position of heteroatoms is on the CDs surface that is covered by multiple functional groups. Consistently with the accepted role of low-lying surface/defects states (Fig. 3B), the attachment of -OH, -COOH or -NH₂ groups usually induces a red shift in a concentration dependent manner in absorption [292,295] as well as fluorescence spectra [37,285,286,288,294,297,337], although Saha *et al.* observed a blue shift in absorption spectra upon introducing -OH or -COOH group to pristine, boron or nitrogen doped GQD [299]. Moreover, Wang *et al.* demonstrated that the O-containing functional groups

did not alter the HLG of the aromatic core, nevertheless, due to the either structural disorder or because of the functional groups themselves, additional energy states were generated [161]. Apart from the red shift, the functionalization of triangular dots with -OH groups leads to a narrower emission peak than in the case of -COOH [54]. The electron donating -OH group induces higher degree of electron delocalization and therefore higher structural stability and reduces electron-phonon coupling. Further, the π -electron density is increased by -OH group and thus facilitates radiative recombination of electrons and holes [54]. Similar CT was observed for -NH₂ groups, where electron donating -NH₂ decreased GQD band gap [37]. Although theoretical calculations could offer the explanation of involved orbitals, not much attention was paid to this topic and no consensus was reached. It is believed that with surface states, the character of electronic transitions changes from $\pi \rightarrow \pi^*$ transitions of aromatic domains to $n \rightarrow \pi^*$ (C=O or C=N) [288,297] or $n \rightarrow \sigma^*$ transition (C-OH) [47,347]. However, Sudolská et al. [211] claimed that lone pair orbitals of oxygen on OH-pyrene hybridized with its π -orbitals and therefore no pure $n \rightarrow \pi^*$ transition was observed. Apart from the study of Saha et al. (using CAM-B3LYP) [299], observations among published studies are consistent with experiments using LDA [37], hybrid B3LYP [54,285,286,288,294,337] or RSH functionals [30,211,295,297,299].

Functional groups can be attached not only on the edges of individual layers, but also to core carbon atoms. For example, epoxy groups attached to GQD induce a blue shift in absorption spectra by reducing the sp^2 domain size [30,211]. Similarly, attaching other oxygen-containing functional groups to GQD plane (which could be the case of edge layers in C-dots) leads to the blue shift in absorption maxima [30,286]. While the edge functionalization -NH₂ does not decrease the absorption intensity significantly and actually increases fluorescence QY [294], the functionalization in the aromatic region of GQD does decrease the absorption intensity [286]. The effect of such functionalization is related to reducing the sp^2 domain size rather than to the direct effect of individual functional groups.

The functionalization also affects the PL characteristics of CDs based on the g -C₃N₄ core. By employing TD-B3LYP calculations of low-lying singlet and triplet states, Yuan et al. [114] successfully rationalized the enhancement of ISC for yellow phosphorescence emission induced by the presence of carbonyl groups at the rim of the g -C₃N₄ core.

4.2.3. Molecular fluorophores and PL

Owing to the small size of MFs, the electronic structure of GS and ES and related absorption/emission characteristics of isolated MFs can be investigated in detail employing advanced quantum chemistry methods (see Section 3). The solvent effects can also be reliably included by either implicit or explicit solvation models, depending on whether specific intermolecular interactions (e.g., hydrogen bonds) play an important role (see Section 3.3.2). The first gas-phase calculations of the structure, HOMO/LUMO and absorption/emission spectra of IPCA (at an unspecified level of theory) were already performed by Song et al. along with the first unambiguous isolation and thorough structural confirmation of this MF [29]. Similar theoretical analyses of the HOMO/LUMO, IR and electronic absorption spectra were performed for pyridone-like derivatives in the gas phase by Wang et al. [164] and Das et al. [144] employing the B3LYP method with the 3-21G and 6-31G basis sets, respectively. Later on, Shamsipur et al. [47] repeated the calculations for the IPCA molecule in the gas phase at the TDDFT/B3LYP/6-31G(d) level. The emission spectra were attributed to the electron transfer between HOMO and LUMO. Although they agreed well with the first component of the experimental spectra, it was suggested that a small observed difference could be caused by calcu-

lating the spectra only for a single fluorophore in vacuum. Zhang et al. investigated TPCA in solution at the B3LYP/6-31G(d) level addressing also photoemission and aggregation effects (TPCA trimer) [142]. Although these studies undoubtedly provided useful qualitative insights into the electronic structure of key MFs, it should be noted that the choice of the B3LYP functional and small basis sets was not fully appropriate taking the non-negligible CT character of the $S_0 \rightarrow S_1$ excitation into account.

A more detailed view into PL properties of IPCA was provided in a recent study applying both QM and MD calculations of IPCA monomers and stacked dimers [274]. The classical MD simulations performed in the GS revealed spontaneous formation of stacked IPCA dimers in aqueous solution. Using the TDDFT approach (cLR-CAM-B3LYP-D3/def2-TZVP in combination with PCM), UV absorption spectra of monomer and dimers were obtained based on vertical excitations and by vibrational broadening with the help of the nuclear ensemble method. The calculated absorption and emission maxima (including the radiative lifetimes) for the monomer were in sound agreement with the experimental values. The character of ESs was further analysed in terms of Natural Transition Orbitals (NTOs) to identify CT and locally ESs (Fig. 9B). The NTOs nicely illustrate for two local minima, structures 1 (1-S₁) and 2 (2-S₁), respectively, the CT character from one to the other IPCA molecule (structure 1) and the local character (on the lower IPCA molecule in Fig. 9B). Previous interpretations have determined $\pi \rightarrow \pi^*$ and $n \rightarrow \pi^*$ transitions to contribute to the absorption spectra of CD core and fluorophore, respectively [348]. On the contrary, the results derived from these IPCA calculations predict that the $\pi \rightarrow \pi^*$ transitions are responsible for absorption spectra of both chromophores. The S₁ optimization procedure has shown preferential formation of stacked dimers and pointed toward a possible non-radiative relaxation competing with fluorescence via opening of IPCA dimers.

4.2.4. Clusters

Although the CNDs and CQDs are multilayered structures, doped and functionalized GQDs seem to be useful models for simple CQDs. However, the effects of MFs in CNDs need to be addressed even in a more complex manner. With increasing computational power, studies of more layers and their interactions were performed. According to current knowledge, no significant effect of second and third layers on the electronic structure of PAHs and their doped and/or functionalized derivatives was observed, and thus the absorption and emission spectra of π -stacked dimers and trimers were very similar to spectra of individual monomers, as studied with RSH functional [211,296,297]. Considering CQDs as an ensemble of individual GQDs explains well its spectral versatility and excitation dependent wavelengths. As each layer can have different composition, they can be excited independently under different conditions and the resulting fluorescence is then dependent on which fragment was excited and which internal conversion takes place prior to fluorescence. Recently, (co-)assembling of MFs with PAHs was studied by MD simulations [195], and the role of such (co-)assembling on the resulting PL properties is under the investigation in our group.

Theoretical investigations of PL of CPDs require slightly different approach than studying GQDs-like fragments. Vallan et al. [335] used RSH functional ω B97X-D to calculate PL properties of CPDs prepared from CA and ethylenediamine by modeling its basic unit [C₈H₁₂O₅N₂]_n in form of dimer, octamer and decamer. After geometry optimization, the oligomer was indeed entangled with a network of intra- and intermolecular hydrogen bonds, which was actually responsible for the CEE effect (see Fig. 3C). Further, analysis of the absorption properties revealed that HOMO was localized mostly on the amide moiety, while LUMO resides on carboxyl, therefore the transition had a strong CT character. When they used

a model with intermolecular hydrogen bonds (two chains), a significant red shift in the emission with respect to absorption was observed, but no fluorescence was observed with a model considering only intramolecular hydrogen bonds. This is consistent with the CEE effect and rationalization of CPDs PL.

4.2.5. Solvent effect

Although CDs are usually prepared and applied in solution, most of QM studies were performed for the gas phase, with only few exceptions employing implicit solvent models. Generally, the presence of solvent caused a red shift in studied spectra, which was shown for water [211,288,297,299] as well as other solvents, such as toluene [337], dichloromethane [288] or benzene and acetonitrile [299]. In the case of N-doped QDs, enhanced red shift and intensity in PL was observed with increasing polarity of a solvent [337]. However, in other studies no significant effect of polarity of the solvents was observed [288,299]. It can be expected that the polarity of a solvent affects more significantly the PL properties of surface functionalized QDs, but we are not aware of any systematic theoretical study dealing with this issue.

5. Perspectives

Challenges concerning reliable characterization of the optical spectra and the explanation of the PL of CDs lie in the large size of realistic model systems, their structural complexity, and the intricate character of their GS and ESs. Computationally feasible DFT methods provide a reliable description for the majority of applications. However, the lack of doubly ESs in the absorption spectra and the wrong ordering of the lowest ESs observed in several important cases represent serious drawbacks and can lead to false characterization of the optical spectra. These issues can be kept under control by comparison with multireference methods, which can identify critical cases and thus help avoid the problems in photodynamical studies. Future studies should be focused on a reliable description of electronic states and PL properties of more realistic CD models. In any case, affordable methods should be benchmarked against available advanced QM methods, using as many reliable (but still tractable) molecular systems as possible. It is expected that the utilization of hybrid QM/MM methods will enable to reach the controlled accuracy also in computational studies of larger model systems. Importantly, such hybrid methods can be combined with armament of approaches capable to cover effects of solvent and generally surrounding environment such as, e.g., the polarizable embedding approach and ONIOM method. Special attention should be paid to the identification of processes and structural features that can be behind the excitation-dependent PL of CDs. In addition, theoretical approaches that can assess the PL QYs should be adapted and thoroughly tested for CDs. Another research field should be focused on the electron-phonon coupling and vibrationally resolved spectra of CD models. Dynamical effects, including also the fate of electronic excitation, belong to absolutely unexplored and very appealing tasks in the modeling of photo-physics of CDs. Processes involving the (R)ISC such as, e.g., TADF and phosphorescence are particularly interesting but very challenging for current theoretical tools. Moreover, contrary to organic molecular fluorophores, the trap states in CDs involved in such processes have often charge-separated character, which requires consideration of sufficiently large structural models thus putting limitations on applicable computational methods. Nonlinear optical properties of CDs will also undoubtedly soon become a target of theoretical efforts, because some CDs can exhibit strong two-photon absorption (TPA). This dramatically increases their application potential by the possibility of (i) extending their absorption range to near-infrared region, (ii) obtaining spatially resolved

photo-responses (two-photon fluorescence) of CDs, and (iii) addressing excited states distinct from those active in one-photon spectra. In the case of classical MD, a special attention should be paid to the interaction of CDs with biomolecular systems, cellular compartments and other nanomaterials. MD simulations will certainly provide important insights into many important processes including, e.g., CDs membrane permeation and cellular transport. The reliable structural models of such complex systems can be used for not only understanding the CD interactions but also designing specific CDs, alongside with further calculations addressing, e.g., the electron/energy transfer between the CDs and nanomaterials.

6. Conclusion

CDs represent a challenging class of nanomaterials with extraordinary PL properties and highly appealing applications. Their PL behavior puts them into the spotlight of both experimental and theoretical efforts. The structural complexity and limitations of experimental characterization of CDs in early studies complicated the development of structural models treatable by theoretical methods. However, recent progress on experiments has made the structural models more robust and well representing individual types of CDs, thus opening a route to deep theoretical investigations. In this review, we surveyed current structural models as well as theoretical studies focused on the structural features and PL properties of CDs. We showed that theoretical methods mostly based on the TDDFT approach could provide useful information, but might fail in specific cases, e.g., if the multireference character of ground and excited states plays a significant role. In such a case, NEVPT2 or DFT/MRCI methods can be effectively used, but their employment is hampered by high computational costs allowing treatment of only relatively small structural models. We showed that for large models semiempirical methods could provide useful semi-quantitative insights. Although a general theoretical approach applicable for all types of CDs can hardly be established, current state-of-the-art methods can help rationalize many important structural and spectral features of CDs. Perspectives towards more general computational protocols including hybrid QM/MM approaches and methods addressing dynamical phenomena in CDs were outlined, but a universal reliable computational strategy remains to be a challenge requiring close collaboration of theoreticians (including software developers) and experimentalists. It is our hope that this review will help to draw the attention of the community to this fascinating field.

Declaration of Competing Interest

The authors declare that they have no known competing financial interests or personal relationships that could have appeared to influence the work reported in this paper.

Acknowledgment

We are grateful for support from the School of Pharmaceutical Science and Technology (SPST), Tianjin University, Tianjin, China, including computer time on the SPST computer cluster Arran. This work was supported by the Center for Integrated Nanotechnologies (Project No. 2019BC0064), an Office of Science User Facility operated for the U.S. Department of Energy Office of Science by Los Alamos National Laboratory (Contract No. 89233218CNA000001) and Sandia National Laboratories (Contract No. DE-NA-0003525). We also gratefully acknowledge support from the Ministry of Education, Youth and Sports of the Czech Republic, Operational Programme for Research, Development and Education of the European Regional Development Fund (Project

No. CZ.02.1.01/0.0/0.0/16_019/0000754), ERC (project No. 683024 from the European Union's Horizon 2020) and Internal Student Grant Agency of the Palacký University in Olomouc, Czech Republic (IGA_PrF_2020_022). DN acknowledges support by the Czech Science Foundation (19-27454X).

Bibliography

- [1] X. Xu, R. Ray, Y. Gu, H.J. Ploehn, L. Gearheart, K. Raker, W.A. Scrivens, Electrostatic analysis and purification of fluorescent single-walled carbon nanotube fragments, *J. Am. Chem. Soc.* 126 (2004) 12736–12737, doi:10.1021/ja040082h.
- [2] S.K. Misra, I. Srivastava, I. Tripathi, E. Daza, F. Ostadhossein, D. Pan, Macromolecularly caged carbon nanoparticles for intracellular trafficking via switchable photoluminescence, *J. Am. Chem. Soc.* 139 (2017) 1746–1749, doi:10.1021/jacs.6b11595.
- [3] C. Rizzo, F. Arcudi, L. Dordević, N.T. Dintcheva, R. Noto, F. D'Anna, M. Prato, Nitrogen-doped carbon nanodots-ionogels: Preparation, characterization, and radical scavenging activity, *ACS Nano* 12 (2018) 1296–1305, doi:10.1021/acsnano.7b07529.
- [4] X. Xu, K. Zhang, L. Zhao, C. Li, W. Bu, Y. Shen, Z. Gu, B. Chang, C. Zheng, C. Lin, H. Sun, B. Yang, Aspirin-based carbon dots, a good biocompatibility of material applied for bioimaging and anti-inflammation, *ACS Appl. Mater. Interfaces*. 8 (2016) 32706–32716, doi:10.1021/acsami.6b12252.
- [5] T.H. Kim, J.P. Sirdaarta, Q. Zhang, E. Eftekhari, J. St. John, D. Kennedy, I.E. Cock, Q. Li, Selective toxicity of hydroxyl-rich carbon nanodots for cancer research, *Nano Res* 11 (2018) 2204–2216, doi:10.1007/s12274-017-1838-2.
- [6] S. Li, W. Su, H. Wu, T. Yuan, C. Yuan, J. Liu, G. Deng, X. Gao, Z. Chen, Y. Bao, F. Yuan, S. Zhou, H. Tan, Y. Li, X. Li, L. Fan, J. Zhu, A.T. Chen, F. Liu, Y. Zhou, M. Li, X. Zhai, J. Zhou, Targeted tumour theranostics in mice via carbon quantum dots structurally mimicking large amino acids, *Nat. Biomed. Eng.* 4 (2020) 704–716, doi:10.1038/s41551-020-0540-y.
- [7] S. Kalychuk, Y. Wang, K. Poláková, R. Zbořil, Carbon dot fluorescence-lifetime-encoded anti-counterfeiting, *ACS Appl. Mater. Interfaces*. 10 (2018) 29902–29908, doi:10.1021/acsami.8b11663.
- [8] S. Mei, X. Liu, W. Zhang, R. Liu, L. Zheng, R. Guo, P. Tian, High-bandwidth white-light system combining a micro-LED with perovskite quantum dots for visible light communication, *ACS Appl. Mater. Interfaces*. 10 (2018) 5641–5648, doi:10.1021/acsami.7b17810.
- [9] Z. Zhou, P. Tian, X. Liu, S. Mei, D. Zhou, D. Li, P. Jing, W. Zhang, R. Guo, S. Qu, A.L. Rogach, Hydrogen peroxide-treated carbon dot phosphor with a bathochromic-shifted, aggregation-enhanced emission for light-emitting devices and visible light communication, *Adv. Sci.* 5 (2018) 1–8, doi:10.1002/adv.201800369.
- [10] F. Yuan, Z. Wang, X. Li, Y. Li, Z. Tan, L. Fan, S. Yang, Bright multicolor bandgap fluorescent carbon quantum dots for electroluminescent light-emitting diodes, *Adv. Mater.* (2017) 29, doi:10.1002/adma.201604436.
- [11] Z. Wang, F. Yuan, X. Li, Y. Li, H. Zhong, L. Fan, S. Yang, 53% Efficient red emissive carbon quantum dots for high color rendering and stable warm white-light-emitting diodes, *Adv. Mater.* 29 (2017) 1702910, doi:10.1002/adma.201702910.
- [12] M. Semeniuk, Z. Yi, V. Poursorkhabi, J. Tjong, S. Jaffer, Z.H. Lu, M. Sain, Future perspectives and review on organic carbon dots in electronic applications, *ACS Nano* 13 (2019) 6224–6255, doi:10.1021/acsnano.9b00688.
- [13] H. Tetsuka, A. Nagoya, T. Fukusumi, T. Matsui, Molecularely designed, nitrogen-functionalized graphene quantum dots for optoelectronic devices, *Adv. Mater.* 28 (2016) 4632–4638, doi:10.1002/adma.201600058.
- [14] F. Arcudi, V. Strauss, L. Dordević, A. Cadranel, D.M. Guldi, M. Prato, Porphyrin antennas on carbon nanodots: Excited state energy and electron transduction, *Angew. Chemie Int. Ed.* 56 (2017) 12097–12101, doi:10.1002/anie.201704544.
- [15] T. Yuan, T. Meng, P. He, Y. Shi, Y. Li, X. Li, L. Fan, S. Yang, Carbon quantum dots: An emerging material for optoelectronic applications, *J. Mater. Chem. C* 7 (2019) 6820–6835, doi:10.1039/c9tc01730e.
- [16] J. Liu, Y. Liu, N. Liu, Y. Han, X. Zhang, H. Huang, Y. Lifshitz, S. Lee, J. Zhong, Z. Kang, Metal-free efficient photocatalyst for stable visible water splitting via a two-electron pathway, *Science* 347 (2015) 970–974, doi:10.1126/science.aaa3145.
- [17] X. Shan, L. Chai, J. Ma, Z. Qian, J. Chen, H. Feng, B-doped carbon quantum dots as a sensitive fluorescence probe for hydrogen peroxide and glucose detection, *Analyst* 139 (2014) 2322–2325, doi:10.1039/c3an02222f.
- [18] M. Zhang, L. Hu, H. Wang, Y. Song, Y. Liu, H. Li, M. Shao, H. Huang, Z. Kang, One-step hydrothermal synthesis of chiral carbon dots and their effects on mung bean plant growth, *Nanoscale* 10 (2018) 12734–12742, doi:10.1039/c8nr01644e.
- [19] Y. Dong, C. Chen, X. Zheng, L. Gao, Z. Cui, H. Yang, C. Guo, Y. Chi, C.M. Li, One-step and high yield simultaneous preparation of single- and multi-layer graphene quantum dots from CX-72 carbon black, *J. Mater. Chem.* 22 (2012) 8764–8766, doi:10.1039/c2jm30658a.
- [20] Y. Li, Y. Hu, Y. Zhao, G. Shi, L. Deng, Y. Hou, L. Qu, An electrochemical avenue to green-luminescent graphene quantum dots as potential electron-acceptors for photovoltaics, *Adv. Mater.* 23 (2011) 776–780, doi:10.1002/adma.201003819.
- [21] Q. Xue, H. Huang, L. Wang, Z. Chen, M. Wu, Z. Li, D. Pan, Nearly monodisperse graphene quantum dots fabricated by amine-assisted cutting and ultrafiltration, *Nanoscale* 5 (2013) 12098–12103, doi:10.1039/c3nr03623e.
- [22] Y.P. Sun, B. Zhou, Y. Lin, W. Wang, K. a. S. Fernando, P. Pathak, M.J. Meziani, B. a. Harruff, X. Wang, H. Wang, P.G. Luo, H. Yang, M.E. Kose, B. Chen, L.M. Veca, S.Y. Xie, Quantum-sized carbon dots for bright and colorful photoluminescence, *J. Am. Chem. Soc.* 128 (2006) 7756–7757, doi:10.1021/ja062677d.
- [23] R.L. Calabro, D.S. Yang, D.Y. Kim, Liquid-phase laser ablation synthesis of graphene quantum dots from carbon nano-onions: Comparison with chemical oxidation, *J. Colloid Interface Sci.* 527 (2018) 132–140, doi:10.1016/j.jcis.2018.04.113.
- [24] J. Xu, S. Sahu, L. Cao, P. Anilkumar, K.N. Tackett, H. Qian, C.E. Bunker, E.A. Gullants, A. Parenzan, Y.-P. Sun, Carbon nanoparticles as chromophores for photon harvesting and photoconversion, *ChemPhysChem* 12 (2011) 3604–3608, doi:10.1002/cphc.201100640.
- [25] J. Lee, K. Kim, W.I. Park, B.H. Kim, J.H. Park, T.H. Kim, S. Bong, C.H. Kim, G. Chae, M. Jun, Y. Hwang, Y.S. Jung, S. Jeon, Uniform graphene quantum dots patterned from self-assembled silica nanodots, *Nano Lett.* 12 (2012) 6078–6083, doi:10.1021/nl302520m.
- [26] L.A. Ponomarenko, F. Schedin, M.I. Katsnelson, R. Yang, E.W. Hill, K.S. Novoselov, A.K. Geim, Chaotic dirac billiard in graphene quantum dots, *Science* 320 (2008) 356–358, doi:10.1126/science.1154663.
- [27] Y. Weng, Z. Li, L. Peng, W. Zhang, G. Chen, Fabrication of carbon quantum dots with nano-defined position and pattern in one step via sugar-electron-beam writing, *Nanoscale* 9 (2017) 19263–19270, doi:10.1039/c7nr07892g.
- [28] C. Xia, S. Zhu, T. Feng, M. Yang, B. Yang, Evolution and synthesis of carbon dots: From carbon dots to carbonized polymer dots, *Adv. Sci.* 6 (2019) 1901316, doi:10.1002/adv.201901316.
- [29] Y. Song, S. Zhu, S. Zhang, Y. Fu, L. Wang, X. Zhao, B. Yang, Investigation from chemical structure to photoluminescent mechanism: a type of carbon dots from the pyrolysis of citric acid and an amine, *J. Mater. Chem. C* 3 (2015) 5976–5984, doi:10.1039/c5tc00813a.
- [30] V. Strauss, J.T. Margraf, C. Dolle, B. Butz, T.J. Nacken, J. Walter, W. Bauer, W. Peukert, E. Spiecker, T. Clark, D.M. Guldi, Carbon nanodots: Toward a comprehensive understanding of their photoluminescence, *J. Am. Chem. Soc.* 136 (2014) 17308–17316, doi:10.1021/ja510183c.
- [31] W. Kasprzyk, S. Bednarz, D. Bogdał, Luminescence phenomena of biodegradable photoluminescent poly(diols citrates), *Chem. Commun.* 49 (2013) 6445–6447, doi:10.1039/c3cc42661k.
- [32] S. Zhu, X. Zhao, Y. Song, S. Lu, B. Yang, Beyond bottom-up carbon nanodots: Citric-acid derived organic molecules, *Nano Today* 11 (2016) 128–132, doi:10.1016/j.nantod.2015.09.002.
- [33] D. Qu, Z. Sun, The formation mechanism and fluorophores of carbon dots synthesized: Via a bottom-up route, *Mater. Chem. Front.* 4 (2020) 400–420, doi:10.1039/c9qm00552h.
- [34] S. Zhu, Y. Song, X. Zhao, J. Shao, J. Zhang, B. Yang, The photoluminescence mechanism in carbon dots (graphene quantum dots, carbon nanodots, and polymer dots): current state and future perspective, *Nano Res* 8 (2015) 355–381, doi:10.1007/s12274-014-0644-3.
- [35] A. Cayuela, M.L. Soriano, C. Carrillo-Carrión, M. Valcárcel, Semiconductor and carbon-based fluorescent nanodots: the need for consistency, *Chem. Commun.* 52 (2016) 1311–1326, doi:10.1039/c5cc07754k.
- [36] J. Lu, J. Yang, J. Wang, A. Lim, S. Wang, K.P. Loh, One-Pot synthesis of fluorescent carbon nanoribbons, nanoparticles, and graphene by the exfoliation of graphite in ionic liquids, *ACS Nano* 3 (2009) 2367–2375, doi:10.1021/nn900546h.
- [37] S.H. Jin, D.H. Kim, G.H. Jun, S.H. Hong, S. Jeon, Tuning the photoluminescence of graphene quantum dots through the charge transfer effect of functional groups, *ACS Nano* 7 (2013) 1239–1245, doi:10.1021/nn304675g.
- [38] K. Holá, Y. Zhang, Y. Wang, E.P. Giannelis, R. Zbořil, A.L. Rogach, Carbon dots – Emerging light emitters for bioimaging, cancer therapy and optoelectronics, *Nano Today* 9 (2014) 590–603, doi:10.1016/j.nantod.2014.09.004.
- [39] M. Li, W. Wu, W. Ren, H.M. Cheng, N. Tang, W. Zhong, Y. Du, Synthesis and upconversion luminescence of N-doped graphene quantum dots, *Appl. Phys. Lett.* 101 (2012) 103107, doi:10.1063/1.4750065.
- [40] R. Liu, D. Wu, X. Feng, K. Müllen, Bottom-up fabrication of photoluminescent graphene quantum dots with uniform morphology, *J. Am. Chem. Soc.* 133 (2011) 15221–15223, doi:10.1021/ja204953k.
- [41] S. Kim, S.W. Hwang, M.K. Kim, D.Y. Shin, D.H. Shin, C.O. Kim, S.B. Yang, J.H. Park, E. Hwang, S.H. Choi, G. Ko, S. Sim, C. Sone, H.J. Choi, S. Bae, B.H. Hong, Anomalous behaviors of visible luminescence from graphene quantum dots: Interplay between size and shape, *ACS Nano* 6 (2012) 8203–8208, doi:10.1021/nn302878r.
- [42] H. Sun, L. Wu, W. Wei, X. Qu, Recent advances in graphene quantum dots for sensing, *Mater. Today*. 16 (2013) 433–442, doi:10.1016/j.mattod.2013.10.020.
- [43] C.S. Lim, K. Holá, A. Ambrosi, R. Zbořil, M. Pumera, Graphene and carbon quantum dots electrochemistry, *Electrochem. Commun.* 52 (2015) 75–79, doi:10.1016/j.elecom.2015.01.023.
- [44] H. Li, X. He, Z. Kang, H. Huang, Y. Liu, J. Liu, S. Lian, C.H.A. Tsang, X. Yang, S.-T. Lee, Water-soluble fluorescent carbon quantum dots and photocatalyst design, *Angew. Chemie Int. Ed.* 49 (2010) 4430–4434, doi:10.1002/anie.200906154.
- [45] A.B. Bourlinos, A. Stassinopoulos, D. Anglos, R. Zbořil, V. Georgakilas, E.P. Giannelis, Photoluminescent carbogenic dots, *Chem. Mater.* 20 (2008) 4539–4541, doi:10.1021/cm800506r.

- [46] H. Yoon, Y.H. Chang, S.H. Song, E.-S. Lee, S.H. Jin, C. Park, J. Lee, B.H. Kim, H.J. Kang, Y.-H. Kim, S. Jeon, Intrinsic photoluminescence emission from sub-domained graphene quantum dots, *Adv. Mater.* 28 (2016) 5255–5261, doi:10.1002/adma.201600616.
- [47] M. Shamsipur, A. Barati, A.A. Taherpour, M. Jamshidi, Resolving the multiple emission centers in carbon dots: From fluorophore molecular states to aromatic domain states and carbon-core states, *J. Phys. Chem. Lett.* 9 (2018) 4189–4198, doi:10.1021/acs.jpclett.8b02043.
- [48] S. Tao, S. Zhu, T. Feng, C. Xia, Y. Song, B. Yang, The polymeric characteristics and photoluminescence mechanism in polymer carbon dots: a review, *Mater. Today Chem.* 6 (2017) 13–25, doi:10.1016/j.mtchem.2017.09.001.
- [49] Y. Song, S. Zhu, J. Shao, B. Yang, Polymer carbon dots—a highlight reviewing their unique structure, bright emission and probable photoluminescence mechanism, *J. Polym. Sci. Part A Polym. Chem.* 55 (2017) 610–615, doi:10.1002/pola.28416.
- [50] S. Zhu, Q. Meng, L. Wang, J. Zhang, Y. Song, H. Jin, K. Zhang, H. Sun, H. Wang, B. Yang, Highly photoluminescent carbon dots for multicolor patterning, sensors, and bioimaging, *Angew. Chemie Int. Ed.* 52 (2013) 3953–3957, doi:10.1002/anie.201300519.
- [51] C. Xia, S. Tao, S. Zhu, Y. Song, T. Feng, Q. Zeng, J. Liu, B. Yang, Hydrothermal addition polymerization for ultrahigh-yield carbonized polymer dots with room temperature phosphorescence via nanocomposite, *Chem. A Eur. J.* 24 (2018) 11303–11308, doi:10.1002/chem.201802712.
- [52] S. Tao, Y. Song, S. Zhu, J. Shao, B. Yang, A new type of polymer carbon dots with high quantum yield: From synthesis to investigation on fluorescence mechanism, *Polymer* 116 (2017) 472–478, doi:10.1016/j.polymer.2017.02.039.
- [53] C. Wu, D.T. Chiu, Highly fluorescent semiconducting polymer dots for biology and medicine, *Angew. Chemie Int. Ed.* 52 (2013) 3086–3109, doi:10.1002/anie.201205133.
- [54] F. Yuan, T. Yuan, L. Sui, Z. Wang, Z. Xi, Y. Li, X. Li, L. Fan, Z. Tan, A. Chen, M. Jin, S. Yang, Engineering triangular carbon quantum dots with unprecedented narrow bandwidth emission for multicolored LEDs, *Nat. Commun.* 9 (2018) 1–11, doi:10.1038/s41467-018-04635-5.
- [55] S. Yang, W. Li, C. Ye, G. Wang, H. Tian, C. Zhu, P. He, G. Ding, X. Xie, Y. Liu, Y. Lifshitz, S.T. Lee, Z. Kang, M. Jiang, C₃N–A 2D crystalline, hole-free, tunable-narrow-bandgap semiconductor with ferromagnetic properties, *Adv. Mater.* (2017) 29, doi:10.1002/adma.201605625.
- [56] N. Suzuki, Y. Wang, P. Elvati, Z.-B. Qu, K. Kim, S. Jiang, E. Baumeister, J. Lee, B. Yeom, J.H. Bahng, J. Lee, A. Violi, N.A. Kotov, Chiral graphene quantum dots, *ACS Nano* 10 (2016) 1744–1755, doi:10.1021/acsnano.5b06369.
- [57] Y. Zhang, L. Hu, Y. Sun, C. Zhu, R. Li, N. Liu, H. Huang, Y. Liu, C. Huang, Z. Kang, One-step synthesis of chiral carbon quantum dots and their enantioselective recognition, *RSC Adv* 6 (2016) 59956–59960, doi:10.1039/c6ra12420h.
- [58] L. Hu, H. Li, C. Liu, Y. Song, M. Zhang, H. Huang, Y. Liu, Z. Kang, Chiral evolution of carbon dots and the tuning of laccase activity, *Nanoscale* 10 (2018) 2333–2340, doi:10.1039/c7nr08335a.
- [59] Z. Tian, D. Li, E.V. Ushakova, V.G. Maslov, D. Zhou, P. Jing, D. Shen, S. Qu, A.L. Rogach, Multilevel data encryption using thermal-treatment controlled room temperature phosphorescence of carbon dot/polyvinylalcohol composites, *Adv. Sci.* 5 (2018) 1800795, doi:10.1002/advs.201800795.
- [60] J. Li, B. Wang, H. Zhang, J. Yu, Carbon dots-in-matrix boosting intriguing luminescence properties and applications, *Small* 15 (2019) 1805504, doi:10.1002/sml.201805504.
- [61] J. Liu, N. Wang, Y. Yu, Y. Yan, H. Zhang, J. Li, J. Yu, Carbon dots in zeolites: A new class of thermally activated delayed fluorescence materials with ultralong lifetimes, *Sci. Adv.* 3 (2017) e1603171, doi:10.1126/sciadv.1603171.
- [62] K. Holá, A.B. Bourlinos, O. Kozák, K. Berka, K.M. Šišková, M. Havrdová, J. Tuček, K. Šafařová, M. Otyepka, E.P. Giannelis, R. Zbořil, Photoluminescence effects of graphitic core size and surface functional groups in carbon dots: COO⁻ induced red-shift emission, *Carbon* 70 (2014) 279–286, doi:10.1016/j.carbon.2014.01.008.
- [63] Y. Mu, H. Shi, Y. Wang, H. Ding, J. Li, CNDs@zeolite: New room-temperature phosphorescent materials derived by pyrolysis of organo-templated zeolites, *J. Mater. Chem. C* 5 (2017) 10894–10899, doi:10.1039/c7tc03487c.
- [64] S.N. Baker, G.A. Baker, Luminescent carbon nanodots: Emergent nanolights, *Angew. Chemie Int. Ed.* 49 (2010) 6726–6744, doi:10.1002/anie.200906623.
- [65] J.B. Essner, G.A. Baker, The emerging roles of carbon dots in solar photovoltaics: a critical review, *Environ. Sci. Nano.* 4 (2017) 1216–1263, doi:10.1039/c7en00179g.
- [66] X. Li, M. Rui, J. Song, Z. Shen, H. Zeng, Carbon and graphene quantum dots for optoelectronic and energy devices: a review, *Adv. Funct. Mater.* 25 (2015) 4929–4947, doi:10.1002/adfm.201501250.
- [67] Y. Wang, Y. Zhu, S. Yu, C. Jiang, Fluorescent carbon dots: Rational synthesis, tunable optical properties and analytical applications, *RSC Adv* 7 (2017) 40973–40989, doi:10.1039/c7ra07573a.
- [68] K.A.S. Fernando, S. Sahu, Y. Liu, W.K. Lewis, E.A. Gulians, A. Jafariyan, P. Wang, C.E. Bunker, Y.P. Sun, Carbon quantum dots and applications in photocatalytic energy conversion, *ACS Appl. Mater. Interfaces.* 7 (2015) 8363–8376, doi:10.1021/acsami.5b00448.
- [69] Z.L. Wu, Z.X. Liu, Y.H. Yuan, Carbon dots: Materials, synthesis, properties and approaches to long-wavelength and multicolor emission, *J. Mater. Chem. B* 5 (2017) 3794–3809, doi:10.1039/c7tb00363c.
- [70] C.M. Carbonaro, R. Corpino, M. Salis, F. Mocci, S.V. Thakkar, C. Olla, P.C. Ricci, On the emission properties of carbon dots: reviewing data and discussing models, *C.-J. Carbon Res.* 5 (2019) 1–15, doi:10.3390/c5040060.
- [71] S. Lu, L. Sui, M. Wu, S. Zhu, X. Yong, B. Yang, Graphitic nitrogen and high-crystalline triggered strong photoluminescence and room-temperature ferromagnetism in carbonized polymer dots, *Adv. Sci.* 6 (2019), doi:10.1002/advs.201801192.
- [72] Y. Xiong, J. Schneider, E.V. Ushakova, A.L. Rogach, Influence of molecular fluorophores on the research field of chemically synthesized carbon dots, *Nano Today* 23 (2018) 124–139, doi:10.1016/j.nantod.2018.10.010.
- [73] P. Lazar, R. Mach, M. Otyepka, Spectroscopic fingerprints of graphitic, pyrrolic, pyridinic, and chemisorbed nitrogen in N-doped graphene, *J. Phys. Chem. C* 123 (2019) 10695–10702, doi:10.1021/acs.jpcc.9b02163.
- [74] S. Chung, R.A. Revia, M. Zhang, Graphene quantum dots and their applications in bioimaging, biosensing, and therapy, *Adv. Mater.* (2019) 1904362, doi:10.1002/adma.201904362.
- [75] Q. Xu, Q. Zhou, Z. Hua, Q. Xue, C. Zhang, X. Wang, D. Pan, M. Xiao, Single-particle spectroscopic measurements of fluorescent graphene quantum dots, *ACS Nano* 7 (2013) 10654–10661, doi:10.1021/nn4053342.
- [76] W. Wu, J. Cao, M. Zhong, H. Wu, F. Zhang, J. Zhang, S. Guo, Separating graphene quantum dots by lateral size through gel column chromatography, *RSC Adv* 9 (2019) 18898–18901, doi:10.1039/c9ra03623g.
- [77] Y. Sun, S. Wang, C. Li, P. Luo, L. Tao, Y. Wei, G. Shi, Large scale preparation of graphene quantum dots from graphite with tunable fluorescence properties, *Phys. Chem. Chem. Phys.* 15 (2013) 9907–9913, doi:10.1039/c3cp50691f.
- [78] J. Zdražil, R. Zahradníček, R. Mohan, P. Sedláček, L. Nejd, V. Schmiedová, J. Pospíšil, M. Horák, M. Weiter, O. Zmeškal, J. Hubálek, Preparation of graphene quantum dots through liquid phase exfoliation method, *J. Lumin.* 204 (2018) 203–208, doi:10.1016/j.jlumin.2018.08.017.
- [79] X. Yan, B. Li, L.S. Li, Colloidal graphene quantum dots with well-defined structures, *Acc. Chem. Res.* 46 (2013) 2254–2262, doi:10.1021/ar300137p.
- [80] S. Kang, Y.K. Jeong, K.H. Jung, Y. Son, S.C. Choi, G.S. An, H. Han, K.M. Kim, Simple preparation of graphene quantum dots with controllable surface states from graphite, *RSC Adv* 9 (2019) 38447–38453, doi:10.1039/c9ra07555k.
- [81] F. Yuan, P. He, Z. Xi, X. Li, Y. Li, H. Zhong, L. Fan, S. Yang, Highly efficient and stable white LEDs based on pure red narrow bandwidth emission triangular carbon quantum dots for wide-color gamut backlight displays, *Nano Res* 12 (2019) 1669–1674, doi:10.1007/s12274-019-2420-x.
- [82] P. Tian, L. Tang, K.S. Teng, S.P. Lau, Graphene quantum dots from chemistry to applications, *Mater. Today Chem.* 10 (2018) 221–258, doi:10.1016/j.mtchem.2018.09.007.
- [83] Y. Wang, W. Kong, L. Wang, J.Z. Zhang, Y. Li, X. Liu, Y. Li, Optimizing oxygen functional groups in graphene quantum dots for improved antioxidant mechanism, *Phys. Chem. Chem. Phys.* 21 (2019) 1336–1343, doi:10.1039/c8cp06768f.
- [84] H. Park, S. Hyun Noh, J. Hye Lee, J. Yun Jaung, S. Geol Lee, T. Hee Han, Large scale synthesis and light emitting fibers of tailor-made graphene quantum dots, *Sci. Rep.* 5 (2015) 14163, doi:10.1038/srep14163.
- [85] T. Pillar-Little, D.Y. Kim, Differentiating the impact of nitrogen chemical states on optical properties of nitrogen-doped graphene quantum dots, *RSC Adv* 7 (2017) 48263–48267, doi:10.1039/c7ra09252k.
- [86] D. Qu, M. Zheng, L. Zhang, H. Zhao, Z. Xie, X. Jing, R.E. Haddad, H. Fan, Formation mechanism and optimization of highly luminescent N-doped graphene quantum dots, *Sci. Rep.* 4 (2014) 1–11, doi:10.1038/srep05294.
- [87] K. Holá, M. Sudolská, S. Kalytchuk, D. Nachtigallová, A.L. Rogach, M. Otyepka, R. Zbořil, Graphitic nitrogen triggers red fluorescence in carbon dots, *ACS Nano* 11 (2017) 12402–12410, doi:10.1021/acsnano.7b06399.
- [88] R. Li, Y. Liu, Z. Li, J. Shen, Y. Yang, X. Cui, G. Yang, Bottom-up fabrication of single-layered nitrogen-doped graphene quantum dots through intermolecular carbonization arrayed in a 2D plane, *Chem. A Eur. J.* 22 (2016) 272–278, doi:10.1002/chem.201503191.
- [89] Y. Li, Y. Zhao, H. Cheng, Y. Hu, G. Shi, L. Dai, L. Qu, Nitrogen-doped graphene quantum dots with oxygen-rich functional groups, *J. Am. Chem. Soc.* 134 (2012) 15–18, doi:10.1021/ja206030c.
- [90] W.-S. Kuo, C.-Y. Chang, K.-S. Huang, J.-C. Liu, Y.-T. Shao, C.-H. Yang, P.-C. Wu, Amino-functionalized nitrogen-doped graphene-quantum-dot-based nanomaterials with nitrogen and amino-functionalized group content dependence for highly efficient two-photon bioimaging, *Int. J. Mol. Sci.* 21 (2020) 2939, doi:10.3390/ijms21082939.
- [91] M.J. Sweetman, S.M. Hickey, D.A. Brooks, J.D. Hayball, S.E. Plush, A Practical guide to prepare and synthetically modify graphene quantum dots, *Adv. Funct. Mater.* 29 (2019) 1808740, doi:10.1002/adfm.201808740.
- [92] S. Zhu, J. Shao, Y. Song, X. Zhao, J. Du, L. Wang, H. Zhang, K. Zhang, J. Zhang, B. Yang, Investigating the surface state of graphene quantum dots, *Nanoscale* 7 (2015) 7927–7933, doi:10.1039/c5nr01178g.
- [93] C.I.M. Santos, I.F.A. Mariz, S.N. Pinto, G. Gonçalves, I. Bdkin, P.A.A.P. Marques, M.G.P.M.S. Neves, J.M.G. Martinho, E.M.S. Macôas, Selective two-photon absorption in carbon dots: A piece of the photoluminescence emission puzzle, *Nanoscale* 10 (2018) 12505–12514, doi:10.1039/c8nr03365j.
- [94] D. Mombrú, M. Romero, R. Faccio, A.W. Mombrú, Curvature and vacancies in graphene quantum dots, *Appl. Surf. Sci.* 462 (2018) 540–548, doi:10.1016/j.apsusc.2018.08.141.
- [95] J. Wu, P. Wang, F. Wang, Y. Fang, Investigation of the microstructures of graphene quantum dots (GQDs) by surface-enhanced Raman spectroscopy, *Nanomaterials* 8 (2018) 864, doi:10.3390/nano8100864.
- [96] G. Rajender, P.K. Giri, Formation mechanism of graphene quantum dots and their edge state conversion probed by photoluminescence and Raman spectroscopy, *J. Mater. Chem. C* 4 (2016) 10852–10865, doi:10.1039/c6tc03469a.

- [97] D. Pan, J. Zhang, Z. Li, M. Wu, Hydrothermal route for cutting graphene sheets into blue-luminescent graphene quantum dots, *Adv. Mater.* 22 (2010) 734–738, doi:10.1002/adma.200902825.
- [98] S.C. Ray, A. Saha, N.R. Jana, R. Sarkar, Fluorescent carbon nanoparticles: Synthesis, characterization, and bioimaging application, *J. Phys. Chem. C* 113 (2009) 18546–18551, doi:10.1021/jp905912n.
- [99] H. Luo, N. Papaioannou, E. Salvadori, M.M. Roessler, G. Ploenes, E.R.H. Eck, L.C. Tanase, J. Feng, Y. Sun, Y. Yang, M. Danaie, A. Belen Jorge, A. Sapelkin, J. Durrant, S.D. Dimitrov, M. Titirici, Manipulating the optical properties of carbon dots by fine-tuning their structural features, *ChemSusChem* 12 (2019) 4432–4441, doi:10.1002/cssc.201901795.
- [100] K.J. Mintz, Y. Zhou, R.M. Leblanc, Recent development of carbon quantum dots regarding their optical properties, photoluminescence mechanism, and core structure, *Nanoscale* 11 (2019) 4634–4652, doi:10.1039/c8nr10059d.
- [101] O. Kozák, M. Sudolská, G. Pramanik, P. Cígler, M. Otyepka, R. Zbořil, Photoluminescent carbon nanostructures, *Chem. Mater.* 28 (2016) 4085–4128, doi:10.1021/acs.chemmater.6b01372.
- [102] H. Ding, S.B. Yu, J.S. Wei, H.M. Xiong, Full-color light-emitting carbon dots with a surface-state-controlled luminescence mechanism, *ACS Nano* 10 (2016) 484–491, doi:10.1021/acsnano.5b05406.
- [103] W. Zhang, S.F. Yu, L. Fei, L. Jin, S. Pan, P. Lin, Large-area color controllable remote carbon white-light emitting diodes, *Carbon* 85 (2015) 344–350, doi:10.1016/j.carbon.2014.12.107.
- [104] H. Zhu, X. Wang, Y. Li, Z. Wang, F. Yang, X. Yang, Microwave synthesis of fluorescent carbon nanoparticles with electrochemiluminescence properties, *Chem. Commun.* (2009) 5118–5120, doi:10.1039/b907612c.
- [105] Y. Zhou, S.K. Sharma, Z. Peng, R.M. Leblanc, Polymers in carbon dots: a review, *Polymers* 9 (2017) 67, doi:10.3390/polym9020067.
- [106] A.B. Bourlinos, A. Stassinopoulos, D. Anglos, R. Zbořil, M. Karakassides, E.P. Giannelis, Surface functionalized carbogenic quantum dots, *Small* 4 (2008) 455–458, doi:10.1002/sml.200700578.
- [107] S.A. Hill, D. Benito-Alifonso, D.J. Morgan, S.A. Davis, M. Berry, M.C. Galan, Three-minute synthesis of sp³ nanocrystalline carbon dots as non-toxic fluorescent platforms for intracellular delivery, *Nanoscale* 8 (2016) 18630–18634, doi:10.1039/c6nr07336k.
- [108] A.B. Siddique, A.K. Pramanik, S. Chatterjee, M. Ray, Amorphous carbon dots and their remarkable ability to detect 2,4,6-trinitrophenol, *Sci. Rep.* 8 (2018) 1–10, doi:10.1038/s41598-018-28021-9.
- [109] X. Sun, C. Brückner, Y. Lei, One-pot and ultrafast synthesis of nitrogen and phosphorus co-doped carbon dots possessing bright dual wavelength fluorescence emission, *Nanoscale* 7 (2015) 17278–17282, doi:10.1039/c5nr05549k.
- [110] A. Sciortino, A. Cayuela, M.L. Soriano, F.M. Gelardi, M. Cannas, M. Valcárcel, F. Messina, Different natures of surface electronic transitions of carbon nanoparticles, *Phys. Chem. Chem. Phys.* 19 (2017) 22670–22677, doi:10.1039/c7cp04548d.
- [111] A. Sciortino, N. Mauro, G. Buscarino, L. Sciortino, R. Popescu, R. Schneider, G. Giammona, D. Gerthsen, M. Cannas, F. Messina, β -C₃N₄ nanocrystals: carbon dots with extraordinary morphological, structural, and optical homogeneity, *Chem. Mater.* 30 (2018) 1695–1700, doi:10.1021/acs.chemmater.7b05178.
- [112] J. Zhou, Y. Yang, C.Y. Zhang, A low-temperature solid-phase method to synthesize highly fluorescent carbon nitride dots with tunable emission, *Chem. Commun.* 49 (2013) 8605–8607, doi:10.1039/c3cc42266f.
- [113] M. Rong, X. Song, T. Zhao, Q. Yao, Y. Wang, X. Chen, Synthesis of highly fluorescent P,O-g-C₃N₄ nanodots for the label-free detection of Cu²⁺ and acetylcholinesterase activity, *J. Mater. Chem. C* 3 (2015) 10916–10924, doi:10.1039/c5c02584b.
- [114] T. Yuan, F. Yuan, X. Li, Y. Li, L. Fan, S. Yang, Fluorescence-phosphorescence dual emissive carbon nitride quantum dots show 25% white emission efficiency enabling single-component WLEDs, *Chem. Sci.* 10 (2019) 9801–9806, doi:10.1039/c9sc03492g.
- [115] W. Liu, C. Li, X. Sun, W. Pan, G. Yu, J. Wang, Highly crystalline carbon dots from fresh tomato: UV emission and quantum confinement, *Nanotechnology* 28 (2017) 485705, doi:10.1088/1361-6528/aa900b.
- [116] Q.-L. Zhao, Z.-L. Zhang, B.-H. Huang, J. Peng, M. Zhang, D.-W. Pang, Facile preparation of low cytotoxicity fluorescent carbon nanocrystals by electrooxidation of graphite, *Chem. Commun.* 0 (2008) 5116, doi:10.1039/b812420e.
- [117] Y. Xu, D. Li, M. Liu, F. Niu, J. Liu, E. Wang, Enhanced-quantum yield sulfur/nitrogen co-doped fluorescent carbon nanodots produced from biomass *Enteromorpha prolifera*: Synthesis, posttreatment, applications and mechanism study, *Sci. Rep.* 7 (2017) 1–12, doi:10.1038/s41598-017-04754-x.
- [118] L. Tian, D. Ghosh, W. Chen, S. Pradhan, X. Chang, S. Chen, Nanosized carbon particles from natural gas soot, *Chem. Mater.* 21 (2009) 2803–2809, doi:10.1021/cm900709w.
- [119] S.K. Bajpai, A. D'Souza, B. Suhail, Blue light-emitting carbon dots (CDs) from a milk protein and their interaction with *Spinacia oleracea* leaf cells, *Int. Nano Lett.* 9 (2019) 203–212, doi:10.1007/s40089-019-0271-9.
- [120] D.G. Babar, S.S. Garje, Nitrogen and phosphorus co-doped carbon dots for selective detection of nitro explosives, *ACS Omega* 5 (2020) 2710–2717, doi:10.1021/acsomega.9b03234.
- [121] I.J. Gomez, B. Arnaiz, M. Cacioppo, F. Arcudi, M. Prato, Nitrogen-doped carbon nanodots for bioimaging and delivery of paclitaxel, *J. Mater. Chem. B* 6 (2018) 5540–5548, doi:10.1039/c8tb01796d.
- [122] Y. Liu, L. Jiang, B. Li, X. Fan, W. Wang, P. Liu, S. Xu, X. Luo, Nitrogen doped carbon dots: Mechanism investigation and their application for label free CA125 analysis, *J. Mater. Chem. B* 7 (2019) 3053–3058, doi:10.1039/c9tb00021f.
- [123] A.B. Bourlinos, G. Trivizas, M.A. Karakassides, M. Baikousi, A. Kouloumpis, D. Gournis, A. Bakandritsos, K. Holá, O. Kozák, R. Zbořil, I. Papagiannouli, P. Aloukos, S. Couris, Green and simple route toward boron doped carbon dots with significantly enhanced non-linear optical properties, *Carbon* 83 (2015) 173–179, doi:10.1016/j.carbon.2014.11.032.
- [124] Q. Xu, P. Pu, J. Zhao, C. Dong, C. Gao, Y. Chen, J. Chen, Y. Liu, H. Zhou, Preparation of highly photoluminescent sulfur-doped carbon dots for Fe(III) detection, *J. Mater. Chem. A* 3 (2015) 542–546, doi:10.1039/c4ta05483k.
- [125] H. Peng, J. Travas-Sejdic, Simple aqueous solution route to luminescent carbogenic dots from carbohydrates, *Chem. Mater.* 21 (2009) 5563–5565, doi:10.1021/cm901593y.
- [126] Y. Dong, H. Pang, H. Bin Yang, C. Guo, J. Shao, Y. Chi, C.M. Li, T. Yu, Carbon-based dots co-doped with nitrogen and sulfur for high quantum yield and excitation-independent emission, *Angew. Chemie Int. Ed.* 52 (2013) 7800–7804, doi:10.1002/anie.201301114.
- [127] Y. Park, J. Yoo, B. Lim, W. Kwon, S.W. Rhee, Improving the functionality of carbon nanodots: Doping and surface functionalization, *J. Mater. Chem. A* 4 (2016) 11582–11603, doi:10.1039/c6ta04813g.
- [128] Q. Xu, B. Li, Y. Ye, W. Cai, W. Li, C. Yang, Y. Chen, M. Xu, N. Li, X. Zheng, J. Street, Y. Luo, L. Cai, Synthesis, mechanical investigation, and application of nitrogen and phosphorus co-doped carbon dots with a high photoluminescent quantum yield, *Nano Res.* 11 (2018) 3691–3701, doi:10.1007/s12274-017-1937-0.
- [129] L.J. Mohammed, K.M. Omer, Dual functional highly luminescence B, N co-doped carbon nanodots as nanothermometer and Fe³⁺/Fe²⁺ sensor, *Sci. Rep.* 10 (2020) 1–12, doi:10.1038/s41598-020-59958-5.
- [130] F. Yan, Y. Jiang, X. Sun, Z. Bai, Y. Zhang, X. Zhou, Surface modification and chemical functionalization of carbon dots: a review, *Microchim. Acta.* 185 (2018) 1–34, doi:10.1007/s00604-018-2953-9.
- [131] I. Papagiannouli, M. Patanen, V. Blanchet, J.D. Bozek, M. De Anda Villa, M. Huttula, E. Kokkonen, E. Lamour, E. Mevel, E. Pelimanni, A. Scalabre, M. Trassinelli, D.M. Bassani, A. Lévy, J. Gaudin, Depth profiling of the chemical composition of free-standing carbon dots using X-ray photoelectron spectroscopy, *J. Phys. Chem. C* 122 (2018) 14889–14897, doi:10.1021/acs.jpcc.8b03800.
- [132] F. Meierhofer, F. Dissinger, F. Weigert, J. Jungclaus, K. Müller-Caspary, S.R. Waldvogel, U. Resch-Genger, T. Voss, Citric acid based carbon dots with amine type stabilizers: pH-Specific luminescence and quantum yield characteristics, *J. Phys. Chem. C* 124 (2020) 8894–8904, doi:10.1021/acs.jpcc.9b11732.
- [133] E.A. Stepanidenko, I.A. Arefina, P.D. Khavlyuk, A. Dubavik, K.V. Bogdanov, V.P. Bondarenko, S.A. Cherevkov, E.V. Kondelev, A.V. Fedorov, A.V. Baranov, D.G. Maslov, E.V. Ushakova, A.L. Rogach, Influence of the solvent environment on luminescent centers within carbon dots, *Nanoscale* 12 (2020) 602–609, doi:10.1039/c9nr08663c.
- [134] T. Wang, A. Wang, R. Wang, Z. Liu, Y. Sun, G. Shan, Y. Chen, Y. Liu, Carbon dots with molecular fluorescence and their application as a "turn-off" fluorescent probe for ferricyanide detection, *Sci. Rep.* 9 (2019) 1–9, doi:10.1038/s41598-019-47168-7.
- [135] A.N. Starukhin, D.K. Nelson, D.A. Eurov, D.A. Kurdyukov, V.G. Golubev, Manifestation of fluorophore segmental motion in carbon dots in steady-state fluorescence experiments, *Phys. Chem. Chem. Phys.* 22 (2020) 8401–8408, doi:10.1039/d0cp00056f.
- [136] M. Righetto, A. Privitera, I. Fortunati, D. Mosconi, M. Zerbetto, M.L. Curri, M. Corricelli, A. Moretto, S. Agnoli, L. Franco, R. Bozico, C. Ferrante, Spectroscopic insights into carbon dot systems, *J. Phys. Chem. Lett.* 8 (2017) 2236–2242, doi:10.1021/acs.jpclett.7b00794.
- [137] M. Righetto, F. Carraro, A. Privitera, G. Marafon, A. Moretto, C. Ferrante, The Elusive nature of carbon nanodot fluorescence: an unconventional perspective, *J. Phys. Chem. C* 124 (2020) 22314–22320, doi:10.1021/acs.jpcc.0c06996.
- [138] W.J. Sell, T.H. Easterfield, LXXIII. - Studies on citrazinic acid. Part I, *J. Chem. Soc. Trans.* 63 (1893) 1035–1051, doi:10.1039/CT8936301035.
- [139] X. Liu, H.B. Li, L. Shi, X. Meng, Y. Wang, X. Chen, H. Xu, W. Zhang, X. Fang, T. Ding, Structure and photoluminescence evolution of nanodots during pyrolysis of citric acid: From molecular nanoclusters to carbogenic nanoparticles, *J. Mater. Chem. C* 5 (2017) 10302–10312, doi:10.1039/c7tc03429f.
- [140] S. Khan, A. Sharma, S. Ghoshal, S. Jain, M.K. Hazra, C.K. Nandi, Small molecular organic nanocrystals resemble carbon nanodots in terms of their properties, *Chem. Sci.* 9 (2017) 175–180, doi:10.1039/c7sc02528a.
- [141] L. Shi, J.H. Yang, H.B. Zeng, Y.M. Chen, S.C. Yang, C. Wu, H. Zeng, O. Yoshihito, Q. Zhang, Carbon dots with high fluorescence quantum yield: The fluorescence originates from organic fluorophores, *Nanoscale* 8 (2016) 14374–14378, doi:10.1039/c6nr00451b.
- [142] J. Zhang, L. Yang, Y. Yuan, J. Jiang, S.H. Yu, One-pot gram-scale synthesis of nitrogen and sulfur embedded organic dots with distinctive fluorescence behaviors in free and aggregated states, *Chem. Mater.* 28 (2016) 4367–4374, doi:10.1021/acs.chemmater.6b01360.
- [143] W. Kasprzyk, T. Świergosz, S. Bednarczyk, K. Walas, N.V. Bashmakova, D. Bogała, Luminescence phenomena of carbon dots derived from citric acid and urea—a molecular insight, *Nanoscale* 10 (2018) 13889–13894, doi:10.1039/c8nr03602k.
- [144] A. Das, V. Gude, D. Roy, T. Chatterjee, C.K. De, P.K. Mandal, On the molecular origin of photoluminescence of nonblinking carbon dot, *J. Phys. Chem. C* 121 (2017) 9634–9641, doi:10.1021/acs.jpcc.7b02433.
- [145] S. Cailotto, E. Amadio, M. Facchin, M. Selva, E. Pontoglio, F. Rizzolio, P. Riello, G. Toffoli, A. Benedetti, A. Perosa, Carbon dots from sugars and ascorbic acid:

- Role of the precursors on morphology, properties, toxicity, and drug uptake, *ACS Med. Chem. Lett.* 9 (2018) 832–837, doi:10.1021/acsmchemlett.8b00240.
- [146] A.P. Demchenko, M.O. Dekaliuk, The origin of emissive states of carbon nanoparticles derived from ensemble-averaged and single-molecular studies, *Nanoscale* 8 (2016) 14057–14069, doi:10.1039/c6nr02669a.
- [147] A. Sharma, T. Gady, A. Gupta, A. Ballal, S.K. Ghosh, M. Kumbhakar, Origin of excitation dependent fluorescence in carbon nanodots, *J. Phys. Chem. Lett.* 7 (2016) 3695–3702, doi:10.1021/acs.jpclett.6b01791.
- [148] C.J. Reckmeier, J. Schneider, Y. Xiong, J. Häusler, P. Kasák, W. Schnick, A.L. Rogach, Aggregated molecular fluorophores in the ammonothermal synthesis of carbon dots, *Chem. Mater.* 29 (2017) 10352–10361, doi:10.1021/acs.chemmater.7b03344.
- [149] X. Wang, K. Qu, B. Xu, J. Ren, X. Qu, Microwave assisted one-step green synthesis of cell-permeable multicolor photoluminescent carbon dots without surface passivation reagents, *J. Mater. Chem.* 21 (2011) 2445, doi:10.1039/c0jm02963g.
- [150] Y. Sun, W. Cao, S. Li, S. Jin, K. Hu, L. Hu, Y. Huang, X. Gao, Y. Wu, X.J. Liang, Ultrabright and multicolorful fluorescence of amphiphilic polyethyleneimine polymer dots for efficiently combined imaging and therapy, *Sci. Rep.* 3 (2013) 1–6, doi:10.1038/srep03036.
- [151] S.Y. Lim, W. Shen, Z. Gao, Carbon quantum dots and their applications, *Chem. Soc. Rev.* 44 (2014) 362–381, doi:10.1039/c4cs00269e.
- [152] Y. Chen, M. Zheng, Y. Xiao, H. Dong, H. Zhang, J. Zhuang, H. Hu, B. Lei, Y. Liu, A self-quenching-resistant carbon-dot powder with tunable solid-state fluorescence and construction of dual-fluorescence morphologies for white light-emission, *Adv. Mater.* 28 (2016) 312–318, doi:10.1002/adma.201503380.
- [153] W. Li, Z. Zhang, B. Kong, S. Feng, J. Wang, L. Wang, J. Yang, F. Zhang, P. Wu, D. Zhao, Simple and green synthesis of nitrogen-doped photoluminescent carbonaceous nanospheres for bioimaging, *Angew. Chemie Int. Ed.* 52 (2013) 8151–8155, doi:10.1002/anie.201303927.
- [154] M.L. Liu, B. Bin Chen, C.M. Li, C.Z. Huang, Carbon dots: Synthesis, formation mechanism, fluorescence origin and sensing applications, *Green Chem.* 21 (2019) 449–471, doi:10.1039/c8gc02736f.
- [155] X. Hai, J. Feng, X. Chen, J. Wang, Tuning the optical properties of graphene quantum dots for biosensing and bioimaging, *J. Mater. Chem. B.* 6 (2018) 3219–3234, doi:10.1039/c8tb00428e.
- [156] M. Fu, F. Ehrat, Y. Wang, K.Z. Milowska, C. Reckmeier, A.L. Rogach, J.K. Stolarczyk, A.S. Urban, J. Feldmann, Carbon dots: A Unique fluorescent cocktail of polycyclic aromatic hydrocarbons, *Nano Lett.* 15 (2015) 6030–6035, doi:10.1021/acs.nanolett.5b02215.
- [157] M.L. Mueller, X. Yan, J.A. McGuire, L.S. Li, Triplet states and electronic relaxation in photoexcited graphene quantum dots, *Nano Lett.* 10 (2010) 2679–2682, doi:10.1021/nl101474d.
- [158] A. Chemie, I. Edition, S. Uni, Water-soluble fluorescent carbon quantum dots and photocatalyst, (2010) 4532–4536, doi:10.1002/anie.200906154.
- [159] W. Kwon, G. Lee, S. Do, T. Joo, S.W. Rhee, Size-controlled soft-template synthesis of carbon nanodots toward versatile photoactive materials, *Small* 10 (2014) 506–513, doi:10.1002/smll.201301770.
- [160] L. Wang, S.J. Zhu, H.Y. Wang, S.N. Qu, Y.L. Zhang, J.H. Zhang, Q.D. Chen, H.L. Xu, W. Han, B. Yang, H.B. Sun, Common origin of green luminescence in carbon nanodots and graphene quantum dots, *ACS Nano* 8 (2014) 2541–2547, doi:10.1021/nm500368m.
- [161] S. Wang, I.S. Cole, D. Zhao, Q. Li, The dual roles of functional groups in the photoluminescence of graphene quantum dots, *Nanoscale* 8 (2016) 7449–7458, doi:10.1039/c5nr07042b.
- [162] X. Guo, Y. Zhu, L. Zhou, L. Zhang, Y. You, H. Zhang, J. Hao, A facile and green approach to prepare carbon dots with pH-dependent fluorescence for patterning and bioimaging, *RSC Adv* 8 (2018) 38091–38099, doi:10.1039/c8ra07584k.
- [163] S. Lu, R. Cong, S. Zhu, X. Zhao, J. Liu, J. S. tse, S. Meng, B. Yang, pH-Dependent synthesis of novel structure-controllable polymer-carbon nanodots with high acidophilic luminescence and super carbon dots assembly for white light-emitting diodes, *ACS Appl. Mater. Interfaces.* 8 (2016) 4062–4068, doi:10.1021/acsami.5b11579.
- [164] W. Wang, B. Wang, H. Embrechts, C. Damm, A. Cadranell, V. Strauss, M. Distaso, V. Hinterberger, D.M. Guldi, W. Peukert, Shedding light on the effective fluorophore structure of high fluorescence quantum yield carbon nanodots, *RSC Adv.* 7 (2017) 24771–24780, doi:10.1039/c7ra04421f.
- [165] S. Zhu, J. Zhang, S. Tang, C. Qiao, L. Wang, H. Wang, X. Liu, B. Li, Y. Li, W. Yu, X. Wang, H. Sun, B. Yang, Surface chemistry routes to modulate the photoluminescence of graphene quantum dots: from fluorescence mechanism to up-conversion bioimaging applications, *Adv. Funct. Mater.* 22 (2012) 4732–4740, doi:10.1002/adfm.201201499.
- [166] V. Strauss, A. Kahnt, E.M. Zolnhofer, K. Meyer, H. Maid, C. Placht, W. Bauer, T.J. Nacken, W. Peukert, S.H. Etschel, M. Halik, D.M. Guldi, Assigning electronic states in carbon nanodots, *Adv. Funct. Mater.* 26 (2016) 7975–7985, doi:10.1002/adfm.201602325.
- [167] M.J. Krysmann, A. Kellarakis, P. Dallas, E.P. Giannelis, Formation mechanism of carbogenic nanoparticles with dual photoluminescence emission, *J. Am. Chem. Soc.* 134 (2012) 747–750, doi:10.1021/ja204661r.
- [168] S. Zhu, L. Wang, N. Zhou, X. Zhao, Y. Song, S. Maharjan, J. Zhang, L. Lu, H. Wang, B. Yang, The crosslink enhanced emission (CEE) in non-conjugated polymer dots: From the photoluminescence mechanism to the cellular uptake mechanism and internalization, *Chem. Commun.* 50 (2014) 13845–13848, doi:10.1039/c4cc05806b.
- [169] F. Plasser, H. Pašalić, M.H. Gerzabek, F. Libisch, R. Reiter, J. Burgdörfer, T. Müller, R. Shepard, H. Lischka, The multidirectional character of one- and two-dimensional graphene nanoribbons, *Angew. Chemie - Int. Ed.* 52 (2013) 2581–2584, doi:10.1002/anie.201207671.
- [170] S. Horn, F. Plasser, T. Müller, F. Libisch, J. Burgdörfer, H. Lischka, A comparison of singlet and triplet states for one- and two-dimensional graphene nanoribbons using multireference theory, *Theor. Chem. Acc.* 133 (2014) 1–9, doi:10.1007/s00214-014-1511-8.
- [171] Y. Yang, E.R. Davidson, W. Yang, Nature of ground and electronic excited states of higher acenes, *Proc. Natl. Acad. Sci. U. S. A.* 113 (2016) E5098–E5107, doi:10.1073/pnas.1606021113.
- [172] F. Bettanin, L.F.A. Ferrão, M. Pinheiro, A.J.A. Aquino, H. Lischka, F.B.C. Machado, D. Nachtigallova, Singlet L_a and L_b bands for N-acenes (N=2–7): A CASSCF/CASPT2 study, *J. Chem. Theory Comput.* 13 (2017) 4297–4306, doi:10.1021/acs.jctc.7b00302.
- [173] T. Wassmann, A.P. Seitsonen, A.M. Saitta, M. Lazzeri, F. Mauri, Clar's theory, π -electron distribution, and geometry of graphene nanoribbons, *J. Am. Chem. Soc.* 132 (2010) 3440–3451, doi:10.1021/ja909234y.
- [174] A.T. Balaban, D.J. Klein, Claromatic carbon nanostructures, *J. Phys. Chem. C.* 113 (2009) 19123–19133, doi:10.1021/jp9082618.
- [175] M. Solà, Forty years of Clar's aromatic π -sextet rule, *Front. Chem.* 1 (2013) 22, doi:10.3389/fchem.2013.00022.
- [176] S. Xin, A. Aquino, M. Otyepka, D. Nachtigallova, H. Lischka, Tuning the UV spectrum of PAHs by means of different N-doping types taking pyrene as paradigmatic example: categorization via valence bond theory and high-level computational approaches, *Phys. Chem. Chem. Phys.* (2020), doi:10.1039/d0cp2688c.
- [177] A. Das, T. Müller, F. Plasser, D.B. Krisiloff, E.A. Carter, H. Lischka, Local electron correlation treatment in extended multireference calculations: Effect of acceptor-donor substituents on the biradical character of the polycyclic aromatic hydrocarbon heptazethrene, *J. Chem. Theory Comput.* 13 (2017) 2612–2622, doi:10.1021/acs.jctc.7b00156.
- [178] M. Pinheiro, L.F.A. Ferrão, F. Bettanin, A.J.A. Aquino, F.B.C. Machado, H. Lischka, How to efficiently tune the biradicaloid nature of acenes by chemical doping with boron and nitrogen, *Phys. Chem. Chem. Phys.* 19 (2017) 19225–19233, doi:10.1039/c7cp03198j.
- [179] A. Das, M. Pinheiro, F.B.C. Machado, A.J.A. Aquino, H. Lischka, Tuning the biradicaloid nature of polycyclic aromatic hydrocarbons: The effect of graphitic nitrogen doping in zethrenes, *ChemPhysChem* 19 (2018) 2492–2499, doi:10.1002/cphc.201800650.
- [180] M. Kasha, Characterization of electronic transitions in complex molecules, *Discuss. Faraday Soc.* 9 (1950) 14–19, doi:10.1039/DF9500900014.
- [181] P. Hohenberg, W. Kohn, Inhomogeneous electron gas, *Phys. Rev.* 136 (1964) B864, doi:10.1103/PhysRev.136.B864.
- [182] W. Kohn, L.J. Sham, Self-consistent equations including exchange and correlation effects, *Phys. Rev.* 140 (1965) A1133, doi:10.1103/PhysRev.140.A1133.
- [183] J.D. Da Motta Neto, M.C. Zerner, New parametrization scheme for the resonance integrals ($H_{\mu\nu}$) within the INDO/1 approximation. Main group elements, *Int. J. Quantum Chem.* 81 (2001) 187–201.
- [184] J.J.P. Stewart, Optimization of parameters for semiempirical methods VI: More modifications to the NDDO approximations and re-optimization of parameters, *J. Mol. Model.* 19 (2013) 1–32, doi:10.1007/s00894-012-1667-x.
- [185] J.T. Margraf, V. Strauss, D.M. Guldi, T. Clark, The electronic structure of amorphous carbon nanodots, *J. Phys. Chem. B.* 119 (2015) 7258–7265, doi:10.1021/jp510620j.
- [186] P.O. Dral, T. Clark, Semiempirical UNO-CAS and UNO-CI: Method and applications in nanoelectronics, *J. Phys. Chem. A.* 115 (2011) 11303–11312, doi:10.1021/jp204939x.
- [187] A.V. Vorontsov, E.V. Tretyakov, Determination of graphene's edge energy using hexagonal graphene quantum dots and PM7 method, *Phys. Chem. Chem. Phys.* 20 (2018) 14740–14752, doi:10.1039/c7cp08411k.
- [188] M.F. Budyka, Semiempirical study on the absorption spectra of the coronene-like molecular models of graphene quantum dots, *Spectrochim. Acta - Part A Mol. Biomol. Spectrosc.* 207 (2019) 1–5, doi:10.1016/j.saa.2018.09.007.
- [189] M. Elstner, D. Porezag, G. Jungnickel, J. Elsner, M. Haugk, T. Frauenheim, Self-consistent-charge density-functional tight-binding method for simulations of complex materials properties, *Phys. Rev. B - Condens. Matter Mater. Phys.* 58 (1998) 7260–7268, doi:10.1103/PhysRevB.58.7260.
- [190] G. Seifert, Tight-binding density functional theory: an approximate Kohn-Sham DFT scheme, *J. Phys. Chem. A.* 111 (2007) 5609–5613, doi:10.1021/jp069056r.
- [191] G. Seifert, D. Porezag, T. Frauenheim, Calculations of molecules, clusters, and solids with a simplified LCAO-DFT-LDA scheme, *Int. J. Quantum Chem.* 58 (1996) 185–192.
- [192] A.F. Oliveira, G. Seifert, T. Heine, H.A. Duarte, Density-functional based tight-binding: an approximate DFT method, *J. Braz. Chem. Soc.* 20 (2009) 1193–1205, doi:10.1590/S0103-50532009000700002.
- [193] A.J. Page, H. Yamane, Y. Ohta, S. Irlé, K. Morokuma, QM/MD simulation of SWNT nucleation on transition-metal carbide nanoparticles, *J. Am. Chem. Soc.* 132 (2010) 15699–15707, doi:10.1021/ja106264q.
- [194] T. Lei, W. Guo, Q. Liu, H. Jiao, D.B. Cao, B. Teng, Y.W. Li, X. Liu, X.D. Wen, Mechanism of graphene formation via detonation synthesis: A DFTB nanoreactor approach, *J. Chem. Theory Comput.* 15 (2019) 3654–3665, doi:10.1021/acs.jctc.9b00158.

- [195] M. Langer, M. Paloncýová, M. Medved, M. Otyepka, Molecular fluorophores self-organize into c-dot seeds and incorporate into C-dot structures, *J. Phys. Chem. Lett.* 11 (2020) 8252–8258, doi:10.1021/acs.jpclett.0c01873.
- [196] M. Paloncýová, M. Langer, M. Otyepka, Structural dynamics of carbon dots in water and *N,N*-dimethylformamide probed by all-atom molecular dynamics simulations, *J. Chem. Theory Comput.* 14 (2018) 2076–2083, doi:10.1021/acs.jctc.7b01149.
- [197] P.G. Szalay, T. Müller, G. Gidofalvi, H. Lischka, R. Shepard, Multiconfiguration self-consistent field and multireference configuration interaction methods and applications, *Chem. Rev.* 112 (2012) 108–181, doi:10.1021/cr200137a.
- [198] H. Lischka, D. Nachtigallová, A.J.A. Aquino, P.G. Szalay, F. Plasser, F.B.C. Machado, M. Barbatti, Multireference approaches for excited states of molecules, *Chem. Rev.* 118 (2018) 7293–7361, doi:10.1021/acs.chemrev.8b00244.
- [199] J.B. Foresman, M. Head-Gordon, J.A. Pople, M.J. Frisch, Toward a systematic molecular orbital theory for excited states, *J. Phys. Chem.* 96 (1992) 135–149, doi:10.1021/j100180a030.
- [200] C. Möller, M.S. Plesset, Note on an approximation treatment for many-electron systems, *Phys. Rev.* 46 (1934) 618–622, doi:10.1103/PhysRev.46.618.
- [201] J. Čížek, On the correlation problem in atomic and molecular systems. Calculation of wavefunction components in *ur*-sell-type expansion using quantum-field theoretical methods, *J. Chem. Phys.* 45 (1966) 4256–4266, doi:10.1063/1.1727484.
- [202] B.O. Roos, P.R. Taylor, P.E.M. Sigbahn, A complete active space SCF method (CASSCF) using a density matrix formulated super-CI approach, *Chem. Phys.* 48 (1980) 157–173, doi:10.1016/0301-0104(80)80045-0.
- [203] K. Andersson, P.Å. Malmqvist, B.O. Roos, A.J. Sadlej, K. Wolinski, Second-order perturbation theory with a CASSCF reference function, *J. Phys. Chem.* 94 (1990) 5483–5488, doi:10.1021/j100377a012.
- [204] K. Andersson, P.Å. Malmqvist, B.O. Roos, Second-order perturbation theory with a complete active space self-consistent field reference function, *J. Chem. Phys.* 96 (1992) 1218–1226, doi:10.1063/1.462209.
- [205] N. Mardirossian, M. Head-Gordon, Thirty years of density functional theory in computational chemistry: an overview and extensive assessment of 200 density functionals, *Mol. Phys.* 115 (2017) 2315–2372, doi:10.1080/00268976.2017.1333644.
- [206] J.P. Perdew, Jacob's ladder of density functional approximations for the exchange-correlation energy, *AIP Conf. Proc.* 577 (2003) 1–20, doi:10.1063/1.1390175.
- [207] H. Iikura, T. Tsuneda, T. Yanai, K. Hirao, A long-range correction scheme for generalized-gradient-approximation exchange functionals, *J. Chem. Phys.* 115 (2001) 3540–3544, doi:10.1063/1.1383587.
- [208] J. Dai, M. Head-Gordon, Long-range corrected hybrid density functionals with damped atom-atom dispersion corrections, *Phys. Chem. Chem. Phys.* 10 (2008) 6615–6620, doi:10.1039/b810189b.
- [209] T.M. Henderson, A.F. Izmaylov, G. Scalmani, G.E. Scuseria, Can short-range hybrids describe long-range-dependent properties? *J. Chem. Phys.* 131 (2009) 044108, doi:10.1063/1.3185673.
- [210] T. Yanai, D.P. Tew, N.C. Handy, A new hybrid exchange-correlation functional using the Coulomb-attenuating method (CAM-B3LYP), *Chem. Phys. Lett.* 393 (2004) 51–57, doi:10.1016/j.cplett.2004.06.011.
- [211] M. Sudolská, M. Dubecký, S. Sarkar, C.J. Reckmeier, R. Zbořil, A.L. Rogach, M. Otyepka, Nature of absorption bands in oxygen-functionalized graphitic carbon dots, *J. Phys. Chem. C* 119 (2015) 13369–13373, doi:10.1021/acs.jpcc.5b04080.
- [212] A.D. Laurent, D. Jacquemin, TD-DFT benchmarks: a review, *Int. J. Quantum Chem.* 113 (2013) 2019–2039, doi:10.1002/qua.24438.
- [213] J. Klimeš, A. Michaelides, Perspective: advances and challenges in treating van der Waals dispersion forces in density functional theory, *J. Chem. Phys.* 137 (2012) 120901, doi:10.1063/1.4754130.
- [214] F. Furche, R. Ahlrichs, Adiabatic time-dependent density functional methods for excited state properties, *J. Chem. Phys.* 117 (2002) 7433–7447, doi:10.1063/1.1508368.
- [215] R. Grotjahn, M. Kaupp, Validation of local hybrid functionals for excited states: Structures, fluorescence, phosphorescence, and vibronic spectra, *J. Chem. Theory Comput.* 16 (2020) 5821–5834, doi:10.1021/acs.jctc.0c00520.
- [216] P. Elliott, S. Goldson, C. Canahui, N.T. Maitra, Perspectives on double-excitations in TDDFT, *Chem. Phys.* 391 (2011) 110–119, doi:10.1016/j.chemphys.2011.03.020.
- [217] M. Parac, S. Grimme, A TDDFT study of the lowest excitation energies of polycyclic aromatic hydrocarbons, *Chem. Phys.* 292 (2003) 11–21, doi:10.1016/S0301-0104(03)00250-7.
- [218] S. Grimme, M. Parac, Substantial errors from time-dependent density functional theory for the calculation of excited states of large π systems, *ChemPhysChem* 4 (2003) 292–295, doi:10.1002/cphc.200390047.
- [219] B.M. Wong, T.H. Hsieh, Optoelectronic and excitonic properties of oligoacenes: Substantial improvements from range-separated time-dependent density functional theory, *J. Chem. Theory Comput.* 6 (2010) 3704–3712, doi:10.1021/ct100529s.
- [220] R.M. Richard, J.M. Herbert, Time-dependent density-functional description of the 1L_a state in polycyclic aromatic hydrocarbons: Charge-transfer character in disguise? *J. Chem. Theory Comput.* 7 (2011) 1296–1306, doi:10.1021/ct100607w.
- [221] L. Goerigk, S. Grimme, Double-hybrid density functionals provide a balanced description of excited 1L_a and 1L_b states in polycyclic aromatic hydrocarbons, *J. Chem. Theory Comput.* 7 (2011) 3272–3277, doi:10.1021/ct100380v.
- [222] L. Goerigk, J. Moellmann, S. Grimme, Computation of accurate excitation energies for large organic molecules with double-hybrid density functionals, *Phys. Chem. Chem. Phys.* 11 (2009) 4611–4620, doi:10.1039/b902315a.
- [223] A. Karton, A. Tarnopolsky, J.F. Lamère, G.C. Schatz, J.M.L. Martin, Highly accurate first-principles benchmark data sets for the parametrization and validation of density functional and other approximate methods. Derivation of a robust, generally applicable, double-hybrid functional for thermochemistry and thermochemical kinetics, *J. Phys. Chem. A* 112 (2008) 12868–12886, doi:10.1021/jp801805p.
- [224] B. Shi, D. Nachtigallová, A.J.A. Aquino, F.B.C. Machado, H. Lischka, High-level theoretical benchmark investigations of the UV-vis absorption spectra of paradigmatic polycyclic aromatic hydrocarbons as models for graphene quantum dots, *J. Chem. Phys.* 150 (2019) 124302, doi:10.1063/1.5086760.
- [225] A.D. Becke, Density-functional thermochemistry. III. The role of exact exchange, *J. Chem. Phys.* 98 (1993) 5648–5652, doi:10.1063/1.464913.
- [226] P.J. Stephens, F.J. Devlin, C.F. Chabalowski, M.J. Frisch, Ab initio calculation of vibrational absorption and circular dichroism spectra using density functional force fields, *J. Phys. Chem.* 98 (1994) 11623–11627, doi:10.1021/j100096a001.
- [227] O. Christiansen, H. Koch, P. Jørgensen, The second-order approximate coupled cluster singles and doubles model CC2, *Chem. Phys. Lett.* 243 (1995) 409–418, doi:10.1016/0009-2614(95)00841-Q.
- [228] J. Schirmer, Beyond the random-phase approximation: A new approximation scheme for the polarization propagator, *Phys. Rev. A* 26 (1982) 2395–2416, doi:10.1103/PhysRevA.26.2395.
- [229] S. Knippenberg, D.R. Rehn, M. Wormit, J.H. Starcke, I.L. Rusakova, A.B. Trofimov, A. Dreuw, Calculations of nonlinear response properties using the intermediate state representation and the algebraic-diagrammatic construction polarization propagator approach: two-photon absorption spectra, *J. Chem. Phys.* (2012) 064107, doi:10.1063/1.3682324.
- [230] S. Knippenberg, J.H. Starcke, M. Wormit, A. Dreuw, The low-lying excited states of neutral polyacenes and their radical cations: a quantum chemical study employing the algebraic diagrammatic construction scheme of second order, *Mol. Phys.* 108 (2010) 2801–2813, doi:10.1080/00268976.2010.526643.
- [231] A. Dreuw, M. Wormit, The algebraic diagrammatic construction scheme for the polarization propagator for the calculation of excited states, *Wiley Interdiscip. Rev. Comput. Mol. Sci.* 5 (2015) 82–95, doi:10.1002/wcms.1206.
- [232] H. Koch, O. Christiansen, P. Jørgensen, A.M. Sanchez De Merás, T. Helgaker, The CC3 model: An iterative coupled cluster approach including connected triples, *J. Chem. Phys.* 106 (1997) 1808–1818, doi:10.1063/1.473322.
- [233] J.D. Watts, R.J. Bartlett, Economical triple excitation equation-of-motion coupled-cluster methods for excitation energies, *Chem. Phys. Lett.* 233 (1995) 81–87, doi:10.1016/0009-2614(94)01434-W.
- [234] M. Estévez-Fregoso, J. Hernández-Trujillo, Electron delocalization and electron density of small polycyclic aromatic hydrocarbons in singlet excited states, *Phys. Chem. Chem. Phys.* 18 (2016) 11792–11799, doi:10.1039/c5cp06993a.
- [235] C. Angeli, R. Cimraglia, J.P. Malrieu, N-electron valence state perturbation theory: A fast implementation of the strongly contracted variant, *Chem. Phys. Lett.* 350 (2001) 297–305, doi:10.1016/S0009-2614(01)01303-3.
- [236] C. Angeli, R. Cimraglia, J.P. Malrieu, N-electron valence state perturbation theory: a spinless formulation and an efficient implementation of the strongly contracted and of the partially contracted variants, *J. Chem. Phys.* 117 (2002) 9138–9153, doi:10.1063/1.1515317.
- [237] L. Cusinato, S. Evangelisti, T. Leininger, A. Monari, The Electronic Structure of Graphene Nanoislands: A CAS-SCF and NEVPT2 Study, *Adv. Condens. Matter Phys.* 2018 (2018) 9097045, doi:10.1155/2018/9097045.
- [238] N. Nakatani, S. Guo, Density matrix renormalization group (DMRG) method as a common tool for large active-space CASSCF/CASPT2 calculations, *J. Chem. Phys.* 146 (2017) 094102, doi:10.1063/1.4976644.
- [239] A.Y. Sokolov, S. Guo, E. Ronca, G.K.L. Chan, Time-dependent N-electron valence perturbation theory with matrix product state reference wavefunctions for large active spaces and basis sets: Applications to the chromium dimer and all-trans polyenes, *J. Chem. Phys.* 146 (2017) 244102, doi:10.1063/1.4986975.
- [240] Y. Kurashige, J. Chalupský, T.N. Lan, T. Yanai, Complete active space second-order perturbation theory with cumulant approximation for extended active-space wavefunction from density matrix renormalization group, *J. Chem. Phys.* 141 (2014) 174111, doi:10.1063/1.4900878.
- [241] Y. Kurashige, T. Yanai, Theoretical study of the $\pi \rightarrow \pi^*$ excited states of oligoacenes: A full π -Valence DMRG-CASPT2 study, *Bull. Chem. Soc. Jpn.* 87 (2014) 1071–1073, doi:10.1246/bcsj.20140180.
- [242] M. Das, Computational investigation on tunable optical band gap in armchair polyacenes, *J. Chem. Phys.* 143 (2015) 064704, doi:10.1063/1.4928571.
- [243] S. Shirai, Y. Kurashige, T. Yanai, Computational evidence of inversion of 1L_a and 1L_b -derived excited states in naphthalene excimer formation from *ab initio* multireference theory with large active space: DMRG-CASPT2 study, *J. Chem. Theory Comput.* 12 (2016) 2366–2372, doi:10.1021/acs.jctc.6b00210.
- [244] C.M. Marian, N. Gilka, Performance of the density functional theory/multireference configuration interaction method on electronic excitation of extended π -systems, *J. Chem. Theory Comput.* 4 (2008) 1501–1515, doi:10.1021/ct8001738.
- [245] S. Grimme, M. Waletzke, A combination of Kohn-Sham density functional theory and multi-reference configuration interaction methods, *J. Chem. Phys.* 111 (1999) 5645–5655, doi:10.1063/1.479866.
- [246] H.F. Bettinger, C. Tönshoff, M. Doerr, E. Sanchez-Garcia, Electronically excited states of higher acenes up to nonacene: A Density functional the-

- ory/multireference configuration interaction study, *J. Chem. Theory Comput.* 12 (2016) 305–312, doi:10.1021/acs.jctc.5b00671.
- [247] M.R. Silva-Junior, M. Schreiber, S.P.A. Sauer, W. Thiel, Benchmarks for electronically excited states: Time-dependent density functional theory and density functional theory based multireference configuration interaction, *J. Chem. Phys.* 129 (2008) 104103, doi:10.1063/1.2973541.
- [248] B. Shi, D. Nachtigallová, A.J.A. Aquino, F.B.C. Machado, H. Lischka, Excited states and excitonic interactions in prototypic polycyclic aromatic hydrocarbon dimers as models for graphitic interactions in carbon dots, *Phys. Chem. Chem. Phys.* 21 (2019) 9077–9088, doi:10.1039/c9cp00635d.
- [249] X. Yan, X. Cui, L.S. Li, Synthesis of large, stable colloidal graphene quantum dots with tunable size, *J. Am. Chem. Soc.* 132 (2010) 5944–5945, doi:10.1021/ja1009376.
- [250] B. Shi, D. Nachtigallová, A.J.A. Aquino, F.B.C. Machado, H. Lischka, Emission energies and Stokes shifts for single polycyclic aromatic hydrocarbon sheets in comparison to the effect of excimer formation, *J. Phys. Chem. Lett.* 10 (2019) 5592–5597, doi:10.1021/acs.jpclett.9b02214.
- [251] J. Tomasi, B. Mennucci, R. Cammi, Quantum mechanical continuum solvation models, *Chem. Rev.* 105 (2005) 2999–3093, doi:10.1021/cr9904009.
- [252] A.V. Marenich, C.J. Cramer, D.G. Truhlar, Universal solvation model based on solute electron density and on a continuum model of the solvent defined by the bulk dielectric constant and atomic surface tensions, *J. Phys. Chem. B* 113 (2009) 6378–6396, doi:10.1021/jp810292n.
- [253] A. Klamt, G. Schüürmann, COSMO: A new approach to dielectric screening in solvents with explicit expressions for the screening energy and its gradient, *J. Chem. Soc. Perkin Trans. 2* (1993) 799–805, doi:10.1039/P29930000799.
- [254] B. Mennucci, Modeling absorption and fluorescence solvatochromism with QM/Classical approaches, *Int. J. Quantum Chem.* 115 (2015) 1202–1208, doi:10.1002/qua.24889.
- [255] R. Cammi, B. Mennucci, Linear response theory for the polarizable continuum model, *J. Chem. Phys.* 110 (1999) 9877–9886, doi:10.1063/1.478861.
- [256] M. Caricato, B. Mennucci, J. Tomasi, F. Ingrosso, R. Cammi, S. Corni, G. Scalmani, Formation and relaxation of excited states in solution: A new time dependent polarizable continuum model based on time dependent density functional theory, *J. Chem. Phys.* 124 (2006) 124520, doi:10.1063/1.2183309.
- [257] A.V. Marenich, C.J. Cramer, D.G. Truhlar, C.A. Guido, B. Mennucci, G. Scalmani, M.J. Frisch, Practical computation of electronic excitation in solution: Vertical excitation model, *Chem. Sci.* 2 (2011) 2143–2161, doi:10.1039/c1sc00313e.
- [258] L.W. Chung, W.M.C. Sameera, R. Ramozzi, A.J. Page, M. Hatanaka, G.P. Petrova, T.V. Harris, X. Li, Z. Ke, F. Liu, H.B. Li, L. Ding, K. Morokuma, The ONIOM method and its applications, *Chem. Rev.* 115 (2015) 5678–5796, doi:10.1021/cr5004419.
- [259] M. Bondanza, M. Nottoli, L. Cupellini, F. Lipparini, B. Mennucci, Polarizable embedding QM/MM: The future gold standard for complex (bio)systems? *Phys. Chem. Chem. Phys.* 22 (2020) 14433–14448, doi:10.1039/d0cp02119a.
- [260] J.M. Olsen, K. Aidas, J. Kongsted, Excited states in solution through polarizable embedding, *J. Chem. Theory Comput.* 6 (2010) 3721–3734, doi:10.1021/ct1003803.
- [261] C. Filippi, F. Buda, L. Guidoni, A. Sinicropi, Bathochromic shift in green fluorescent protein: a puzzle for QM/MM approaches, *J. Chem. Theory Comput.* 8 (2012) 112–124, doi:10.1021/ct200704k.
- [262] S. Osella, S. Knippenberg, Triggering on/off states of photoswitchable probes in biological environments, *J. Am. Chem. Soc.* 139 (2017) 4418–4428, doi:10.1021/jacs.6b13024.
- [263] H. Köppel, W. Domcke, L.S. Cederbaum, Multimode molecular dynamics beyond the Born-Oppenheimer approximation, *Adv. Chem. Phys.* 57 (1984) 59–246.
- [264] R. Improta, V. Barone, F. Santoro, Ab initio calculations of absorption spectra of large molecules in solution: Coumarin C153, *Angew. Chemie - Int. Ed.* 46 (2007) 405–408, doi:10.1002/anie.200602907.
- [265] V. Barone, J. Bloino, M. Biczysko, F. Santoro, Fully integrated approach to compute vibrationally resolved optical spectra: from small molecules to macrosystems, *J. Chem. Theory Comput.* 5 (2009) 540–554, doi:10.1021/ct8004744.
- [266] T. Petrenko, F. Neese, Analysis and prediction of absorption band shapes, fluorescence band shapes, resonance Raman intensities, and excitation profiles using the time-dependent theory of electronic spectroscopy, *J. Chem. Phys.* 127 (2007) 164319, doi:10.1063/1.2770706.
- [267] O. Svoboda, M. Ončák, P. Slaviček, Simulations of light induced processes in water based on ab initio path integrals molecular dynamics. I. Photoabsorption, *J. Chem. Phys.* 135 (2011) 154301, doi:10.1063/1.3649942.
- [268] M. Barbatti, A.J.A. Aquino, H. Lischka, The UV absorption of nucleobases: Semi-classical ab initio spectra simulations, *Phys. Chem. Chem. Phys.* 12 (2010) 4959–4967, doi:10.1039/b924956g.
- [269] R. Crespo-Otero, M. Barbatti, Spectrum simulation and decomposition with nuclear ensemble: Formal derivation and application to benzene, furan and 2-phenylfuran, *Theor. Chem. Acc.* 131 (2012) 1–14, doi:10.1007/s00214-012-1237-4.
- [270] F. Plasser, M. Wormit, A. Dreuw, New tools for the systematic analysis and visualization of electronic excitations. I. Formalism, *J. Chem. Phys.* 141 (2014) 024106, doi:10.1063/1.4885819.
- [271] F. Plasser, Visualisation of electronic excited-state correlation in real space, *ChemPhotoChem* 3 (2019) 702–706, doi:10.1002/cptc.201900014.
- [272] S.A. Mewes, F. Plasser, A. Krylov, A. Dreuw, Benchmarking excited-state calculations using exciton properties, *J. Chem. Theory Comput.* 14 (2018) 710–725, doi:10.1021/acs.jctc.7b01145.
- [273] F. Plasser, H. Lischka, Analysis of excitonic and charge transfer interactions from quantum chemical calculations, *J. Chem. Theory Comput.* 8 (2012) 2777–2789, doi:10.1021/ct300307c.
- [274] F. Siddique, M. Langer, M. Paloncýová, M. Medved', M. Otyepka, D. Nachtigallová, H. Lischka, A.J.A. Aquino, Conformational behavior and optical properties of a fluorophore dimer as model of luminescent centers in carbon dots, *J. Phys. Chem. C* 124 (2020) 14327–14337, doi:10.1021/acs.jpcc.0c02175.
- [275] N.D. Marsh, M.J. Wornat, Polycyclic aromatic hydrocarbons with five-membered rings: Distributions within isomer families in experiments and computed equilibria, *J. Phys. Chem. A* 108 (2004) 5399–5407, doi:10.1021/jp026319i.
- [276] T.M. Figueira-Duarte, K. Müllen, Pyrene-based materials for organic electronics, *Chem. Rev.* 111 (2011) 7260–7314, doi:10.1021/cr100428a.
- [277] S. Shirai, S. Inagaki, Ab initio study on the excited states of pyrene and its derivatives using multi-reference perturbation theory methods, *RSC Adv* 10 (2020) 12988–12998, doi:10.1039/c9ra10483f.
- [278] C. Glidewell, D. Lloyd, Mndo study of bond orders in some conjugated BI- and tri-cyclic hydrocarbons, *Tetrahedron* 40 (1984) 4455–4472, doi:10.1016/S0040-4020(01)98821-0.
- [279] O.EI Bakouri, J. Poater, F. Feixas, M. Solà, Exploring the validity of the Glidewell–Lloyd extension of Clar's π -s sextet rule: assessment from polycyclic conjugated hydrocarbons, *Theor. Chem. Acc.* 135 (2016) 205, doi:10.1007/s00214-016-1970-1.
- [280] C.N. Yeh, J.Da Chai, Role of Kekulé and Non-Kekulé structures in the radical character of alternant polycyclic aromatic hydrocarbons: A TAO-DFT study, *Sci. Rep.* 6 (2016) 1–14, doi:10.1038/srep30562.
- [281] K. Yoneda, M. Nakano, Y. Inoue, T. Inui, K. Fukuda, Y. Shigeta, T. Kubo, B. Champagne, Impact of antidot structure on the multiradical characters, aromaticities, and third-order nonlinear optical properties of hexagonal graphene nanoflakes, *J. Phys. Chem. C* 116 (2012) 17787–17795, doi:10.1021/jp305171k.
- [282] S. Schumacher, Photophysics of graphene quantum dots: Insights from electronic structure calculations, *Phys. Rev. B - Condens. Matter Mater. Phys.* 83 (2011) 081417, doi:10.1103/PhysRevB.83.081417.
- [283] S.S.R.K.C. Yamijala, M. Mukhopadhyay, S.K. Pati, Linear and nonlinear optical properties of graphene quantum dots: a computational study, *J. Phys. Chem. C* 119 (2015) 12079–12087, doi:10.1021/acs.jpcc.5b03531.
- [284] A.M. Silva, M.S. Pires, V.N. Freire, E.L. Albuquerque, D.L. Azevedo, E.W.S. Caetano, Graphene nanoflakes: thermal stability, infrared signatures, and potential applications in the field of spintronics and optical nanodevices, *J. Phys. Chem. C* 114 (2010) 17472–17485, doi:10.1021/jp105728p.
- [285] M.A. Sk, A. Ananthanarayanan, L. Huang, K.H. Lim, P. Chen, Revealing the tunable photoluminescence properties of graphene quantum dots, *J. Mater. Chem. C* 2 (2014) 6954–6960, doi:10.1039/C4TC01191K.
- [286] J. Feng, H. Dong, L. Yu, L. Dong, The optical and electronic properties of graphene quantum dots with oxygen-containing groups: a density functional theory study, *J. Mater. Chem. C* 5 (2017) 5984–5993, doi:10.1039/c7tc00631d.
- [287] H. Abdelsalam, H. Elhaes, M.A. Ibrahim, First principles study of edge carbonylated graphene quantum dots, *Phys. B Condens. Matter* 537 (2018) 77–86, doi:10.1016/j.physb.2018.02.001.
- [288] M. Zhao, F. Yang, Y. Xue, D. Xiao, Y. Guo, A Time-dependent DFT study of the absorption and fluorescence properties of graphene quantum dots, *ChemPhysChem* 15 (2014) 950–957, doi:10.1002/cphc.201301137.
- [289] K.R. Geethalakshmi, T.Y. Ng, R. Crespo-Otero, Tunable optical properties of OH-functionalised graphene quantum dots, *J. Mater. Chem. C* 4 (2016) 8429–8438, doi:10.1039/c6tc02785g.
- [290] L. Hedin, On correlation effects in electron spectroscopies and the GW approximation, *J. Phys. Condens. Matter* 11 (1999) 489–528, doi:10.1088/0953-8984/11/42/201.
- [291] E.E. Salpeter, H.A. Bethe, A relativistic equation for bound-state problems, *Phys. Rev.* 84 (1951) 1232–1242, doi:10.1103/PhysRev.84.1232.
- [292] Y. Li, H. Shu, X. Niu, J. Wang, Electronic and optical properties of edge-functionalized graphene quantum dots and the underlying mechanism, *J. Phys. Chem. C* 119 (2015) 24950–24957, doi:10.1021/acs.jpcc.5b05935.
- [293] A.T. Sheardy, D.M. Arvapalli, J. Wei, Experimental and time-dependent density functional theory modeling studies on the optical properties of carbon nanodots, *J. Phys. Chem. C* 124 (2020) 4684–4692, doi:10.1021/acs.jpcc.9b10373.
- [294] E.V. Kundelev, N.V. Tepliakov, M.Y. Leonov, V.G. Maslov, A.V. Baranov, A.V. Fedorov, I.D. Rukhlenko, A.L. Rogach, Amino functionalization of carbon dots leads to red emission enhancement, *J. Phys. Chem. Lett.* 10 (2019) 5111–5116, doi:10.1021/acs.jpclett.9b01724.
- [295] J. Wang, S. Cao, Y. Ding, F. Ma, W. Lu, M. Sun, Theoretical investigations of optical origins of fluorescent graphene quantum dots, *Sci. Rep.* 6 (2016) 1–5, doi:10.1038/srep24850.
- [296] S. Sarkar, M. Sudolská, M. Dubecký, C.J. Reckmeier, A.L. Rogach, R. Zbořil, M. Otyepka, Graphitic nitrogen doping in carbon dots causes red-shifted absorption, *J. Phys. Chem. C* 120 (2016) 1303–1308, doi:10.1021/acs.jpcc.5b10186.
- [297] M. Sudolská, M. Otyepka, Exact roles of individual chemical forms of nitrogen in the photoluminescent properties of nitrogen-doped carbon dots, *Appl. Mater. Today* 7 (2017) 190–200, doi:10.1016/j.apmt.2017.03.004.
- [298] G. Sandeep Kumar, R. Roy, D. Sen, U.K. Ghorai, M. Mazumder, S. Saha, K.K. Chattopadhyay, Amino-functionalized graphene quantum dots: Origin of tunable heterogeneous photoluminescence, *Nanoscale* 6 (2014) 3384–3391, doi:10.1039/c3nr05376h.

- [299] B. Saha, P.K. Bhattacharyya, Understanding reactivity, aromaticity and absorption spectra of carbon cluster mimic to graphene: A DFT study, *RSC Adv.* 6 (2016) 79768–79780, doi:10.1039/c6ra15016k.
- [300] H.X. Wang, J. Xiao, Z. Yang, H. Tang, Z.T. Zhu, M. Zhao, Y. Liu, C. Zhang, H.L. Zhang, Rational design of nitrogen and sulfur co-doped carbon dots for efficient photoelectrical conversion applications, *J. Mater. Chem. A.* 3 (2015) 11287–11293, doi:10.1039/c5ta02057c.
- [301] Z. Fan, Y. Li, X. Li, L. Fan, S. Zhou, D. Fang, S. Yang, Surrounding media sensitive photoluminescence of boron-doped graphene quantum dots for highly fluorescent dyed crystals, chemical sensing and bioimaging, *Carbon* 70 (2014) 149–156, doi:10.1016/j.carbon.2013.12.085.
- [302] J. Feng, H. Dong, B. Pang, F. Shao, C. Zhang, L. Yu, L. Dong, Theoretical study on the optical and electronic properties of graphene quantum dots doped with heteroatoms, *Phys. Chem. Chem. Phys.* 20 (2018) 15244–15252, doi:10.1039/c8cp01403e.
- [303] M. Ghoshghae, Z. Azizi, M. Ghambarian, Conductivity tuning of charged triazine and heptazine graphitic carbon nitride ($g\text{-C}_3\text{N}_4$) quantum dots via non-metal (B, O, S, P) doping: DFT calculations, *J. Phys. Chem. Solids.* 141 (2020) 109422, doi:10.1016/j.jpcs.2020.109422.
- [304] S. Mura, L. Stagi, L. Malfatti, C.M. Carbonaro, R. Ludmerczki, P. Innocenzi, Modulating the optical properties of citrazinic acid through the monomer-to-dimer transformation, *J. Phys. Chem. A.* 124 (2020) 197–203, doi:10.1021/acs.jpca.9b10884.
- [305] P. Elvati, E. Baumeister, A. Violi, Graphene quantum dots: effect of size, composition and curvature on their assembly, *RSC Adv* 7 (2017) 17704–17710, doi:10.1039/c7ra01029j.
- [306] S. Osella, S. Knippenberg, Environmental effects on the charge transfer properties of graphene quantum dot based interfaces, *Int. J. Quantum Chem.* 119 (2019) e25882, doi:10.1002/qua.25882.
- [307] S. Gu, C. Te Hsieh, Y. Ashraf Gandomi, J.K. Chang, J. Li, J. Li, H. Zhang, Q. Guo, K.C. Lau, R. Pandey, Microwave growth and tunable photoluminescence of nitrogen-doped graphene and carbon nitride quantum dots, *J. Mater. Chem. C.* 7 (2019) 5468–5476, doi:10.1039/c9tc00233b.
- [308] H.M. Yoon, S. Kondaraju, J.S. Lee, Molecular dynamics simulations of the friction experienced by graphene flakes in rotational motion, *Tribol. Int.* 70 (2014) 170–178, doi:10.1016/j.triboint.2013.10.005.
- [309] H. Ren, X. Shen, J. Dai, G. Peng, L. Liang, J.-W. Shen, L. Zhang, On the mechanism of graphene quantum dot encapsulation by chitosan: A molecular dynamics study, *J. Mol. Liq.* 320 (2020) 113453, doi:10.1016/j.molliq.2020.113453.
- [310] M. Wang, Y. Sun, X. Cao, G. Peng, I. Javed, A. Kallinen, T.P. Davis, S. Lin, J. Liu, F. Ding, P.C. Ke, Graphene quantum dots against human IAPP aggregation and toxicity: In vivo, *Nanoscale* 10 (2018) 19995–20006, doi:10.1039/c8nr07180b.
- [311] M. Zhou, Q. Shen, J.W. Shen, L. Jin, L. Zhang, Q. Sun, Q. Hu, L. Liang, Understanding the size effect of graphene quantum dots on protein adsorption, *Colloids Surfaces B: Biointerfaces* 174 (2019) 575–581, doi:10.1016/j.colsurfb.2018.11.059.
- [312] A. Faridi, Y. Sun, M. Mortimer, R.R. Aranha, A. Nandakumar, Y. Li, I. Javed, A. Kallinen, Q. Fan, A.W. Purcell, T.P. Davis, F. Ding, P. Faridi, P.C. Ke, Graphene quantum dots rescue protein dysregulation of pancreatic β -cells exposed to human islet amyloid polypeptide, *Nano Res* 12 (2019) 2827–2834, doi:10.1007/s12274-019-2520-7.
- [313] C. Martín, G. Jun, R. Schurhammer, G. Reina, P. Chen, A. Bianco, C. Ménard-Moyon, Enzymatic degradation of graphene quantum dots by human peroxidases, *Small* 15 (2019) 1905405, doi:10.1002/sml.201905405.
- [314] S. Jeong, R.L. Pinals, B. Dharmadhikari, H. Song, A. Kalluri, D. Debnath, Q. Wu, M.H. Ham, P. Patra, M.P. Landry, Graphene quantum dot oxidation governs noncovalent biopolymer adsorption, *Sci. Rep.* 10 (2020) 1–14, doi:10.1038/s41598-020-63769-z.
- [315] M. Vatanparast, Z. Shariatnia, Revealing the role of different nitrogen functionalities in the drug delivery performance of graphene quantum dots: A combined density functional theory and molecular dynamics approach, *J. Mater. Chem. B.* 7 (2019) 6156–6171, doi:10.1039/c9tb00971j.
- [316] C. Liu, P. Elvati, S. Majumder, Y. Wang, A.P. Liu, A. Violi, Predicting the time of entry of nanoparticles in lipid membranes, *ACS Nano* 13 (2019) 10221–10232, doi:10.1021/acs.nano.9b03434.
- [317] L. Liang, Z. Kong, Z. Kang, H. Wang, L. Zhang, J.-W. Shen, Theoretical evaluation on potential cytotoxicity of graphene quantum dots, *ACS Biomater. Sci. Eng.* 2 (2016) 1983–1991, doi:10.1021/acsbiomaterials.6b00390.
- [318] C. Yao, Y. Tu, L. Ding, C. Li, J. Wang, H. Fang, Y. Huang, K. Zhang, Q. Lu, M. Wu, Y. Wang, Tumor cell-specific nuclear targeting of functionalized graphene quantum dots in vivo, *Bioconjug. Chem.* 28 (2017) 2608–2619, doi:10.1021/acs.bioconjugchem.7b00466.
- [319] D. Mombrú, M. Romero, R. Faccio, Á.W. Mombrú, Electronic structure of edge-modified graphene quantum dots interacting with polyaniline: vibrational and optical properties, *J. Phys. Chem. C.* 121 (2017) 16576–16583, doi:10.1021/acs.jpcc.7b03604.
- [320] H. Li, J. Huang, Y. Song, M. Zhang, H. Wang, F. Lu, H. Huang, Y. Liu, X. Dai, Z. Gu, Z. Yang, R. Zhou, Z. Kang, Degradable carbon dots with broad-spectrum antibacterial activity, *ACS Appl. Mater. Interfaces.* 10 (2018) 26936–26946, doi:10.1021/acsami.8b08832.
- [321] F. Ehrat, S. Bhattacharyya, J. Schneider, A. Löf, R. Wyrwich, A.L. Rogach, J.K. Stolarczyk, A.S. Urban, J. Feldmann, Tracking the source of carbon dot photoluminescence: Aromatic domains versus molecular fluorophores, *Nano Lett* 17 (2017) 7710–7716, doi:10.1021/acs.nanolett.7b03863.
- [322] E.V. Kundelev, N.V. Teplakov, M.Y. Leonov, V.G. Maslov, A.V. Baranov, A.V. Fedorov, I.D. Rukhlenko, A.L. Rogach, Toward bright red-emissive carbon dots through controlling interaction among surface emission centers, *J. Phys. Chem. Lett.* (2020) 8121–8127, doi:10.1021/acs.jpcclett.0c02373.
- [323] S. Erimban, S. Daschakraborty, Translocation of a hydroxyl functionalized carbon dot across a lipid bilayer: An all-atom molecular dynamics simulation study, *Phys. Chem. Chem. Phys.* 22 (2020) 6335–6350, doi:10.1039/c9cp05999g.
- [324] W. Liu, S. Xu, R. Liang, M. Wei, D.G. Evans, X. Duan, In situ synthesis of nitrogen-doped carbon dots in the interlayer region of a layered double hydroxide with tunable quantum yield, *J. Mater. Chem. C.* 5 (2017) 3536–3541, doi:10.1039/c6tc05463c.
- [325] D. Sen, P. Błoński, M. Otyepka, Band-edge engineering at the carbon dot-TiO₂ interface by substitutional boron doping, *J. Phys. Chem. C.* 123 (2019) 5980–5988, doi:10.1021/acs.jpcc.8b11554.
- [326] G. Rajender, J. Kumar, P.K. Giri, Interfacial charge transfer in oxygen deficient TiO₂-graphene quantum dot hybrid and its influence on the enhanced visible light photocatalysis, *Appl. Catal. B Environ.* 224 (2018) 960–972, doi:10.1016/j.apcatb.2017.11.042.
- [327] S.V. Badalov, R. Wilhelm, W.G. Schmidt, Photocatalytic properties of graphene-supported titania clusters from density-functional theory, *J. Comput. Chem.* 41 (2020) 1921–1930, doi:10.1002/jcc.26363.
- [328] S. Chen, N. Ullah, R. Zhang, Engineering the excited state of graphitic carbon nitride nanostructures by covalently bonding with graphene quantum dots, *Theor. Chem. Acc.* 139 (2020) 20, doi:10.1007/s00214-019-2525-z.
- [329] L. Zhang, J. Zhang, Y. Xia, M. Xun, H. Chen, X. Liu, X. Yin, Metal-free carbon quantum dots implant graphitic carbon nitride: Enhanced photocatalytic dye wastewater purification with simultaneous hydrogen production, *Int. J. Mol. Sci.* 21 (2020) 1052, doi:10.3390/ijms21031052.
- [330] R.B. Dos Santos, F. De Brito Mota, R. Rivelino, A theoretical evaluation of the effect of water on the electronic properties of low density amorphous carbon nanoparticles, *Carbon N. Y.* 50 (2012) 2788–2795, doi:10.1016/j.carbon.2012.02.041.
- [331] L. Li, M. Xu, W. Song, A. Ovcharenko, G. Zhang, D. Jia, The effect of empirical potential functions on modeling of amorphous carbon using molecular dynamics method, *Appl. Surf. Sci.* 286 (2013) 287–297, doi:10.1016/j.apusc.2013.09.073.
- [332] S. Best, J.B. Wasley, C. de Tomas, A. Aghajamali, I. Suarez-Martinez, N.A. Marks, Evidence for glass behavior in amorphous carbon, *C. J. Carbon Res.* 6 (2020) 50, doi:10.3390/c6030050.
- [333] V.L. Deringer, G. Csányi, Machine learning based interatomic potential for amorphous carbon, *Phys. Rev. B.* 95 (2017) 094203, doi:10.1103/PhysRevB.95.094203.
- [334] B. Bhattarai, A. Pandey, D.A. Drabold, Evolution of amorphous carbon across densities: An inferential study, *Carbon N. Y.* 131 (2018) 168–174, doi:10.1016/j.carbon.2018.01.103.
- [335] L. Vallan, E.P. Urriolabeitia, F. Rupiérrez, J.M. Matxain, R. Canton-Vitoria, N. Tagmatarchis, A.M. Benito, W.K. Maser, Supramolecular-enhanced charge transfer within entangled polyamide chains as the origin of the universal blue fluorescence of polymer carbon dots, *J. Am. Chem. Soc.* 140 (2018) 12862–12869, doi:10.1021/jacs.8b06051.
- [336] N.V. Teplakov, E.V. Kundelev, P.D. Khavlyuk, Y. Xiong, M.Y. Leonov, W. Zhu, A.V. Baranov, A.V. Fedorov, A.L. Rogach, I.D. Rukhlenko, sp²-sp³-Hybridized atomic domains determine optical features of carbon dots, *ACS Nano* 13 (2019) 10737–10744, doi:10.1021/acs.nano.9b05444.
- [337] X. Niu, Y. Li, H. Shu, J. Wang, Revealing the underlying absorption and emission mechanism of nitrogen doped graphene quantum dots, *Nanoscale* 8 (2016) 19376–19382, doi:10.1039/c6nr06447g.
- [338] R. Rieger, K. Müllen, Forever young: Polycyclic aromatic hydrocarbons as model cases for structural and optical studies, *J. Phys. Org. Chem.* 23 (2010) 315–325, doi:10.1002/poc.1644.
- [339] A. Kuc, T. Heine, G. Seifert, Structural and electronic properties of graphene nanoflakes, *Phys. Rev. B - Condens. Matter Mater. Phys.* 81 (2010) 1–7, doi:10.1103/PhysRevB.81.085430.
- [340] S.S.R.K.C. Yamijala, A. Bandyopadhyay, S.K. Pati, Electronic properties of zigzag, armchair and their hybrid quantum dots of graphene and boron-nitride with and without substitution: a DFT study, *Chem. Phys. Lett.* 603 (2014) 28–32, doi:10.1016/j.cplett.2014.04.025.
- [341] G. Eda, Y.Y. Lin, C. Mattevi, H. Yamaguchi, H.A. Chen, I.S. Chen, C.W. Chen, M. Chhowalla, Blue photoluminescence from chemically derived graphene oxide, *Adv. Mater.* 22 (2010) 505–509, doi:10.1002/adma.200901996.
- [342] Z. Qian, J. Ma, J. Zhou, P. Lin, C. Chen, J. Chen, H. Feng, Facile synthesis of halogenated multi-walled carbon nanotubes and their unusual photoluminescence, *J. Mater. Chem.* 22 (2012) 22113–22119, doi:10.1039/c2jm34275h.
- [343] R. Sharma, N. Nair, M.S. Strano, Structure-reactivity relationships for graphene nanoribbons, *J. Phys. Chem. C.* 113 (2009) 14771–14777, doi:10.1021/jp904814h.
- [344] K. Yoshizawa, K. Yahara, K. Tanaka, T. Yamabe, Bandgap oscillation in polyphenanthrenes, *J. Phys. Chem. B.* 102 (1998) 498–506, doi:10.1021/jp972799f.
- [345] F. Yan, Z. Sun, H. Zhang, X. Sun, Y. Jiang, Z. Bai, The fluorescence mechanism of carbon dots, and methods for tuning their emission color: a review, *Micromol. Acta.* 186 (2019) 583, doi:10.1007/s00604-019-3688-y.
- [346] S. Li, Y. Li, J. Cao, J. Zhu, L. Fan, X. Li, Sulfur-doped graphene quantum dots as a novel fluorescent probe for highly selective and sensitive detection of Fe³⁺, *Anal. Chem.* 86 (2014) 10201–10207, doi:10.1021/ac503183y.

[347] M. Li, S.K. Cushing, X. Zhou, S. Guo, N. Wu, Fingerprinting photoluminescence of functional groups in graphene oxide, *J. Mater. Chem.* 22 (2012) 23374, doi:[10.1039/c2jm35417a](https://doi.org/10.1039/c2jm35417a).

[348] J. Schneider, C.J. Reckmeier, Y. Xiong, M. Von Seckendorff, A.S. Sussha, P. Kasák, A.L. Rogach, Molecular fluorescence in citric acid-based carbon dots, *J. Phys. Chem. C* 121 (2017) 2014–2022, doi:[10.1021/acs.jpcc.6b12519](https://doi.org/10.1021/acs.jpcc.6b12519).